Imaging Discontinuities in the Lithospheric Mantle Using a New, Automated Ps and Sp Receiver Function Workflow

by

Peter Makus

Thesis for the Degree
Master of Science in Geophysics

Department of Earth Science
University of Bergen

November 2020

Abstract

Over the last decades, the receiver function technique has been widely established as a standard tool for surveying sharp changes in elastic properties of the Earth's crust and upper mantle. To date, very few studies have attempted to use receiver functions for global imaging. To overcome the lack of toolsets for global receiver function imaging, I have developed PyGLImER - a Python-based software suite capable of creating global images from both P-to-S and S-to-P converted teleseismic waves via a comprehensive receiver function workflow. In this thesis, I discuss the functionalities of PyGLImER and demonstrate its efficiency, effectiveness, and robustness on synthetic and real earthquake data examples. I show images from receiver functions, binned and stacked by conversion point, from four regions, one of which - North America - is the focus of a more thorough discussion. The receiver function survey of the North American continent presented here is of unprecedented size resulting in high-resolution images which allow to accurately constrain the depth of the cratonic lithosphere-asthenosphere boundary, make new observations of a positive correlation between the number of midlithospheric discontinuities (MLD) and the age of the lithosphere, and identify a sharp transition from the Proterozoic belts dominated by dipping structures to Archean cratons dominated by horizontal and subhorizontal MLDs. Those observations lead me to make the following hypotheses: (1) Thick continental lithosphere is formed by cyclic (i.e., periodic) processes. (2) In hotter Archean times, the formation of continents was dominated by plume-induced mechanisms (subcretion) causing horizontal MLDs, whereas, in the later Precambrian, the dominance shifted towards subduction accretion. (3) Considering (1) and (2), I deem MLDs to be caused by layers of frozen melt as previously suggested by petrological studies.

Acknowledgements

First and foremost, I would like to thank my supervisor, Stéphane Rondenay, for your contagious enthusiasm for new observations, methods, and interpretation that led me to enjoy doing Science and motivated me to make this thesis become what it is now. I am also grateful to my co-supervisors Lars Ottemöller and Felix Halpaap for the time and patience that you had for my questions and doubts, which, at times, were surely a few.

In addition, I thank Lucas Sawade for the very fruitful discussions about CCP binning and stacking, tips and hints in Python programming, your opinion and help concerning the future of the PyGLImER software, and, ultimate, for joining the project.

I also wish to thank the multitude of scientists, who acquired the data that are vital for this project. Without open data policies and scientists who work by those principles, this thesis would not have been possible.

On a more personal note, I would like to thank those who supported me in my decisions and studies and have provided diversion in the more difficult times. In particular, I would like to thank my wife, Rachel, for her love, support, and patience; my friends, Erik, Camena, Tiffany, Bård, Ida, Victoria, and all those others, who have made the time in Bergen so special and memorable.

Contents

Acronyms

MLDs mid-lithospheric discontinuities. 7–9

NCEDC Nothern California Earthquake Datacenter. 37

NECESSArray NorthEast China Extended SeiSmic Array. 60, 61

NIEP National Institute for Earth Physics - Romania. 37

NOA National Observatory of Athens. 37

NVG downwards negative velocity gradient. 57, 58, 60–64, 68, 70, 71, 80, 82, 83, 85, 88–90, 92–95, 145–148

ORFEUS Observatories and Research Facilities for European Seismology. 37

PRF Ps receiver function. 1, 2, 17, 22, 26, 29, 31, 36, 38, 39, 41, 45, 48, 51–53, 57–65, 70, 74, 75, 80, 85–87, 90, 91, 94, 98, 121, 123, 127, 132

PyGLImER Pythonic Global Lithospheric Imaging using Earthquake Recordings. iv, 34–36, 38–41, 44–46, 48, 49, 56, 61, 68, 70–74, 86–88, 96, 97, 119, 149

QC quality control. 38, 39

RESIF French Seismologic and Geodetic Network. 37

RF receiver function. 1, 9, 21, 22, 26, 28–34, 36, 38, 39, 41, 43–50, 56, 57, 59, 61, 63, 65, 68, 69, 86–88, 97, 98, 120, 132

RMF Rocky Mountain Front. 67, 68, 75, 80–84, 89, 90, 95

SCEDC Southern California Earthquake Datacenter. 37

SNR signal to noise ratio. 30, 38, 39, 45

SRF Sp receiver function. 2, 17, 22, 29–32, 36, 38, 39, 41, 45, 46, 48, 50–52, 55, 57–61, 63–65, 68, 70–74, 80, 83, 85–91, 94, 95, 131

UiB University of Bergen. 37

USGS United States Geological Survey. 37

USP University of São Paulo. 37

Chapter 1

Introduction

One of the main goals in the field of Earth Science has traditionally been the study of the dynamic processes shaping the Earth. To achieve a deeper understanding of the endogenous component of these processes, it is crucial to study the structural composition of the Earth. Close to the surface (i.e., the upper 10 km of the crust), traditional geological methods such as the examination of outcrops or well cores can be employed. In the Earth's deeper layers however, one cannot rely on direct observation and has to utilise geophysical methods to obtain information about their structure, state, and composition. These methods measure variations in physical parameters (e.g., electromagnetic, thermodynamic, or mechanical). The subgroup of methods that surveys the elastic behaviour of the subsurface uses seismic waves to quantify how elastic properties vary.

For studies on regional and global scale, tomography (see e.g., Fowler, 2004; Stein & Wysession, 2009; Shearer, 2019) and receiver function (RF) analysis (Langston, 1979) are the two most-commonly used seismic methods (e.g., Rondenay, 2009; Kind & Yuan, 2011). While tomographic techniques are sensitive to smooth velocity transitions, RFs are more commonly used to image discrete discontinuities (e.g., Rondenay, 2009; Kind & Yuan, 2011).

The RF technique uses converted teleseismic body waves to estimate the impulse response of the subsurface (e.g., Rondenay, 2009; Kind & Yuan, 2011). Most commonly, one analyses the primary P- and S-arrival and their multiples (Gurrola et al., 1995). In theory however, any seismic phase that produces pre-critical conversions can be used. The technique is based on the assumption that the primary phase corresponds to the source-side influence on the seismogram, which one aims to remove (Rondenay, 2009). The majority of RF surveys are conducted using data from P to S conversions (henceforth referred to as Ps receiver function (PRF)) due to the higher frequency content of the P-wave arrival

and, thus, higher resolution (Yuan et al., 2006).

Interpretation of receiver functions created from S to P conversions (from here on Sp receiver function (SRF)) is usually more challenging since the primary S-wave arrival is obscured by the coda of other arrivals (Wilson et al., 2006; Yuan et al., 2006). Recently however, it has become common practice to image the mid-lithospheric discontinuity (MLD) and the lithosphere-asthenosphere boundary (LAB) using SRFs (e.g., Rychert et al., 2007; Hansen et al., 2009; Abt et al., 2010; Lekić & Fischer, 2014; Hopper & Fischer, 2015; O'Driscoll & Miller, 2015; Wang et al., 2016; Lavayssière et al., 2018; Hopper & Fischer, 2018; Kind et al., 2020). SRF data are employed since PRFs are often contaminated by multiples of strong crustal phases, such as the Moho conversion, in a depth range of 80-150 km (Rondenay, 2009), which coincides with the depth in that LAB and MLD often occur (Wilson et al., 2006; Yuan et al., 2006; Lekić & Fischer, 2017).

Understanding LAB and MLD is crucial to determine the origin and mechanics of plate tectonics and the formation of thick continental lithosphere. Despite recent efforts to image LAB and MLD, there are still many unknowns. These include for example the physical cause for these discontinuities or even their depth, which is still only scarcely mapped.

Although SRF surveys have become more common, only few studies discuss and compare results from both PRFs and SRFs. In this thesis, I will use constraints from images created from PRFs and SRFs to shed more light on the mechanics that fuel the dynamics of our planet's upper layers and provide another piece to a vastly complex puzzle. Motivated by this goal, I develop a software suite that includes a workflow capable of producing global images created from both PRF and SRF data with a minimal amount of user interference.

Chapter 2

Earth Structure and Dynamics

2.1 Earth Structure

At global scale, the Earth can be divided into a simplified model consisting of layers with differing thermal, mechanical, chemical, and mineralogical properties. Variations in these properties can be measured using various geophysical techniques. Wherever they cause variations in seismic velocities, seismological tools can be used to identify boundaries (Stein & Wysession, 2009).

Sharp discontinuities in seismic velocities can be associated with distinct seismic phases. Over the last century, seismologists have evaluated those phases to improve our understanding of the Earth's structure. Although models are becoming more accurate, there are still unidentified phases and existing models are of coarse resolution (Stein & Wysession, 2009).

Once a reasonable structural model is defined, one can use travel times for source receiver pairs to refine a model further. In addition to using the measured travel times, amplitudes and waveforms can provide additional information (Stein & Wysession, 2009). Later in this thesis, I will elaborate further on seismic methods and how they are used to explore the Earth's internal structure.

Figure 2.1 shows a wedge as well as a scaled half-circle illustrating the most important layers and boundaries in the Earth's interior. These layers are:

1. **The crust:** A thin, solid layer covering the Earth's surface. On continents and especially under orogens (see Figure 2.1), the crust is thicker than under oceans. Chemically, continental crust is dominated by silicate-rich rocks, whereas oceanic crust is mainly composed of mafic rocks (Stuwe, 2007).

   The base of the crust is defined by the Mohorovičić discontinuity (commonly and

henceforth simply referred to as the Moho). The Moho is a seismic boundary that may coincide with chemical and petrological interfaces. Some authors do therefore refer to the different boundaries at Moho depth as "seismological Moho" and "petrological Moho" (e.g., Mengel & Kern, 1992). Traditionally, the seismological Moho is defined as the depth where the compressional wave velocity exceeds 7.6 km/s. Although reliably sensed using seismic imaging methods, the Moho's nature is highly varying in terms of sharpness, strength, and depth. In receiver function imaging, the Moho often produces the strongest conversion peak (Prodehl et al., 2013; Thybo et al., 2013).

2. **The mantle:** Under the crust lies the mantle, which is mainly composed of olivine (Stuwe, 2007).

   Two very sharp and reliably occurring seismic discontinuities are located at about 410km (d410) and 660km (d660)) depth. These discontinuities bound the mantle transition zone (Zhang & Schmandt, 2019). The d660 is thought to be caused by the post-spinel transition (i.e., the decomposition of ringwoodite into bridgmanite and ferropericlase) and subdivides the mantle into upper and lower mantle (Ishii et al., 2019).

3. **The core:** The core is divided into two layers: The outer core stretches from a depth of approximately 2900 km to about 5100 km. The fact that it is liquid distinguishes it from the other layers. The inner core is solid and is, as the outer core, mainly made up from nickel and iron (e.g., Stuwe, 2007).

When considering rheological rather than chemical properties, the terminology is slightly different. Instead of crust and mantle, we refer to lithosphere and asthenosphere (see Figure 2.1). While the mechanical behaviour of the lithosphere is mostly - though not perfectly - elastic, on a geological timescale, viscous flow occurs in the asthenosphere. In contrast to the relatively clear boundary between crust and mantle, it can be difficult to define a sharp seismological boundary between lithosphere and asthenosphere (Fowler, 2004; Stuwe, 2007).

Since receiver functions mainly target the upper 800 kilometres of the Earth, we shall hereafter only concern ourselves with the lithosphere, the asthenosphere, and their relatively elusive separation.
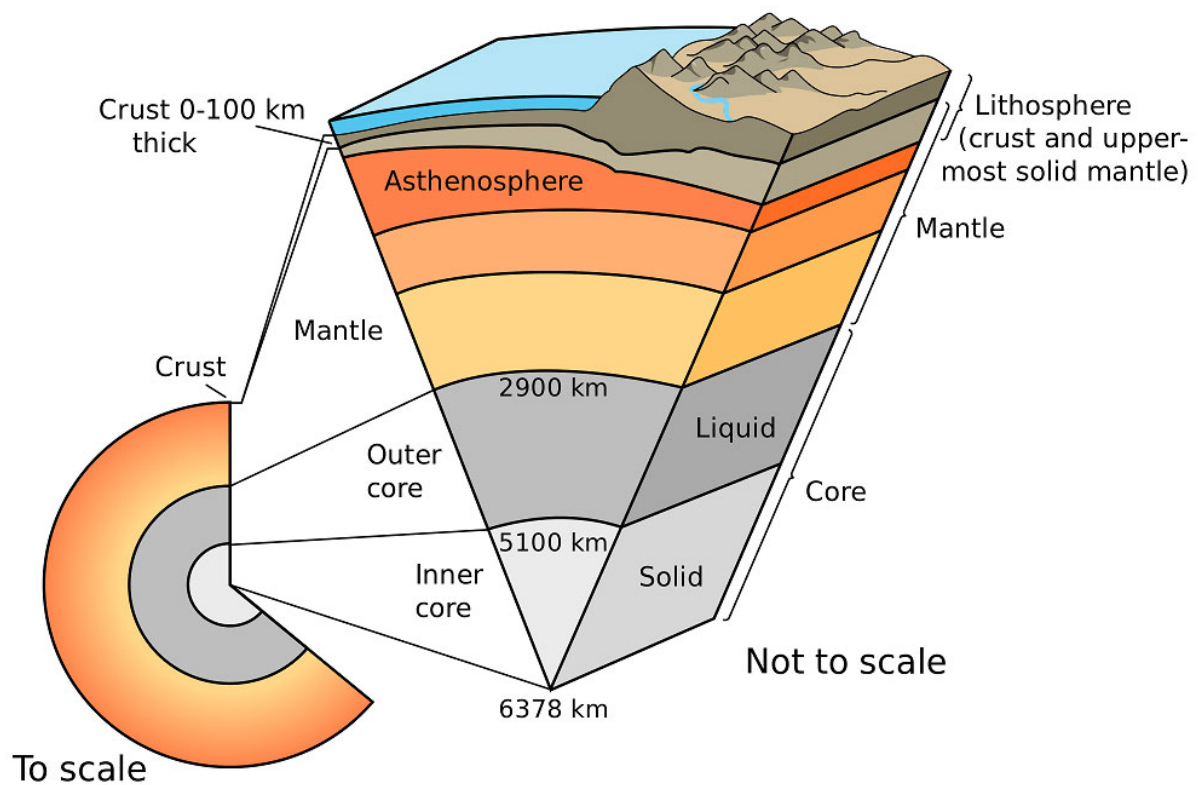
Figure 2.1: **The major boundaries in the Earth.** *Note the difference between rheological and compositional division of the upper layers of the Earth (i.e.,lithosphere and asthenosphere versus crust and mantle, respectively). Figure retrieved from USGS (1999).*

2.2   Plate Tectonics

The central process shaping the lithosphere is plate tectonics. The theory of plate tectonics has arguably been the most controversial and impactful concept in Earth Sciences of the 20th century. The concept of continental drift was first proposed by Alfred Wegener in 1912, but it took until the 1960s for an altered version of the theory (then called plate tectonics) to be widely accepted by the scientific community (e.g., Le Pichon, 2019).

In most basic terms, the theory states that patches of the rigid lithosphere (i.e., the plates) are moving mechanically decoupled over the asthenosphere. The dynamics of the plates' movement cause deformation at their boundaries. These plate boundaries can be divided into three categories with different kinematic nature (Fowler, 2004) (see Figure 2.2):

1. *Divergent* boundaries are locations where plates are drifting away from each other. Such locations include mid-oceanic ridges where new oceanic lithosphere is created from upwelling asthenospheric material.

2. At *convergent* boundaries, plates are moving towards each other. Convergence can cause the denser plate to be subducted under the lighter plate. The slab of the dense plate (most times, of oceanic nature) is then gradually melting in the deep Earth. The collision of two plates causes a great deal of deformation leading to the development of mountain chains (such as the Himalayas, Andes, or Alps).

3. *Conservative* plate boundaries are boundaries where the motion of the two plates is antiparallel and, consequently, no material is destroyed or created. An example of such a boundary is the San Andreas fault in the western United States.

One of the most basic principles underlying this theory is the strong contrast between oceanic and continental lithosphere. As most seismic data have been collected on continents and data coverage on continental lithosphere is thus superior, I will throughout this thesis focus solely on the structure of continental lithosphere. Beyond the clear distinction of continental and oceanic plates, lithosphere differs regionally due to deformation caused by plate tectonics or deep Earth dynamics - such as hot spots. That is, lithosphere is, other than the simple model above might suggest, not internally homogeneous and contains a number of discontinuities, which I will discuss in the following section.
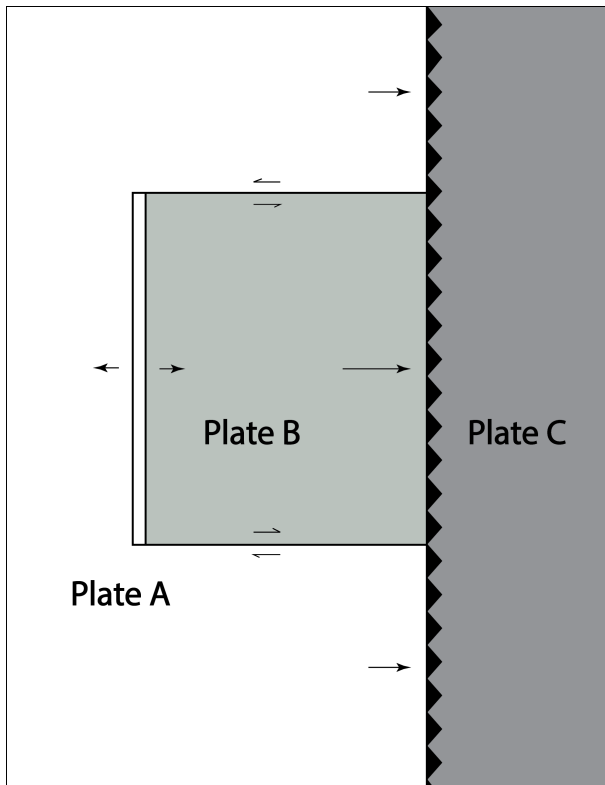
Figure 2.2: **The three types of plate boundaries.** *Movements of the plates are illustrated by arrows. The size of the arrows is proportional to the plates' velocity relative to plate C. In this case, plate C is the lightest plate as plate A and B are subducted under plate C (subduction occurs at the black triangles). The western boundary of plate B is divergent. That is, this boundary represents a mid-oceanic ridge. The other boundaries between Plate A and B are conservative. Figure redrawn from Fowler (2004).*

2.3   Lithospheric Discontinuities

Aside from the Moho, there are a handful of seismic boundaries in the lithosphere, two of which are particularly pronounced: Mid-lithospheric discontinuities (MLDs), which occur predominantly in continental lithosphere, and the lithosphere-asthenosphere boundary (LAB) found in both continental and oceanic lithosphere. In contrast to the Moho, these two boundaries are associated with a drop in seismic velocity with increasing depth (see e.g., Eaton et al., 2009; Fischer et al., 2010; Selway et al., 2015; Yuan & Romanowicz, 2017; Karato & Park, 2017).

2.3.1   The Lithosphere-Asthenosphere Boundary

The concept of plate tectonics implies that there must be a boundary between lithosphere and asthenosphere that is responsible for the decoupling of the layers and enables the plates to move on the asthenosphere. Although researchers generally agree on the existence of the LAB, it has been difficult to detect in many regions of the world. Especially in cratonic lithosphere (i.e., stable thick old continents), the signal of the LAB is particularly elusive (Yuan & Romanowicz, 2017).
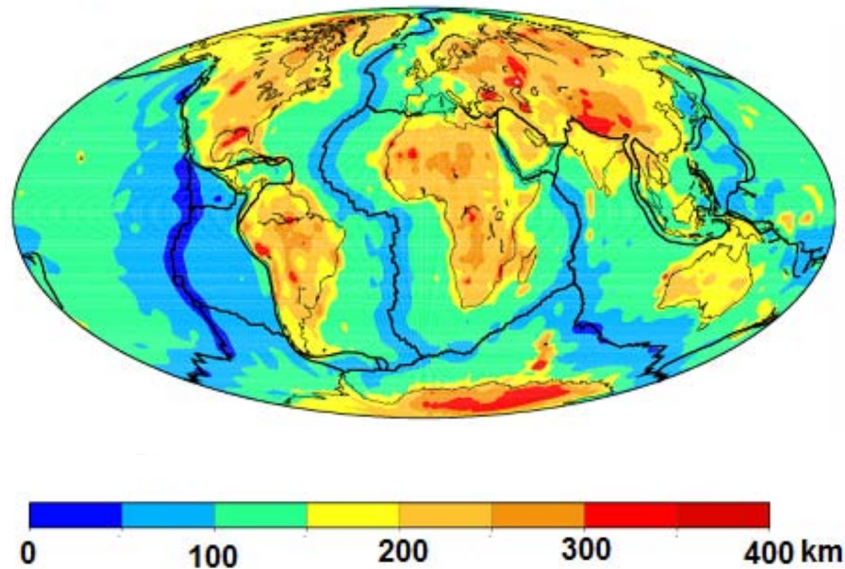
Figure 2.3: **Global depth distribution of the thermal LAB modelled from heat flux data.** *The LAB is particularly deep in old cratonic continents, while it is shallowest in younger, tectonically actives areas. Retrieved from Hamza & Vieira (2012).*

When the LAB is detected in cratons, the signal is often measured at significantly greater depths than in younger lithosphere. In younger, tectonically active parts of the lithosphere, the LAB is located at shallow depths, whereas it can be more than 250 km deep in old, cratonic lithosphere (Hamza & Vieira, 2012; Yuan & Romanowicz, 2017; Karato & Park, 2017; Kind & Yuan, 2017; Hopper & Fischer, 2018; Kind et al., 2020). Hamza & Vieira (2012) have used global heat flux maps to estimate the depth of the thermal LAB (see Figure 2.3). That is, the point where the temperature surpasses a certain threshold and, by definition, the asthenosphere begins (Kind & Yuan, 2017). While providing a useful estimation for the LAB's depth, their model employs many assumptions and does consequently suffer from relatively high uncertainties. Seismological data can provide depth estimates of the seismological LAB with greater resolution and lower uncertainty (Cooper et al., 2017; Karato & Park, 2017).

2.3.2 Midlithospheric Discontinuities

In cratons, other sharp, predominantly negative velocity contrasts can be observed. These velocity contrasts are referred to as mid-lithospheric discontinuities (MLDs). Often, MLDs appear more consistently and stronger than the cratonic LAB. Negative MLDs can predominantly be seen in old and stable cratonic continents at relatively shallow depths (about 70-120 km - similar to the LAB in tectonically active areas) (e.g., Selway et al.,

2015; Karato et al., 2015; Kind et al., 2015; Yuan & Romanowicz, 2017; Kind & Yuan, 2017; Hopper & Fischer, 2018). Most commonly, an MLD is observed as one broad, negative signal. However, some recent seismic studies detect several MLDs in the North American (Cooper & Miller, 2014; Hopper et al., 2014; Lekić & Fischer, 2014; Wirth & Long, 2014; Ford et al., 2016), West Australian (Sun et al., 2018), and West African (Sodoudi et al., 2013) cratons. While less common, also positive MLDs have been observed (Selway et al., 2015; Hopper & Fischer, 2015; Calò et al., 2016).

More recently, some authors have suggested that the signal commonly interpreted as MLD might be at least partially attributed to artefacts. Selway et al. (2015) claim that, while one of the MLD's physical causes may be a phase change in amphibole, the MLD may be the sum of several smaller lithospheric discontinuities. Krueger et al. (2019) and Kind et al. (2020) show that an MLD is more commonly observed, when creating RFs using deconvolution methods that are prone to generating side lobes.

2.3.3 Potential Causes for Seismological LAB and MLD

In places where the LAB and MLD can be identified using seismological methods, the cause for the sharp drop in seismic velocity cannot just simply be a temperature gradient (i.e., the thermal LAB) (Fischer et al., 2010; Karato & Park, 2017; Kind & Yuan, 2017). A number of theories have been proposed on which mechanisms are the cause for LAB and MLD, but, until now, their cause has remained subject of discussion. Unlike the boundaries in the mantle transition zone (i.e., the d410 and d660), these discontinuities cannot be linked to mineral phase transformation because they occur at depths where the minerals constituting the bulk of the mantle have no phase transitions that can cause negative velocity gradients. Amongst the suggested causes are partial melting, layering in anisotropy, layering in mineralogical composition, the temperature dependence of seismic velocity paired with the influence of anelastic relaxation, and grain-boundary sliding (Karato & Park, 2017). However, there is no general agreement on causes (or even the existence) of a seismological LAB and MLD.

Chapter 3

Theoretical Background

In chapter 2, I briefly discussed what is known about the structure and dynamics of the Earth's interior. Although I mentioned key terms such as velocity contrast, I omitted the information on how knowledge of such structures was obtained in the first place. Also, at present, the question on how the Earth's interior is structured remains far from entirely answered. Attempting to find answers to this question takes up a significant part in the work of geophysicists, who employ various techniques to improve our understanding of the Earth's interior.

3.1 Seismic Waves

Seismic energy travels through the solid Earth in form of waves. Those waves are subdivided into the groups of *body waves* and *surface waves*. While surface waves travel along the Earth's surface, body waves penetrate the deeper layers of the Earth.

Body waves themselves are differentiated into compressional or primary *(P-) waves* and secondary or shear *(S-) waves*. P-waves cause particle movement parallel to propagation direction, whereas, for S-waves, particle movement is perpendicular to propagation direction (e.g., Stein & Wysession, 2009) (see Figure 3.1). The velocity at which the two waves travel through a medium are given by the explicit solutions of the seismic wave equation (see for example Shearer, 2019), and are expressed as follows (Shearer, 2019):

$$v_p = \sqrt{\frac{K + \frac{4}{3}\mu}{\rho}} \tag{3.1}$$

$$v_s = \sqrt{\frac{\mu}{\rho}} \tag{3.2}$$

Where v_p and v_s are the P- and S-wave velocities, respectively. K is the *Bulk-modulus* or incompressibility (i.e., the measure of resistance of a material against hydrostatic/lithostatic compression), μ is the *shear modulus* (i.e., the resistance of a material to shearing), and ρ denotes the mass density.

Considering equations 3.1 and 3.2, two things become obvious: Firstly, since by definition K, μ, and ρ are positive, P-waves must propagate faster than S-waves. Secondly, $\mu = 0$ in fluids and, therefore, S-waves cannot travel through fluids[1] (Stein & Wysession, 2009).

S waves: ground motion is perpendicular to wave direction

Direction of wave propagation   Onset of waves

P waves: ground motion is parallel to wave direction
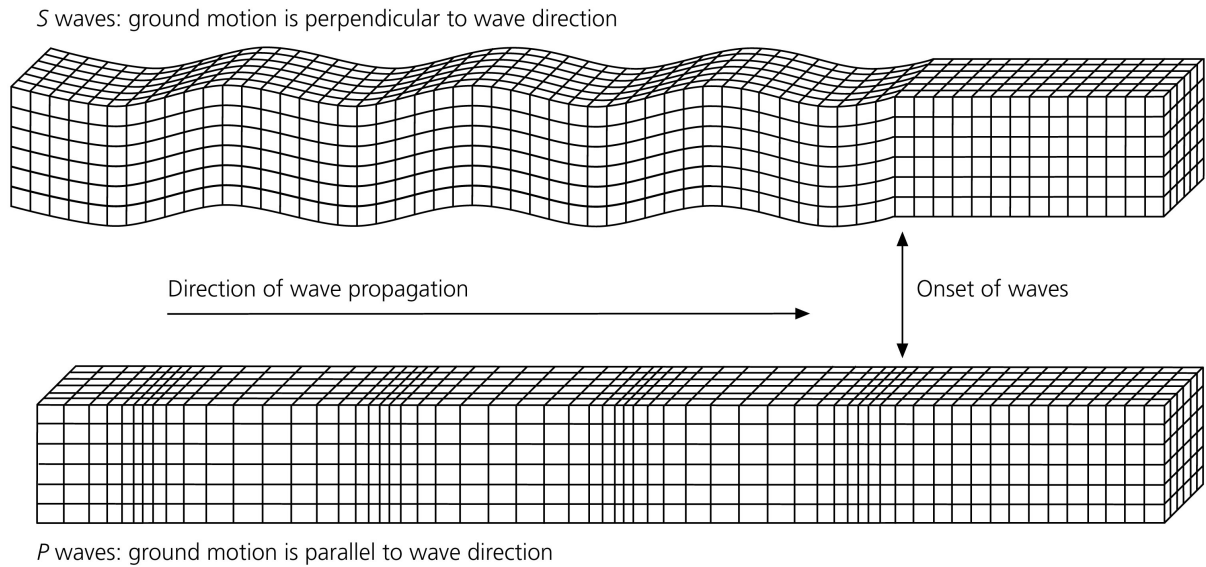
Figure 3.1: **Propagation direction and direction of particle motion for seismic P- and S-waves.** *S-waves (upper panel) cause particle motion perpendicular to propagation direction. P-waves (lower panel) cause particle motion parallel to the direction of propagation. The shown strains are highly exaggerated. Figure from Stein & Wysession (2009).*

Seismic waves can travel large distances and the ground motion caused by a sufficiently large earthquake happening in Japan can still be measured and recorded in Norway (provided one possesses a sufficiently sensitive ground motion sensor). For small scale surveys, which are for example often conducted in oil and gas exploration, seismic waves are measured relatively close to the source. When targeting global and regional structures however, it is often desirable to record seismic waves far from their source. At distances greater than 1000km, we refer to waves as *teleseismic* waves (Rondenay, 2009).

---

[1]That is also the reason, why we know that the outer core is liquid. If the outer core was solid, one would expect additional seismic phases to arrive.

3.1.1 Reflection and Transmission of Seismic Waves at Impedance Contrasts

When the variations in geological properties in the Earth discussed in chapter 2 cause changes in Bulk modulus K, shear modulus μ, or density ρ of the material, they will affect the propagation of seismic waves as well (Stein & Wysession, 2009). These variations are often expressed as variations in *seismic impedance Z* (e.g., Shearer, 2019):

$$Z = v\rho \tag{3.3}$$

It follows from equation 3.3 that the P-wave impedance Z_p differs from the S-wave impedance Z_s.

When a seismic wave passes through an impedance contrast[2], both its amplitude and, if the impedance contrast is caused by a velocity contrast, its travel direction are altered (e.g., Stein & Wysession, 2009; Shearer, 2019). For vertical incidence (i.e., the propagation direction is perpendicular to said boundary), the amplitude change of the refracted wave entering from a material with a seismic impedance Z_1 into a material with Z_2 is given by (e.g., Stein & Wysession, 2009):

$$\frac{A_2}{A_1} = \frac{2\rho_1 v_1}{\rho_1 v_1 + \rho_2 v_2} \tag{3.4}$$

In addition to the transmitted wave, a reflected wave will be created and, thereby, the law of energy conservation will be satisfied (e.g., Stein & Wysession, 2009).

For many applications, it is useful to introduce the concept of rays. A ray is essentially the geometrical description of the wave's travel path. While physically unrealistic (i.e., rays have an infinite frequency), rays can be very useful to explain the behaviour of seismic waves on larger scales.

For any other case than vertical incidence, equation 3.4 becomes complicated by the fact that, aside from transmitted and reflected waves, converted waves appear. Consider for example a P-ray piercing a seismic impedance boundary caused by two layers with differing seismic velocities at an incident angle $i_1 \neq 0°$. In such a case, the energy from only one ray will be split into four "portions" (see Figure 3.2). The amplitudes corresponding to each of the created waves depending on the seismic impedances Z_1, Z_2, and the incident

---

[2]In the following discussion, I consider the case of sharp and infinitesimally thin impedance boundaries.

angle i_1 are then given by the *Zoeppritz equations* (e.g., Aki & Richards, 2002).

In addition to the amplitudes, also the ray direction and, for S-waves the polarisation of particle motion, will be altered at velocity contrasts as rays are refracted and reflected. The angles by which rays will be refracted are governed by *Snell's law* (Stein & Wysession, 2009; Shearer, 2019):

$$\frac{\sin i_1}{v_1} = \frac{\sin i_2}{v_2} = p \tag{3.5}$$

Where i_1 is the incident angle and i_2 the emergent angle at which the ray enters the medium while transitioning from a material with a seismic velocity v_1 to a material with a velocity v_2. Figure 3.2 shows the case of an incident P-wave at a solid to solid transition. For such a case, there are four different seismic velocities to consider and, thus, four different outgoing ray-paths. From equation 3.5, it follows that p is constant for a given ray and independent of material. p provides a measure for a ray's horizontal *slowness* (defining slowness as the inverse of velocity $u = 1/v$) and is called the *ray parameter* (Shearer, 2019). The ray parameter is one of the core parameters needed to define a wave and will keep appearing throughout this thesis.

When $v_2 = v_1/\sin i_1$, i_1 is termed the *critical incident angle*. In the case of critical or supercritical incidence, all energy will be reflected and refracted into phases with pre-critical emergent angles. For a seismic ray at a solid-solid transition, up to two critical angles can occur; one for a P-to-P or S-to-S transmission and a second one for a P-to-S or S-to-P conversion (Shearer, 2019).
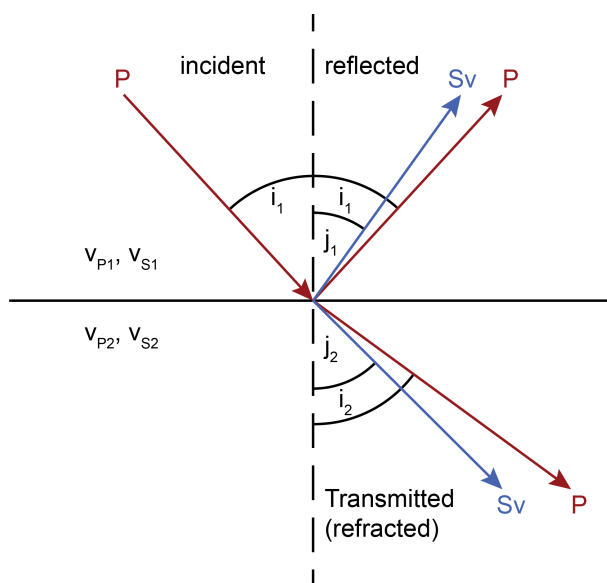
Figure 3.2: **Behaviour of an incident P-ray with non-vertical incidence on a planar velocity contrast.** *An incident P-ray (P) is reflected and refracted at a downwards-positive velocity contrast (i.e., $v_{P1} < v_{P2}$ and $v_{S1} < v_{S2}$). Additionally, the incident P-ray is converted into an S-ray (Sv) with vertically polarised particle motion (i.e., polarisation direction perpendicular to the ray and parallel to the image plane). If the illustrated velocity boundary was not perpendicular to the image plane or the incident ray not parallel to the imagine plane, the incident ray would be converted in both horizontally and vertically polarised S-rays. In accordance with Snell's law, the incident angle i_1 equals the angle in that the P-ray is reflected. All other angles differ from i_1 as given by equation 3.5. Figure redrawn from Stein & Wysession (2009).*

3.1.2   Seismic Waves in a Spherical Earth

In section 3.1.1, we considered the case of a flat Earth (i.e., a Cartesian coordinate system in that the depth is always parallel to the z-direction). Since in this thesis I am concerned with teleseismic waves, it is necessary to understand how rays travel through a quasi-spherical body - such as the Earth.

Even for an entirely one-dimensionally layered Earth, the incident angle at consecutive boundaries will not equal the emergent angle at their respective preceding boundary (see Figure 3.3) (Shearer, 2019). We can therefore establish that the ray parameter p as introduced in equation 3.5 is only valid for a flat Earth. Henceforth, we will be using a spherical ray parameter and, for better differentiation, I will refer to p as established in equation 3.5 solely as the horizontal slowness. The spherical ray parameter is given by (e.g., Shearer, 2019):

$$p_{sph} = \frac{r \sin i}{v} \tag{3.6}$$
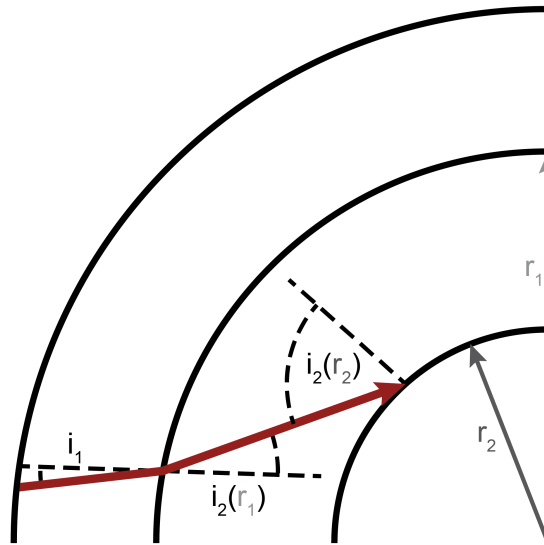
Figure 3.3: **Travel path and incident angles of a teleseismic ray in a layered, spherical Earth.** *Illustrated is the strongly simplified case of a purely one-dimensionally layered Earth with homogeneous layers. Note that the emergent angle i_2 does not equal the incident angle i_2 as the incident angles do not only depend on velocity but also on the distance from the Earth's midpoint as given by equation 3.6. Figure redrawn from Shearer (2019).*

$r = 6371 \, \text{km} - z$ denotes the distance from the Earth's centre. In other words: At the surface, the horizontal slowness equals the ray parameter. However, at depths below 30km, ray-paths predicted with a flat Earth model will become inaccurate (Shearer, 2019).

Given equation 3.6, source and receiver position, and a layered velocity model such as the iasp91 model (Kennett & Engdahl, 1991), it is fairly straight-forward to give a prediction of ray-paths and travel times. In theory, we have an infinite number of phases, scattered and converted at impedance contrasts, arriving at the receiver. In practice, most of these phases are hardly measurable and, aside from the primary phases, only phases reflected and converted at major contrasts will be differentiable from the *seismic coda* (i.e., the sum of many smaller scattered arrivals) (Stein & Wysession, 2009).

Considering that earthquakes release energy both in the form of P- and S-waves and only the boundaries shown in Figure 2.1, we are still left with a considerable amount of phase arrivals. Some of these major phases are shown in Figure 3.4. Examining Figure 3.4a, one can see that some phases (such as SKS) do only appear at certain *epicentral distances* (i.e., the angular distance between earthquake and receiver). The areas where
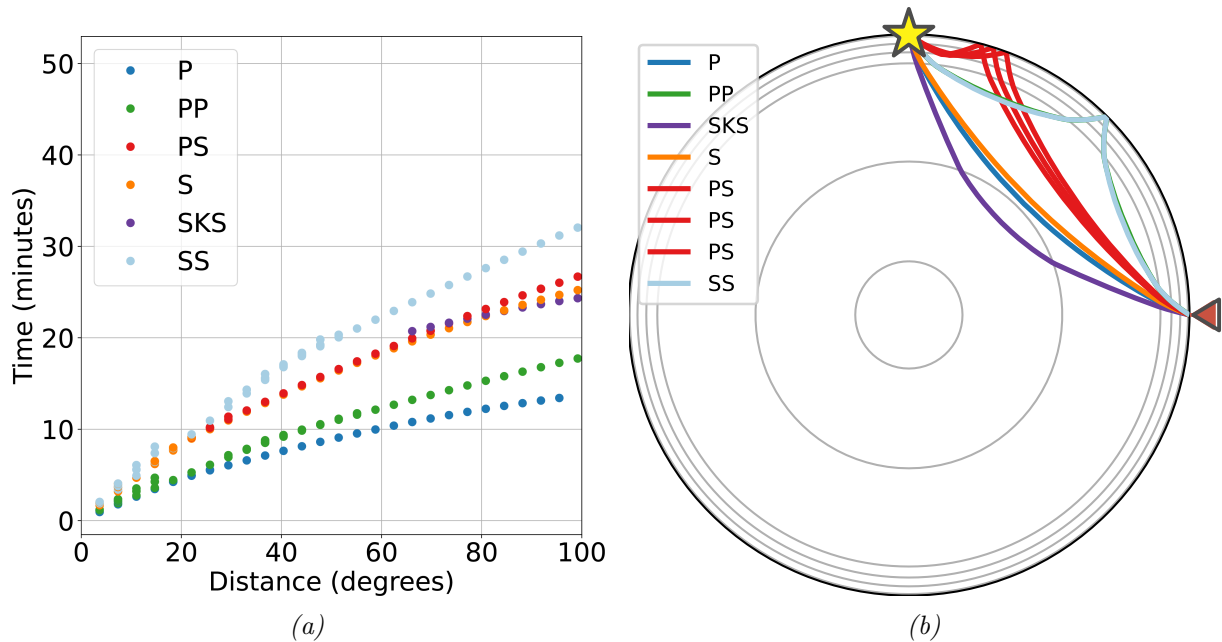
Figure 3.4: **Teleseismic phases in the spherical Earth**. *For an earthquake occurring at a depth of 10km, we can observe a number of phases at teleseismic distance. Travel times (a) and ray-paths (b) of some of those phases and a source depth of 10km are shown here. P and S are called the primary phases because they travel from source to receiver on a direct path without being subject to reflection or conversion. Paths and times are computed and plotted using a spherical Earth model and the iasp91 velocity model with the Obspy toolbox (Krischer et al., 2015). Ray paths shown in (b) correspond to an epicentral distance of 90°*

phases do not arrive are called *shadow zones* and they occur due to supercritical angles or low velocity zones inside of the Earth (such as the outer core), where rays will bend downward instead of upward as for instance in Figure 3.4b (Shearer, 2019).

3.1.3   Attenuation and Imperfect Elasticity

Modelling seismic waves as rays can yield satisfactory explanations for some phenomena observed in the solid Earth. Others, like the attenuation of seismic energy, require a physically more complex explanation, which we can find in wave theory.

Mathematically, a harmonic seismic wave can be described by the elastic wave equation, a second order partial differential equation relating strain to time and space (e.g., Shearer, 2019). Wave equations can be solved using a harmonic wave solution. For an acoustic wave in one dimension, the real part of the solution takes the form (e.g., Stein & Wysession, 2009):

$$p(x,t) = A \cos\left(\omega t \pm kx\right) \tag{3.7}$$

Here, $p(x, t)$ is the pressure at point x and time t and A the maximum amplitude of the wave. Together with the constants ω and k, A defines a certain wave. $\omega = 2\pi f$ is called the *angular frequency*, with f being the *frequency*, and describes the number of oscillations in a given time frame Δt at a fixed point x_0 (Stein & Wysession, 2009). When examining a fixed point in time t_0 at an arbitrary location x, the *wavenumber k* describes the number of oscillations in a given distance Δx. Often, the *wavelength* $\lambda = \frac{1}{2\pi k}$ rather than the wave number is given.

In a perfectly elastic medium, the law of conservation of energy dictates that the sum of the energy at all points $x_s + \Delta x$ has to equal the energy at the source's location x_s. In a three-dimensional, homogeneous medium, all those points are distributed on the surface of a sphere with the radius Δx. The wave's energy at an arbitrary of these points is therefore anti proportional to its travelled distance. Since the square root of the energy equals the amplitude the amplitude reduces by a factor proportional to $\frac{1}{\Delta x}$.

In a real-life medium (i.e., a medium with imperfect elasticity), in addition to energy partitioning at impedance contrasts (see section 3.1.1) and geometrical spreading, one has to consider a third cause of attenuation; the conversion of kinetic energy into other forms of energy such as heat. The so-called *intrinsic attenuation* or absorption, is inversely quantified by a quality factor Q, which is a measure for the energy decay per oscillation (Shearer, 2019).

The fact that the energy loss depends on the number of oscillations has one important consequence: The frequency spectrum of an earthquake recorded at a teleseismic distance will be dominated by significantly lower frequencies than a recording of the same earthquake at a local or regional distance (Shearer, 2019).

Q also differs for P- and S-waves as it depends on two different classes of attenuation: Bulk and shear attenuation, respectively. In the Earth, observation shows that shear attenuation is significantly higher than Bulk attenuation and S-waves have therefore even lower frequency spectra than P-waves at teleseismic distances (Shearer, 2019). In the following section, we will see that the differing frequencies of teleseismic P and S-waves have important implications on the resolution of PRFs and SRFs.

3.2   Seismic Signal

Measurements of seismic waves are conducted at the Earth's surface and, hence, at a fixed point in space $\mathbf{x_r}$. Therefore, we can regard them as a seismic signal that is only

dependent on time.

3.2.1   Representation of Signals in Time and Frequency Domain

We can represent any periodic signal either as a function of time or as a function of frequency. The signal can be transferred from time into frequency domain by applying the *Fourier transform* (Stein & Wysession, 2009):

$$F(\omega) = \int\limits_{-\infty}^{\infty} f(t)e^{-i\omega t}dt \qquad (3.8)$$

The Fourier theorem essentially postulates that any periodic signal can be expressed as a sum of sines and cosines with varying phases, frequencies, and amplitudes. The magnitude of the Fourier transform describes the amplitude distribution in the signal, whereas the angle between real and imaginary part of the Fourier transform expresses the signal's phase as a function of frequency. We call these functions amplitude and phase spectrum, respectively (Stein & Wysession, 2009).

3.2.2   Recording

Seismic signals are recorded with *seismographs*. Seismographs themselves consist of different components, two of which are of particular importance to seismologists - the *seismometer* and the *analogue to digital converter* or digitiser. The seismometer is the component that senses the ground motion and translates it into an electrical signal. Subsequently, the electric signal is digitised by the analogue to digital converter. Digital signals are easy to save, redistribute, and manipulate. Today, almost all earthquake recordings are digital (e.g., Havskov & Alguacil, 2004).

Modern seismometers exploit the Lorentz force principle to translate ground motion into a current whose voltage depends on the ground's velocity. However, the seismometer's sensitivity is frequency dependent. Depending on their frequency band (i.e., the breadth of the spectrum) and the periods to that the sensor is especially sensitive, we classify seismic instrumentation as short-period, long-period, broadband, or ultra-broadband. Mathematically, the instruments sensitivity can be described by the *instrument response*, a complex frequency-dependent function. To normalise the ground motion measured by different seismometers and, thereby, allow for direct comparisons, one has to correct for the instrument response. Seismic stations often accommodate several (most commonly
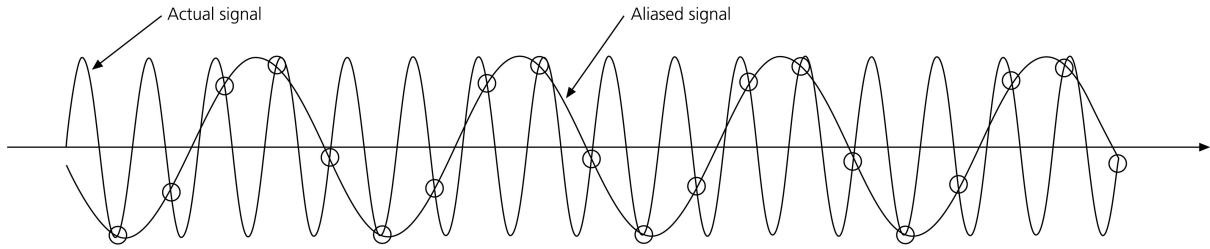
Figure 3.5: ***Aliasing in the time domain.*** *If the signal is sampled with a frequency lower than the Nyquist frequency, the data in between the sample points are interpolated incorrectly and the recorded signal will be aliased. Figure retrieved from Stein & Wysession (2009).*

three) seismic sensors to measure the ground displacement in several linearly-independent directions (Havskov & Alguacil, 2004).

The analogue, electrical signal produced by the sensor is then digitised using an analogue to digital converter. In the process of digitisation, the signal is sampled every Δt seconds and, thus, transferred from a continuous function to a discrete recording with a finite number of samples (i.e., recording points). Δt is called the *sample interval* and its inverse $f_s = \frac{1}{\Delta t}$ is the *sample rate* (Havskov & Alguacil, 2004).

When sampling a signal f_s has to be at least twice of the highest frequency in the signal. If the recorded signal contains any frequencies higher than $f_s/2$, the signal will be irreversibly *aliased*. That is, energy from the higher frequencies will appear in the recording. An illustration of aliasing in the time domain is shown in Figure 3.5. $f_s/2$ is called the *Nyquist frequency* f_{Ny} (Stein & Wysession, 2009).

3.2.3   The Frequency Content of a Seismic Signal

Up to this point, we assumed that the recording of the seismic signal is noise-free. That is, the only element causing ground motion at the receiver position $\mathbf{x}_r$ is the seismic event one aims to record. In reality however, the seismograph records a multitude of overlapping signals originating from a wide variety of natural and man-made sources. Such sources include for example ocean waves, weather-related noise sources, seismic events other than the one that we aim to record, instrument noise (i.e., electrical noise from the seismic instrument), or traffic (Havskov & Ottemoller, 2010). The frequency distribution of global background noise energy is shown by the new global high (NHNM) and new global low noise models (NLNM) (Peterson, 1993) (see Figure 3.6).

In order to enhance the signal and mitigate all unwanted noise, one can filter a signal so that certain frequencies are preserved while others are removed. Filtering is easiest un-
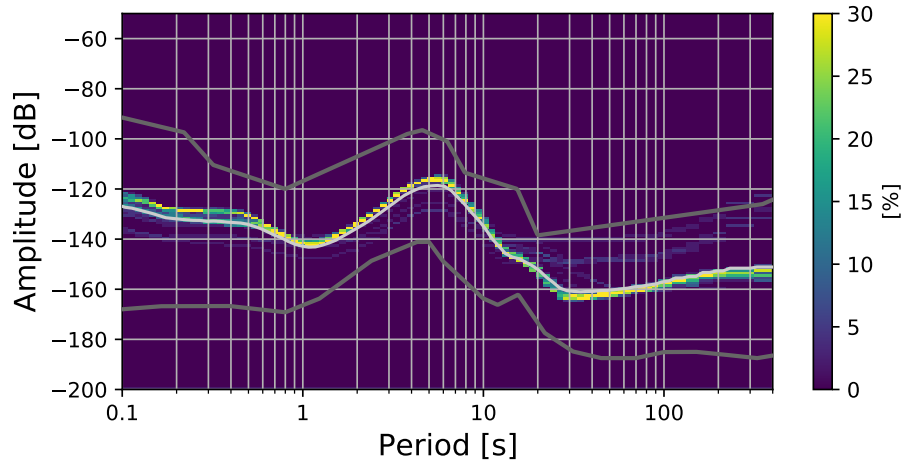
Figure 3.6: **The noise power spectrum of an arbitrary seismic station in comparison to the NHNM and NLNM line** *(upper and lower grey graph, respectively.) The background noise spectra show the primary and secondary seismic peaks at about 5s and 15s period, which are both caused by ocean waves. The noise at the sample station shows the density in form of a histogram (coloured) and the average noise level (white) for 24 hours. Figure created using ObsPy (Krischer et al., 2015).*

derstood in frequency domain, where a filter function (i.e., a function that ranges between 1 and 0) is simply multiplied with the recording. Filters that remove low frequencies are called *low-cut* (or *high-pass*) filters and those that preserve low frequencies while removing higher frequencies are called *high-cut* (or *low-pass*) filters. Multiplying the two filters results in a *bandpass filter* that only preserves a certain frequency band between low-cut and high-cut frequency (for smooth filter functions also referred to as the *corner frequencies*). For example, aliasing is prevented by using a steep high-cut filter with a corner frequency lower than the digitiser's Nyquist frequency (Havskov & Alguacil, 2004). In time domain, the mathematical operation that filters a signal is called *convolution* (Shearer, 2019) and is given by (e.g., Rondenay, 2009):

$$f(t) * s(t) = s(t) * f(t) = \int_{\tau_1}^{\tau_2} s(\tau)f(t-\tau)d\tau \tag{3.9}$$

where τ is the time lag between the signal $s(t)$ and the filter function $f(t)$.

3.2.4   The Resolution of a Seismic Signal

Ultimately, the aim of this thesis is to image structures with the aid of seismic waves. Therefore, it is crucial to understand which parameters influence the resolution that can be achieved, when imaging with seismic signals. In seismic imaging, the resolution that can be achieved is controlled by the wavelength of the signal, which itself is dependent on the signal's frequency content and the seismic velocity at the point $\mathbf{x_1}$ (i.e., the point, which contains the structure that one aims to image) (Fowler, 2004):

$$\lambda(\mathbf{x_1}) = \frac{v(\mathbf{x_1})}{f(\mathbf{x_1})} \tag{3.10}$$

If the distance between receiver point $\mathbf{x_r}$ and $\mathbf{x_1}$ is sufficiently small compared to the distance between the source and $\mathbf{x_1}$, it is reasonable to assume that $f(\mathbf{x_1}) \approxeq f(\mathbf{x_r})$. As established in section 3.1.3, the frequency band for teleseismic waves is very low (i.e., mostly not higher than 1-1.5Hz) and small and intermediate scale structures cannot be resolved with teleseismic waves. The vertical resolving power can be approximated as $\lambda/2$ (Rychert et al., 2007) (i.e., 3km for $v_p = 6km/s$ and a dominant frequency of 1Hz). Teleseismic S-waves are usually ill-suited to target structures with a vertical extent of less than about 10 km (Wittlinger & Farra, 2007; Hopper et al., 2017).

Horizontal resolution depends on the size of the *Fresnel zone* and is significantly lower than vertical resolution (Wittlinger & Farra, 2007). The width of the Fresnel zone is given by (e.g., Fowler, 2004):

$$w = \sqrt{2(\|\mathbf{x_r} - \mathbf{x_1}\|)\lambda + \frac{\lambda^2}{4}} \tag{3.11}$$

where $\|\cdot\|$ denotes the L2-norm of a vector. However, Lekić & Fischer (2017) discuss factors other than the width of the Fresnel zone that influence the resolution of teleseismic wave. They conclude that depending on illumination horizontal resolution might be higher or lower than suggested by equation 3.11.

3.3   Receiver Functions

One of many techniques to image large-scale velocity discontinuities using seismic waves is the receiver function (RF) technique (Langston, 1979) and this thesis is dedicated to imaging with RFs. In the RF technique, teleseismic arrivals and their converted phases

are used to determine the depth and magnitude of the velocity contrasts causing the conversions (see Figure 3.7). The technique is based on the assumption that the primary arrival equals the source-side influence on the seismogram, whilst the converted phase is the result of a convolution of the ground's *impulse response* under the receiver with the incident wavelet. One then seeks to remove the sources influence and, hence, recover the impulse response (Rondenay, 2009).

That RFs use converted and primary arrivals implies that there must be two subgroups of RFs; those that use a primary P phase and its converted Ps phase (see Langston, 1979) and some that rely on primary S arrival and its Sp conversion (e.g., Farra & Vinnik, 2000). The two different families are referred to as Ps receiver function (PRF) and Sp receiver function (SRF), respectively. Since the S primary phase arrives after the P arrival, it is often in the P-coda or the coda of another primary phase. This and the fact that teleseismic S-waves have a significantly lower frequency spectrum causes SRFs to be nosier and of lower resolution (Rondenay, 2009). Consequently, they are harder to interpret and there are fewer examples of their application than for PRFs. However, since Sp conversions arrive prior to their primary phase, conversions are not contaminated by multiples as is the case for Ps conversions (e.g., Wilson et al., 2006; Yuan et al., 2006). Particularly Ps conversions from depths of about 100 km are obstructed by strong Moho-multiples. Therefore, studies using SRFs to survey the MLD and LAB have recently been increasing in number (e.g., Rychert et al., 2005, 2007; Hansen et al., 2009; Abt et al., 2010; Miller & Eaton, 2010; Miller & Piana Agostinetti, 2012; Lekić & Fischer, 2014; Hopper & Fischer, 2015; Kind et al., 2015; Wang et al., 2016; Knapmeyer-Endrun et al., 2017; Hopper & Fischer, 2018; Kind et al., 2020).

3.3.1   Separation of Primary and Converted Phase

To isolate primary wave and near-receiver scattered wavefield, we have to confine them to separate components of the seismogram. By convention, the three components of a seismogram are measured parallel to northern (N), eastern (E), and vertical (Z)[3] direction (Havskov & Alguacil, 2004) with the result that energy from both primary and converted wave is spread over all three components. By using a simple matrix rotation, the seismogram can be cast into a radial-transverse-vertical (RTZ) coordinate system, in which N and E component are rotated until the N-component points antiparallel to the source direction (Rondenay, 2009). The rotation is given by (e.g., Rondenay, 2009):

---

[3]Throughout this thesis, the Z-direction is upward positive.
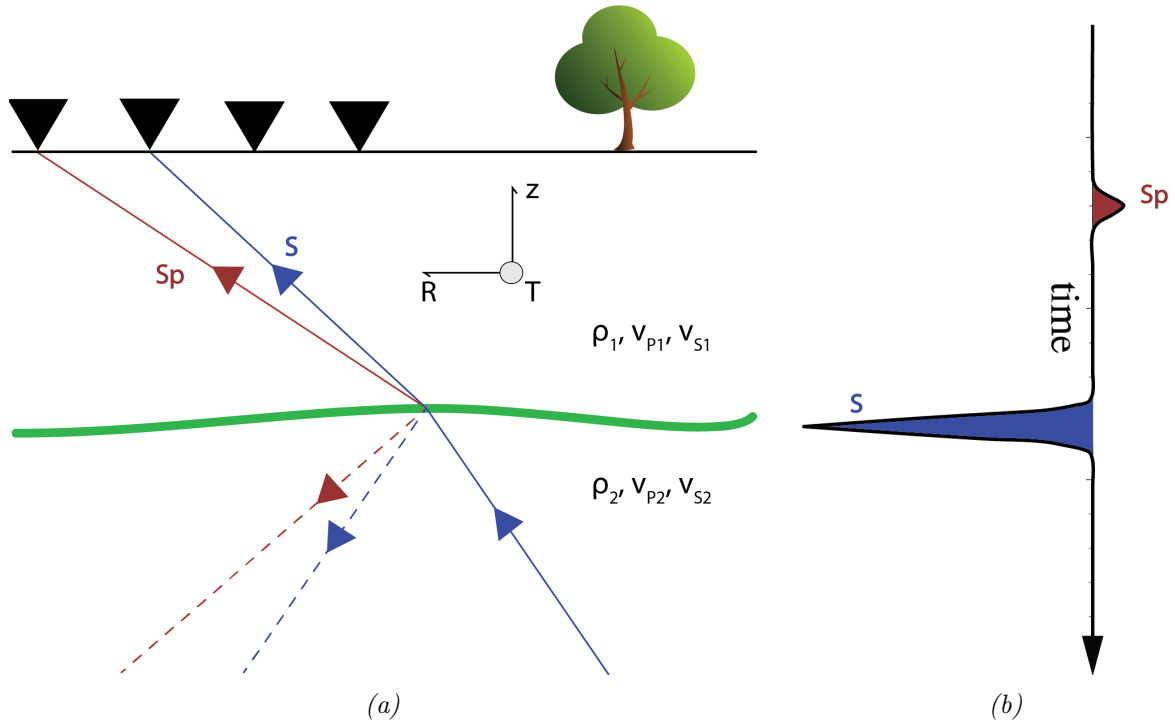
Figure 3.7: **Conversion of an incident, teleseismic S-wave at a downward-negative velocity discontinuity at depth.** *Note that the Sp conversion arrives prior to the primary S-wave, whereas multiples would arrive after the primary phase. (a) shows a vertical cross-section through the subsurface, in which an incident teleseismic S-wave (blue) is converted into a P-wave (red) at a velocity contrast (green) under the receiver (black, downward-pointing triangle). Solid lines represent converted or direct ray-paths, whereas dashed lines show reflected rays. (b) is the theoretical output of the receiver's radial (R) component synthetically created using a Ricker function as incident wavelet (Frederiksen & Bostock, 2000). Red and blue peaks correspond to P- and S-wave energy, respectively.*

$$\begin{pmatrix} R \\ T \\ Z \end{pmatrix} = \begin{pmatrix} -cos(\gamma) & -sin(\gamma) & 0 \\ sin(\gamma) & -cos(\gamma) & 0 \\ 0 & 0 & 1 \end{pmatrix} \begin{pmatrix} N \\ E \\ Z \end{pmatrix} \tag{3.12}$$

γ is the clockwise angle between North and the direction pointing towards the epicentre. γ is termed the *backazimuth* (Havskov & Ottemoller, 2010). Using the RTZ coordinate system as starting point, more advanced rotations can be employed to align the components of the seismogram with incident and scattered wavefield in the plane spanned by the R- and Z-direction. Figure 3.8 compares the different rotations described in this section. All algorithms assume that velocity discontinuities are isotropic, planar, and horizontal. For all other cases, there will be energy leakage between the components (Rondenay, 2009).

One of these approaches rotates radial and vertical component in the RZ-plane while maintaining the 90°angle between the two components. The formed directions are then called the longitudinal (L) and orthogonal (Q) components and can be computed akin to equation 3.13 (Rondenay, 2009).

$$\begin{pmatrix} L \\ Q \\ T \end{pmatrix} = \begin{pmatrix} cos(i) & -sin(i) & 0 \\ -sin(i) & cos(i) & 0 \\ 0 & 0 & 1 \end{pmatrix} \begin{pmatrix} Z \\ R \\ T \end{pmatrix} \tag{3.13}$$

i is the incident angle of the primary ray and can be determined by equation 3.6.

Another approach aligns all three components of the seismogram with the polarisation directions of P-, SV-, and SH-wave, respectively (Rondenay, 2009). To solve for P, SV, and SH component, both P and S-wave velocity have to be known ((Bostock & Rondenay, 1999)).

$$\begin{pmatrix} P \\ SV \\ SH \end{pmatrix} = \begin{pmatrix} \frac{1/2 - v_s^2 p^2}{v_P q_\alpha} & \frac{p v_S^2}{v_P} & 0 \\ -p v_s & \frac{1/2 - v_S^2 p^2}{v_S q_\beta} & 0 \\ 0 & 0 & 1/2 \end{pmatrix} \begin{pmatrix} Z \\ R \\ T \end{pmatrix} \tag{3.14}$$

with the vertical P-slowness

$$q_\alpha = \sqrt{1/v_P^2 - p^2} \tag{3.15}$$

and the vertical S-slowness
$$q_\beta = \sqrt{1/v_S^2 - p^2} \tag{3.16}$$
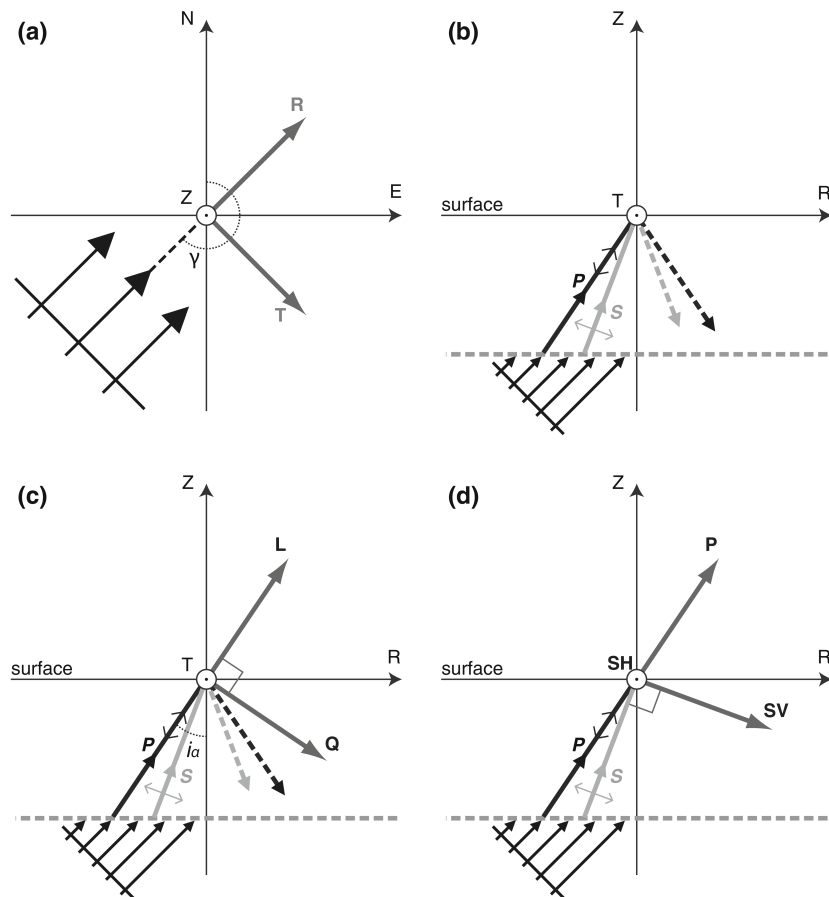
Figure 3.8: **The different viable coordinate systems for a seismogram.** *(a) shows a map view of an incoming teleseismic wavefront to a receiver. The radial (R) component is parallel to the propagation direction of said wavefront, while the transverse (T) component is orthogonal to R and Z. (b) The incoming wavefront is refracted and converted at a velocity discontinuity at depth. Note that neither R nor Z are parallel to the polarisation directions of the primary P and converted S-phase. (c) The longitudinal (L) component is parallel to the P-wave's polarisation direction and the orthogonal (Q) component is normal to the P-wave's polarisation direction, but not parallel to the SV particle motion. (d) The P-SV-SH coordinate system perfectly constrains each polarisation to one component. Figure retrieved from Rondenay (2009).*

In theory, P, SV, and SH component perfectly constrain the three observed particle motions. In practice however, the inaccurate assumptions lead to energy leakage between the components (Rondenay, 2009).

3.3.2   Deconvolution

Deconvolution is the core-step in RF production and a RF is obtained by deconvolving the component of the seismogram containing the incident wavelet from the component containing the scattered wavefield (Gurrola et al., 1995). The goal of this step is to remove the influence of the instrumentation and the source, denoted by $s(t)$, on the scattered wavefield (Rondenay, 2009).

The forward expression describing near-receiver scattering and its resulting wavefield $u(t)$ is given by (Rondenay, 2009):

$$u(t) = s(t) * G(t) \tag{3.17}$$

The ground's impulse response $G(t)$ acts like a filter on the primary wave $s(t)$ (see section 3.2.3). For a one-dimensional velocity model with homogeneous layers and infinitesimally small boundaries, $G(t)$ equals a series of spikes or *Dirac Delta functions* with amplitudes dependent upon the magnitude of their corresponding velocity contrast (Ammon, 1991) . Ideally and for PRFs, the seismogram's SV component would then equal the convolution of the instrument response (see section 3.2.2) and $u(t)$, while the P-component $v(t)$ holds the result of the convolution of $s(t)$ and the instrument response (Rondenay, 2009). For the sake of simplicity, I assume that the instrument response has either been removed or is equal for the two components.

Considering equation 3.17, recovering $G(t)$ should be straight-forward in the frequency domain (Ammon, 1991):

$$G(\omega) = \frac{U(\omega)}{V(\omega)} \tag{3.18}$$

For the ideal case of noise-free records with unlimited bandwidth, the source effect has been removed in equation 3.18 (Langston, 1979; Kind & Yuan, 2011; Rondenay, 2009). However, real-life records are always band-limited and do always contain noise that is independent through the components. Hence, equation 3.18 is ill-posed and, as noise is
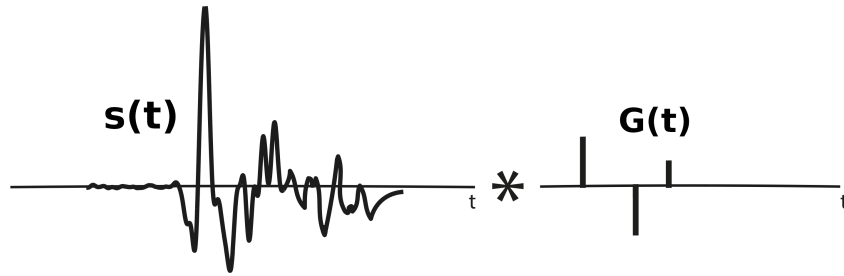
Figure 3.9: **The function of the converted wave is the result of a convolution of the ground's impulse response and a function describing the primary arrival.** *For simple models (see text body), the impulse response can be represented by a series of spikes.*

unknown, one will have to find an inverse filter to estimate $G(t)$ (Rondenay, 2009). A host of methods have been proposed to determine a stable least-squares solution for $G(t)$. The most commonly employed such techniques can be split into the categories of spectral division, time domain deconvolution, and multitaper spectral correlation.

Spectral division is a very simple approach to deconvolution in that the spectrum (i.e., the Fourier transform of the scattered wavefield) is divided by the regularised estimated source spectrum. In this manner, ringing that occurs due to "holes" in the source spectrum is mitigated (Rondenay, 2009). Generally, such a stabilised least-squares solution of the spectral division can be expressed by (altered from Oldenburg, 1981):

$$\hat{G}(\omega) = \frac{U^*(\omega)\bar{V}^*(\omega)}{\bar{V}^*(\omega)V^*(\omega) + \mu} \tag{3.19}$$

Where the asterisks denote a noise-contaminated spectrum (i.e., $V^*(\omega) = V(\omega) + N(\omega)$), ⁻ the complex conjugate, and μ is a damping constant that prevents ringing in the solution for low values in the denominator (Langston, 1979).

In practice, damping can be realised in different ways. One method is the waterlevel damping as introduced by Clayton & Wiggins (1976). Instead of adding a constant damping value as in equation 3.19, the whole denominator is replaced by a so-called waterlevel whenever it undercuts the waterlevel's value (Clayton & Wiggins, 1976). The damping constant μ can also be substituted by a frequency-dependent damping function $\mu(\omega)$ whose amplitude varies depending on the amount of noise per frequency and can for example be estimated from pre-event recordings (see Park, 2000).

From the family of time domain deconvolution, one of the most commonly employed deconvolution methods is the iterative time domain deconvolution (Ligorría & Ammon, 1999; Wang & Pavlis, 2016). This algorithm computes the maximum of the cross-correlation be-

tween source-estimation and scattered wavefield, strips the corresponding peak from the seismogram, and, in consecutive iterations, the maxima of the remaing seismogram's correlations are computed and stripped. Hence, with each iteration, one peak of the impulse response is recovered and the corresponding peak is stripped from the recording of the scattered wavefield. The algorithm interrupts either after a predefined maximum number of iterations is reached or when the energy difference between the estimated scattered wavefield and the real scattered wavefield undercuts a certain threshold. To create a RF, the estimated impulse response is then convolved with, for example, a Gaussian function or a Ricker wavelet (Ligorría & Ammon, 1999).

Another approach proposed by Helffrich (2006) and based on the method of Park (2000) uses moving multitaper spectral correlations to reduce spectral leakage (Helffrich, 2006). The method also quantifies the robustness of each created RF and, thus, allows for RF stacks with robustness-dependent weights (Park, 2000; Rondenay, 2009).

It is worth mentioning that several authors have omitted the step of deconvolution and, instead, stacked depth-migrated recordings of scattered wavefields from various earthquakes (e.g., Kumar et al., 2010, 2012; Kind et al., 2020). This method is based on the assumption that, as each of the recordings is caused by a different source, their incident wavefields vary from recording to recording and will therefore stack destructively (except for the pulse corresponding to the phase's first arrival). The advantage of pure scattered wavefield stacking is that it does, unlike deconvolution, not cause side-lobes due to instabilities. However, a relatively large amount of recordings is needed in order to create a clean stack and the method might consequently not be applicable in all situations (Kind & Yuan, 2011; Kind et al., 2020).

3.3.3 Moveout Correction and Depth Migration

In section 3.3.2, I describe how to obtain a RF that is a function of time. However, as the different RFs stem from waves with differing ray parameters and, thus, ray-paths, they cannot be linearly transferred into depth domain. In order to associate peaks in the RF with certain depths and be able to perform a subsequent stack, one will have to carry out a migration from time to depth domain. Note that depth migration differs from geophysical techniques to account for 2D and 3D scattering effect - often referred to as migration. In contrast to such advanced migration techniques, the theory described in this section assumes a one-dimensionally layered Earth and is often also referred to as moveout correction (Rondenay, 2009).

To understand how such a depth migration has to be performed, it is crucial to under-

stand the domain in which a time-dependent RF is given. The result of a deconvolution, such as a RF, is generally a function of the time lag τ between the two components. Hence, a peak in a PRF that arrives with a positive time lag τ_1 results from a phase that has a travel time difference τ_1 between primary P and converted Ps phase from the conversion point $\mathbf{x_1}$ to the receiver $\mathbf{x_r}$. In an SRF, the converted P-phase arrives prior to the primary S-phase due to higher P-velocities and, therefore, $\tau Sp = -\tau_{Ps}$. Multiple phases arrive after the primary arrival as they travel longer paths, which explains why SRFs are not contaminated by multiples of the primary S-phase (see section 3.3) (Farra & Vinnik, 2000).

Now that we have established that RFs are given as a function of travel time difference between primary arrival and conversion at the point $\mathbf{x}$ and depth z, we can compute $\mathbf{x}(\tau)$ provided that we know a model for v_P and v_S. The forward expression for τ is given by (e.g., Rondenay, 2009):

$$\tau_{Ps}(p, z) = -\tau_{Sp}(p, z) = \int\limits_{z=z_r}^{z} (q_\beta(p, z) - q_\alpha(p, z)) \mathrm{d}z \tag{3.20}$$

To find the depth corresponding to each sample of the RF, we can proceed as follows. Firstly, we compute a conversion time table corresponding to an evenly spaced depth vector using an arbitrary velocity model. Secondly, we interpolate through the RF for the computed conversion times. This will result in a stretching and compressing operation for depth with low and high velocities, respectively. Alternatively, one may opt for a different approach, in which an arbitrary reference ray parameter is used to compute the time delay (see e.g., Rondenay, 2009). The distance between the consecutive piercing points for a certain depth can simply be approximated by setting the ratio of horizontal to vertical slowness equal to the ratio of vertically travelled distance Δz to horizontally travelled distanced Δx:

$$\Delta x_{Ps} = \frac{\Delta z\, p}{q_\beta(z, p)} \tag{3.21}$$

and for SRFs

$$\Delta x_{Sp} = \frac{\Delta z\, p}{q_\alpha(z, p)} \tag{3.22}$$

In order to obtain accurate results, all computations have to be conducted in a spherical coordinate system (see 3.1.2). Alternatively, one may choose to employ a flat Earth model that alters both velocity and depth (e.g., Shearer, 2019), which, for large datasets, may offer a computational advantage. The "Earth-flattened" variables are given by (e.g., Shearer, 2019):

$$z_f = -R_{Earth} \ln \left(\frac{R_{Earth} - z_s}{R_{Earth}} \right) \tag{3.23}$$

and for the velocities

$$v_f = \frac{R_{Earth}}{R_{Earth} - z_s} v_s(z_s) \tag{3.24}$$

where z is the depth and $R_{Earth} \cong 6371$ km the radius of the Earth. Variables with an $_s$ subscript are spherical values, whereas the $_f$ subscript indicates an Earth-flattened approximation.

3.3.4   Stacking

Single RFs do often have a poor signal to noise ratio (SNR) due to instabilities in the deconvolution and noise in the seismic data. By stacking several depth-migrated RFs, SNR can be increased as noise between the single RFs is mostly incoherent, whereas the peaks caused by real features in the subsurface stack coherently. A very simple approach to RF-stacking is stacking data by station. That is, all receiver functions created from different seismic events at one station are stacked into one single RF. Because these RFs are created from events with different ray parameters and backazimuths their piercing points at depth might differ considerably (Rondenay, 2009). Particularly for SRFs, conversion points at depth can be located especially far away from the station since the Sp-conversion is refracted to a high emergent angle (see section 3.1.1). Consequently, single station stacks are only poorly suited to target horizontally varying structures. To overcome this issue, some authors have binned and stacked RFs depending on their epicentral distances and backazimuths (e.g Bostock, 1998; Rychert et al., 2005, 2007).

3.3.4.1   Common Conversion Point Stacking

In areas with denser station coverage, one can employ a more sophisticated stacking approach in which each stack corresponds to an area of conversion. This technique is
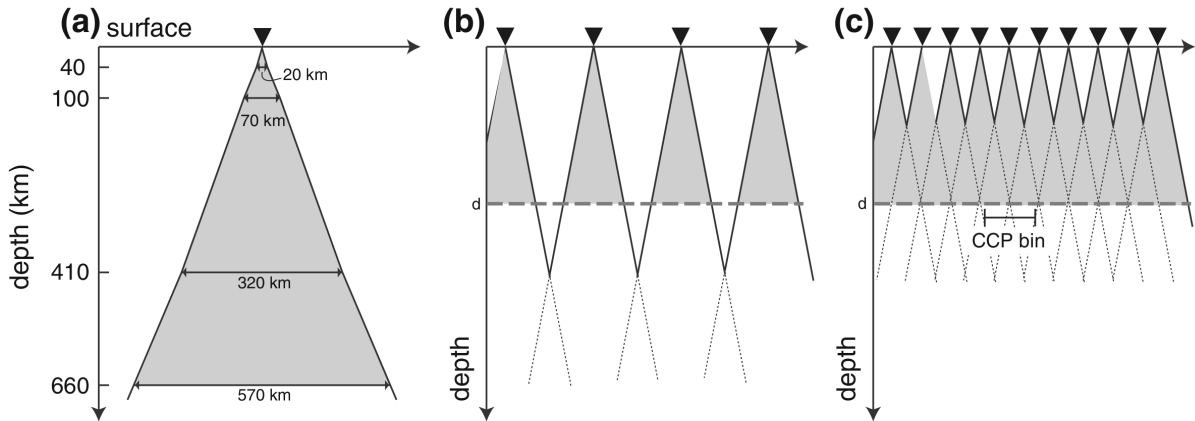
Figure 3.10: **Subsurface illumination by receiver functions at varying depth.** *The aperture width of RFs under a station depends on maximal ray parameter, seismic phase (i.e., the nature of the RF; P or S), and the illumination depth. Panel **(a)** relates the maximal station aperture width for PRFs to the conversion depth. Panel **(b)** shows a case, where the inter-station distance is smaller than the station aperture at depth. Consequently, not all points in the subsurface are illuminated. In **(c)**, the station aperture is larger than the inter-station distance and, therefore, the illustrated CCP bin contains data from several stations. Figure retrieved from Rondenay (2009).*

called common conversion point (CCP) stacking and is an adaptation of common depth point gathers that are commonly used in reflection seismology (Rondenay, 2009). Binning depending on conversion point was first applied to RFs by Dueker & Sheehan (1997) and addresses the aforementioned issues with single station stacks. Additionally, station-coherent noise is mitigated because elements from RFs from different stations are stacked in common bins (Dueker & Sheehan, 1997).

Although in principal superior to station-based stacking approaches, CCP stacking cannot be applied everywhere. In order to illuminate the whole subsurface, the station coverage has to be dense. That is, the inter-station distance must be smaller than the receiver function aperture of a station (see Figure 3.10) (Rondenay, 2009). As the station aperture depends on the maximum incident angle of the converted teleseismic ray and Sp conversions have emergent angles that are greater than the incident angle of the S-ray (see section 3.1.1), CCP stacking of SRFs requires fewer station in a given area than CCP stacking of PRFs.

Different authors have implemented CCP stacking in manners that deviate strongly from each other. As for the ray-tracing, some authors have calculated only few piercing point positions at depth (e.g., Dueker & Sheehan, 1997; Kind et al., 2015), whereas others compute a piercing point corresponding to (almost) each depth-sample (e.g., Hopper &

Fischer, 2018; Kind et al., 2020). The bins' shape may also vary. For example, Kind et al. (2015, 2020) use elongated bins to image the lithosphere and astenosphere under the United States. Lekic et al. (2011) and Lekić & Fischer (2014) weight the individual RFs depending on their distance from the closest bin centres. Even though executed differently, all of these implementations face a trade-off between resolution and noise-content, for which the controlling parameter is the bin size. That is, the bigger the bin the more data are stacked and, thus, the more noise is mitigated. However, horizontal resolution decreases with increasing bin size (Dueker & Sheehan, 1997). In chapter 4, I will propose a new method to compute CCP stacks that is particularly well-suited for large datasets since it combines precision with computational efficiency.

Despite being able to account for lateral structural variations to a certain degree, CCP stacking is still based on the assumption that structures are horizontal. Consequently, diffraction and dipping boundaries inevitably cause artefacts in the final image. Overcoming these issues is the main goal of 2D and 3D migration techniques (Rondenay, 2009).

3.3.5   2D/3D-Migration

In standard 2D and 3D seismic migration, the subsurface is not treated as a layered structure, but rather as a volume containing potential scattering points. To identify those points, the scattered wavefield is traced to potential scattering points in the subsurface. The true scattering points are those locations at which the scattered energy focuses. A schematic representation of the procedure can be found in Figure 3.11. Seismic migration techniques can accurately image any structure that can be represented as an agglomeration of points - in contrast to horizontal layers in CCP stacking. In order to precisely compute the focus points, one requires a very accurate, smoothly varying velocity model (Rondenay, 2009). Some important limitations of seismic migration render it ill-suited for the use with a global RF database. Firstly, overall subsurface illumination is, even in some of the better surveyed regions, not sufficient for migration approaches. Especially, for SRFs that are free of other strong arriving phases for only small epicentral windows (see Wilson et al., 2006; Yuan et al., 2006) the backazimuthal and ray parameter coverage is particularly poor (Lekić & Fischer, 2017). Secondly, migration is computationally extremely expensive and, therefore, not feasible for a global dataset (Rondenay, 2009). Conclusively, we do not yet possess the required data or computational power needed to carry out teleseismic migration on a global scale.
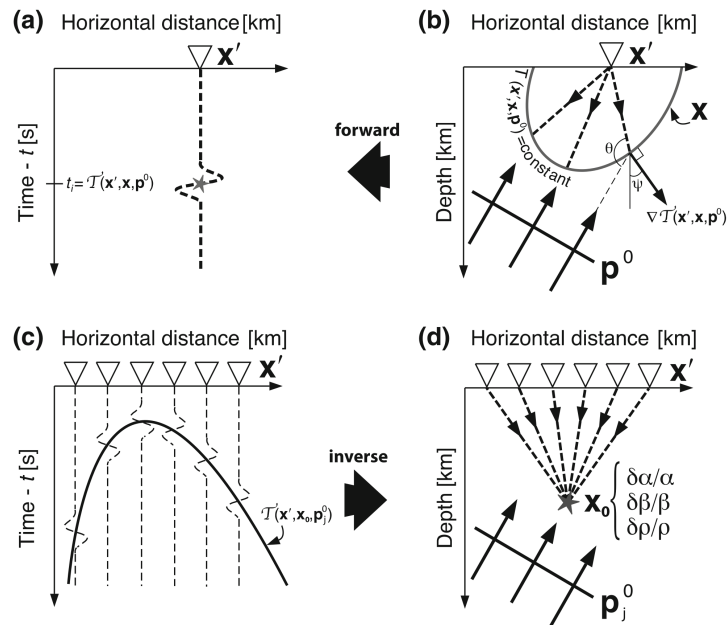
Figure 3.11: **The forward and backward problem of teleseismic scattered-wave migration.** *(a) The RF is measured in time domain. (b) The peak from (a) may correspond to a conversion of the teleseismic wave (marked as* $\mathbf{p}^0$*) scattered at any point on the scatter ellipse (see e.g., Stein & Wysession, 2009). (c) If the station coverage is dense enough, peaks from the same scattering point can be measured at several stations. (d) The energy from each peak is then back-propagated until a bright (i.e., high amplitude) spot is found. Figure from Rondenay (2009).*

Chapter 4

Implementation

In order to be able to rapidly create images of large scale structures in the lithosphere and asthenosphere, I have developed a software suite capable of creating such images from both P-to-S and S-to-P receiver functions - Pythonic Global Lithospheric Imaging using Earthquake Recordings (PyGLImER). PyGLImER is a direct successor of the GLImER software (Rondenay et al., 2017), but comes with some important improvements and additions. Those include, but are not limited to, the ability of updating the database at any time without compromising existing data, inclusion of S-to-P converted data, and an extension of the database to all International Federation of Digital Seismograph Networks (FDSN) servers. The software establishes a RF database with minimal user interference following the scheme outlined in Figure 4.1. PyGLImER is written in a pythonic, object-oriented manner relying heavily on the ObsPy module (Krischer et al., 2015). Minor sections of the code (in *pyglimer.rf.create* and *pyglimer.rf.moveout*) are based on or modified versions of the rf project by Eulenfeld (2020) (those sections are indicated in the code, their copyright information can also be found in the code). The entire source code is attached in the digital Appendix C.

4.1   Data

All waveform, station, and event data used in this thesis have been made freely available by FDSN members. Table 4.1 gives an overview of the used data and their respective origin. In total, the final database comprises recordings of 21,969 events at 22,370 broadband and very-broadband stations resulting in about 24 million raw waveforms (i.e., three-component streams). After quality control and deconvolution, almost 4 million RFs are left. The locations of all stations with available RFs are plotted in Figure 4.2.
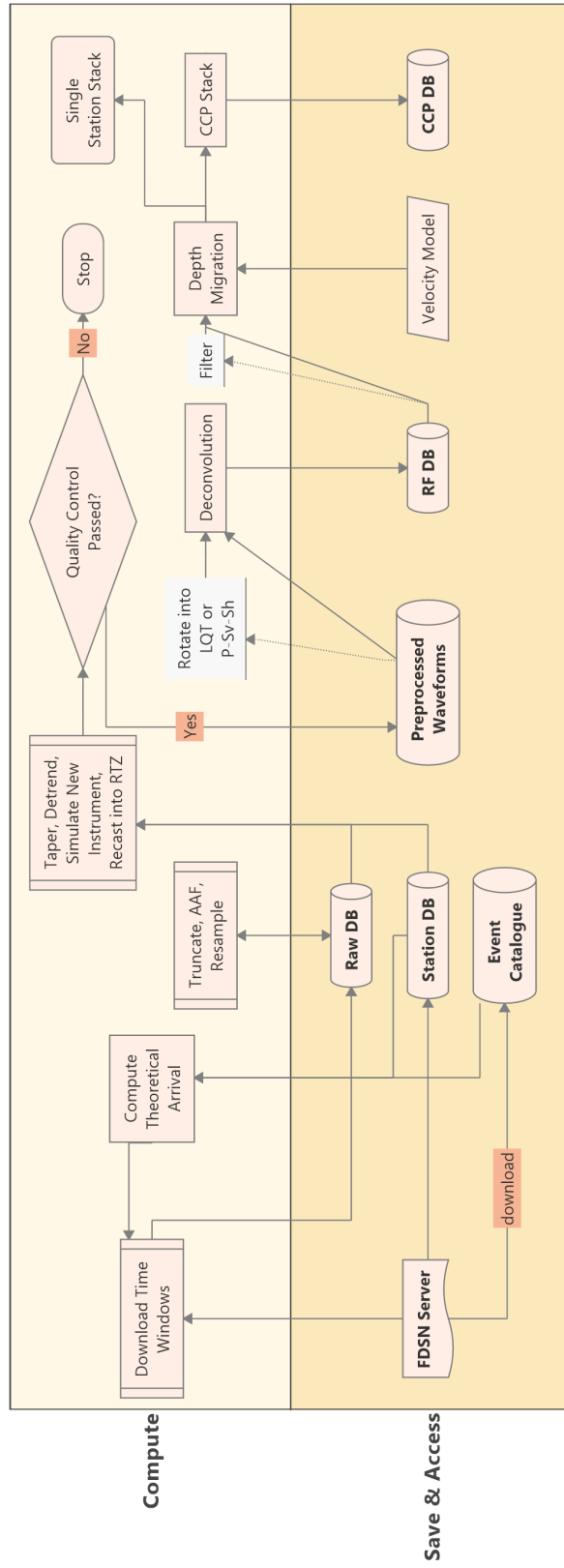
Figure 4.1: ***The processing scheme of PyGLImER's receiver function workflow from a stream containing raw wave-forms to the final CCP stack.*** *A cylinder represents a local database, which PyGLImER constructs, processes with a double-boarder are fully automated, grey steps are voluntary, and single-bordered processes expect a user input that will alter the nature of the respective processing step. For the sake of clarity, the process is simplified and minor steps and branches are omitted.*
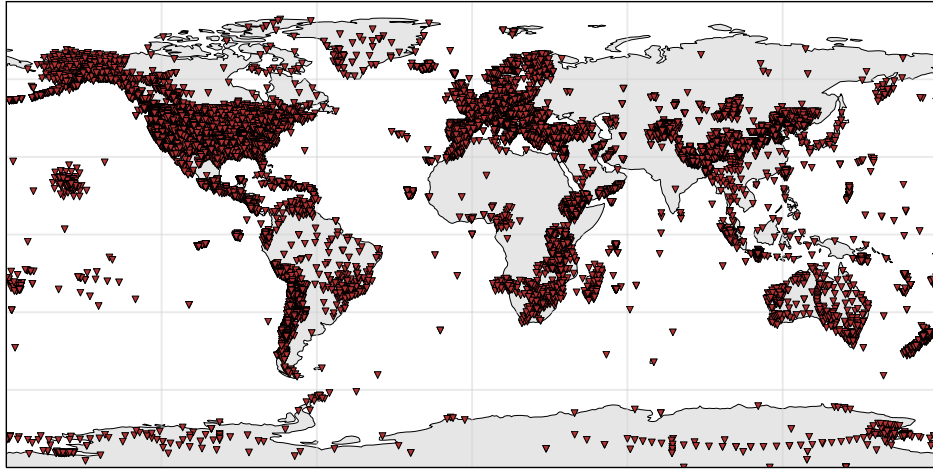
Figure 4.2: **Station coverage of the PyGLImER database.** *Red downward-pointing triangles are seismic broadband stations. The density of the station coverage varies considerably. Generally, coverage is very dense in Europe and the US.*

PyGLImER downloads waveforms corresponding to events with $M_W \geq 5.5$ that occurred between January 1970 and April 2020 for stations where arrivals are pre-critical and, in the case of SRFs, unobstructed by other arrivals (see section 3.1.2). For PRFs, this translates to epicentral distances between 28.1°and 95.8°and for SRFs between 55°and 80°with a maximal hypocentral depth of 300km (Wilson et al., 2006; Yuan et al., 2006). PyGLImER is also capable to create RFs from SKS-to-P and ScS-to-P conversions. For those, epicentral distances are limited to 90-120°and 50-75°, respectively (see Yuan et al., 2006; Zhang et al., 2014). Time windows of 240s length (120s before and after theoretical arrival) are saved in a raw database, the corresponding theoretical arrivals are determined via a Tau-P lookup (see 3.1.2). In the following steps, the downloaded data are prepared for deconvolution.

4.2   Preprocessing

Before creating RFs the raw data must be conditioned. Firstly, the data are resampled to 10Hz (after anti-alias filtering). As discussed in section 3.1.3, the teleseismic data that interests us has dominant frequencies of 1Hz and lower, and downsampling saves disk space (to date, the downsampled database comprises almost two terabytes). Afterwards,

Table 4.1: **List of available FDSN servers, their data coverage in terms of region, and services that are incorporated into PyGLImER.** *In principle, PyGLImER is compatible with all servers supporting FDSN services. Event data are exclusively used from the USGS, while all available station response and waveform data are downloaded (excluding Raspberry Shake). A list of FDSN compatible servers can be found at* `https://www.fdsn.org/webservices/datacenters/`.

Server Name	Region	Event	Station	Dataselect
AusPass	Australia		✓	✓
BGR	Germany		✓	✓
EMSC	Europe		✓	✓
ETH	Switzerland		✓	✓
GeoNet	New Zealand		✓	✓
GFZ	global		✓	✓
ICGC	Spain		✓	✓
INGV	Italy		✓	✓
IPGP	global		✓	✓
IRIS-DMC	global		✓	✓
KNMI	global		✓	✓
KOERI	Turkey		✓	✓
LMU	Germany		✓	✓
NIEP	Romania		✓	✓
NCEDC	USA		✓	✓
NOA	Greece		✓	✓
ORFEUS	global		✓	✓
Raspberry Shake	global			
RESIF	France		✓	✓
SCEDC	USA		✓	✓
TexNet	USA		✓	✓
UiB-NORSAR	Norway		✓	✓
USGS	global	✓		
USP	South America		✓	✓

the traces are detrended, tapered at both ends (to avoid the Gibb's effect), and the instrument response is normalised to be identical in all traces (i.e., all traces are simulated for a new instrument response that is identical for all traces). Finally, all seismograms are converted to the ground velocity (see e.g., Havskov & Alguacil, 2004) and cast into an RTZ coordinate system akin to equation 3.12.

4.2.1   Quality Control

Many of the downloaded recordings suffer from high noise levels that can lead to erroneous peaks in the final RF (see section 3.3.2). Therefore, criteria to remove noisy waveforms have to be defined. For large databases as PyGLImER's, an automatic quality control (QC) is the only feasible way of controlling data quality. QC in PyGLImER is always conducted on streams that have been bandpass filtered around the frequency window where one would expect the dominant frequency of the teleseismic arrival. After filtering, simple signal to noise ratio (SNR)s are computed for different points in the waveform and, dependent upon these SNRs, the waveform is retained or discarded.

For PRFs, the waveforms are evaluated on the basis of three SNRs relating the vertical and radial traces of each stream:

1. $Z_{primary}/Z_{noise} > 10$
2. $R_{primary}/R_{noise} > 7.5$
3. $R_{primary}/R_{coda} \geq 1$

Where $X_{primary}$ is the energy (i.e., the amplitude squared) per sample around the primary arrival on component X, X_{noise} the energy per sample in a time window of the waveform that is free of earthquake energy (P) or where the event's influence is low (S), and X_{coda} is the energy per sample 15-35s after the primary arrival. Those ratios are evaluated up to three times, each time with a different high-pass filter with corner frequencies of 0.03Hz, 0.1Hz, and 0.5Hz, respectively.

For SRFs, QC is conducted in a similar manner albeit with different SNR criteria and different filters:

1. $R_{primary}/R_{noise} > 7$
2. $R_{coda}/R_{primary} < 0.7$
3. $Z_{conversions}/R_{conversions} > 1$

Where $X_{conversions}$ is the energy per sample 50-10s before the S-arrival on component X. Those SNRs are evaluated four times for bandpass filters with a low corner frequency of 0.01Hz and highpass frequencies varying between 0.33Hz and 0.175Hz.

The criteria for P-to-S originate from GLImER, whereas I evaluated and refined the

S-to-P criteria manually based on over 2,000 S-waveforms and their RFs.

After QC, the PyGLImER database reduces to 3 million Ps records (from about 19 million raw records) and to 520,000 Sp records (from about 4.5 million raw records). Waveforms that passed the QC are saved in filtered form in a "preprocessed" database. To reduce the time needed to update the database and avoid costly re-evaluation, raw records that were discarded in the QC are flagged.

In addition to the described QC based on the SNR, the statistics above include waveforms that have been discarded due to corrupted or missing data with the most common issues being either missing or corrupted station response information or missing time windows on one or several components.

4.2.2   Rotation

In the current implementation, the user can choose from different rotation algorithm to isolate primary and converted wave (see section 3.3.1). Depending on their choice, the final coordinate system is either R-T-Z, L-Q-T, or P-Sv-Sh. Hence, the second rotation (i.e., to L-Q-T or P-Sv-Sh) is optional. However, particularly for S-to-P conversions, incident angles can be large (e.g., Yuan et al., 2006) and accounting for those with an additional rotation is advisable.

The rotation to P-Sv-Sh is implemented using a forward approach, whereas L, Q, and T component can be computed via an inverse algorithm. Rotation to a P-Sv-Sh coordinate system is realised via equation 3.14, where the required near surface velocities for each station are obtained from a surface wave tomography by Pasyanos et al. (2014). L, Q, and T component on the other hand are determined by minimising (SRF) or maximising (PRF) the energy of the primary wave at theoretical arrival on the L-component. A three component recording of an S-arrival cast into all three coordinate system is shown in Figure 4.3 to illustrate their differences and similarities.

4.3   Deconvolution

Currently, PyGLImER supports two deconvolution approaches - damped spectral division (e.g., Langston, 1979) and iterative time domain deconvolution (Ligorría & Ammon, 1999). For the spectral division, three different damping variants can be chosen, either frequency-dependent, waterlevel, or constant damping. A discussion of the theoretical background of the deconvolution algorithms is given in section 3.3.2.
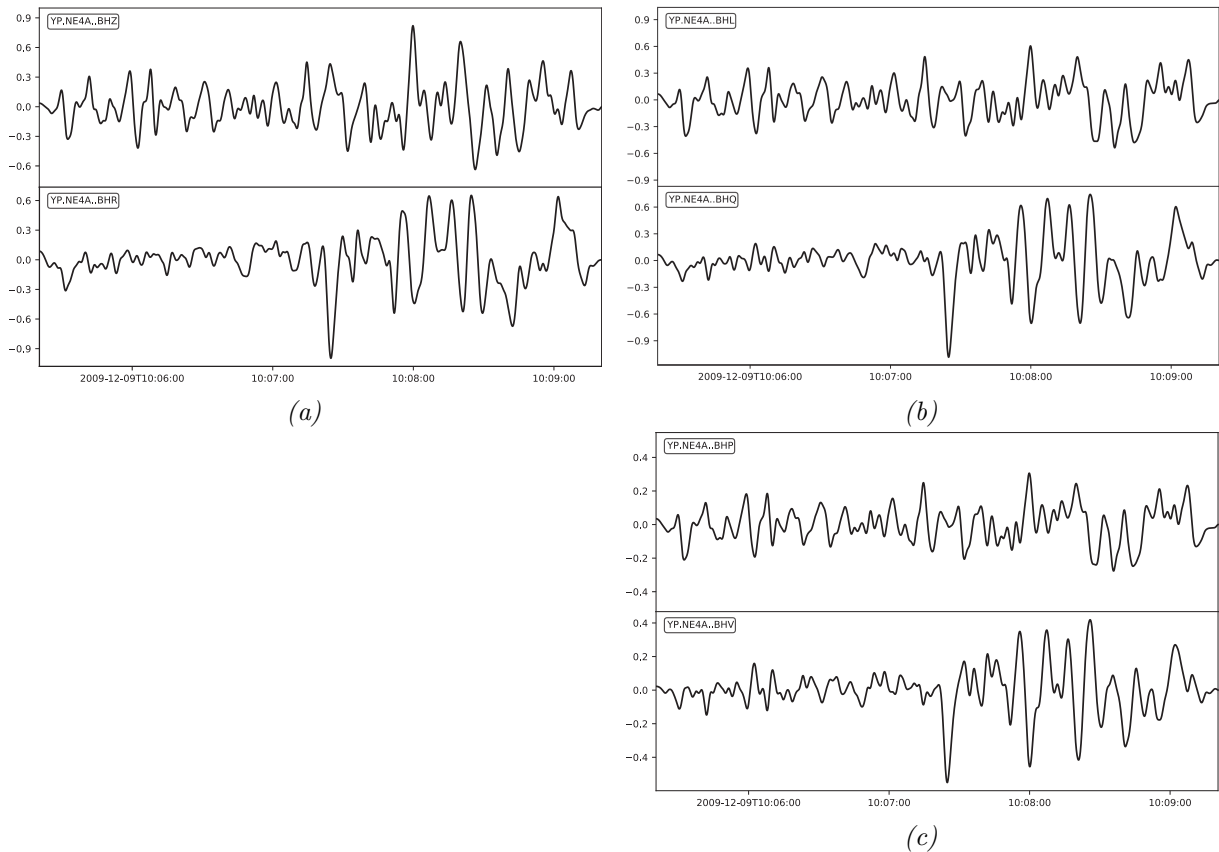
(a)

(b)

(c)

Figure 4.3: **The three different options for rotations offered in PyGLImER.** *All three plots show the same recording of a magnitude 6.4 earthquake that occurred on 09/12/2009 East of New Caledonia. The event was recorded on station NE4A of the temporary North-East China Array. The individual panels show Z and R component (a), L and Q component (b), and P and Sv component (c) of the seismogram. L-Q-T (b) and P-Sv-Sh (c) rotations yield virtually indistinguishable results as already claimed by Rondenay (2009).*

To illustrate how these approaches work, I used a forward modelling approach (Fred-eriksen & Bostock, 2000) that creates seismograms from a Cartesian model using a Ricker wavelet as source-time function (see Figure 4.4 for model parameters). All RFs are PRFs created by deconvolving the P from the Sv component. The resulting RFs are plotted in Figure 4.5.

Looking at Figure 4.5, we can see that the two deconvolution approaches deliver similar albeit not identical results. Pulses of the RF created using iterative time domain decon-volution (4.5a) have a predefined width, determined by the width of the Gaussian that is convolved with the impulse response resulting from the algorithm (see Ligorría & Ammon, 1999; Wang & Pavlis, 2016). The pulse width of the RF created using waterlevel spectral division (4.5b) is a function of the frequency of the deconvolved waveforms, which, in this model, was very high. However, the frequency-domain approach creates small side-lobes (i.e., oscillations) before and after each peak.

4.4   One-Dimensional Depth Migration

After deconvolution, the RFs can be mapped to depth domain as described in section 3.3.3. In practice, the user can choose to execute the depth migration utilising one of the two following global velocity models. Either the one-dimensional, globally invariable iasp91-model (Kennett & Engdahl, 1991) or the semi-three-dimensional GyPSuM velocity model (Simmons et al., 2010), which divides the Earth into 1°- sized bins each with its own one-dimensional velocity model. Simmons et al. (2010) determined the velocities in the GyPSuM model via body-wave tomography. PyGLImER automatically compiles a velocity model from data of the GyPSuM project for each piercing point at depth with a vertical spacing of 1km. Depth-migration is conducted using the Earth-flattening approximation (see section 3.3.3). PyGLImER flips SRFs over both axis (i.e., $H(t)$ is transferred to $-H(-t)$) to allow for easier comparisons between PRFs and SRFs.

Most seismic stations are not installed on sea level. As a result, the travel times for a ray from depth z_1 change by $\Delta T(z_r)$, where z_r is the station elevation. PyGLImER's depth migration accounts for station elevation by adding or subtracting z_r (rounded to the closest multiple of 100m) onto the respective velocity model.

Figure 4.6 shows our synthetic PRF migrated to depth using a layer-over-halfspace model (see Figure 4.4a). Appendix A contains additional figures that compare results us-ing the two velocity models and quantify the impact of the Earth-flattening approximation.
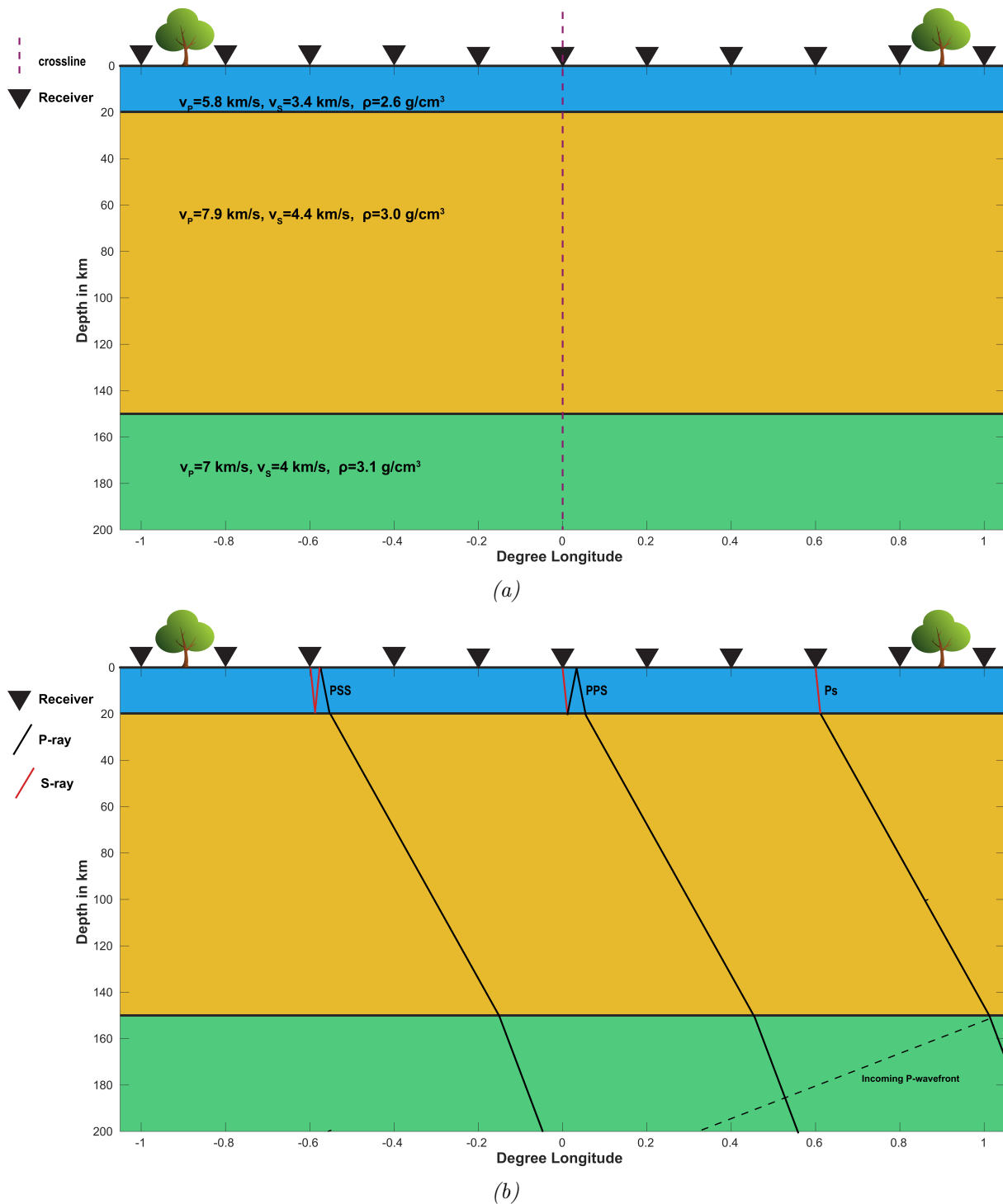
(a)

(b)

Figure 4.4: **The forward-model used to create the synthetic seismograms.** *The velocity model consists of two layers over a halfspace. 21 equidistant receivers are placed on the meridian (11) and on the equator (11) with an inter-station distance of 0.2°, so that the resulting array is cross-shaped (see also Figure 4.13). Seismic discontinuities are marked as bold, horizontal lines. The model parameters are provided in (a). Panel (b) contains the ray-paths corresponding to Ps converted arrival and PPS and PSS multiples.*
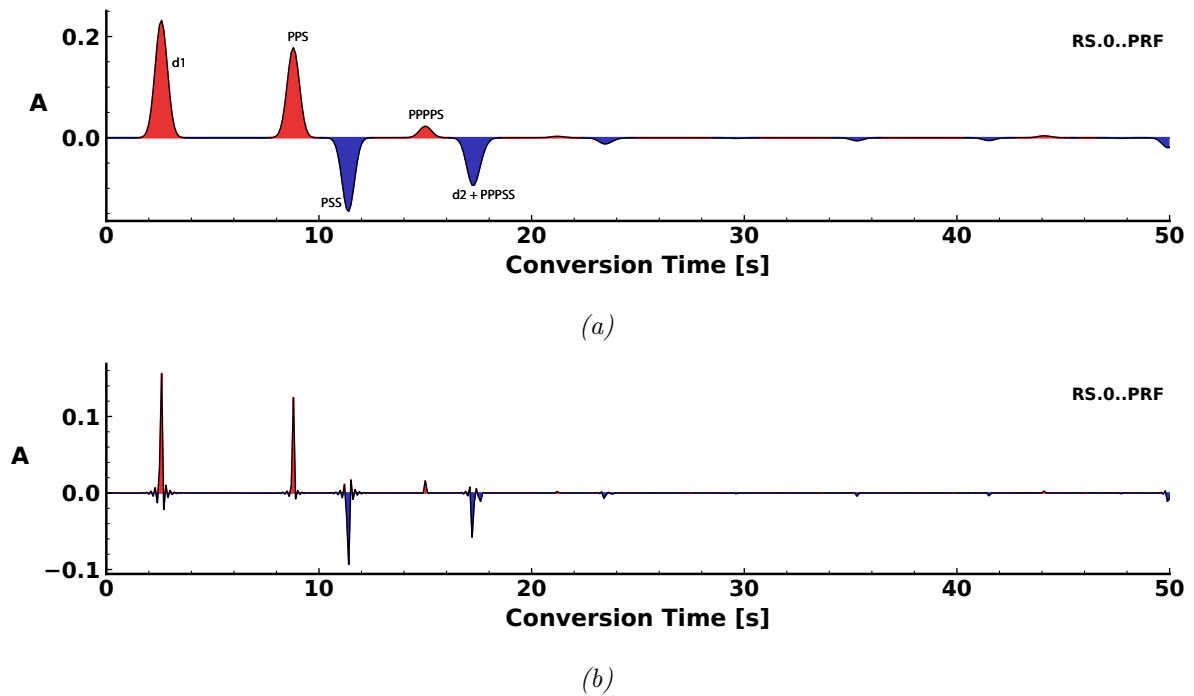
(a)

(b)

Figure 4.5: **The synthetic P-receiver functions resulting from deconvolving the P from the SV component.** *The arrivals corresponding to the RF's major peaks are indicated in panel (a), where d1 and d2 represent the first and second velocity discontinuity, respectively. The RF shown in (a) was produced using iterative time domain deconvolution, whereas the RF in (b) is the result of a waterlevel spectral division. Note that the peaks in the RF produced using iterative time domain deconvolution have an artificial width only defined by the Gaussian width parameter (cf. section 3.3.2) and that the waterlevel spectral division (b) is prone to side-lobes.*
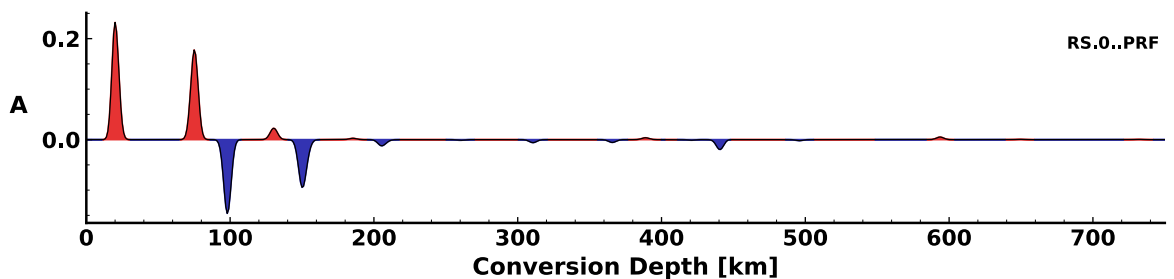

Figure 4.6: **Depth-migrated receiver function created using iterative time domain deconvolution.** *A stretching effect on the individual peaks can clearly be observed.*

4.4.1   Multiples

For simple one-dimensional models, the multiples' ray-paths are known (see 4.4b). For most other cases, these multiple ray-paths are reasonable approximations. Using these ray-paths, we can apply a moveout correction for conversion times corresponding to both primary Ps and multiple arrival (e.g., Schimmel & Paulssen, 1997; Zhu & Kanamori, 2000; Tauzin et al., 2016). In order to minimise the computational cost of computing conversion times for multiple phases, the function in PyGLImER is limited to multiples with ray-paths parallel to the ray-path of the Ps converted phase (i.e., PSS and PPS, cf. Figure 4.4b). The strongest and, hence, most impactful multiples are free-surface multiples. Since multiple travel time differences are significantly greater than those for P-to-S (limit of record's time window), amplitudes become lower due to attenuation, and scattering from multi-dimensional structures influence multiples stronger (due to their longer ray-path), depth migration for multiples is only conducted down to a depth of 200km.

Assuming that the travel times from piercing point **x** for both P and S rays have already been computed, it is straight forward to determine multiple travel times for each boundary. Travel time differences between the converted Ps (or Sp) and primary P-phase are given by equation 3.20 (Zhu & Kanamori, 2000).

$$\tau_{PPS} = 2T_P(p, z) + T_S(p, z) - T_P(p, z) \tag{4.1}$$

$$\text{and}$$
$$\tau_{PSS} = T_P(p, z) + 2T_S(p, z) - T_P(p, z) \tag{4.2}$$

$$\text{with}$$
$$T_P(p, z) = \int_{z=z_r}^{z} q_\alpha(p, z)\mathrm{d}z \tag{4.3}$$

$$\text{and}$$
$$T_S(p, z) = \int_{z=z_r}^{z} q_\beta(p, z)\mathrm{d}z \tag{4.4}$$

Just like a moveout correction on P-to-S, a moveout correction for multiples squeezes and stretches the RF depending on the vertical slownesses q_α and q_β at the corresponding piercing point at depth. However, since the apparent vertical slownesses of multiples are significantly higher than for Ps, the RF that is depth-migrated with multiple delay times

will be more squeezed. This effect leads to an apparent increase in frequency (and, there-
fore, an increase in resolution), which I correct for by imposing a low-pass filter (1Hz for
primary - 0.2Hz for multiples) on the RF in time domain (i.e., prior to moveout correction)
as proposed by Tauzin et al. (2016). Additionally, new "apparent discontinuities" will be
created that result from Ps-conversions depth-migrated with multiple conversion times
(see peaks before peak corresponding to d1 in Figure 4.8).

Theoretically, moveout correction with respect to travel times of multiple phases is
possible for both PRFs and SRFs. However, due to other teleseismic phases arriving
shortly after the primary S-arrival, deconvolution for SRFs tends to be more stable when
the traces are truncated shortly (i.e., around 30s) after the primary S-arrival. As a side
effect, the majority of multiple arrivals are lost. Further investigation is needed to find an
effective way of using multiple modes in SRFs. Currently however, such investigations are
beyond the scope of this thesis and utilising multiple phases for SRFs remains disabled
in PyGLImER.

To use depth migration to its full potential, particularly when it comes to reducing the
influence of multiples and other noise, one should stack depth-migrated RFs created from
several earthquake records and moveout corrected for one or several phases (Rondenay,
2009).

4.5   Single Station Stacking

The simplest form of stacking implemented in PyGLImER is station-based stacking. In
this procedure, moveout corrected RFs are simply stacked into one single trace under
the assumption that all structures under the receiver are entirely horizontal (see section
3.3.4). By stacking different records, we can effectively increase the SNR. As only "real"
(i.e., caused by the P-to-S conversion) peaks from rays with different ray-parameters are
migrated to the same depth, only these will stack coherently, whereas multiples smear
out. The final stack will show a function closer to the ground's Green's function (Kind
& Yuan, 2011). This effect can clearly be observed in Figure 4.7 showing a single station
stack from 100 synthetic PRFs.

4.5.1   Stacks Including Free-Surface Multiples

After filtering and depth-migrating a RF for P-Ps, P-PPS, and P-PSS conversion times,
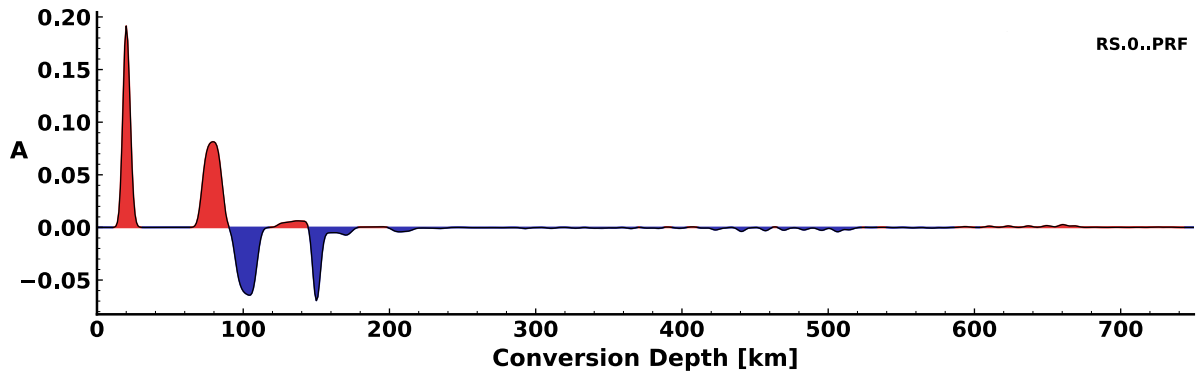one obtains three depth-dependent functions. To mitigate artificial peaks caused by mul-

Figure 4.7: ***A receiver function stack created from 100 synthetic RFs.*** *For each of the RFs, I applied a depth-migration without taking multiples into account. The teleseismic arrivals vary between ten different values for the ray parameter, so that the moveout for real arrivals is consistent, whereas multiples are moved by a different amount for each ray parameter.*

tiples and enhance peaks representing real boundaries most effectively, the three traces should be stacked. Different stacking modes have been proposed (e.g., Schimmel & Paulssen, 1997; Zhu & Kanamori, 2000). PyGLImER incorporates the following stacking modes:

The first option is stacking akin to Zhu & Kanamori (2000) by introducing a constant weight for each of the three traces (Zhu & Kanamori, 2000):

$$H_{stack}(z) = \alpha H_{Ps}(z) + \beta H_{PPS}(z) - \gamma H_{PSS}(z) \tag{4.5}$$

with $\alpha = 0.7$, $\beta = 0.2$, and $\gamma = 0.1$. Note that due to its differing polarity, peaks corresponding to the PSS phase have to be negated (i.e., flipped over the x-axis). The second possibility is simply stacking the three phases linearly (i.e., with equal weights). Stacks from synthetic RFs computed using both modes are plotted in Figure 4.8.

Single station stacks are a viable choice to image one-dimensional (i.e., horizontal) structures under the receiver and wherever station coverage is poor. However, when structures dip, peaks from arrivals with different backazimuth and ray parameter cease to stack constructively since different rays pierce the dipping structure at different depths (Rondenay, 2009). As discussed in section 3.3.2, this is particularly problematic for SRFs that pierce deep structures far away (up to about 14°great circle distance, see Appendix A) from the station. For those cases, common conversion point (CCP) binning and stacking offers a solution with superior lateral resolution.
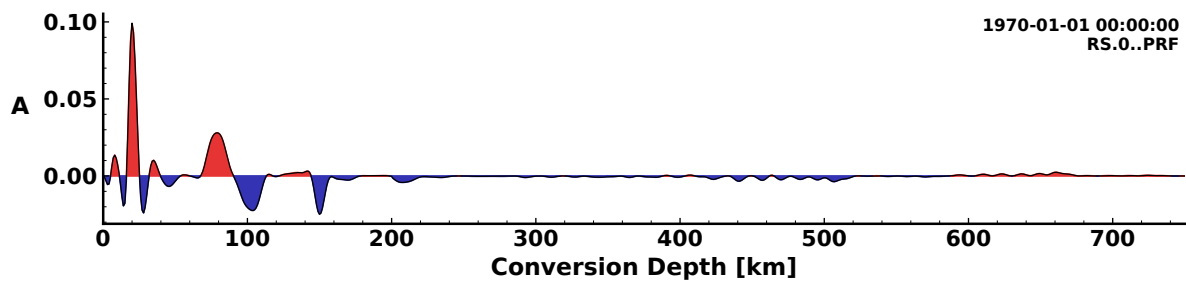
(a)
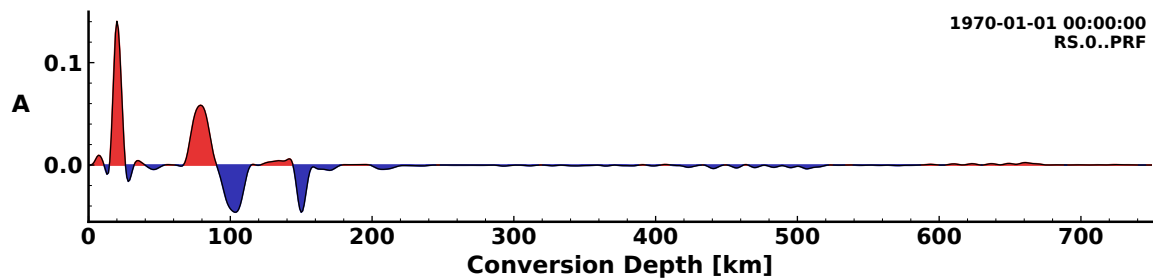
(b)

Figure 4.8: **Single station stacking of receiver functions using RFs that are moveout-corrected for Ps and multiple conversion times.** *Note that the moveout correction for multiples causes additional peaks by moving peaks caused from a simple P-to-S conversion. (a) shows a stack with linear weights, whereas the weights used to create (b) are as given by equation 4.5.*

4.6   Common Conversion Point Stacking

As discussed in section 3.3.4.1, common conversion point (CCP) binning may be implemented in different manners. Figure 4.9 illustrates a particularly efficient (i.e., with a low computational cost) way to implement global CCP stacking. Global CCP stacking has already been discussed and implemented by Lucas Sawade for the scope of his Master's thesis in 2017. In direct comparison to this previous implementation, the novel technique used in PyGLImER offers a ten-fold reduction of computation time. In the following, I will discuss each step in the new CCP binning approach.

One of the problems posed in CCP binning on a global scale is the requirement of an evenly-spaced grid. While creating such a grid in a Cartesian (i.e., rectangular) coordinate system is a rather trivial task, grids on a spherical body can lead to distortion particularly in polar regions (e.g., Teanby, 2006). One common way of addressing this issue is by employing icosahedron binning, where bins have the shape of triangles (Teanby, 2006). A more efficient approximation of an equal-distance grid on a spherical body can be produced using a Fibonacci Lattice or Fibonacci Sphere (Stanley, 1975), which finds the quasi-equidistant points by "wrapping" the spherical body with a spiral vector. This spiral vector has a constant distance to its next loop so that the points in question are evenly distributed on the vector. Figure 4.10 shows a global grid with an inter-bin spacing of 2.5°. Computing this grid took significantly less than one second on a common computer. Taking a closer look at Figure 4.10, we can see that the grid created using a Fibonacci Lattice exhibits some inaccuracies (see artefact between India and Myanmar). However the overall accuracy is more than satisfactory for our purposes.

After creating a global bin-grid, the program removes all bins that exceed a given distance threshold to the closest station. This distance threshold is dependent on the primary phase of the data that the bin-grid will later be populated with. Thresholds are 4°and 12°for PRFs and SRFs, respectively. In order to find the closest station to each bin point, PyGLImER utilises a KD-Tree - an algorithm designed for efficient closest-neighbour determination (Maneewongvatana & Mount, 2002). A KD-Tree is first constructed from all station coordinates (denoted as Station-KD-Tree in Figure 4.9) and can subsequently be queried for arbitrary coordinates (in our case, the bin coordinates). An example for a bin-grid with 1°inter-bin distance d_{Bin} designed for SRF imaging in an arbitrarily chosen area in North-East China is shown in Figure 4.11.

Now that the CCP grid is built, each bin can be populated with RF data. To determine distances of RF piercing points to the bin centres, PyGLImER generates a second KD-Tree from the bin coordinates. After the Bin-KD-Tree is constructed, we can find all
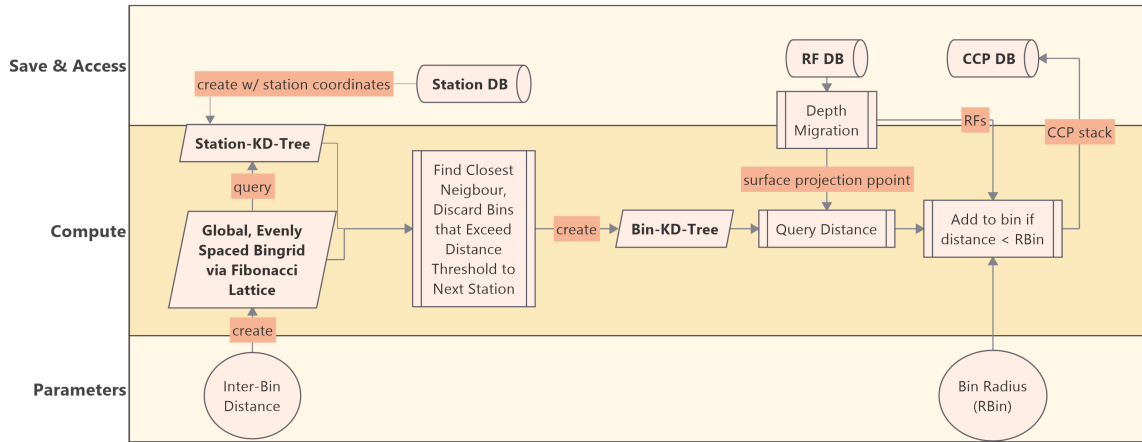
Figure 4.9: **A flow chart illustrating the implementation of CCP binning and stacking in PyGLImER.** *A detailed description is provided in the text body.*
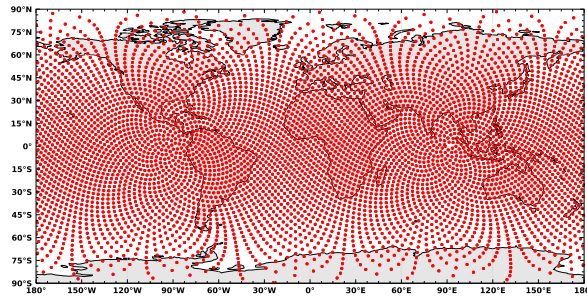

Figure 4.10: **An approximation of a global, evenly-spaced bin-grid with an inter-bin distance of 2.5° created using a Fibonacci Lattice.** *This figure represents the first step of Figure 4.9 (Creation of a global bin-grid).*

bin centres with distances to the surface projection of a given RF piercing point $\mathbf{x}$ that undercuts a user-defined bin radius r_{Bin} (i.e., the piercing point has to be inside a circular bin, see Figure 4.12). The data-point of the depth sample corresponding to $\mathbf{x}$ is then added to the same depth sample in each of those bins.

It is important to note that the two bin-defining parameters r_{Bin} and d_{Bin} (bin radius and inter-bin distance, respectively) are critical to set the degree of lateral averaging (i.e., spatial filtering) versus lateral resolution. The higher r_{Bin} the more averaging will be introduced resulting in decreased noise levels and lateral resolution. Conversely, resolution can be increased by reducing the bin size. Bin spacing and size should be chosen depending on station coverage at the surface (see section 3.3.4.1). Figure 4.12 illustrates that r_{Bin} has
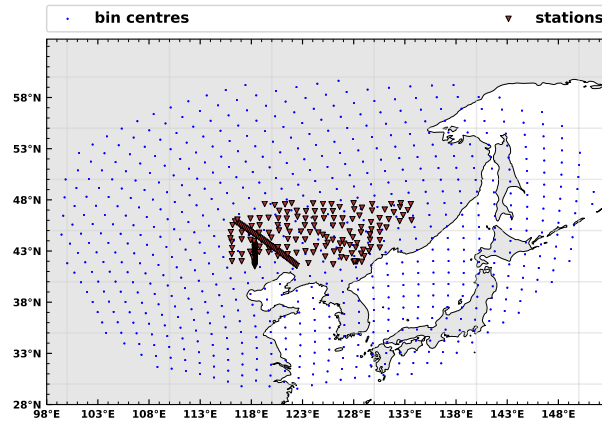
Figure 4.11: **A bin-grid prepared for SRF CCP binning in North-East China.** *The bin-grid was created by discarding all bins with a distance of more than 12 ° to the closest station.*

to be $\geq \frac{d_{Bin}}{2\cos 30°}$ to avoid "holes" in the grid. Chapter 5 will further explore the influence of the binning parameters on the final image.

It should be emphasised that the resulting CCP object is still no spatially even grid. Instead we have determined one depth-dependent vector containing RF data for each bin. Even though the bins' coordinates are known, they are not evenly distributed. In order to visualise the data, we can for example perform an interpolation through the scattered bins resulting in an evenly spaced grid, on which we could apply further manipulations (e.g., spatial filters to increase smoothness along one or several axes).
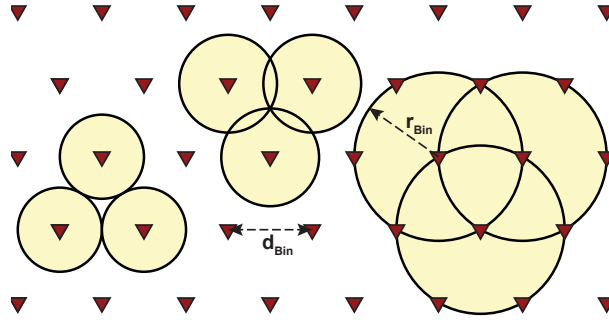
Figure 4.12: **Comparisons of different bin radii** r_{Bin} **in relation to the inter-bin distance** d_{Bin}. *Red, downwards-pointing triangles are the bin centres, the circles represent the bins' sizes. The left case shows bins with* $r_{Bin} = \frac{d_{Bin}}{2}$, *where the bins do not cover the full surface. Full coverage of the surface is achieved when* $r_{Bin} = \frac{d_{Bin}}{2\cos 30°}$ *(middle). The greater the bin radius in relation to the bin distance the more averaging is achieved. More averaging is for example given, when* $r_{Bin} = d_{Bin}$ *(right).*

4.6.1   Examples Using Synthetic Waveforms

In order to assess the method's robustness and limitations, I computed synthetic waveforms from 1D and 3D models using RaySum (Frederiksen & Bostock, 2000). Before diving into real data examples, it is vital to understand the limitations of CCP binning and stacking, which is why this section will not only include synthetic CCP images, but also a short discussion of their implications. To create the synthetic waveforms, I used an identical model as the one shown in Figure 4.4a. To simulate a three dimensional structure, discontinuity 2 (d2) dips with angles varying between 0°and 30°and a strike of 45°, thus violating the assumption of horizontal layering (see section 3.3.4.1). All incoming rays are evenly distributed over all backazimuths and a realistic range of ray parameters. Figure 4.13 shows the setup of the synthetic CCP objects for S-to-P and P-to-S data in map view including illumination.

The resulting data are visualised in Figures 4.14 and 4.15 for PRFs and Figure 4.16 for SRFs. Additional plots of the same data sets can be found in Appendix A. Appendix A does also contain CCP images created using the multiple stacking modes described in section 4.5.1. Upon inspection of the CCP images, we can establish the following:

1. For purely one-dimensional models, the CCP stacking algorithm manages to accurately recover the forward model both from PRF and SRF data (cf. Figures 4.14a and 4.16a).

2. As established before, SRF data illuminate structures that are further away from the station, whereas P-to-S conversions reach the station at quasi-vertical incidence. This effect occurs since S-to-P conversions have greater emergent than incident
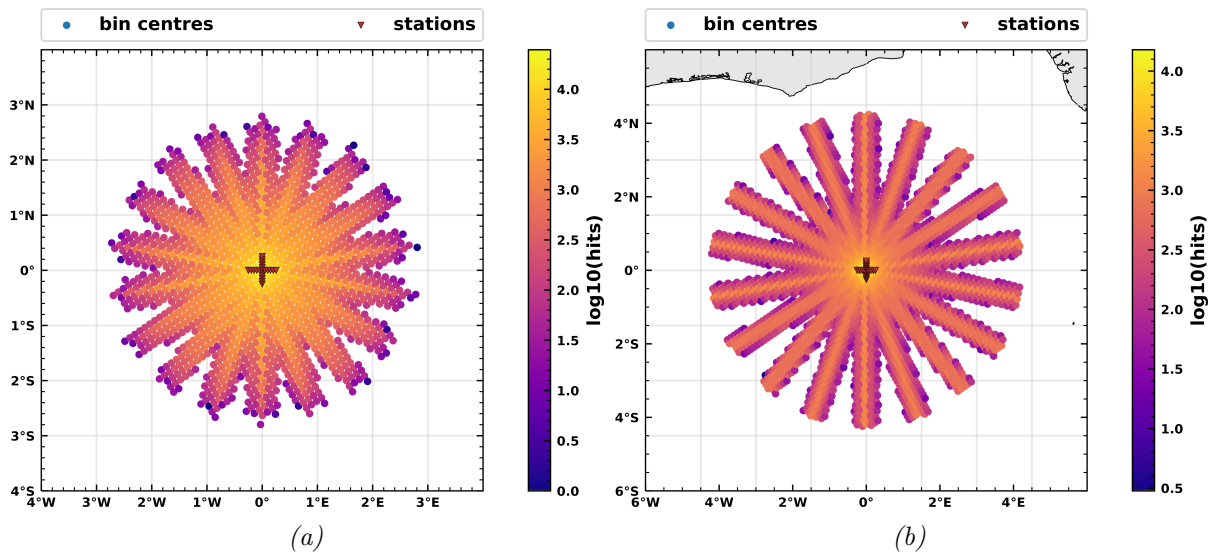
Figure 4.13: **Map view of the synthetic CCP stacks.** *Illumination is given in depth-cumulative hits per bin. Note that that the CCP object created from SRFs (b) covers a significantly larger area and ray-paths are spread wider than for PRF (a).*

angles (see Snell's law, section 3.1.1).

3. Pulses that are caused by multiples appear as concave layers in the depth migrated CCP image since they are migrated to a different depth for different ray parameters (see section 4.4.1).

4. PRFs can be used for dipping layers with a dip of up to 20°(see Figure 4.15).

5. SRFs fail to resolve structures with a dip of more than 10°(see Figure 4.16). Lekić & Fischer (2017) used a more sophisticated forward modelling approach and found that SRFs should not be used to target structures with dips of more than 7°.

6. In both PRFs and SRFs, rays with different ray parameters and backazimuths recorded at different stations can exhibit varying polarisations due to refraction at the dipping layer. These phases are stacking destructively, thereby, effectively masking a boundary partly or entirely (e.g., 4.15b and 4.16c). This effect has for example been described by Lekić & Fischer (2017) and occurs earlier (i.e., for shallower dips) for S-to-P than P-to-S conversions.

Now that we are aware of the method's potential and limitations, we are ready to apply it to real data.
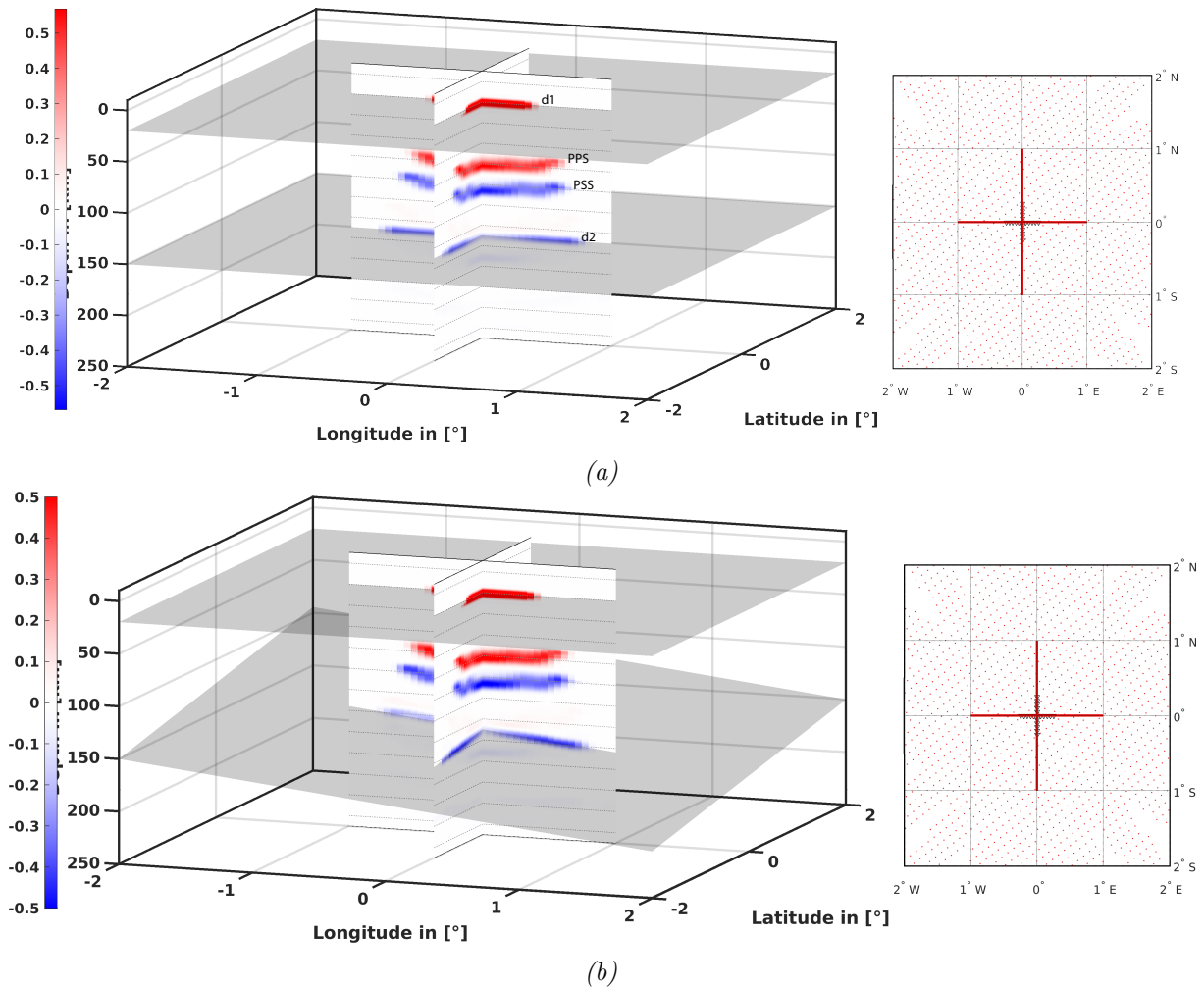
Figure 4.14: **Slices through a CCP volume created using PRFs.** *The dip of boundary d2 increases with every panel from 0° to 30°. The traces of the velocity discontinuities d1 and d2 are plotted as black, semi-transparent surfaces. The different discontinuities or multiples causing each pulse are indicated in panel (a). The dips for d2 are 0° in (a) and 10° in (b).*
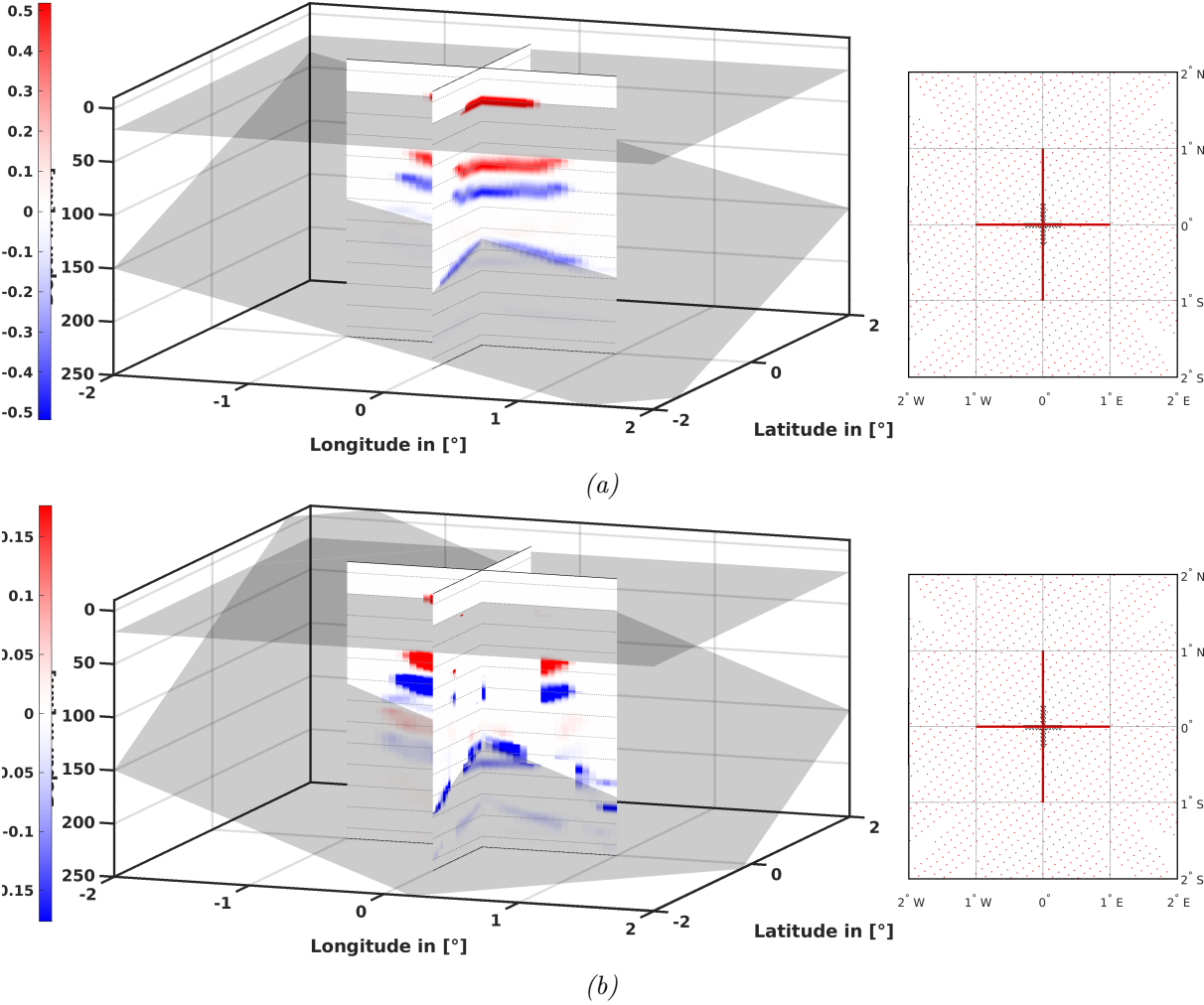
Figure 4.15: **Continuation of Figure 4.14.** d2 dips with a dip of 20 ° in (a) and 30° in (b).
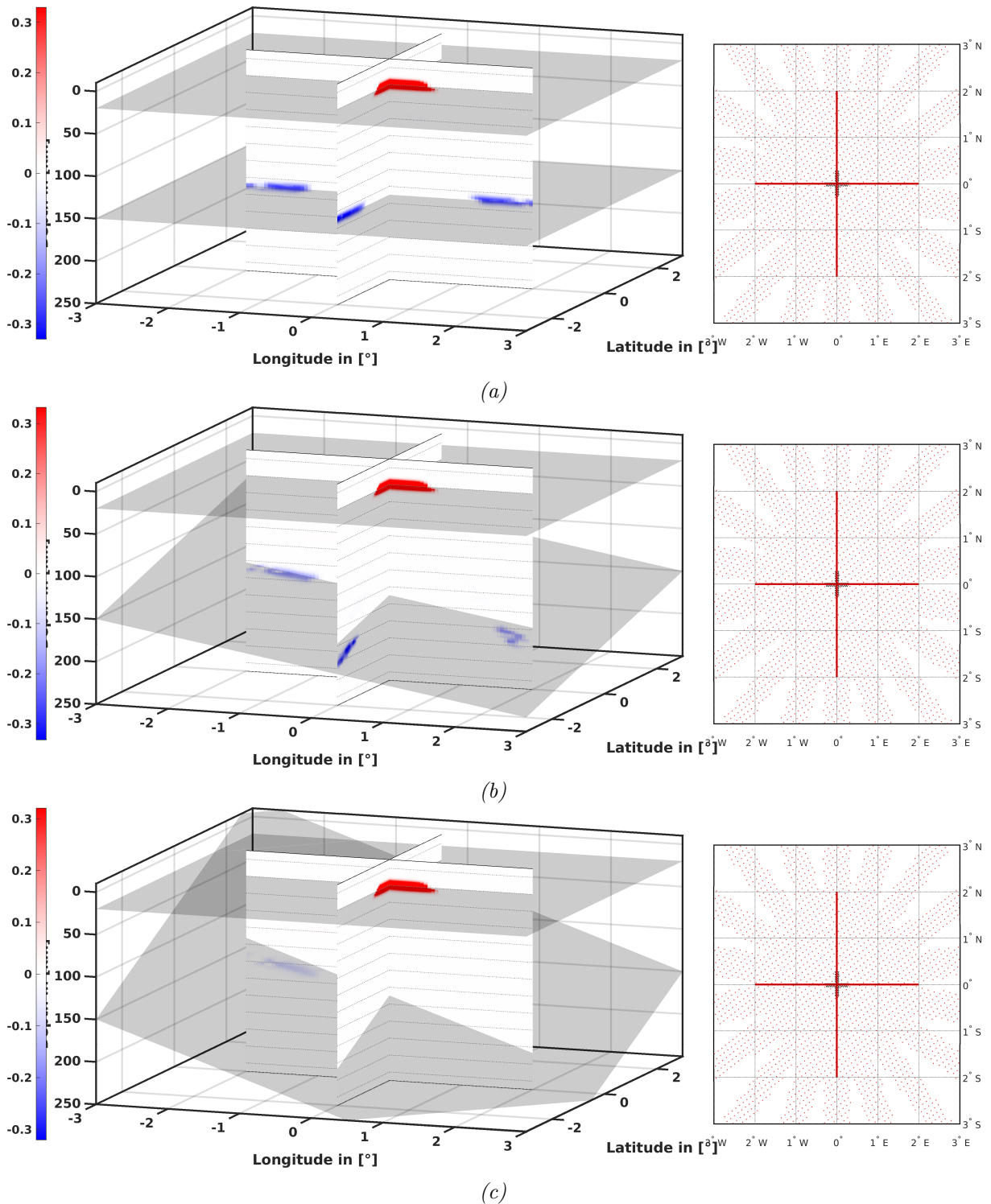
Figure 4.16: **Slices through a CCP volume created using SRFs.** *The dip of boundary d2 increases with every panel from 0° to 20° by 10°. The traces of the velocity discontinuities d1 and d2 are plotted as black, semi-transparent surfaces.*

Chapter 5

Application

5.1 Global Receiver Function Imaging

To demonstrate PyGLImER's capability to create receiver function images using datasets from several FDSN providers anywhere around the world, I will show several large-scale CCP images from various regions with dense station coverage (see map in Figure 4.2). Thereupon, we will take a closer look at one of these regions.

5.1.1 Eastern Europe

The first cross-section covers RF data from southern Germany over Austria, Hungary, and Romania to the Black Sea (see Figure 5.1). The main geodynamic driving force influencing the study area is the alpine orogenesis caused by the ongoing collision of the African with the European plate (Kind et al., 2017). The eastern European lithosphere is divided into the Phanerozoic West and the Precambrian East by the Trans-European Suture Zone. Most of the discussed cross-section cuts through the young, western lithosphere. Only the easternmost part of the profile reaches the Moesian Platform (Proterozooic) (Petrescu et al., 2019). In eastern Romania under the Carpathian Mountains, signals of a subducting slab, which causes strong seismicity, have been observed (Diehl & Ritter, 2005). The geodynamically diverse and active history of the region lead to a high degree of structural complexity in the lithosphere (Diehl & Ritter, 2005).

The CCP objects, from which the shown cross-sections (Figure 5.2) are created, contain data recorded by 1,130 stations, from which PyGLImER created 71,858 P-to-S and 12,378 S-to-P RFs. For waveforms containing the direct P arrival and the P-to-S conversions, I
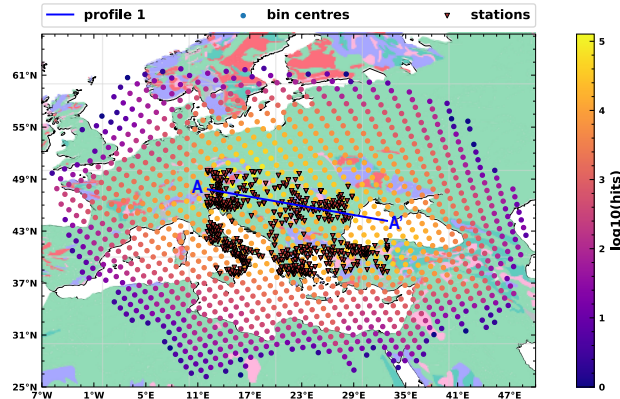
Figure 5.1: ***A map view of the first cross-section exploring the eastern European litho-sphere.*** *The map shows locations of the stations, from which data have been used, bin locations, illumination per bin, and the exact location of the cross-section. The illumination is given as depth-cumulative illumination per bin for SRF-data. The simplified geological background map was retrieved from* Generalized geological map of the world and linked databases *(1995).*

imposed a 1.5Hz highcut filter before deconvolution[1]. All waveforms are rotated to a P-Sv-Sh coordinate system[1], subsequently, the RFs are created using iterative time domain deconvolution with a Gaussian width parameters of 2.5 and 1.75 for PRFs and SRFs, respectively[1], to account for the different frequency contents of teleseismic P and S waves. Thereafter, the RFs are transferred to depth domain using velocities from the GyPSUM velocity model[1]. Finally, I bin and stack the RFs depending upon their piercing points (i.e., CCP binning) for a bin grid with an inter-bin distance of $d_{Bin} = 1°$ for PRFs and $d_{Bin} = 0.85°$ for SRFs and a bin radius of $r_{Bin} = \cos{(30°)}d_{Bin}$[1].

Previous converted wave studies have already targeted structures located in the greater region of the presented cross-section. For example, Kind et al. (2017) covered the discussed region in a large-scale SRF survey (see Figures 8C and 8D in their paper). Diehl & Ritter (2005) and Petrescu et al. (2019) focused on lithospheric structures under Romania.

Considering the results shown in Figure 5.2, we can make the following observations. (1) The strongest observed phase is a positive (red for this and all following images) and corresponds to the Moho conversion (labelled as "I" on PRF and SRF data). (2) For both phases, in the West, a downwards negative velocity gradient (NVG) (blue for this and all following images) with the label "II" between 50-85km depth can be seen. (Kind et al., 2017) associated this NVG with the Phanerozoic LAB. PRF data show evidence for internal layering in the Phanerozoic LAB. However, the PRF image is masked by

---

[1]These parameters remain identical for this and all following CCP stacks. However, the inter-bin distance varies from CCP stack to CCP stack.

strong multiples in the depth range of 80-150km and these multiples might contribute to the apparent internal layering of the LAB. (3) SRF data (panel (b)) seem to indicate an abrupt eastwards thickening of the lithosphere between 1000-1200km offset (i.e, the transition from "II" to "IV" under Romania). Such a thickening would coincide well with the transition from younger Phanerozoic lithosphere to older and thicker cratonic lithosphere (i.e., pieces of continental lithosphere that remained rigid and stable since the Precambrian (Hoffman, 1988)). (4) At 150-160km depth, a fairly sharp NVG with a slight westwards dip is visible in the PRF image ("III"). This structure could correspond to the sublithospheric discontinuity that Kind et al. (2017) detected with SRFs at slightly greater depths.
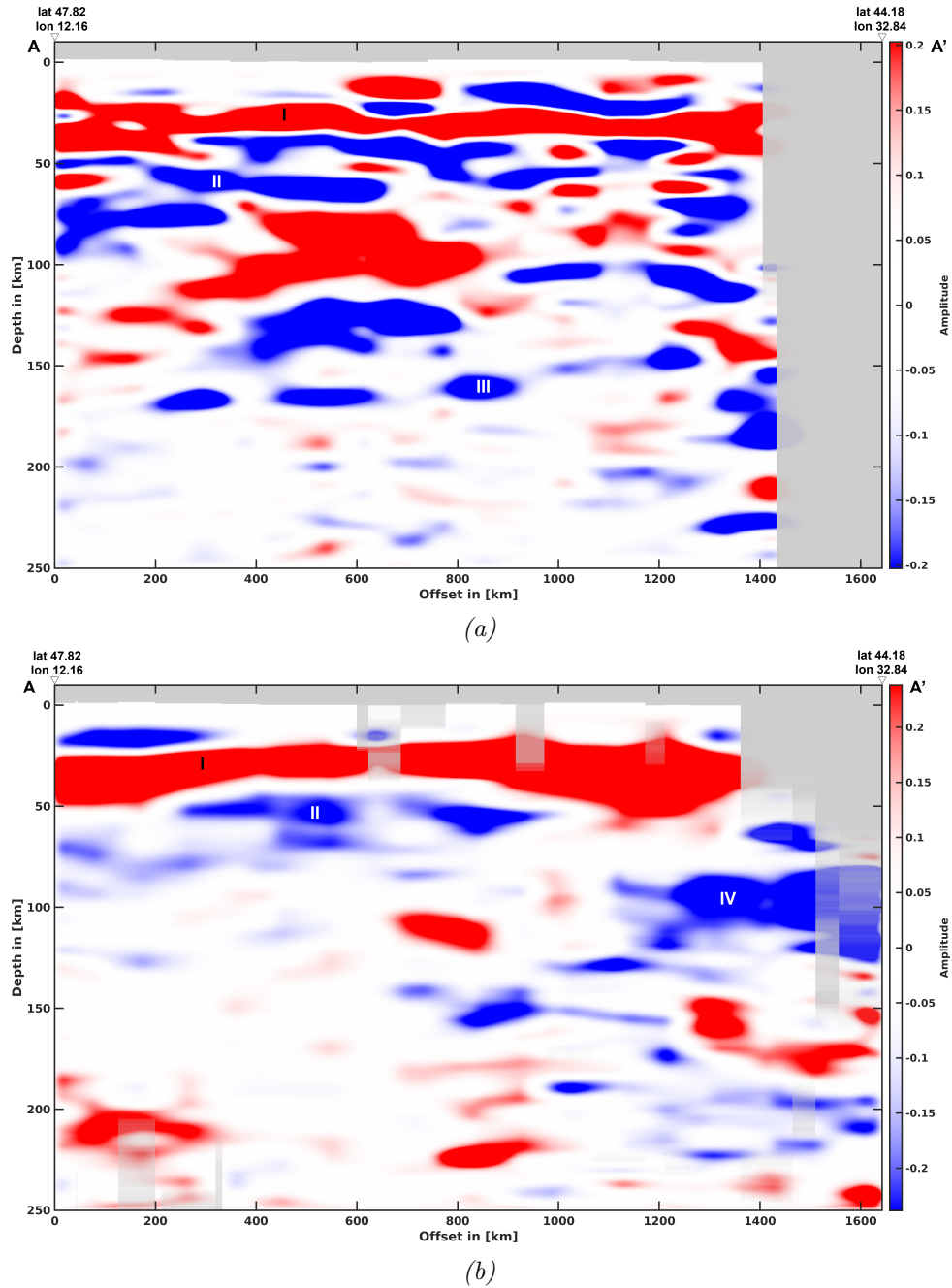
(a)

(b)

Figure 5.2: **Cross-sections through the CCP stacks for eastern Europe.** *Illumination is plotted as transition from opaque data to opaque grey background. (a) shows an image created with P-to-S data and (b) an image from S-to-P data. Data are greying out for grid points (i.e, a bin at depth z) with fewer than 50 and 25 hits, respectively.*

5.1.2   Hindu Kush - Pamir

The second profile crosses the Hindu Kush and the Pamir mountains from Afghanistan over Tajikistan, and China to Kyrgyzstan (see map in Figure 5.3). Of the presented sections, this one is, with a total offset of about 550km, by far the shortest. Geodynamically, the Pamir region belongs to the westernmost Himalayas and is still subject to active deformation. From a tectonic viewpoint, this region is very unique as it is one of the few places where subduction of continental lithosphere can directly be observed. At the Main Pamir thrust, the Eurasian plate subducts under the Indian plate (Schneider et al., 2013; Kufner et al., 2018). Evidence for a detachment of the Indian plate has been reported by Kufner et al. (2016).
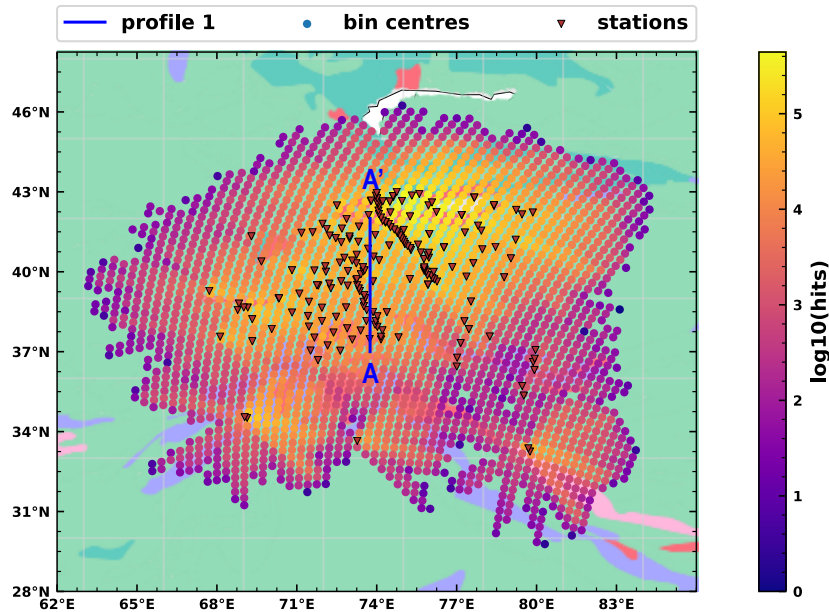

Figure 5.3: ***A map view of the cross-section through the Hindu Kush and the Pamir orogen.*** *The map shows locations of the stations, from which data have been used, bin locations, illumination per bin, and the exact location of the cross-section (blue line). The illumination is given as depth-cumulative illumination per bin for PRF-data. The simplified geological background map was retrieved from* Generalized geological map of the world and linked databases *(1995).*

Due to a very dense station coverage (i.e., about 10km interstation spacing on local level), I could realise a very low interbin distance of 0.25°for PRF data. Owing to a lower data density for S-to-P data, the spacing had to be coarser (i.e., 0.35°). The final CCP objects comprise 29,988 and 7,529 RFs from 199 stations for P-to-S and S-to-P data, respectively, where the PRF CCP stack includes RFs that were also depth migrated with

respect to multiple conversion times in the form of a weighted stacking approach (see section 4.5.1).

Other authors used data recorded on the dense deployments in the region for RF surveys. For example, Schneider et al. (2013) used PRF data to image the subducting Eurasian slab. Kumar et al. (2005) examined SRF data and found a negative discontinuity between 100km (north) and ca 230km (south), which they interpreted as the LAB. Chen et al. (2018), on the other hand, found no evidence for a LAB shallower than 200km using surface wave tomography.

The cross-section in Figure 5.3 closely resembles the north-south section by Schneider et al. (2013). As before, the strongest phase (label "I") is caused by the Moho conversion. On the PRF image (panel (a)), a positve southwards-dipping signal (dashed line labelled as "II", present between 0km and 280km offset), appears at the same location, where Schneider et al. (2013) imaged the subducting slab of the Eurasian plate. In both PRF and SRF data, evidence for strong deformation can be seen (e.g., strong heterogeneities in the Moho topography). As S-to-P data are not well-suited for imaging dipping layers (see section 4.6.1), the subducting slab cannot be clearly identified in panel (b). At similar depths, one can observe a southwards dipping NVG (labelled as "II?") that might be associated with the Eurasian slab. Additionally, S-to-P data exhibit hints of a negative discontinuity between 150km and 200km depth ("III") possibly correlated to the base of the lithosphere (i.e., the LAB).
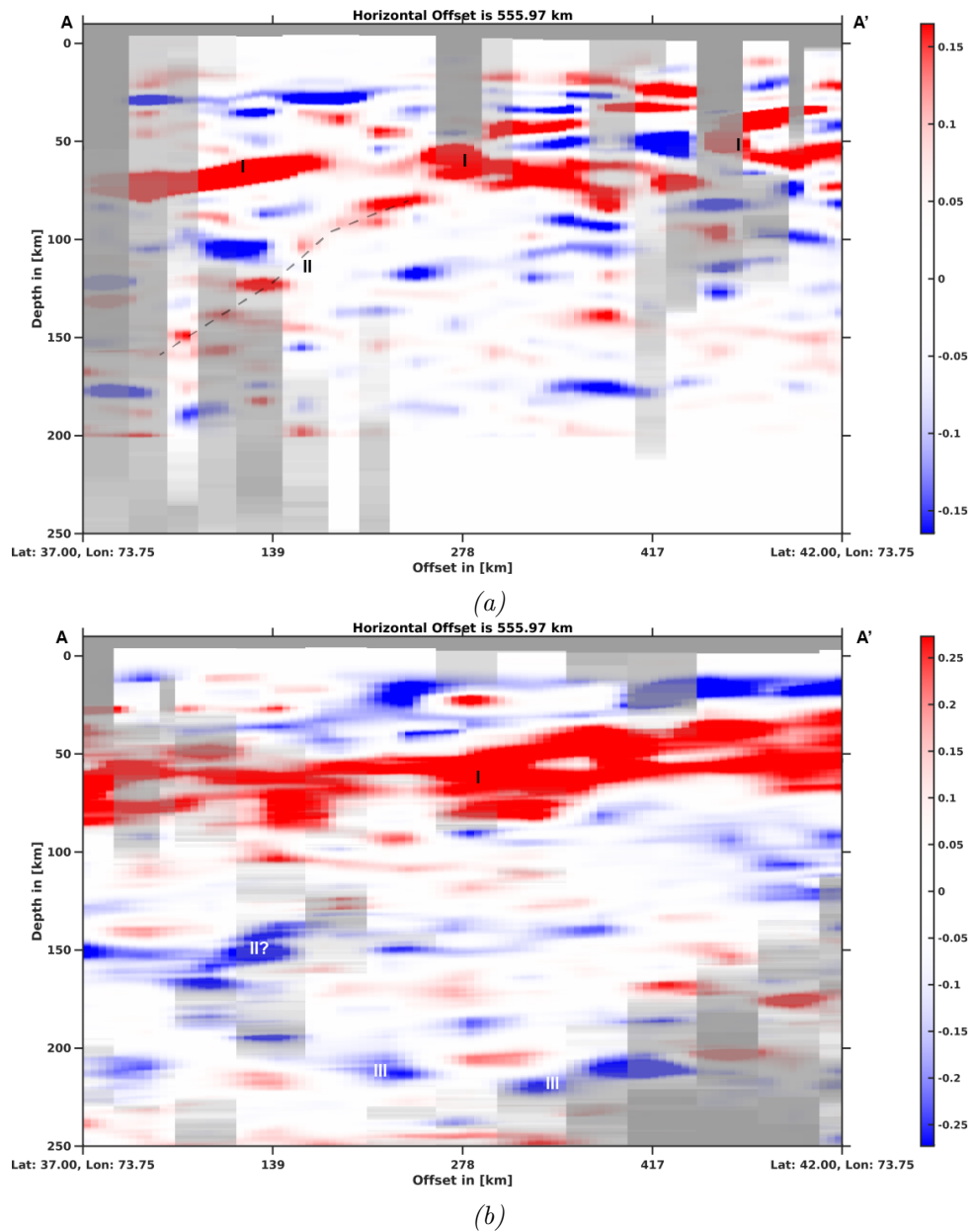
Figure 5.4: **Cross-section through the CCP stacks for the Pamir orogen.** *Illumination is plotted as transition from opaque data to opaque grey background. Panel (a) shows an image created from P-to-S data and panel (b) an image from S-to-P data. Data are greying out for grid points with fewer than 25 and 15 hits, respectively.*

5.1.3   North China Craton

Cross-section number three targets the North China craton and strikes ENE-WSW (see Figure 5.5). On the coarsest scale, the North China craton can be divided into a tectonically stable West (virtually unaltered for ≥1.5Ga) and a tectonically and magmatically active East (Chen, 2010) with evidence for ongoing intra-plate volcanism (Guo et al., 2016) that could be linked to a mantle plume (He, 2019). An extensional setting led to the development of the Songlia Basin (Zhang et al., 2014). A large part of the root of the eastern North China craton has been destroyed and replaced by a hotter and thinner mantle. Cenozoic, basaltic magmatism indicates that the replacement of the cratonic root did only happen recently (Aulbach et al., 2017).

The study area is densely spatially sampled by the temporary NorthEast China Extended SeiSmic Array (NECESSArray) deployment, which consists of 127 broadband stations, and other permanent and temporary seismic networks. In total, the final CCP stacks are created using 23,676 PRFs and 2,904 SRFs from 226 stations. Despite the low interstation distance, the number of RFs in the final stacks remains fairly low since the NECESSArray was only active for a maximum of about two years. However, I was still able to create a fairly dense CCP bingrid with an interbin distance of 0.5°.

Due to its excellent seismic coverage and its diverse tectonic features, the North China Craton has recently been subject to a great number of seismic studies targeting crustal and lithospheric structures. Amongst these studies, Guo et al. (2014) and Zhang et al. (2014) focused on the structure of the lithospheric mantle utilising the RF technique. While Guo et al. (2014) interpreted the LAB to be of a relative constant depth between 60km and 80km, Zhang et al. (2014) presented evidence for a thicker lithosphere with strong thinning under the Songliao Basin. Further south, (Chen, 2010) saw signs of a topographically varying LAB.

Figure 5.6 shows the images created from data of the PyGLImER database. The strongest positive velocity gradient in both P-to-S and S-to-P data is the Moho phase ("I") with a depth varying between 40km and 30km depth. It is shallowest on the edges of the Songlia Basin and deepens westwards (i.e., crustal thickening in the unaltered craton). In P-to-S data (see Figure 5.6a), the Songlia Basin can be clearly identified based on strong crustal conversions most likely caused by the transition from unsolidified sediments to bedrock (i.e., the base of the sediment basin). Right under the Moho in the upper mantle, a westwards dipping NVG varying between 70km and 55km depth can be seen ("II"). The rest of the PRF image is masked by strong multiples. In the image created from S-to-P data, a broad and strong NVG appears between 50km and 100km
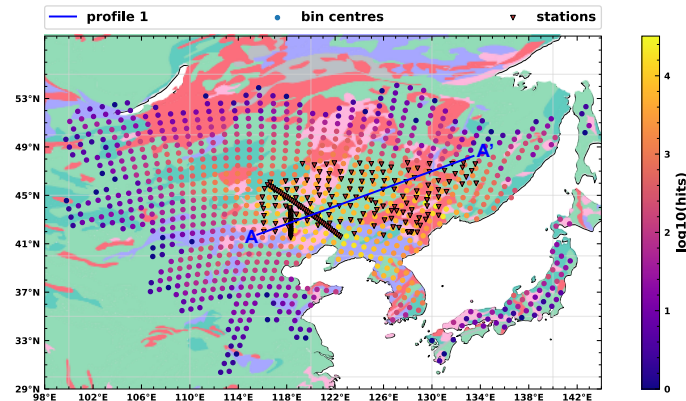
Figure 5.5: **A map view of the discussed cross-section targeting the North China craton.** *The map shows locations of the stations, for which data have been used, bin locations, illumination per bin, and the exact location of the cross-section. The illumination is given as depth-cumulative illumination per bin for SRF-data. The simplified geological background map has been retrieved from* Generalized geological map of the world and linked databases *(1995).*

depth ("III"), which Guo et al. (2014) called the LAB. Right under the Songlia Basin (100km to 120km depth), a "frown-shaped" NVG, which is demarked by a dashed line and labelled as "IV", stretches from 500km to 1200km offset. The structure might be an artefact caused by scattering, although it seems unlikely considering its lateral extent. Alternatively, this NVG could be caused by the structure that Zhang et al. (2014) termed the LAB. Conclusively, the presented figures do not suffice to rule out either of the two found NVGs to be caused by the LAB. However, it is worth pointing out that Zhang et al. (2014) had access to waveform data that is not publicly available and was not at Guo et al. (2014)'s or my disposal.
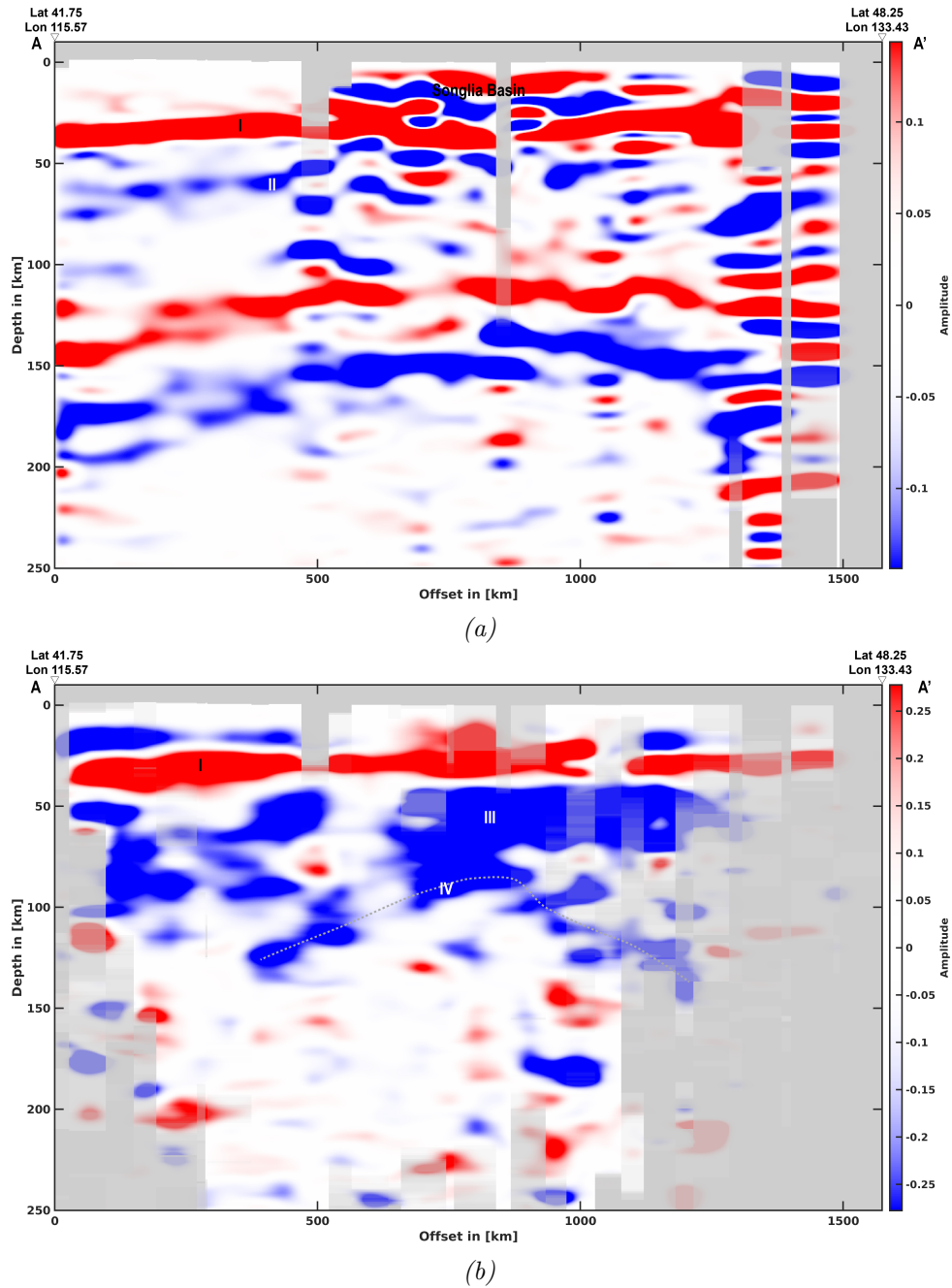
(a)

(b)

Figure 5.6: **Cross-section through the CCP stacks for the North China craton.** *Illumination is plotted as transition from opaque data to opaque grey background. Panel (a) shows an image created with P-to-S data and panel (b) an image from S-to-P data. Data are greying out for grid points with fewer than 50 and 15 hits, respectively.*

5.1.4   North America

The fourth profile crosses North America on its W-E axis (starting in Vancouver Island and ending in Miami). A large portion of North America is composed of the Precambrian continent Laurentia. Laurentia itself is an assembly of several Archean cratons and Proterozoic mobile belts and surrounded by the younger Paleozoic Appalachian orogen and Atlantic Coastal planes in the East and tectonically active Phanerozoic lithosphere in the West (Williams et al., 1991). The very diverse nature of the lithospheric large-scale components in North America makes the continent ideal to study the evolution of continental lithosphere.

The US is one of the most densely sampled areas in the world owing its spatially even coverage mainly to the Earthscope Transportable Array, which was active in the 48 mainland states and southern Canada between 2004 and 2014. From the resulting data together with data from other permanent and temporary seismic networks in the US, southern Canada, and northern Mexico, I created a CCP object consisting of about 650,000 P-to-S and 135,000 S-to-P RFs from an unprecedented number of 5,909 seismic broadband stations. The spatially even, short interstation distance allows for a relatively small CCP bin distance of 0.58°.

A host of studies have targeted the lithospheric mantle under the US. Figure 5.11 shows an overview of recent RF studies amongst those. The key structures that those studies have confirmed are: (1) In the tectonically active West, a thin lithosphere with a shallow LAB at about 70km depth can reliably be seen from SRF data (e.g., Li et al., 2007; Abt et al., 2010; Lekic et al., 2011; Kumar et al., 2012). (2) In the rest of the US, both phases reveal a broad negative discontinuity at equal depths (e.g., Kumar et al., 2012), which is now widely regarded as a MLD (Abt et al., 2010; Hopper et al., 2014; Kind et al., 2015; Hopper & Fischer, 2018; Kind et al., 2020). (3) Only few studies provide evidence of a deep, cratonic LAB utilising the SRF technique sometimes with depth discrepancies (Foster et al., 2014; Chichester et al., 2018; Kind et al., 2020). Surface wave tomography has generally proven a more reliable mean to place constraints on the LAB's depth under the North American cratons (e.g., Schaeffer & Lebedev, 2014). The fact that the NVG associated with the cratonic LAB is seen more clearly on low-frequent surface wave data could be an indicator for a purely thermal LAB with a smooth, gradual velocity transition (Fischer et al., 2010).

Slices through the CCP objects along the cross-section indicated in Figure 5.7 are plotted in Figure 5.8. Again, the strongest conversion of both teleseismic phases is produced by the Moho ("I"). The Moho depth varies between approximately 30km to 50km. In
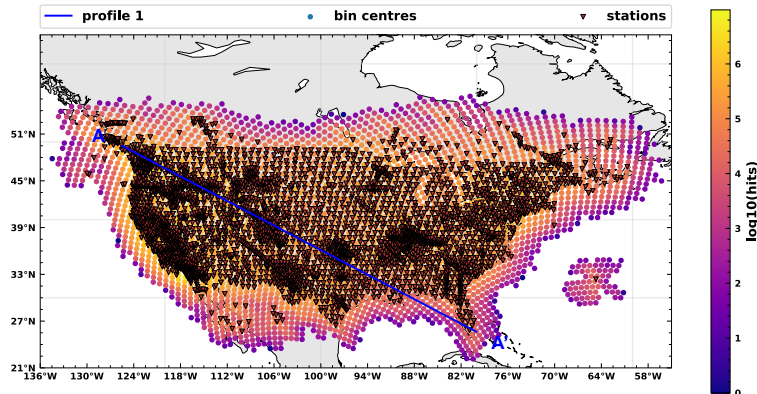
Figure 5.7: **A map view of the cross-section through North America.** *The map shows locations of the stations, from which data have been used, bin locations, illumination per bin, and the exact location of the cross-section. The illumination is given as depth-cumulative illumination per bin for PRF-data.*

the western part of the PRF and SRF image (i.e., panel (a) and (b), respectively), we can clearly see a strong NVG extending until about 1200km offset, which I labelled as "II". This NVG corresponds to what has been agreed to be the Phanerozoic LAB. Further east, SRF data exhibit a broad NVG ("III") ranging between 50km to 110km depth most likely corresponding to a MLD. Hints of an internal structure/layering are visible. Another weak, less continuous NVG is present between 150km and 200km depth ("IV"). The PRF image (i.e., Figure 5.8a), on the other hand, is mostly masked by crustal multiples caused by strong crustal phases in the southeastern US. However, traces of one or possibly several MLDs ("III") are visible in the East.

These observations are in general agreement with previous studies. However, only few authors have reported evidence for several MLDs under North America (Hopper et al., 2014; Lekić & Fischer, 2014; Wirth & Long, 2014; Ford et al., 2016). It does thus make sense to investigate the number of MLDs utilising images from P-to-S data since their higher frequencies yield a higher resolution. In addition, the weak signal occurring at depths, at which one would expect the cratonic LAB based in results from surface wave tomography is worth investigating. Therefore, I will dedicate the following section to a more exhaustive analysis of the structures in the lithospheric mantle under the North American continent.
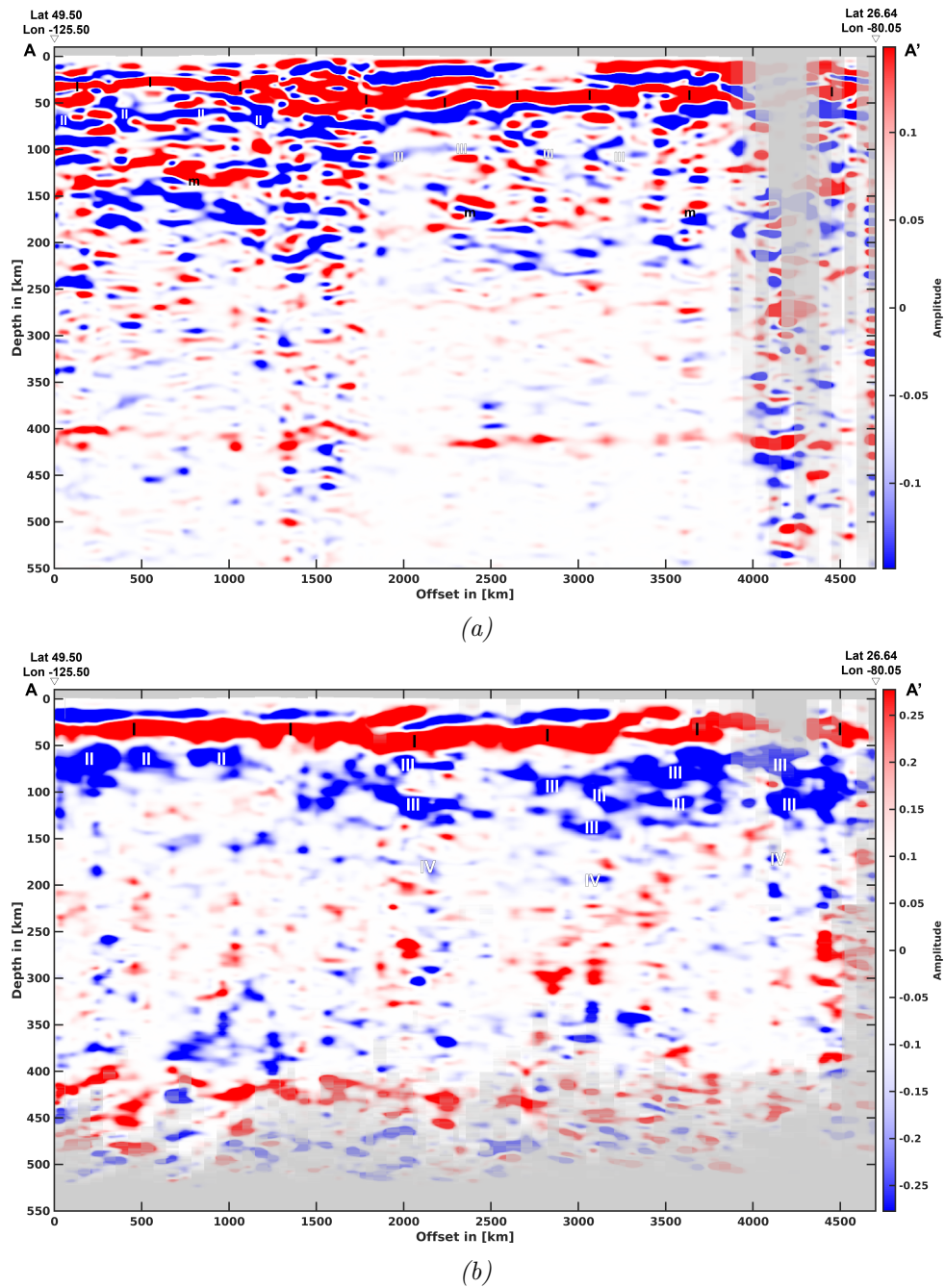
Figure 5.8: **Cross-section through the CCP stacks for North America.** *Illumination is plotted as transition from opaque data to opaque grey background. (a) shows an image created with P-to-S data and (b) an image from S-to-P data. Data are greying out for grid points with fewer than 50 and 25 hits, respectively.*

5.2 Lithospheric Discontinuities in the North American Continent

5.2.1 Geological Setting

On the coarsest scale, the North American continent may be divided into three parts. Firstly, the cratonic part that is constituted by the paleo continent Laurentia, secondly, the Phanerozoic, tectonically active West which is separated from the craton by the Rocky Mountains, and, thirdly, the Paleozoic Atlantic Coastal Plains (Hoffman, 1988).

On a finer scale, a division dependent upon the last tectonic or magmatic overprinting event makes sense. Such a division is shown in Figure 5.9. On this scale, we can distinguish between the actively deforming West and the Paleozoic Appalachian orogen as the younger regions. Regions with Proterozoic overprints are the Grenville orogen, which resulted from the collision that created the supercontinent Rondinia (Boyce et al., 2019)), and the Central Plains. Undeformed relics from the Archean are the Superior and Wyoming Craton in Canada and the northern United States.

The Precambrian elements can further be grouped into a finer division as shown in Figure 5.10. The northern US and Canada are dominated by undeformed Archean lithosphere (grey areas in Figure 5.10). Further south, a progressive accretion of volcanic arcs and oceanic terranes in the Proterozoic caused a number of NW-SE striking sutures (Whitmeyer, 2007). One of the most striking features in the northern US is the Kewanowan rift, a failed, Proterozoic midcontinent rift (e.g., Chichester et al., 2018).

Heatflow modelling (e.g., Hamza & Vieira, 2012; Cammarano & Guerri, 2017) and surface wave tomography (e.g., Schaeffer & Lebedev, 2014; Priestley et al., 2018) constrain high lithospheric thicknesses in the North American cratonic regions (i.e., up to about 200km for surface tomography) and a thin lithosphere in the active West. Lithospheric thickness decreases gradually in the South and Southeast. Rychert et al. (2005) and Rychert et al. (2007) found a shallow LAB in the Northern Appalachians; a finding that can be confirmed using surface wave tomography (Schaeffer & Lebedev, 2014).

5.2.2 Previous Studies

A multitude of RF studies have been conducted in North America, many of which target crustal structures or the Moho using P-to-S data. More recently, the emerging SRF technique has been employed to image structures in the deeper lithosphere, where crustal and Moho multiples interfere with primary conversions in PRF data (e.g., Kumar et al.,
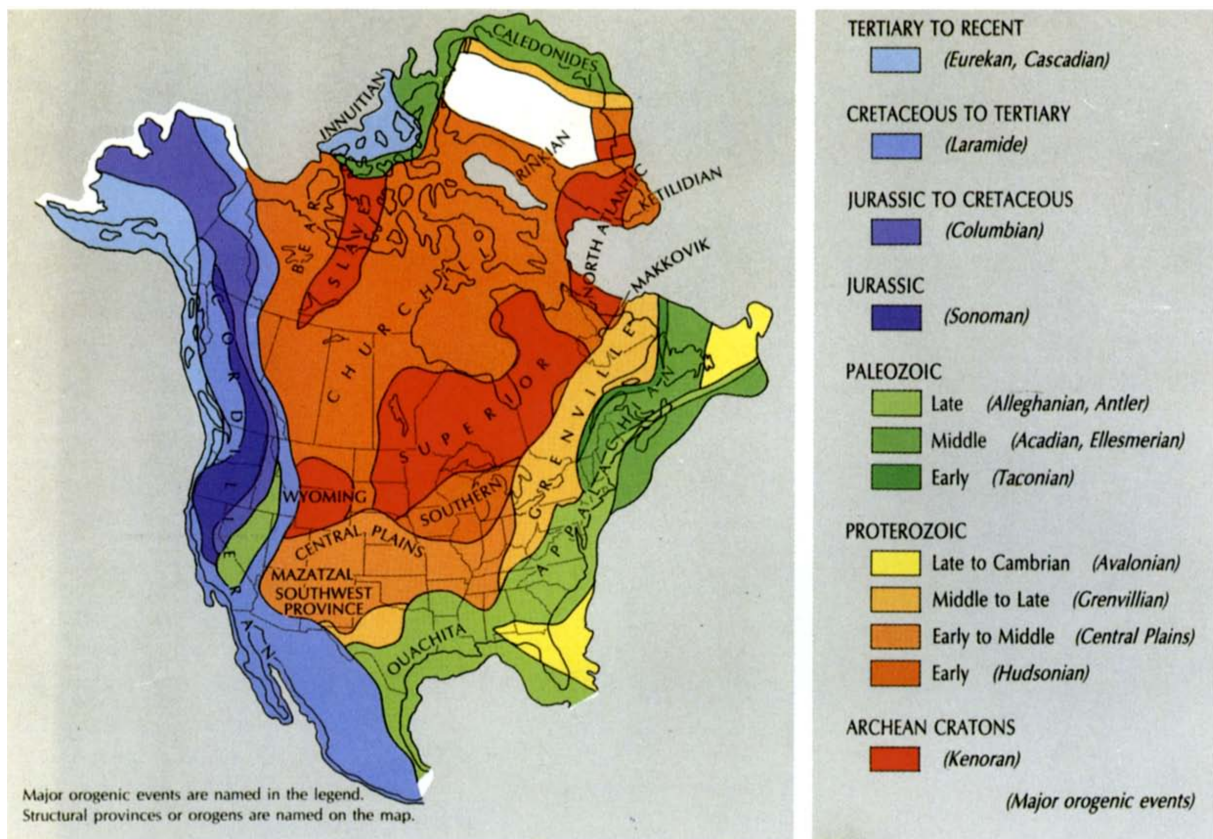
Figure 5.9: **Last major events of deformation on the North American continent.** *Figure retrieved from Williams et al. (1991).*

Figure 5.10: **Precambrian elements in the North American continent.** *The following abbreviations have been used: RW, re-worked; GBA, Great Bear Arc; BHT, Buffalo Head Terrane; Tl.A, Talston Arc; RA, Rimbey Arc; NA, Narajusaq Arc; Tn.A, Torngat Arc; LBA, Little Belt Arc; LRA; La Ronge A; Pnk., Penokean Province; NQB, New Quebec Belt; THO, Trans-Hudson Orogen; RGR, Rio Grande Rift; Kwn.R, Kewanowan Rift; Sask, Sask Craton; WY, Wyoming Province; MHB, Medicine Hat Block; Grt. Rhy, Granite–Rhyolite Province; Grenv., Grenville Province; and Lbrdn., Labradorian Province. The Rocky Mountain Front (RMF) is indicated by the black dashed line, the paleo continental margin by the red line, and the westwards extent of the Greenville Front by the blue line. Figure is retrieved from Schaeffer & Lebedev (2014) and was originally altered from Whitmeyer (2007).*

2012; Kind et al., 2015; Hopper & Fischer, 2018; Chen et al., 2018; Kind et al., 2020).
Figure 5.11 provides an overview of recent RF studies and their study areas targeting the
lithospheric mantle under the US. Considering those studies, we can see that employing
only S-to-P data has recently become more common practice, whereas the last continent-
wide publication using P-to-S data is by Hansen et al. (2015).

The various studies show different degrees of agreement on structural features in the
lower lithosphere. As expected, the Moho is the interface that causes the strongest positive
velocity gradient. However, this thesis focuses on mantle structures. In the lithospheric
mantle, the probably best constrained feature is a strong NVG west of the RMF corre-
sponding to the Phanerozoic LAB. In the East, a NVG at similar depths is found, which
all recent publications agree to be an MLD (e.g., Abt et al., 2010; Hopper et al., 2014;
Wirth & Long, 2014; Lekić & Fischer, 2014; Chen et al., 2018). Some studies found evi-
dence for several MLD-like signals in the cratonic parts of the North American continent
(Hopper et al., 2014; Wirth & Long, 2014; Lekić & Fischer, 2014; Ford et al., 2016; Chen
et al., 2018). Only a handful of RF surveys detect a NVG that could correspond to a
deeper, cratonic LAB and the resulting depth estimates vary considerably (Rychert et al.,
2005, 2007; Hansen et al., 2013; Foster et al., 2014; Chichester et al., 2018; Kind et al.,
2020).

To confirm the robustness of images created from PyGLImER's RF database, I chose
to compare my results with results from four of the aforementioned studies that span the
whole of the US and parts of southern Canada. From those studies, only Hansen et al.
(2015) (see Figures 5.12 and 5.13) used both P-to-S and S-to-P RFs.
Comparison shows that the new dataset reproduces most pulses seen by Hansen et al.
(2015). However, the new dataset shows a significantly higher amount of discontinu-
ities. Differences may be caused by several factors such as a higher data density for the
PyGLImER dataset, particularly in the East where only PyGLImER uses all stations of
the Eartscope Transportable array. In addition, Hansen et al. (2015) used a skewed colour
scale with very high contrasts.

More recently, Hopper & Fischer (2018) implemented an algorithm to automatically
pick the strongest negative velocity gradient from SRFs in the mantle. In Figure 5.14,
their results are plotted onto an SRF CCP stack from the PyGLImER database. The two
datasets show a high degree of coherency even for small scale depth variations.

In contrast to other SRF studies, Kind et al. (2015) and Kind et al. (2020) use elongated
bins for their CCP stacking. That is, their cross-sections have a width varying between
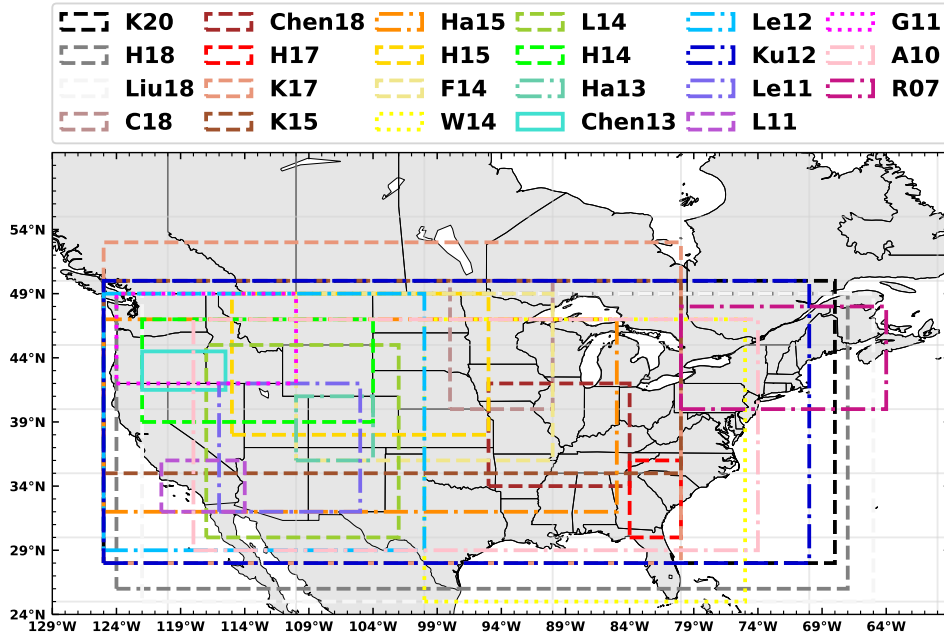about 5°to 10°. To reproduce their results, I applied a running mean on the gridded

Figure 5.11: **Map view of recent publications targeting the structure of the lithospheric mantle under the United States using converted teleseismic waves.** *Dotted lines are studies using P-to-S converted waves, dashed lines demark studies using S-to-P converted waves, and dashed and dotted lines mark areas surveyed with both phases. Abbreviations are as follows: K20: Kind et al. (2020), H18: Hopper & Fischer (2018), Liu18: Liu & Gao (2018), C18: Chichester et al. (2018), Chen18: Chen et al. (2018), H17: Hopper et al. (2017), K17: Kind & Yuan (2017), K15: Kind et al. (2015), Ha15: Hansen et al. (2015), F14: Foster et al. (2014), W14: Wirth & Long (2014), L14: Lekić & Fischer (2014), H14: Hopper et al. (2014), Ha13: Hansen et al. (2013), Chen13: Chen et al. (2013), Le12: Levander & Miller (2012), Ku12: Kumar et al. (2012), Le11: Levander et al. (2011), L11: Lekic et al. (2011), G11: Gao et al. (2011), A10: Abt et al. (2010), and R07: Rychert et al. (2007) and Rychert et al. (2005). Chen et al. (2013) used a migration approach (see Rondenay et al., 2005) and Kind et al. (2020) stack the component of the seismogram holding the scattered wavefield instead of employing a more prevalent approach relying on deconvolution. All other cited articles use RF data.*
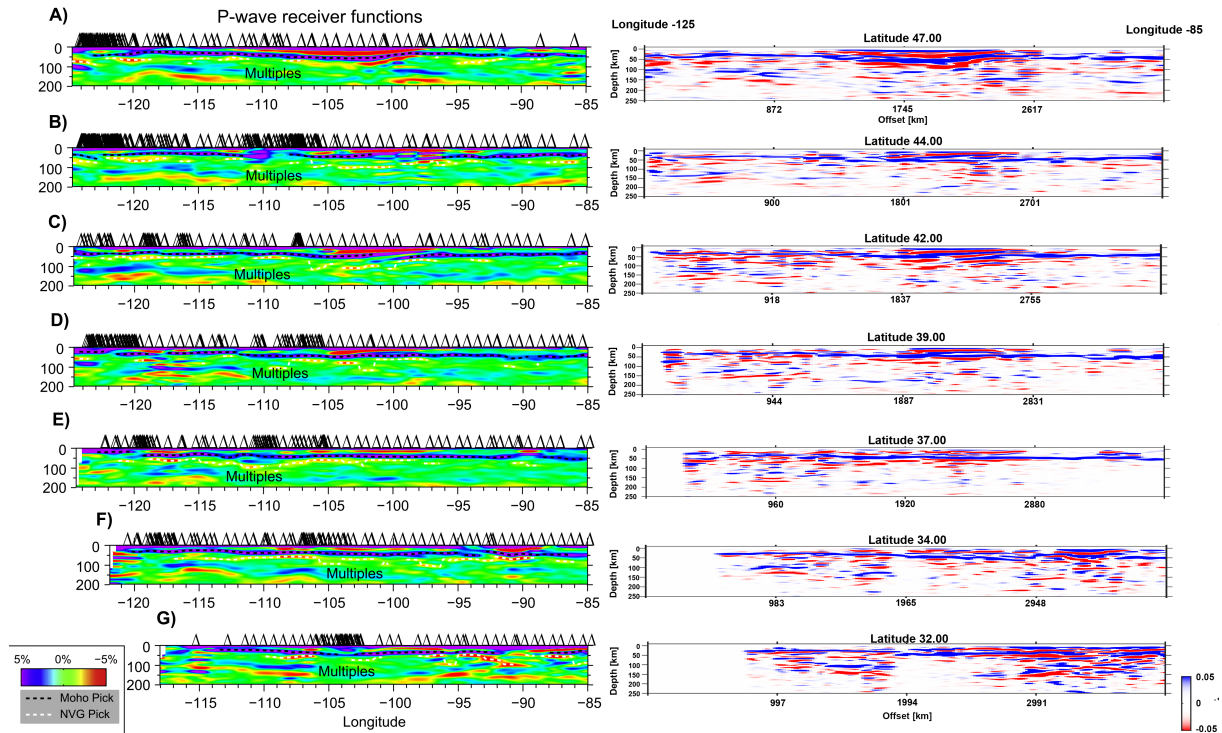
Figure 5.12: **West-East slices through a CCP stack created from PRF data.** *The figure compares data from Hansen et al. (2015) (left) to a CCP object created from the PyGLImER database (right). Blue peaks indicate (downwards) positive velocity gradients, whereas red peaks are downwards negative velocity gradients.*

dataset in North-South direction prior to plotting. The spatial filtering results in a strong averaging as seen for example in Figure 5.15. The Moho's topography is virtually constant and most other features are strongly smoothed and flattened. However, the features that are visible have comparable geometries in both images. A fairly similar picture can be seen when comparing PyGLImER's results to the results by Kind et al. (2020) (see Figure 5.16), who published the most recent SRF study for the discussed area. Although similar, the two images show some pronounced differences, such as an apparently more focused MLD and no pronounced Moho topography in the CCP stack created by PyGLImER. Those differences may arise from the differences in the used datasets and, more importantly, the differing smoothing. For my image, I applied a N-S running mean window, whereas Kind et al. (2020) smoothed their data perpendicular to their cross-section.
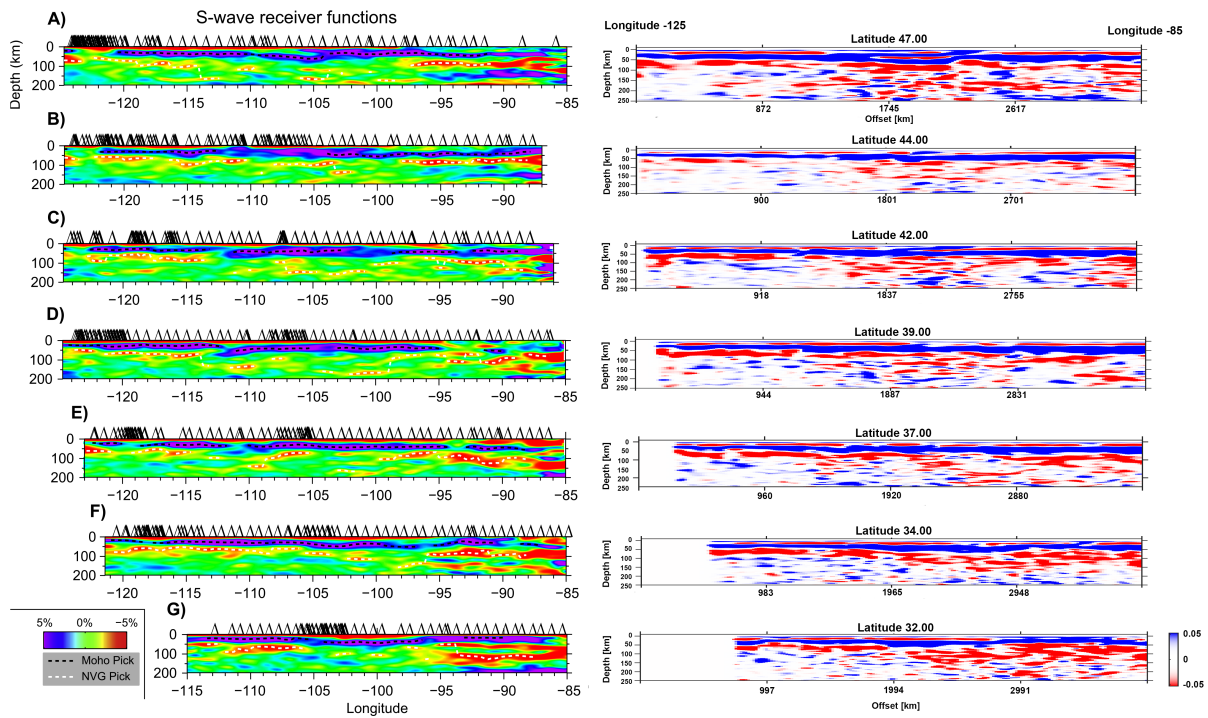
Figure 5.13: **West-East slices through a CCP stack created from SRF data.** *The figure compares data from Hansen et al. (2015) (left) to a CCP object created from the PyGLImER database (right). Blue peaks indicate downwards positive velocity gradients, whereas red peaks are NVGs.*
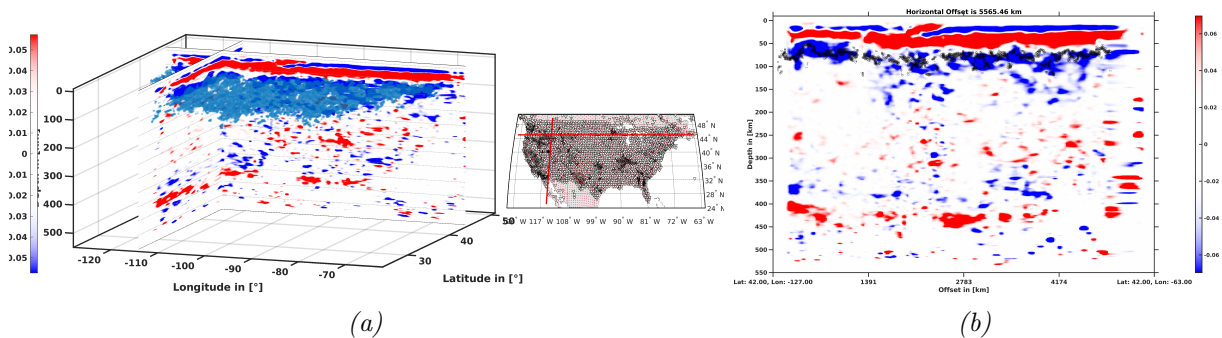

Figure 5.14: **Strongest negative velocity gradient from Hopper & Fischer (2018) projected onto the PyGLImER CCP object.** *In panel (a), each light blue dot indicates the coordinates of a pick for a strongest NVG from Hopper & Fischer (2018). Panel (b) shows the projection of the picks (black dots) for the strongest NVG onto a W-E slice at 42° latitude. Picks are projected onto the slice if they have a distance of 50km or less to the slice.*
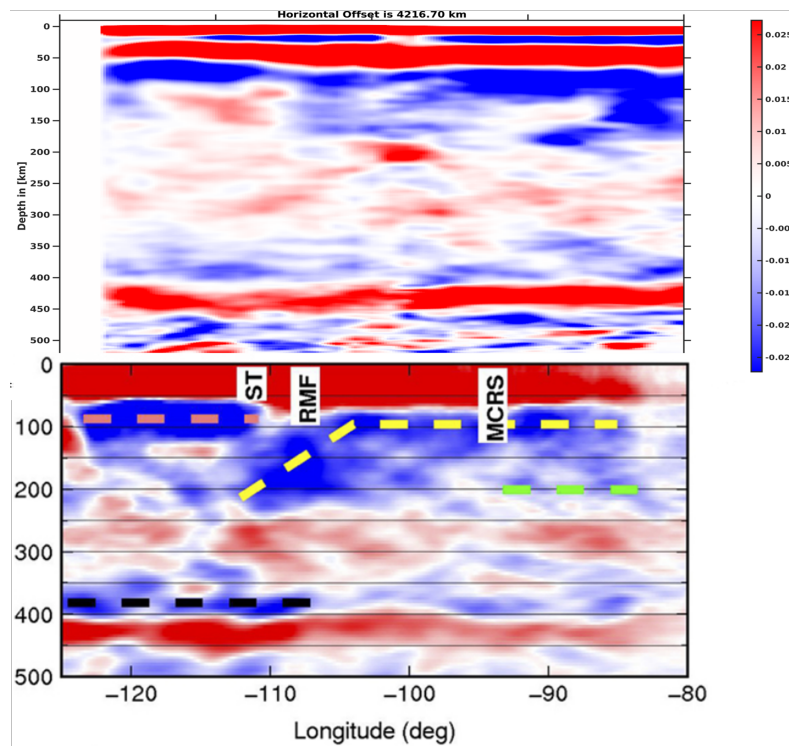
Figure 5.15: **Comparison of PyGLImER's SRF dataset (top panel) to the results from Kind et al. (2015) (bottom panel).** *The profile shows a W-E section at 42° latitude. To reproduce their cross-section, I applied a running mean window of 6° width to the gridded dataset. Downwards positive velocity gradients are blue and downwards negative velocity gradients are red.*
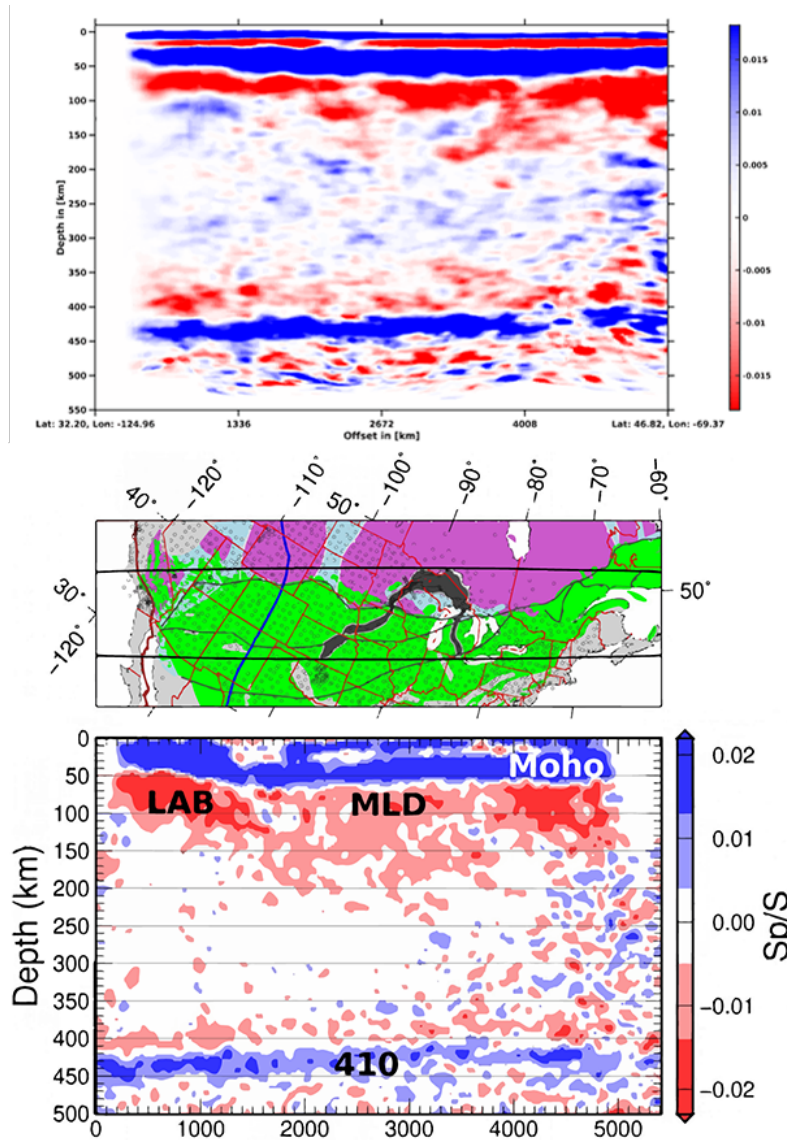
Figure 5.16: **Comparison of PyGLImER's SRF dataset (top panel) to the results from Kind et al. (2020) (bottom panel).** *Location and width of the profiles are indicated in the map (middle panel). To match the width of the cross-section by Kind et al. (2020), I applied a running mean window to the gridded dataset.*

5.2.3   Results

Most lithospheric large-scale variations in North America are approximately N-S striking. W-E cross-sections should therefore provide the best visualisation of spatial and, thus also, age-related variations. In this section, we will take a closer look at four W-E sections (see Figure 5.17). In addition, I produced a number of unlabelled N-S and W-E slices that can be found in Appendix B. Data and preprocessing steps are identical to those described in section 5.1.4 with the exception of the following spatial filters that I applied to the gridded PRF CCP stack: (1) A Gaussian window along lateral direction with a width of 1.8°and (2) a Gaussian window along the z-axis with a width of 20km. Experience shows that spatial filtering tends to attenuate multiples as multiples are effected stronger by lateral variations in the subsurface (see section 4.6.1).

Figures 5.18 to 5.21 show the images created from PRFs in the upper panel and the images from SRFs in the lower panel. A number of large scale features can be traced through all shown sections. Clear features (excluding the Moho) are labelled, where white and black symbols correspond to negative and positive velocity gradients, respectively. The most evident large-scale features include the Moho (i.e., the strongest positive velocity gradient marking the base of the crust), the Phanerozoic LAB (demarked as "LAB"), the cratonic MLD (demarked as "MLD"), and, below the asthenosphere, the d410 (demarked as "d410"). In the images created from PRF data, multiples do often mask the lower half of the lithosphere. Those are labelled with black "m"s.

5.2.3.1   The Moho and Crustal Structures

I will restrict the description and discussion of crustal structures to the most obvious phases since, to target the crust, a pure PRF survey with shorter periods than those used here would yield more insights due to a higher resolution. The strongest positive velocity gradient varying between 25km to about 45km depth can be associated with the Moho. Particularly in regions with thick layers of sediments (such as the Rocky Mountain foreland), strong crustal phases appear that are probably caused by the transition from unconsolidated sediments to bedrock (i.e., the base of the sedimentary basin). These strong conversions lead to strong multiples at quite shallow depths of about 50km to 70km. Comparing images from PRFs to those from SRFs, the Moho phase exhibits a very similar topography although P-to-S data deliver an obvious advantage in resolution and do, consequently, reveal finer structural variations.

To map the Moho depth, PyGLImER includes a function that picks the highest peak
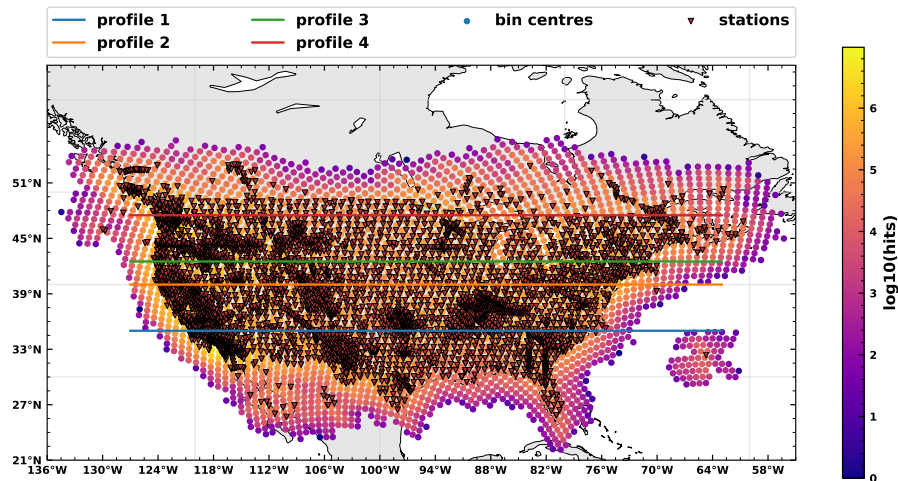
(a)
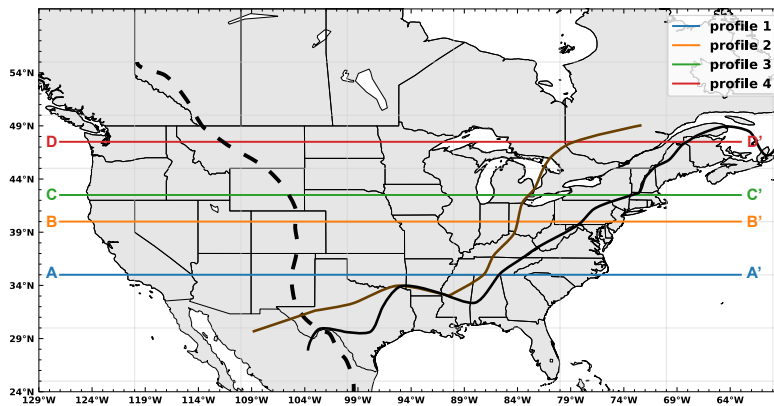
(b)

Figure 5.17: **The cross-sections through North America in map view.** *Panel (a) shows the locations of the stations, for which data have been used, the bin locations, illumination per bin, and the exact location of the cross-sections. The illumination is given as depth-cumulative illumination per bin for PRF data. In panel (b), the following major suture zones are indicated (obtained from Schaeffer & Lebedev (2014)): the surface trace of the RMF (dashed black line), extent of the Grenville/Llano Front (brown line), and the paleo continental margin (black solid line).*
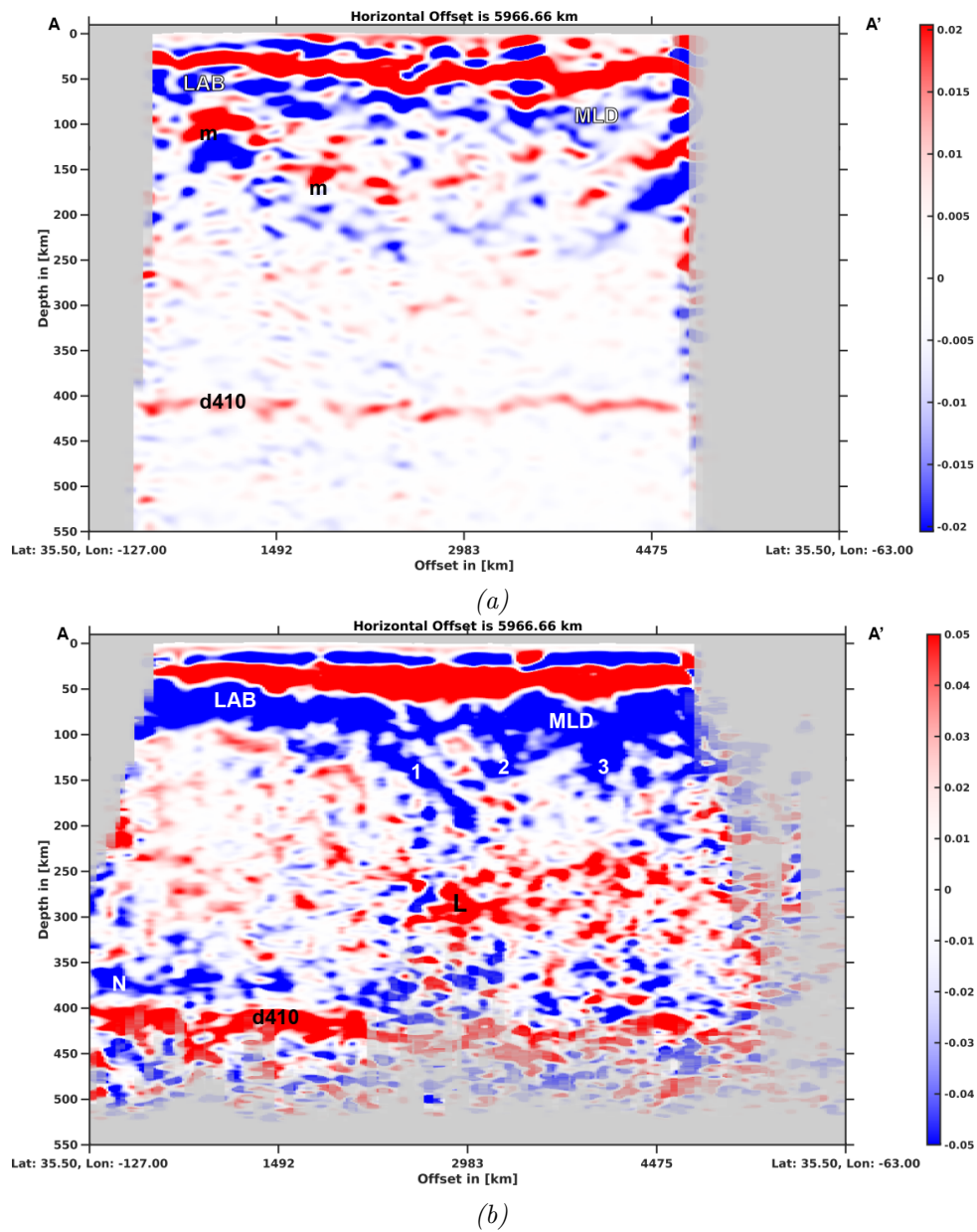
(a)

(b)

Figure 5.18: **Slices through the CCP objects for P-to-S (a) and S-to-P data at 35.5° north (profile 1 in Figure 5.17).** *The data start greying out for less than 50 and 25 hits per grid point for (a) and (b), respectively.*

(a)

(b)

Figure 5.19: **Slices through the CCP objects for P-to-S (a) and S-to-P data at 40.0° north (profile 2 in Figure 5.17).** *The data start greying out for less than 50 and 25 hits per grid point for (a) and (b), respectively.*

(a)

(b)

Figure 5.20: **Slices through the CCP objects for P-to-S (a) and S-to-P data at 42.5° north (profile 3 in Figure 5.17).** *The data start greying out for less than 50 and 25 hits per grid point for (a) and (b), respectively.*
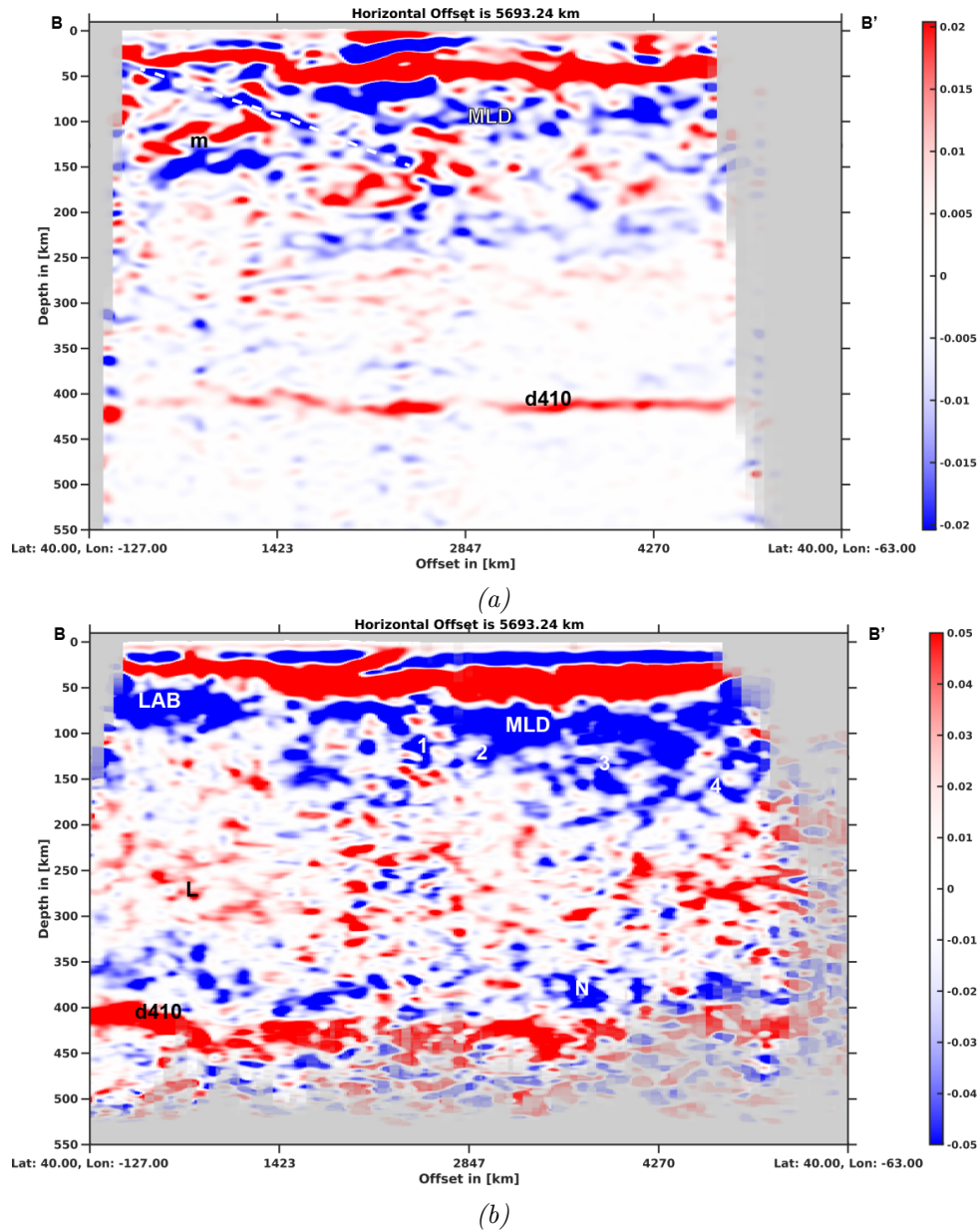
(a)

(b)

Figure 5.21: **Slices through the CCP objects for P-to-S (a) and S-to-P data at 47.5°north (profile 4 in Figure 5.17).** *The data start greying out for less than 50 and 25 hits per grid point for (a) and (b), respectively.*
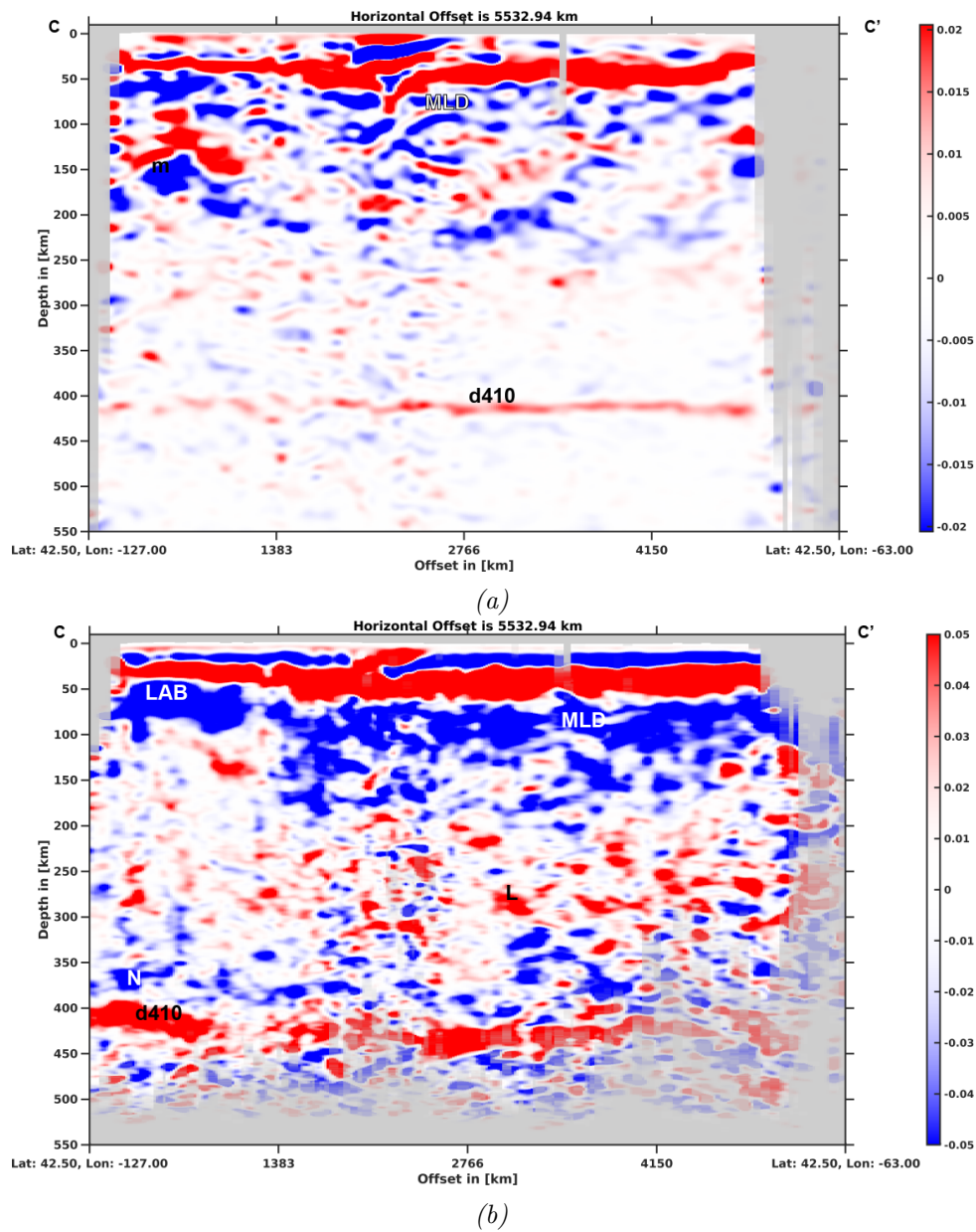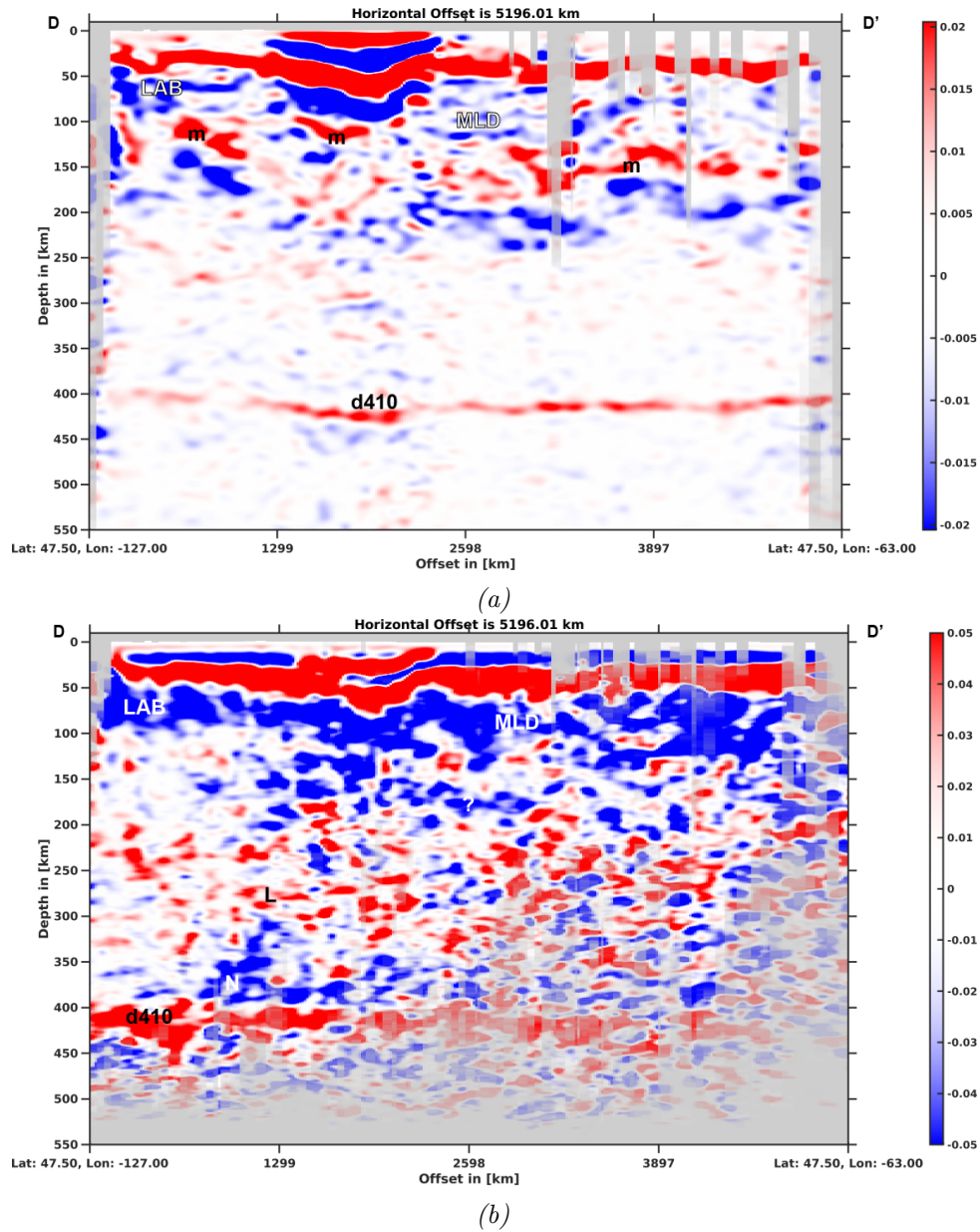
for each sufficiently illuminated column of bins (i.e., illumination in the depth range 0-50km has to be higher than 10 hits per grid point). The resulting maps for P-to-S and S-to-P data are plotted in Figure 5.22. West of the Rocky Mountain Front (RMF), the crustal thickness is fairly constant and varies between 20km and 35km with an average of about 30km. Under the Colorado Plateau, the crust is significantly thicker (i.e., 40km to 45km) than in the surrounding areas. East of the paleo-continental margin with the exception of Florida peninsula (discrepancy between P-to-S and S-to-P data), the Moho shallows to depths around 40km. Areas with the thickest crust are in the cratonic regions of North America with crustal thicknesses of about 40-45km. In eastern Montana, western North Dakota and Nothern Wyoming, crustal thicknesses estimated from SRF data and PRF data are inconsistent most likely due to strong crustal conversions, which are picked as strongest velocity gradient, as for example seen in Figure 5.21.

5.2.3.2 The Phanerozoic Lithosphere-Asthenosphere Boundary

A feature that can be traced through all SRF images with a high degree of confidence is a strong downwards negative velocity gradient (NVG) in the West. As discussed before, this NVG is commonly interpreted as the Phanerozoic LAB. In the presented slices, this NVG is labelled as "LAB". In the southern US (Figure 5.18), the Phanerozoic LAB reaches further into the continent than further north. Although usually visible in PRF data, the Phanerozoic LAB does not produce an equally strong peak for P-to-S conversions. The depth of the Phanerozoic LAB stays relatively constant at around 70km with a slight shallowing towards the Pacific Coast.

5.2.3.3 Midlithospheric Discontinuities

Further to the East and at equivalent depths as the Phanerozoic LAB, SRF images reveal a broader NVG labelled as "MLD". Also in SRF images, this pulse broadens northwards and shows signs of internal structuring or layering. In the corresponding PRF images (i.e., Figures 5.20a and 5.21a), two and three fine NVGs instead of one broad pulse are detected.

In an attempt to map locations with (several) MLD-like signals, I examined PRF CCP images and catalogued the number of MLDs on a regular grid. Figure 5.23 shows the resulting map. While there is no evidence for a MLD west of the RMF (i.e., in the tectonically active regions), all other regions show at least one NVG that I attribute to a MLD. In the Precambrian regions, an apparent south to north increase in number of MLDs seems to occur - with only few areas with more than 2 MLDs east of the Grenville

(a)

(b)

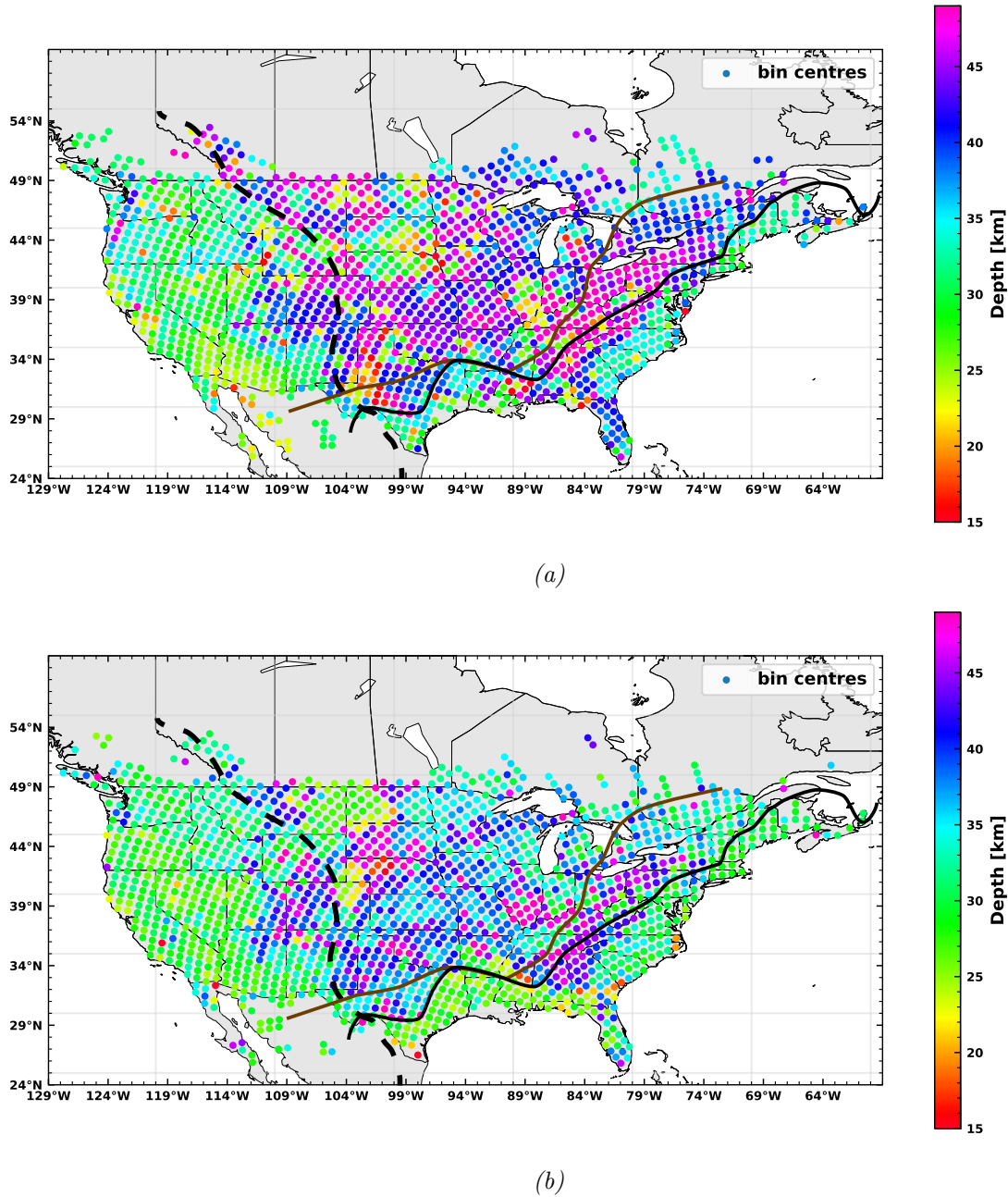*Figure 5.22: **Moho depth maps for P-to-S (a) and S-to-P (b) phases.** The picked depths correspond to the depth of the element with the maximum amplitude in each bin. The following major suture zones are indicated (obtained from Schaeffer & Lebedev (2014)): the surface trace of the RMF (dashed black line), extent of the Grenville/Llano Front (brown line), and the paleo continental margin (black solid line).*

Figure 5.23: **Number of observed mid-lithospheric discontinuitys.** *The number of MLDs has been picked manually. The following major suture zones are indicated (obtained from Schaeffer & Lebedev (2014)): the surface trace of the RMF (dashed black line), extent of the Grenville/Llano Front (brown line), and the paleo continental margin (black solid line).*
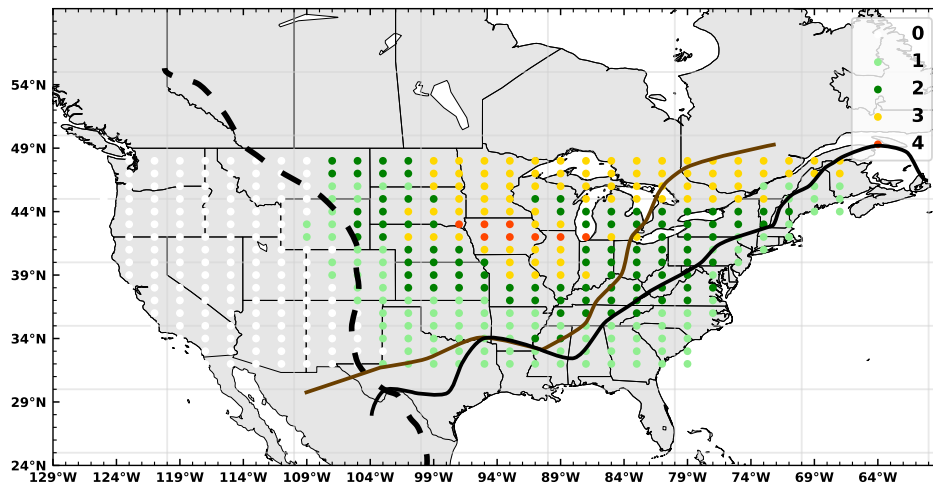
Front and virtually no areas with more than one MLD in the Paleozoic regions (i.e., the Appalachians). I identify the most MLDs in the Superior Craton and the northern Grenville orogen.

5.2.3.4   A Negative Velocity Gradient in the Lower Lithosphere

Particularly in the Superior Craton, another weak NVG can be observed that is not as continuous as the MLD(s) or the Phanerozoic LAB. This NVG can be seen at a depth zone governed by a general, structural transition from a massive, negative velocity gradient zone to a positive velocity gradient zone mostly between 150km to 200km depth. In Figures 5.19b (labelled as "4"), 5.20b, 5.21b(labelled as "?"), and less so in 5.18b, this NVG appears in patches at 150km to 200km depth.

Using manually picked depth estimates of this NVG and the Phanerozoic LAB, I compiled the depths into a map view (see Figure 5.24). Considering the bigger picture, we are again confronted with a familiar pattern. That is, a clear boundary can be drawn approximately along the RMF. West of this boundary, we find the picks correspond to the Phanerozoic LAB at depths of around 70km. To the east of this boundary, in the craton, the deeper NVG was picked. In the younger South, this NVG appears at shallower depth down to 150km than in the cratonic North. The deepest picks are located slightly west
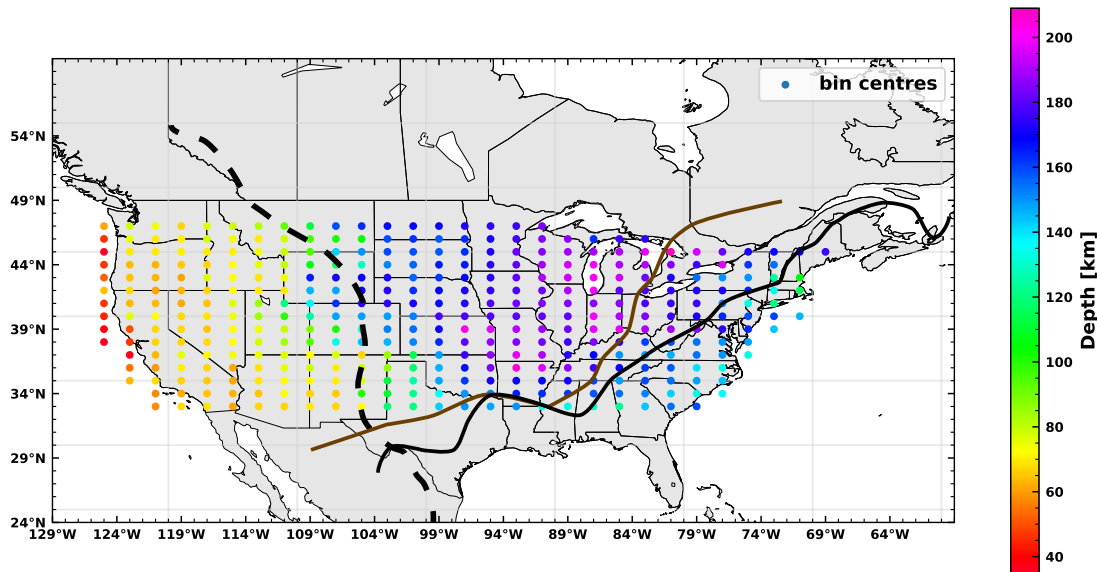
Figure 5.24: **Depth map for the Phanerozoic lithosphere-asthenosphere boundary and the downwards negative velocity gradient in the lower lithosphere.** *All depth have been picked manually frolm SRF data. The following major suture zones are indicated (obtained from Schaeffer & Lebedev (2014)): the surface trace of the RMF (dashed black line), extent of the Grenville/Llano Front (brown line), and the paleo continental margin (black solid line).*

of the Grenville Front. Around Massachusetts, a fairly local negative depth anomaly can be found. Here, I found the NVG at shallower depths of around 110km. In the remainder of the Appalachians, only a slight eastwards shallowing trend is visible. In Appendix B, an alternative pick for the described NVG is provided, for which, instead of picking the actual NVG, I picked the transition from the massive blue zone to a massive red zone. Slices showing both picks are also given in Appendix B.

To illustrate and emphasise that this NVG does usually not coincide with the strongest NVG in the lithospheric mantle, I used the implemented peak picker to find the strongest NVG in a depth range between 50km and 250km (see Figure 5.25). As expected, the results from P-to-S data show no clear pattern most likely due to strong crustal multiples in this depth range (see Figure 5.25a). The map compiled from S-to-P data (i.e., Figure 5.25b) show very similar depth in the West as the manually picked Phanerozoic LAB. In the East on the other hand, most picks vary between 80km and 150km with a few deeper outliers.

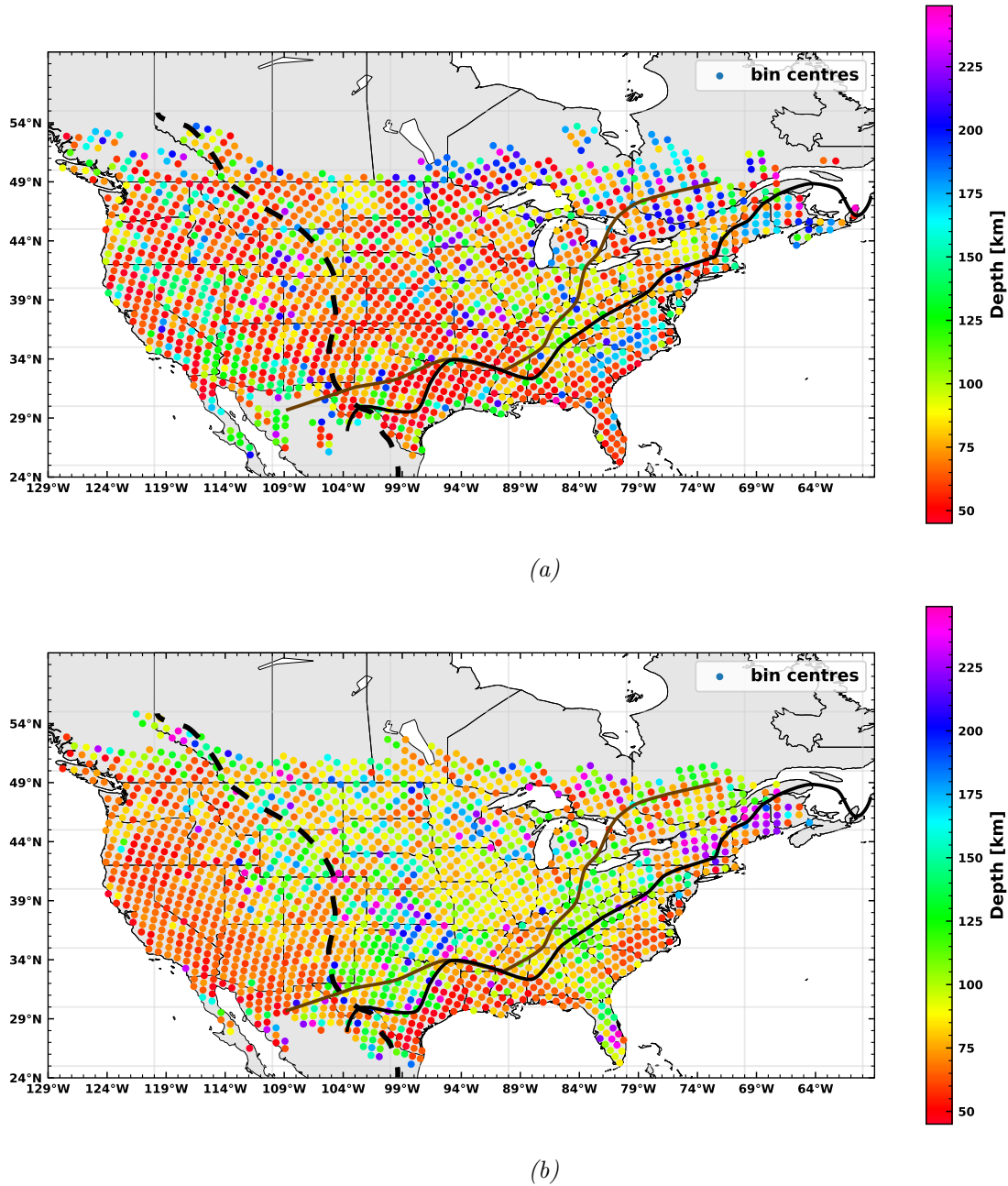*(a)*

(b)

Figure 5.25: **Depth of the strongest negative velocity gradient between 50km and 300km depth for P-to-S (a) and S-to-P (b) phases.** *The following major suture zones are indicated (obtained from Schaeffer & Lebedev (2014)): the surface trace of the RMF (dashed black line), extent of the Grenville/Llano Front (brown line), and the paleo continental margin (black solid line).*

5.2.3.5 Other Structures and Discontinuities in the Lithosphere

Other structures that are not continuous enough to be termed as MLDs appear in the lithospheric mantle. In this depth range, strong Moho and crustal multiples obscure most of the images created from PRFs, which is why we will spend more time examining those features in SRF images. The features in question appear strongly focussed as dipping, strong NVG in the South (see Figure 5.18b) and are labelled with the digits 1 to 3. Further north, at about 42°north, the dipping structures are replaced by a rather massive, thick NVG. Somewhat similar features can also be observed in north-south sections (see Figure B.11b). Whilst in the western parts of the craton most features are dipping eastwards, in the East, structures dip predominantly in a western direction. Additionally to the dipping features in S-to-P data, at 40°north, a long, eastwards-dipping NVG seems to be present over the western half of the continent. This NVG is marked with a dashed line in Figure 5.19a.

5.2.3.6 Discontinuities Below the Lithosphere

At depths deeper than typical estimations of lithospheric thickness, both P-to-S and S-to-P data exhibit some fairly horizontal features. In P-to-S and S-to-P images, the d410 is clearly visible as strong and sharp positive velocity gradient (labelled as "d410"). It is worth noting that PRF and SRF data place the d410 at slightly differing depths with discrepancies of up to 25km. Right above the d410, S-to-P images exhibit a broad NVG that was already reported by Kind et al. (2015) and Kind et al. (2020). This NVG is marked with an "N" throughout the figures. At 250-275km depth under the craton and shallowing to around 210km at the Pacific Coast, SRF data reveal another broad positive pulse that is labelled with an "L". This positive velocity gradient has been suggested to be associated with the Lehmann discontinuity (Kind et al., 2020) (for a discussion on the Lehmann discontinuity, see for example Deuss & Woodhouse (2004)).

Chapter 6

Discussion

6.1 Methodological Implications

From the presented synthetic images and examples from different study regions, we can draw conclusions concerning PyGLImER's capabilities and limitations in comparison to previous studies.

6.1.1 Novel Aspects of PyGLImER Compared to Previous Approaches

PyGLImER introduced a new method filling a gap for global, fast receiver function analysis. To date, only very few attempts of global RF imaging have been made (e.g., Lawrence & Shearer, 2006; Andrews & Deuss, 2008; Rondenay et al., 2017). Lawrence & Shearer (2006) and Andrews & Deuss (2008) used global RF analysis to map specific boundaries in the mantle. Only Rondenay et al. (2017) introduced a method (i.e., GLImER) that allows a free exploration of RF volumes. However, global RF analysis has to the best of my knowledge only been conducted using P-to-S data and with a somewhat limited amount of data. PyGLImER tackles those shortcomings by introducing global RF imaging for P-to-S, S-to-P, and SKS-to-P RF imaging using data from all FDSN servers. The result is a RF database of unprecedented size (see section 4.1).

One of the main goals of this thesis was the implementation of global SRF imaging. While automatic processing of PRFs has become standardised (e.g., Crotwell & Owens, 2005), SRFs are still commonly processed (partly) manually (Knapmeyer-Endrun et al., 2017; Chichester et al., 2018; Lavayssière et al., 2018) or utilising very simple routines (e.g., Hopper & Fischer, 2018; Molina-Aguilera et al., 2019; Kind et al., 2020). Here, I

demonstrate that a more complex processing scheme for SRFs is able to create images whose resolving power is on par with manually processed and controlled images and surpasses the quality of those with a simpler processing and quality control routine. The new automatic processing routine enables fast processing of data volumes that, due to their sheer extent, are not suited for manual processing. It does so without compromising the quality of the final image.

Compared to its predecessor, GLImER (Rondenay et al., 2017), PyGLImER implements a number of vital and useful additional tools and features. Along with S-to-P data and full data availability, those include:

1. The ability to update the RF database at any time without having to overwrite any existing data.
2. A new, more efficient CCP stacking algorithm (see section 4.6).
3. The convenience of a user-friendly, object oriented pythonic implementation.

In addition to those major advances, a host of smaller functions and tools, some of which are presented in this thesis, were added.

6.1.2   Robustness of the Presented Method

Most importantly, we have to assess whether PyGLImER delivers reliable results that are consistent with previous findings.

A first evaluation of PyGLImER's robustness can be given when considering the examples from synthetic data (see section 4.6.1 and appendix A). A full discussion of those results is already provided together with the results. The most important conclusions from this discussion are: (1) When the assumptions of an entirely one-dimensional model are fulfilled, the starting model can be recovered perfectly (within the limitations of illumination). (2) The further we move away from those assumptions, the stronger the image quality degrades due to the effect of scattering. Scattering has a stronger effect on SRF than on PRF data.

While tests with synthetic data provide useful insights into the functionality and robustness of some part of the workflow (e.g., deconvolution, CCP stacking, interpolation, plotting), they cannot be used to assess whether download, preprocessing, and quality control deliver reliable results. In order to make a statement about those steps of the workflow, we have to use real data comparisons with previously published studies (see sections 5.1 and 5.2.2). Real data examples are shown in direct comparison to previous studies in section 5.2.2. All images deliver comparable results with major discontinuities appearing in similar depth ranges. The same can be said for the images created for other

regions (i.e., section 5.1). Consequently, it seems reasonable to argue that the presented method delivers robust results, whose data-quality is at least comparable to previous studies. For SRF, the implemented quality control discards more low quality RFs than other comparable studies did. That is, while the number of stations in PyGLImER is higher than in other studies, the final number of SRF is lower than in those studies (e.g., Hopper & Fischer, 2018; Kind et al., 2020). This might be a possible explanation for an apparently higher quality of SRF images compared to previously produced images and, thus, suggests that PyGLImER's more elaborate quality control scheme outperforms simpler approaches.

6.2 Lithospheric and Sublithospheric Structures in North America

Compared to other recent studies, the images presented here are created using data from a larger number of stations and the resulting increase in resolution permits placing new constraints on the lithospheric structure under the North American continent.

6.2.1 The Lithosphere-Asthenosphere Boundary

One of the lithospheric discontinuities that previous studies have devoted the most attention to is certainly the LAB (e.g., Rychert et al., 2005; Li et al., 2007; Lekic et al., 2011; Kumar et al., 2012; Foster et al., 2014). Using the RF-technique to place constraints on lithospheric thickness has the appeal of achieving higher resolution and a lower error margin than surface wave tomography or thermal modelling due to lower frequencies and fewer necessary assumptions, respectively. However, P-to-S and S-to-P RFs are only sensitive to sharp velocity gradients with a thickness of less than 11km (Rychert et al., 2007) and 50km (Kind et al., 2020), respectively.

6.2.1.1 The Phanerozoic LAB

In the West, the downwards negative velocity gradient marked as "LAB" in Figures 5.18, 5.19, 5.20, and 5.21 at 70km depth can be identified as the LAB. Both location and depth of the discontinuity are in strong agreement with previous RF studies (e.g., Kind et al., 2015; Hopper & Fischer, 2018; Kind et al., 2020). However, in contrast to the results by Hansen et al. (2015), the Phanerozoic LAB also produces a strong P-to-S conversion. Consequently, the velocity gradient associated with the Phanerozoic LAB has

to be sharper than 11km. The strong and sharp LAB signal west of the RMF is usually interpreted as an indicator for partial melt in the upper asthenosphere (Fischer et al., 2010).

6.2.1.2   The Cratonic LAB

The LAB under the North American cratons does not produce an equally strong or continuous signal as the LAB in the tectonically active West. However, since the depth of the described NVG in the lower lithosphere is in strong agreement with velocity reductions observed using surface wave tomography (Schaeffer & Lebedev, 2014; Calò et al., 2016; Priestley et al., 2018) and results presented by Foster et al. (2014) and Kind et al. (2020), it seems reasonable to interpret this signal as the cratonic LAB.

Where the LAB is observed with SRFs, it produces a sharper (i.e., $\leq$ 50km) velocity transition than in those with no LAB signal on SRF data. While a broad signal at LAB depth is consistent with a signal solely caused by a temperature gradient, the sharper parts of the LAB need to have an additional mechanism, such as partial melt or an increase in hydration in the asthenosphere (Fischer et al., 2010; Hopper & Fischer, 2018), causing a NVG. Whereas the majority of previous studies have inferred a cratonic LAB of purely thermal nature (e.g., Kind et al., 2015, 2017; Chen et al., 2018; Liu & Gao, 2018), a sharper signal (i.e., $\leq$50km) suggests that the cratonic LAB is accompanied by another mechanism (Aulbach et al., 2017).

The observation of a sharper LAB is consistent with global negative velocity contrasts found by Tharimena et al. (2017) employing SS precursor analysis. However, Tharimena et al. (2017) report a slightly shallower depth for this NVG and the SRF data shown here do not provide evidence for a ubiquitous cratonic LAB. Yuan et al. (2011) proposed that the sharper cratonic LAB is caused by a change in radial anisotropy, whereas, for example, Hopper et al. (2014) invoke the presence of "melt pockets" to explain these velocity gradients - where under 1% partial melt suffice to produce the observed NVGs (Aulbach et al., 2017). The latter claim is supported by evidence for the presence of melt at some cratonic LABs in hand samples (Aulbach et al., 2017). Such magmatism seems to be particularly strong at the craton edges (Aulbach et al., 2017), which could explain the strong, eastwards-dipping NVG at western edge of the Wyoming craton and the Proterozoic belts south of the cratons seen in my data and previously reported by Foster et al. (2014). Such regions of apparently stronger magmatism at the base of the lithosphere could be linked to mechanisms in the deeper mantle (e.g., thermochemical mantle upwellings) that cause stronger melting in some cratonic regions (Aulbach et al.,

2017).

6.2.2   Seismic Discontinuities Below the Lithosphere

Below the lithosphere, I previously identified three fairly flat discontinuities. The Lehmann discontinuity can only be detected using the SRF technique, suggesting that it is a relatively broad velocity transition rather than a sharp seismic boundary. While my results seem to be in agreement with those presented by Kind et al. (2020), Calò et al. (2016) found a Lehmann discontinuity with a stronger variation in depth.

Under the Lehmann discontinuity and above the d410, a NVG reported by Kind et al. (2015) and Kind et al. (2020) is seen on S-to-P data. Again, that this "N" discontinuity does not appear on PRF data, implies a velocity transition of 15km to 50km width. Previously, Deuss & Woodhouse (2004) found a NVG in the same depth range and termed it the "X-population" and Tauzin et al. (2010) found global evidence for a NVG just above the d410 (at around 350km depth), which has been proposed to be caused by mechanisms involving partial melt. The depth range in which the deep NVG appears in the SRF data coincides very well with the NVG found by Tauzin et al. (2010). However, they found no evidence for this NVG to be present under the Proterozoic Yavapai and Mazatzai belts (see Figure 3 in Tauzin et al. (2010)), whereas the "N" discontinuity is ubiquitous in my SRF images.

6.2.3   Lithospheric Structures in the North American Cratons and Their Implications for Craton Formation and Deformation

The compiled Moho (Figure 5.22), LAB (Figure 5.24) and MLD maps (Figure 5.23) show clear lateral zonations, most of which seem to be related to tectonic suture zones. Of those zonations, the clearest division can be seen along the Rocky Mountain Front, to the west of which the crust is thin and the shallow Lithosphere-Asthenosphere transition coincides with a seismically strong LAB. I do not observe any seismic MLDs west of the RMF. The second zone is located east of the paleo-continental margin. It is characterized by a thinned crust (relative to the lithosphere to the West), only one seismic MLD, and a thinned lithosphere. The third zone is comprised by Laurentia, which constitutes the core of modern North American continent. This zone shows signals of several MLDs and is characterised by a thick crust and lithosphere. The zonation into three regions agrees with the clusters Hopper & Fischer (2018) found using k-means cluster analysis.

South of the Great Lakes, the thickest lithosphere and the highest number of MLDs are found west of the Grenville Front, whereas, to the North, lithospheric thickness and number of MLDs are seemingly independent of the Grenville Front. This observation is consistent with a hypothesis of Boyce et al. (2019) claiming that the regions of the cratonic North, which were already more than 250 My old at the time of deformation, had a stronger resistance to deformation and, thus, the overprinting effect of the Grenville orogeny is stronger in the younger Proterozoic belts in the South. Seemingly, the very strong deformation caused by the Grenville orogeny (see Whitmeyer, 2007) led to a reduction of MLDs and reduced the lithospheric thickness to about 160km.

In contrast to Kind et al. (2020), I observe clear MLD signals in all parts of the craton from both PRFs and SRFs. Thus, my observations are at odds with their conclusion that MLDs are not a general feature in North America. Considering the following, it seems unlikely that MLDs are an artefact caused by deconvolution: (1) Several MLDs that are topographically independent from the Moho appear on both P-to-S and S-to-P data at similar depths. (2) Signals from seismic MLDs have also been reported using other methods, of which many do not require deconvolution, such as PP- and SS-precursor analysis (Shearer, 1993; Heit et al., 2010; Zheng & Romanowicz, 2012; Tharimena et al., 2017), active source seismic refractions (Thybo & Perchu, 1997), SKS wave splitting (Yuan et al., 2011), surface wave tomography (Adams et al., 2012; Fishwick & Rawlinson, 2012; Jiang et al., 2013), or direct inversion (Calò et al., 2016). Therefore, I interpret my results as another indication that sharp (i.e., sharper than ≈11km) seismic MLDs are a ubiquitous feature in the North American and - considering results from previous studies - other stable cratons.

A general trend of increasing lithospheric thickness and increasing number of MLDs with increasing age of the lithosphere can be seen (i.e., south to north). The lithosphere is thickest and has the most MLDs in the northern cratons and is slightly thinning southwards with decreasing age. MLDs are commonly interpreted as remnants from the craton's formation (e.g., Cooper & Miller, 2014; Hopper & Fischer, 2015; Aulbach et al., 2017; Cooper et al., 2017) and given that the number of MLDs increases with increasing age it seems possible that each MLD represents one thickening event and, hence, that continental lithosphere does not thicken gradually but by accretionary or subcretionary cyclic events. Each MLD would thus represent the bottom of the lithospheric root on a previous cycle (i.e., a paleo LAB). This interpretation agrees with and extends the findings by Yuan & Romanowicz (2010), who use a study of seismic anisotropy to infer a two layered North American craton, of which the uppermost less depleted layer is likely

younger (Yuan & Romanowicz, 2010).

Considering the nature of such cyclic events, the observations of a general structural change from a lithosphere with complex, negative, dipping structures in the younger South of the craton to a dominance of horizontal to sub-horizontal NVGs in the older North allow for two possible conclusions:

1. The two different structural regimes are equal to different temporal states of lithospheric evolution. As a consequence, there has to be some kind of mechanism that will eventually lead to a flattening of the dipping NVGs.

2. The topographically diverging systems were caused by different formation mechanisms.

If the two structural regimes were to represent different states of craton evolution, one would expect a gradual flattening of the NVGs with increasing age. However, the results from North America show an abrupt change in structure (at around 42-43°north). Therefore and because a geodynamic process that flattens dipping structures seems counterintuitive, the first option is more likely. Then, the lithosphere in the North could have been built by a pre-plate tectonic system (i.e., underplating/subcretion by plume-caused mantle upwelling (e.g., Griffin et al., 1999, 2004; Arndt et al., 2009), see panel (a) in Figure 6.1), which Cooper & Miller (2014) have shown to be able to create horizontal and quasi-horizontal discontinuities[1]. The more complex structures in the South indicate a plate tectonic related process, where the dipping structures are Precambrian slabs involved in a form of craton evolution by progressive stacking of slabs (i.e., subduction-accretion, see panel (b) in Figure 6.1). Saha et al. (2018) have shown that imbricated slabs are able to produce negative S-wave velocity gradients by invoking crystallisation of phlogopite in the region of the subducted slab. Such a model for lithospheric formation is usually linked to early Precambrian subduction and, for example, advocated by Bostock (1998), Helmstaedt (2009), Miller & Eaton (2010), Wirth & Long (2014), or Hopper & Fischer (2015).

The model of subduction-accretion requires the dipping structures observed in the southern Proterozoic belts to be identified as subduction slabs. While comparable structures have been imaged in cratons before and evidence seems to indicate that they are in fact remnants of Precambrian subduction (e.g., Hopper & Fischer, 2015; Kind et al., 2020), relatively little is known about the geodynamic history of the early Proterozoic and Archean (van Hunen & Moyen, 2012), which makes it difficult to associate structures

---

[1]Alternatively, such geometries could have been caused by Archean flat subduction. However, there is no compelling geochemical or geodynamical evidence for a prevalence of flat subduction in the Archean (van Hunen & Moyen, 2012).
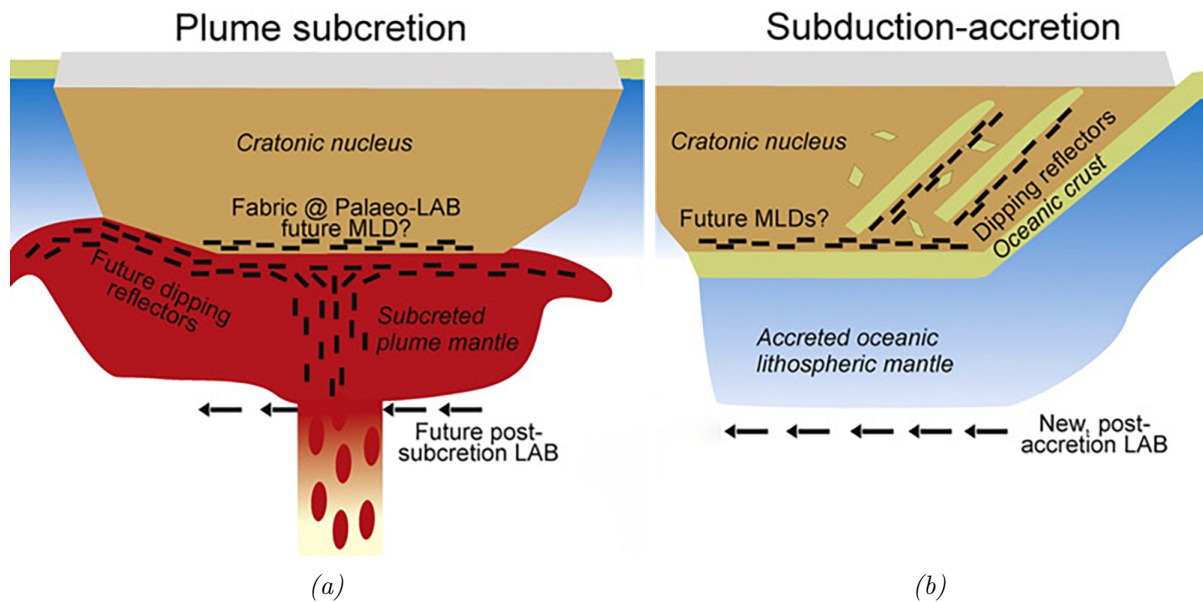
Figure 6.1: **The two discussed models for the formation of cratons.** *(a) A mantle plume causes the subcretion of a cratonic nucleus (e.g., Griffin et al., 1999, 2004; Arndt et al., 2009). The structural geometry in the older North (e.g., the Superior craton) seems to indicate a dominance of such mantle driven craton formation. (b) Subduction of oceanic crust causes the craton to be accreted by a form of slab-stacking (e.g., Bostock, 1998; Helmstaedt, 2009; Miller & Eaton, 2010; Pearson & Wittig, 2013; Wirth & Long, 2014). The imbricated dipping reflectors in the southern Proterozoic belts support a dominance of subduction-accretion in the formation process of the craton. For both mechanism, the current MLDs correspond to paleo-LABs. Figures are altered from Aulbach et al. (2017).*

with particular events. In the data presented here, probably the most prominent dipping feature seen in the lithospheric mantle is the eastwards-dipping NVG seen under the Llano uplift (labelled as "1" in Figures 5.18b and 5.19b). The last event of deformation that took place in this region is the Paleozoic Ouachiata orogen which, together with the Appalachian orogen, formed in the assembly of the supercontinent Pangea (Keller & Hatcher, 1999). Indeed, subduction of an interior ocean has been inferred under the Ouachiata orogen albeit southwards-dipping (Lillie et al., 1983; Mickus & Keller, 1992). More recently, Yao & Li (2016) found evidence for southeastwards dipping subduction slabs under the Ouachita mountain belt - a finding that would be more consistent with the observed NVG. However to the best of my knowledge, no images of such a subducting slab have been produced. That is, if the observed NVG is caused by a subducting slab under the Ouachiata orogen, it would be the first direct lithospheric evidence for subduction below the region. While evidence points towards the NVG being a (imbricated) slab, currently, the data are too limited to make a conclusive assessment regarding the nature

of the NVG under the Llano uplift.

The results presented here seem to suggest that tectonically driven formation of lithosphere was not active in the early Archean (or at the least its activity was minimal), but rather in the late Archean and early Proterozoic. However, it is not clear whether such events do still contribute to lithospheric thickening. In younger lithosphere, dipping structures are not present (Aulbach, 2018). Looking at the example of the Phanerozoic West, the lithosphere appears mostly homogeneous. This could indicate that modern lithospheric thickening is happening constantly rather than periodically, whereas, in the Archean, strong periodic events were more common (van Hunen & Moyen, 2012). In addition, modelling suggests that slab break-off was more common in the hotter early Precambrian Earth (van Hunen & Moyen, 2012). Several shorter dipping structures incorporated in the Proterozoic regions seem more likely to originate from slab fragments. Another way of explaining the fairly homogeneous lithosphere in the Phanerozoic West is simply that this part of the lithosphere is too young and did not yet experience a second cycle.

Assuming that MLDs originate from mechanisms akin to the ones described above, we can place some constraints on the cause of the seismic discontinuities associated to MLDs. Selway et al. (2015) provide an in-depth review of the proposed causes for NVGs at MLD depths. In addition to their discussion, I can state the following: A mechanism involving cyclic/periodic formation of lithospheric layers renders all thermal causes for MLDs unlikely as one would not expect temperature gradients and discontinuities to remain stable over several billion years, which is a condition for several MLDs of various ages to exist. MLD models that are compatible with the proposed mechanism are either those that rely on variations in anisotropy or compositional variations. However, there are no simple conditions under which azimuthal anisotropy can produce constant downwards-negative velocity discontinuities (Selway et al., 2015) as they are observed in North America in both PRF and SRF data. As for radial anisotropy, different observations are in stark contrast to each other. In North America, many authors find different, complex patterns of anisotropy (Yuan & Romanowicz, 2010; Yuan et al., 2011; Wirth & Long, 2014), whereas Ford et al. (2016) find no evidence for a direct link of seismic MLDs and variations in anisotropy and conclude that seismic MLDs are associated to isotropic NVGs. Another possible cause for seismic MLDs is compositional variations. Rader et al. (2015) analysed xenoliths from mantle depths and found evidence for crystallised (i.e., frozen) melt layers at MLD depth. Considering that melt has been the favoured mechanism to explain the signal of the Phanerozoic LAB, a seismic MLD caused by a layer of frozen melt is highly

compatible with a model that postulates the MLD to be a paleo LAB. Therefore, it is not necessary to invoke the mechanism of melt compaction layers (i.e., capped layers that trap upwelling melt at shallower depth, in which the melt eventually crystallises) to explain an MLD associated with crystallised melts (as done by Rader et al. (2015) and Hopper & Fischer (2015)). Figure 6.2 shows a simplified model of the modern North American continent and its transition from the western Phanerozoic regions to the eastern cratonic regions. Note that the structure in the Proterozoic regions becomes further complicated by the presence of frozen Precambrian slabs in the lithosphere.
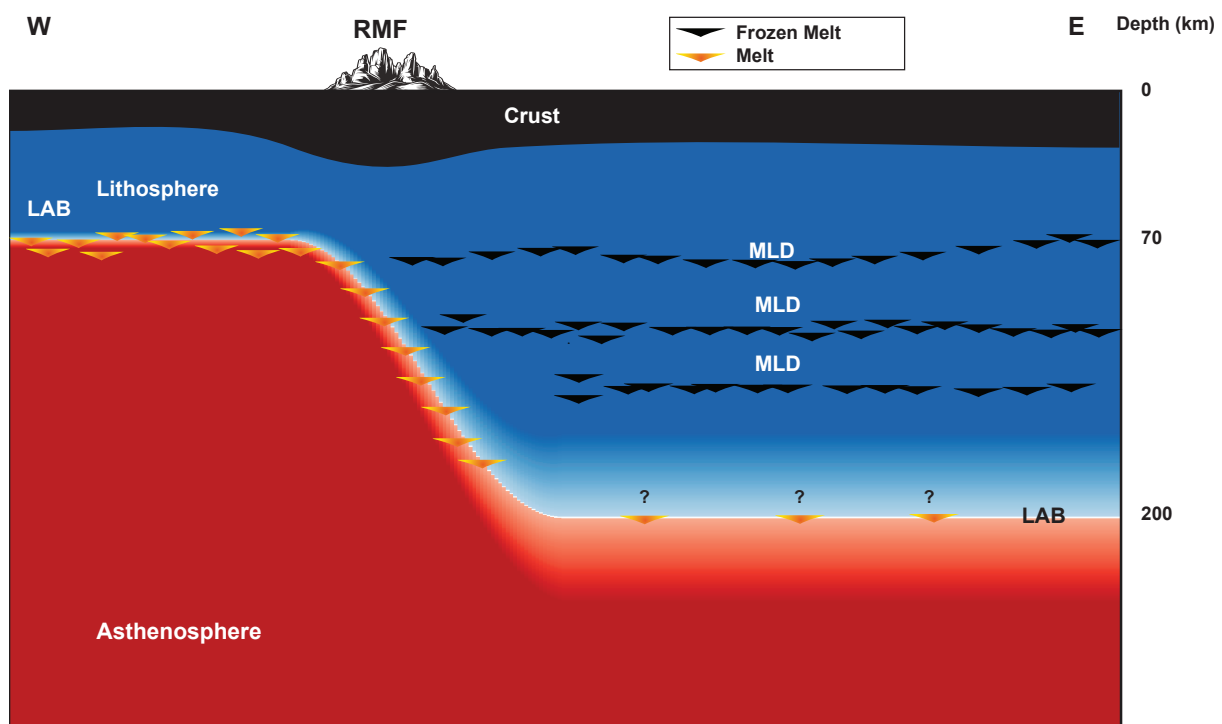
Figure 6.2: **Simplified Model of the lithosphere and asthenosphere under the cratonic East and the tectonically active West.** *The Phanerozoic LAB in the West is a sharp boundary between the lithosphere (blue) and asthenosphere (red) most likely caused by the presence partial melt. In the cratonic regions (east), the transition from the lithosphere to the asthenosphere is more gradual and can only be detected by SRFs in certain regions that could contain a small fraction of melt (see e.g., Aulbach et al., 2017). The strong NVG associated with the dipping LAB in the transition from the Phanerozoic West to the cratonic East could be an indicator for the presence of melt. The MLDs in the craton are most likely caused by a change in composition possibly induced by layers of crystallised melt as suggested by Rader et al. (2015). The following abbreviations are used in the figure: Rocky Mountain Front (RMF), lithosphere-asthenosphere boundary (LAB), and mid-lithospheric discontinuity (MLD).*

Another interesting observation is that while the number of seismic MLDs increases significantly with increasing age of the lithosphere, lithospheric thickness increases only

slightly from the younger Proterozoic regions in the South to the old Archean cratons in the North. Together with previous observations of a maximum thickness of continental lithosphere of 200-250km (Priestley & McKenzie, 2006; Eaton et al., 2009; Fischer et al., 2010; Yuan et al., 2011; Foster et al., 2014; Calò et al., 2016; Priestley et al., 2018; Kind et al., 2020), this seems to indicate that the lithospheric thicknesses observed in both Archean and the majority of the Proterozoic regions represent a stable "equilibrium thickness" (i.e., an equilibrium between lithospheric accretion and asthenospheric erosion). At such an equilibrium thickness, conditions could be favourable for the observed smooth transitions from lithosphere to asthenosphere rather than sharp seismic boundaries.

It should be emphasised that not every seismic discontinuity that has previously been called a MLD has to be associated with a "lithospheric formation cycle" or a paleo LAB. For example, MLDs of positive polarity (e.g., Calò et al., 2016) or varying anisotropy (e.g., Yuan & Romanowicz, 2010; Yuan et al., 2011; Wirth & Long, 2014; Ford et al., 2016) have been described. Over the last decade and in the framework of the discussion about the potential causes of seismic MLDs, a host of mechanisms that could cause intralithospheric discontinuities have been proposed (see Selway et al., 2015; Aulbach, 2018; Karato & Park, 2017), of which many could lead to local and regional discontinuities in the lithosphere. Ideally, the term MLD should be replaced by new, more precise terms that take the discontinuity's polarity, anisotropy, and topography into account. However, creating such categories is beyond the scope of this thesis and should be done under careful consideration of not only seismic data, but also with the help of geodynamic and mineralogical modelling. For the same reason, it is difficult to evaluate the exact number of formation cycles that certain parts of the lithosphere in North America have undergone. Hence, Figure 5.23 should be viewed with a certain caution given that discontinuities counted as MLDs could be caused by other mechanisms or sediment basin multiples (in regions with thick sedimentary basins), whereas other seismic MLDs could be masked by multiples or not be resolved. These effects could lead to an overestimation of the number of formation cycles in some regions and an underestimation of those in other regions. Nevertheless, Figure 5.23 provides a good overview of regions with fewer and more seismic MLDs.

Finally, I acknowledge that the presented hypothesis should be tested for compatibility with other regions than only North America. Such tests are an important next step to verify, whether the presented hypothesis is universally applicable. Using PyGLImER, such additional studies can be easily conducted. However, they are nonetheless beyond the scope of this thesis and should be targeted in future studies.

Chapter 7

Conclusion and Outlook

In this thesis, I developed a method capable of producing global P-to-S and S-to-P receiver function (RF) images. This method is implemented in the form of a workflow making up the new pythonic modular software PyGLImER, which allows the user to automatically download, preprocess, deconvolve, and, finally, plot large volumes of common conversion point (CCP) stacked data. All these steps are conducted automatically and require only minimal user input. Tests with synthetic and real earthquake data confirm the method's robustness. Particularly, images from S-to-P RFs, for which, to date, only few efforts of full automation have been made, exhibit a high quality.

Future functions that should be implemented into PyGLImER include a bootstrap method to insure robustness of the produced CCP images, a toolset to facilitate studies of changes in anisotropy, and the ability to easily use waveform data from other sources than FDSN servers. Ultimately, PyGLImER will be distributed as an open-source software providing an easy and complete tool for global RF imaging.

The method was applied to several regions, of which the North American continent was subject to a more exhaustive discussion. The RF study targeting the North American continent that I present in the framework of this thesis is unprecedented in terms of its data density. Using the new, high-resolution images, I image previously unknown structures in the North American cratons. My new observations and interpretations can be summed up in the following points:

1. The velocity discontinuity associated with the Phanerozoic lithosphere-asthenosphere boundary (LAB) in the West of the continent is sharper than ≈11km since it is seen on both P-to-S and S-to-P data. The depth of this discontinuity is fairly constant at around 70km.

2. In the North American cratons, the lithosphere is significantly thicker than in the

younger, adjacent parts of the continent. I observe a less continuous signal of the cratonic LAB on S-to-P data, which I interpret to be associated with regions containing partial melt at the bottom of the lithosphere. Nevertheless, the signals of the cratonic LAB allows me to create the first continuous LAB depth map from RF data for North America. In the craton, these depths vary between 120km and 200km and are thereby in good agreement with previous studies employing surface-wave tomography although RF data has a higher resolution and, thus, reveals new small scale variations.

3. In the cratons and Proterozoic belts, I observe several downwards negative mid-lithospheric discontinuity (MLD)s. The higher resolution of PRF data enables me to map the number of MLDs in the various regions. The resulting map shows an intriguing positive correlation between the number of MLDs in the lithosphere and the age of the lithosphere. I interpret this correlation as an indicator for a cyclic (or periodic) formation of the oldest and thickest continents with each MLD representing a paleo LAB.

4. Structurally, the craton can be divided into two sharply separated regimes. In the oldest, Archean parts of the craton in the North, the discontinuities are predominantly horizontal to subhorizontal, whereas, in the Proterozoic belts in the South, I observe a multitude of dipping structures, which I interpret as imbricated slabs from Precambrian subduction events. I speculate that the two structural regimes highlight a shift of mechanisms forming thick continental crust. In the older, hotter Earth, those continents were predominantly built by plume subcretion, whereas, from the late Archean to early Proterozoic on, subduction-accretion has been the dominant mechanism to build thick continental lithosphere.

5. Of the competing theories discussing the cause of seismic MLDs, I consider compositional changes to be the most compatible with the hypothesis presented above. My preferred mechanism to explain those compositional changes are layers of frozen melt (i.e., frozen paleo LABs) as proposed by Rader et al. (2015).

In order to support the hypothesis on the formation of thick continental lithosphere outlined above, the following questions should be answered in future studies:

1. Do other cratonic regions show the same correlation between number of MLDs and lithospheric age?

2. Does a similar change in internal structure occur everywhere in lithosphere of the same age? If so, at which precise age does this shift occur and is it more gradual or always sharp?

3. What is the current mechanism to build modern thick continents? Is it at all possible to build stable thick continental lithosphere under modern conditions?

Bibliography

Abt, D. L., Fischer, K. M., French, S. W., Ford, H. A., Yuan, H., & Romanowicz, B. (2010, sep). North American lithospheric discontinuity structure imaged by Ps and Sp receiver functions. *Journal of Geophysical Research*, *115*(B9), B09301. Retrieved from `http://doi.wiley.com/10.1029/2009JB006914` doi: 10.1029/2009JB006914

Adams, A., Nyblade, A., & Weeraratne, D. (2012, apr). Upper mantle shear wave velocity structure beneath the East African plateau: evidence for a deep, plateauwide low velocity anomaly. *Geophysical Journal International*, *189*(1), 123–142. Retrieved from `https://academic.oup.com/gji/article-lookup/doi/10.1111/j.1365-246X.2012.05373.x` doi: 10.1111/j.1365-246X.2012.05373.x

Aki, K., & Richards, P. G. (2002). *Quantitative seismology* (Vol. II).

Ammon, C. J. (1991). The isolation of receiver effects from teleseismic P -waveforms. *Bulletin of the Seismological Society of America*, *81*(6), 2504–2510. Retrieved from `http://www.bssaonline.org/content/81/6/2504.short` doi: 10.1029/2005JB004161

Andrews, J., & Deuss, A. (2008, jun). Detailed nature of the 660 km region of the mantle from global receiver function data. *Journal of Geophysical Research*, *113*(B6), B06304. Retrieved from `http://doi.wiley.com/10.1029/2007JB005111` doi: 10.1029/2007JB005111

Arndt, N., Coltice, N., Helmstaedt, H., & Gregoire, M. (2009, apr). Origin of Archean subcontinental lithospheric mantle: Some petrological constraints. *Lithos*, *109*(1-2), 61–71. Retrieved from `http://dx.doi.org/10.1016/j.lithos.2008.10.019https://linkinghub.elsevier.com/retrieve/pii/S0024493708002387` doi: 10.1016/j.lithos.2008.10.019

Aulbach, S. (2018, nov). Cratonic Lithosphere Discontinuities. In H. Yuan (Ed.), *Lithospheric discontinuities* (Vol. M, pp. 177–203). American Geophysical Union. Retrieved from `https://onlinelibrary.wiley.com/doi/abs/10.1002/9781119249740.ch10` doi: 10.1002/9781119249740.ch10

Aulbach, S., Massuyeau, M., & Gaillard, F. (2017). Origins of cratonic mantle discontinuities: A view from petrology, geochemistry and thermodynamic models. *Lithos*, *268-271*, 364–382. Retrieved from `http://dx.doi.org/10.1016/j.lithos.2016.11.004` doi: 10.1016/j.lithos.2016.11.004

Bostock, M. G. (1998, sep). Mantle stratigraphy and evolution of the Slave province. *Journal of Geophysical Research: Solid Earth*, *103*(B9), 21183–21200. Retrieved from `http://doi.wiley.com/10.1029/98JB01069` doi: 10.1029/98JB01069

Bostock, M. G., & Rondenay, S. (1999, jun). Migration of scattered teleseismic body waves. *Geophysical Journal International*, *137*(3), 732–746. Retrieved from `https://academic.oup.com/gji/article-lookup/doi/10.1046/j.1365-246x.1999.00813.x` doi: 10.1046/j.1365-246x.1999.00813.x

Boyce, A., Bastow, I. D., Golos, E. M., Rondenay, S., Burdick, S., & Van der Hilst, R. D. (2019). Variable modification of continental lithosphere during the Proterozoic Grenville orogeny: Evidence from teleseismic P-wave tomography. *Earth and Planetary Science Letters*, *525*, 115763. Retrieved from `https://doi.org/10.1016/j.epsl.2019.115763` doi: 10.1016/j.epsl.2019.115763

Calò, M., Bodin, T., & Romanowicz, B. (2016). Layered structure in the upper mantle across North America from joint inversion of long and short period seismic data. *Earth and Planetary Science Letters*, *449*, 164–175. Retrieved from `http://dx.doi.org/10.1016/j.epsl.2016.05.054` doi: 10.1016/j.epsl.2016.05.054

Cammarano, F., & Guerri, M. (2017, jul). Global thermal models of the lithosphere. *Geophysical Journal International*, *210*(1), 56–72. Retrieved from `https://academic.oup.com/gji/article-lookup/doi/10.1093/gji/ggx144` doi: 10.1093/gji/ggx144

Chen, C., Gilbert, H., Fischer, K. M., Andronicos, C. L., Pavlis, G. L., Hamburger, M. W., . . . Yang, X. (2018). Lithospheric discontinuities beneath the U.S. Midcontinent – signatures of Proterozoic terrane accretion and failed rifting. *Earth and Planetary Science Letters*, *481*, 223–235. Retrieved from `https://doi.org/10.1016/j.epsl.2017.10.033` doi: 10.1016/j.epsl.2017.10.033

Chen, C.-W., James, D. E., Fouch, M. J., & Wagner, L. S. (2013, nov). Lithospheric structure beneath the High Lava Plains, Oregon, imaged by scattered teleseismic waves. *Geochemistry, Geophysics, Geosystems*, *14*(11), 4835–4848. Retrieved from `http://doi.wiley.com/10.1002/ggge.20284` doi: 10.1002/ggge.20284

Chen, L. (2010). Concordant structural variations from the surface to the base of the upper mantle in the North China Craton and its tectonic implications. *Lithos*, *120*(1-2), 96–115. Retrieved from `http://dx.doi.org/10.1016/j.lithos.2009.12.007` doi: 10.1016/j.lithos.2009.12.007

Chichester, B., Rychert, C., Harmon, N., Lee, S., Frederiksen, A., & Zhang, H. (2018, sep). Seismic Imaging of the North American Midcontinent Rift Using S -to- P Receiver Functions. *Journal of Geophysical Research: Solid Earth*, *123*(9), 7791–7805. Retrieved from `https://onlinelibrary.wiley.com/doi/abs/10.1029/2018JB015771` doi: 10.1029/2018JB015771

Clayton, R. W., & Wiggins, R. A. (1976, oct). Source shape estimation and deconvolution of teleseismic bodywaves. *Geophysical Journal International*, *47*(1), 151–177. Retrieved from `https://academic.oup.com/gji/article-lookup/doi/10.1111/j.1365-246X.1976.tb01267.x` doi: 10.1111/j.1365-246X.1976.tb01267.x

Cooper, C., & Miller, M. (2014, feb). Craton formation: Internal structure inherited from closing of the early oceans. *Lithosphere*, *6*(1), 35–42. Retrieved from `http://pubs.geoscienceworld.org/lithosphere/article/6/1/35/145696/Craton-formation-Internal-structure-inherited-from` doi: 10.1130/L321.1

Cooper, C. M., Miller, M. S., & Moresi, L. (2017). The structural evolution of the deep continental lithosphere. *Tectonophysics*, *695*, 100–121. Retrieved from `http://dx.doi.org/10.1016/j.tecto.2016.12.004` doi: 10.1016/j.tecto.2016.12.004

Crotwell, H. P., & Owens, T. J. (2005, nov). Automated Receiver Function Processing. *Seismological Research Letters*, *76*(6), 702–709. Retrieved from `https://pubs.geoscienceworld.org/srl/article/76/6/702-709/143184` doi: 10.1785/gssrl.76.6.702

Deuss, A., & Woodhouse, J. H. (2004, sep). The nature of the Lehmann discontinuity from its seismological Clapeyron slopes. *Earth and Planetary Science Letters*, *225*(3-4), 295–304. Retrieved from `https://linkinghub.elsevier.com/retrieve/pii/S0012821X04004340` doi: 10.1016/j.epsl.2004.06.021

Diehl, T., & Ritter, J. R. R. (2005, oct). The crustal structure beneath SE Romania from teleseismic receiver functions. *Geophysical Journal International*, *163*(1), 238–251. Retrieved from `https://academic.oup.com/gji/article-lookup/doi/10.1111/j.1365-246X.2005.02715.x` doi: 10.1111/j.1365-246X.2005.02715.x

Dueker, K. G., & Sheehan, A. F. (1997, apr). Mantle discontinuity structure from midpoint stacks of converted P to S waves across the Yellowstone hotspot track. *Journal of Geophysical Research: Solid Earth*, *102*(B4), 8313–8327. Retrieved from `http://doi.wiley.com/10.1029/96JB03857` doi: 10.1029/96JB03857

Eaton, D. W., Darbyshire, F., Evans, R. L., Grütter, H., Jones, A. G., & Yuan, X. (2009). The elusive lithosphere-asthenosphere boundary (LAB) beneath cratons. *Lithos*, *109*(1-2), 1–22. Retrieved from `http://dx.doi.org/10.1016/j.lithos.2008.05.009` doi: 10.1016/j.lithos.2008.05.009

Eulenfeld, T. (2020, apr). rf: Receiver function calculation in seismology. *Journal of Open Source Software*, *5*(48), 1808. Retrieved from `https://joss.theoj.org/papers/10.21105/joss.01808` doi: 10.21105/joss.01808

Farra, V., & Vinnik, L. (2000, jun). Upper mantle stratification by P and S receiver functions. *Geophysical Journal International*, *141*(3), 699–712. Retrieved

from `https://academic.oup.com/gji/article-lookup/doi/10.1046/j.1365-246x` `.2000.00118.x` doi: 10.1046/j.1365-246x.2000.00118.x

Fischer, K. M., Ford, H. A., Abt, D. L., & Rychert, C. A. (2010, apr). The Lithosphere-Asthenosphere Boundary. *Annual Review of Earth and Planetary Sciences*, *38*(1), 551–575. Retrieved from `http://www.annualreviews.org/doi/10.1146/annurev-earth` `-040809-152438` doi: 10.1146/annurev-earth-040809-152438

Fishwick, S., & Rawlinson, N. (2012, aug). 3-D structure of the Australian lithosphere from evolving seismic datasets. *Australian Journal of Earth Sciences*, *59*(6), 809–826. Retrieved from `http://www.tandfonline.com/doi/abs/10.1080/08120099` `.2012.702319` doi: 10.1080/08120099.2012.702319

Ford, H. A., Long, M. D., & Wirth, E. A. (2016, sep). Midlithospheric discontinuities and complex anisotropic layering in the mantle lithosphere beneath the Wyoming and Superior Provinces. *Journal of Geophysical Research: Solid Earth*, *121*(9), 6675–6697. Retrieved from `http://doi.wiley.com/10.1002/2016JB012978` doi: 10.1002/2016JB012978

Foster, K., Dueker, K., Schmandt, B., & Yuan, H. (2014). A sharp cratonic lithosphere-asthenosphere boundary beneath the American Midwest and its relation to mantle flow. *Earth and Planetary Science Letters*, *402*(C), 82–89. Retrieved from `http://dx.doi.org/10.1016/j.epsl.2013.11.018` doi: 10.1016/j.epsl.2013.11.018

Fowler, C. M. R. (2004). *The Solid Earth* (2nd ed.). Cambridge University Press. Retrieved from `https://www.cambridge.org/core/product/identifier/9780511819643/type/book` doi: 10.1017/cbo9780511819643

Frederiksen, A. W., & Bostock, M. G. (2000, may). Modelling teleseismic waves in dipping anisotropic structures. *Geophysical Journal International*, *141*(2), 401–412. Retrieved from `https://academic.oup.com/gji/article-lookup/doi/10.1046/j.1365-246x` `.2000.00090.x` doi: 10.1046/j.1365-246x.2000.00090.x

Gao, H., Humphreys, E. D., Yao, H., & van der Hilst, R. D. (2011). Crust and lithosphere structure of the northwestern U.S. with ambient noise tomography: Terrane accretion and Cascade arc development. *Earth and Planetary Science Letters*, *304*(1-2), 202–211. Retrieved from `http://dx.doi.org/10.1016/j.epsl.2011.01.033` doi: 10.1016/j.epsl.2011.01.033

Generalized geological map of the world and linked databases (Tech. Rep.). (1995). Geological Survey of Canada. Retrieved from `https://geoscan.nrcan.gc.ca/starweb/geoscan/servlet.starweb?path=geoscan/fulle.web{&}search1=R=195142` doi: 10.4095/195142

Griffin, W., O'Reilly, S. Y., Doyle, B., Pearson, N., Coopersmith, H., Kivi, K., ... Pokhilenko, N. (2004, sep). Lithosphere mapping beneath the North American

plate. *Lithos*, *77*(1-4), 873–922. Retrieved from `https://linkinghub.elsevier.com/retrieve/pii/S002449370400088X` doi: 10.1016/j.lithos.2004.03.034

Griffin, W. L., Doyle, B. J., Ryan, C. G., Pearson, N. J., Suzanne, Y. O., Davies, R., ... Natapov, L. M. (1999, may). Layered Mantle Lithosphere in the Lac de Gras Area, Slave Craton: Composition, Structure and Origin. *Journal of Petrology*, *40*(5), 705–727. Retrieved from `https://academic.oup.com/petrology/article-lookup/doi/10.1093/petroj/40.5.705` doi: 10.1093/petroj/40.5.705

Guo, Z., Cao, Y., Wang, X., John Chen, Y., Ning, J., He, W., ... Feng, Y. (2014, jun). Crust and upper mantle structures beneath Northeast China from receiver function studies. *Earthquake Science*, *27*(3), 265–275. Retrieved from `http://link.springer.com/10.1007/s11589-014-0076-x` doi: 10.1007/s11589-014-0076-x

Guo, Z., Chen, Y. J., Ning, J., Yang, Y., Afonso, J. C., & Tang, Y. (2016, jan). Seismic evidence of on-going sublithosphere upper mantle convection for intra-plate volcanism in Northeast China. *Earth and Planetary Science Letters*, *433*, 31–43. Retrieved from `https://linkinghub.elsevier.com/retrieve/pii/S0012821X1500610X` doi: 10.1016/j.epsl.2015.09.035

Gurrola, H., Baker, G. E., & Minster, J. B. (1995, mar). Simultaneous time-domain deconvolution with application to the computation of receiver functions. *Geophysical Journal International*, *120*(3), 537–543. Retrieved from `https://doi.org/10.1111/j.1365-246X.1995.tb01837.xhttps://academic.oup.com/gji/article-lookup/doi/10.1111/j.1365-246X.1995.tb01837.x` doi: 10.1111/j.1365-246X.1995.tb01837.x

Hamza, V. M., & Vieira, F. P. (2012, aug). Global distribution of the lithosphere-asthenosphere boundary: a new look. *Solid Earth*, *3*(2), 199–212. Retrieved from `https://se.copernicus.org/articles/3/199/2012/` doi: 10.5194/se-3-199-2012

Hansen, S. E., Nyblade, A. A., Julià, J., Dirks, P. H., & Durrheim, R. J. (2009, aug). Upper-mantle low-velocity zone structure beneath the Kaapvaal craton from S -wave receiver functions. *Geophysical Journal International*, *178*(2), 1021–1027. Retrieved from `https://academic.oup.com/gji/article-lookup/doi/10.1111/j.1365-246X.2009.04178.x` doi: 10.1111/j.1365-246X.2009.04178.x

Hansen, S. M., Dueker, K., & Schmandt, B. (2015). Thermal classification of lithospheric discontinuities beneath USArray. *Earth and Planetary Science Letters*, *431*, 36–47. Retrieved from `http://dx.doi.org/10.1016/j.epsl.2015.09.009` doi: 10.1016/j.epsl.2015.09.009

Hansen, S. M., Dueker, K. G., Stachnik, J. C., Aster, R. C., & Karlstrom, K. E. (2013, aug). A rootless rockies-Support and lithospheric structure of the Colorado Rocky Mountains inferred from CREST and TA seismic data. *Geochemistry, Geophysics, Geosystems*, *14*(8), 2670–2695. Retrieved from `http://doi.wiley.com/10.1002/ggge.20143` doi: 10.1002/ggge.20143

Havskov, J., & Alguacil, G. (2004). *Instrumentation in Earthquake Seismology* (3rd ed.). Springer.

Havskov, J., & Ottemoller, L. (2010). *Routine Data Processing in Earthquake Seismology.* Dordrecht: Springer Netherlands. Retrieved from `http://link.springer.com/10.1007/978-90-481-8697-6` doi: 10.1007/978-90-481-8697-6

He, C. (2019, dec). Evidence for an upwelling mantle plume beneath the Songliao Basin, Northeast China. *Physics of the Earth and Planetary Interiors*, *297*, 106316. Retrieved from `https://linkinghub.elsevier.com/retrieve/pii/S0031920119301141` doi: 10.1016/j.pepi.2019.106316

Heit, B., Yuan, X., Bianchi, M., Kind, R., & Gossler, J. (2010, oct). Study of the lithospheric and upper-mantle discontinuities beneath eastern Asia by SS precursors. *Geophysical Journal International*, *183*(1), 252–266. Retrieved from `https://academic.oup.com/gji/article-lookup/doi/10.1111/j.1365-246X.2010.04714.x` doi: 10.1111/j.1365-246X.2010.04714.x

Helffrich, G. (2006). Extended-time multitaper frequency domain cross-correlation receiver-function estimation. *Bulletin of the Seismological Society of America*, *96*(1), 344–347. doi: 10.1785/0120050098

Helmstaedt, H. (2009, nov). Crust–mantle coupling revisited: The Archean Slave craton, NWT, Canada. *Lithos*, *112*, 1055–1068. Retrieved from `http://dx.doi.org/10.1016/j.lithos.2009.04.046https://linkinghub.elsevier.com/retrieve/pii/S0024493709002035` doi: 10.1016/j.lithos.2009.04.046

Hoffman, P. F. (1988, may). United Plates of America, The Birth of a Craton: Early Proterozoic Assembly and Growth of Laurentia. *Annual Review of Earth and Planetary Sciences*, *16*(1), 543–603. Retrieved from `http://www.annualreviews.org/doi/10.1146/annurev.ea.16.050188.002551` doi: 10.1146/annurev.ea.16.050188.002551

Hopper, E., & Fischer, K. M. (2015). The meaning of midlithospheric discontinuities: A case study in the northern U.S. craton. *Geochemistry, Geophysics, Geosystems*, *16*(12), 4057–4083. Retrieved from `https://onlinelibrary.wiley.com/doi/abs/10.1002/2015GC006030` doi: 10.1002/2015GC006030

Hopper, E., & Fischer, K. M. (2018, aug). The Changing Face of the Lithosphere-Asthenosphere Boundary: Imaging Continental Scale Patterns in Upper Mantle Structure Across the Contiguous U.S. With Sp Converted Waves. *Geochemistry, Geophysics, Geosystems*, *19*(8), 2593–2614. Retrieved from `http://doi.wiley.com/10.1029/2018GC007476` doi: 10.1029/2018GC007476

Hopper, E., Fischer, K. M., Wagner, L. S., & Hawman, R. B. (2017, jan). Reconstructing the end of the Appalachian orogeny. *Geology*, *45*(1), 15–18. Retrieved from `https://pubs.geoscienceworld.org/geology/article/45/1/15-18/191503` doi: 10.1130/G38453.1

Hopper, E., Ford, H. A., Fischer, K. M., Lekic, V., & Fouch, M. J. (2014). The lithosphere-asthenosphere boundary and the tectonic and magmatic history of the northwestern United States. *Earth and Planetary Science Letters*, *402*(C), 69–81. Retrieved from `http://dx.doi.org/10.1016/j.epsl.2013.12.016` doi: 10.1016/j.epsl.2013.12.016

Ishii, T., Huang, R., Myhill, R., Fei, H., Koemets, I., Liu, Z., . . . Katsura, T. (2019). Sharp 660-km discontinuity controlled by extremely narrow binary post-spinel transition. *Nature Geoscience*, *12*(10), 869–872. Retrieved from `http://dx.doi.org/10.1038/s41561-019-0452-1` doi: 10.1038/s41561-019-0452-1

Jiang, M., Ai, Y., Chen, L., & Yang, Y. (2013, nov). Local modification of the lithosphere beneath the central and western North China Craton: 3-D constraints from Rayleigh wave tomography. *Gondwana Research*, *24*(3-4), 849–864. Retrieved from `http://dx.doi.org/10.1016/j.gr.2012.06.018https://linkinghub.elsevier.com/retrieve/pii/S1342937X1200247X` doi: 10.1016/j.gr.2012.06.018

Karato, S.-i., Olugboji, T., & Park, J. (2015, jul). Mechanisms and geologic significance of the mid-lithosphere discontinuity in the continents. *Nature Geoscience*, *8*(7), 509–514. Retrieved from `http://www.nature.com/articles/ngeo2462` doi: 10.1038/ngeo2462

Karato, S. I., & Park, J. (2017, nov). On the origin of the upper mantle seismic discontinuities. In H. Yuan & B. Romanowicz (Eds.), *Lithospheric discontinuities* (pp. 5–34). Wiley. Retrieved from `https://onlinelibrary.wiley.com/doi/book/10.1002/9781119249740https://onlinelibrary.wiley.com/doi/abs/10.1002/9781119249740.ch1` doi: 10.1002/9781119249740.ch1

Keller, G., & Hatcher, R. D. (1999, dec). Some comparisons of the structure and evolution of the southern Appalachian–Ouachita orogen and portions of the Trans-European Suture Zone region. *Tectonophysics*, *314*(1-3), 43–68. Retrieved from `https://linkinghub.elsevier.com/retrieve/pii/S004019519900236X` doi: 10.1016/S0040-1951(99)00236-X

Kennett, B. L. N., & Engdahl, E. R. (1991, may). Traveltimes for global earthquake location and phase identification. *Geophysical Journal International*, *105*(2), 429–465. Retrieved from `https://academic.oup.com/gji/article-lookup/doi/10.1111/j.1365-246X.1991.tb06724.x` doi: 10.1111/j.1365-246X.1991.tb06724.x

Kind, R., Handy, M. R., Yuan, X., Meier, T., Kämpf, H., & Soomro, R. (2017, mar). Detection of a new sub-lithospheric discontinuity in Central Europe with S-receiver functions. *Tectonophysics*, *700-701*, 19–31. Retrieved from `https://linkinghub.elsevier.com/retrieve/pii/S0040195117300501` doi: 10.1016/j.tecto.2017.02.002

Kind, R., Mooney, W. D., & Yuan, X. (2020, apr). New insights into the structural elements of the upper mantle beneath the contiguous United States from S-to-P converted seismic waves. *Geophysical Journal International*, 646–659. Retrieved from `https://`

`academic.oup.com/gji/advance-article/doi/10.1093/gji/ggaa203/5825119` doi: 10.1093/gji/ggaa203

Kind, R., & Yuan, X. (2011). Seismic, Receiver Function Technique. In *Encyclopedia of earth sciences series* (Vol. Part 5, pp. 1258–1269). Retrieved from `http://link.springer.com/10.1007/978-90-481-8702-7{_}12` doi: 10.1007/978-90-481-8702-7_12

Kind, R., & Yuan, X. (2017, nov). Perspectives of the S-receiver-function method to image upper mantle discontinuities. In *Lithospheric discontinuities* (pp. 139–154). American Geophysical Union. Retrieved from `https://onlinelibrary.wiley.com/doi/abs/10.1002/9781119249740.ch8` doi: 10.1002/9781119249740.ch8

Kind, R., Yuan, X., Mechie, J., & Sodoudi, F. (2015, jul). Structure of the upper mantle in the north-western and central United States from USArray S-receiver functions. *Solid Earth*, *6*(3), 957–970. Retrieved from `https://se.copernicus.org/articles/6/957/2015/` doi: 10.5194/se-6-957-2015

Knapmeyer-Endrun, B., Krüger, F., & Geissler, W. H. (2017, jan). Upper mantle structure across the Trans-European Suture Zone imaged by S-receiver functions. *Earth and Planetary Science Letters*, *458*, 429–441. Retrieved from `https://linkinghub.elsevier.com/retrieve/pii/S0012821X16306458` doi: 10.1016/j.epsl.2016.11.011

Krischer, L., Megies, T., Barsch, R., Beyreuther, M., Lecocq, T., Caudron, C., & Wassermann, J. (2015, may). ObsPy: a bridge for seismology into the scientific Python ecosystem. *Computational Science & Discovery*, *8*(1), 014003. Retrieved from `https://iopscience.iop.org/article/10.1088/1749-4699/8/1/014003` doi: 10.1088/1749-4699/8/1/014003

Krueger, H. E., Fischer, K. M., Gama, I., Hua, J., & Eilon, Z. (2019). Do Mid-Lithospheric Discontinuities exist? In *Agu fall meeting abstracts* (pp. T12A–03). Retrieved from `https://ui.adsabs.harvard.edu/abs/2019AGUFM.T12A..03K`

Kufner, S., Eken, T., Tilmann, F., Schurr, B., Yuan, X., Mechie, J., ... Schneider, F. (2018, dec). Seismic Anisotropy Beneath the Pamir and the Hindu Kush: Evidence for Contributions From Crust, Mantle Lithosphere, and Asthenosphere. *Journal of Geophysical Research: Solid Earth*, *123*(12), 2018JB015926. Retrieved from `https://onlinelibrary.wiley.com/doi/abs/10.1029/2018JB015926` doi: 10.1029/2018JB015926

Kufner, S. K., Schurr, B., Sippl, C., Yuan, X., Ratschbacher, L., Akbar, A. s. M., ... Tilmann, F. (2016). Deep India meets deep Asia: Lithospheric indentation, delamination and break-off under Pamir and Hindu Kush (Central Asia). *Earth and Planetary Science Letters*, *435*, 171–184. Retrieved from `http://dx.doi.org/10.1016/j.epsl.2015.11.046` doi: 10.1016/j.epsl.2015.11.046

Kumar, P., Kind, R., & Yuan, X. (2010, mar). Receiver function summation without deconvolution. *Geophysical Journal International*, *180*(3), 1223–1230. Retrieved from `https://academic.oup.com/gji/article-lookup/doi/10.1111/j.1365-246X.2009.04469.x` doi: 10.1111/j.1365-246X.2009.04469.x

Kumar, P., Kind, R., Yuan, X., & Mechie, J. (2012, may). USArray Receiver Function Images of the Lithosphere-Asthenosphere Boundary. *Seismological Research Letters*, *83*(3), 486–491. Retrieved from `https://pubs.geoscienceworld.org/srl/article/83/3/486-491/143922` doi: 10.1785/gssrl.83.3.486

Kumar, P., Yuan, X., Kind, R., & Kosarev, G. (2005, apr). The lithosphere-asthenosphere boundary in the Tien Shan-Karakoram region from S receiver functions: Evidence for continental subduction. *Geophysical Research Letters*, *32*(7), n/a–n/a. Retrieved from `http://doi.wiley.com/10.1029/2004GL022291` doi: 10.1029/2004GL022291

Langston, C. A. (1979). Structure under Mount Rainier, Washington, inferred from teleseismic body waves. *Journal of Geophysical Research*, *84*(B9), 4749. Retrieved from `http://doi.wiley.com/10.1029/JB084iB09p04749` doi: 10.1029/JB084iB09p04749

Lavayssière, A., Rychert, C., Harmon, N., Keir, D., Hammond, J. O., Kendall, J. M., ... Leroy, S. (2018). Imaging Lithospheric Discontinuities Beneath the Northern East African Rift Using S-to-P Receiver Functions. *Geochemistry, Geophysics, Geosystems*. Retrieved from `http://www.mendeley.com/catalogue/imaging-lithospheric-discontinuities-beneath-northern-east-african-rift-using-stop-receiver-function` doi: 10.1029/2018GC007463

Lawrence, J. F., & Shearer, P. M. (2006, jun). A global study of transition zone thickness using receiver functions. *Journal of Geophysical Research: Solid Earth*, *111*(B6), n/a–n/a. Retrieved from `http://doi.wiley.com/10.1029/2005JB003973` doi: 10.1029/2005JB003973

Le Pichon, X. (2019, aug). Fifty Years of Plate Tectonics: Afterthoughts of a Witness. *Tectonics*, *38*(8), 2919–2933. Retrieved from `https://onlinelibrary.wiley.com/doi/abs/10.1029/2018TC005350` doi: 10.1029/2018TC005350

Lekić, V., & Fischer, K. M. (2014, sep). Contrasting lithospheric signatures across the western United States revealed by Sp receiver functions. *Earth and Planetary Science Letters*, *402*, 90–98. Retrieved from `https://linkinghub.elsevier.com/retrieve/pii/S0012821X13006602` doi: 10.1016/j.epsl.2013.11.026

Lekić, V., & Fischer, K. M. (2017, aug). Interpreting spatially stacked Sp receiver functions. *Geophysical Journal International*, *210*(2), 874–886. Retrieved from `https://academic.oup.com/gji/article-lookup/doi/10.1093/gji/ggx206` doi: 10.1093/gji/ggx206

Lekic, V., French, S. W., & Fischer, K. M. (2011, nov). Lithospheric Thinning Beneath Rifted Regions of Southern California. *Science*, *334*(6057), 783–787. Retrieved

from `https://www.sciencemag.org/lookup/doi/10.1126/science.1208898` doi: 10.1126/science.1208898

Levander, A., & Miller, M. S. (2012, jul). Evolutionary aspects of lithosphere discontinuity structure in the western U.S. *Geochemistry, Geophysics, Geosystems*, *13*(7), n/a–n/a. Retrieved from `http://doi.wiley.com/10.1029/2012GC004056` doi: 10.1029/2012GC004056

Levander, A., Schmandt, B., Miller, M. S., Liu, K., Karlstrom, K. E., Crow, R. S., ... Humphreys, E. D. (2011, apr). Continuing Colorado plateau uplift by delamination-style convective lithospheric downwelling. *Nature*, *472*(7344), 461–465. Retrieved from `http://www.nature.com/articles/nature10001` doi: 10.1038/nature10001

Li, X., Yuan, X., & Kind, R. (2007, aug). The lithosphere-asthenosphere boundary beneath the western United States. *Geophysical Journal International*, *170*(2), 700–710. Retrieved from `https://academic.oup.com/gji/article-lookup/doi/10.1111/j.1365-246X.2007.03428.x` doi: 10.1111/j.1365-246X.2007.03428.x

Ligorría, J. P., & Ammon, C. J. (1999). Iterative deconvolution and receiver-function estimation. *Bulletin of the Seismological Society of America*, *89*(5), 1395–1400.

Lillie, R. J., Nelson, K. D., de Voogd, B., Brewer, J. A., Oliver, J. E., Brown, L., ... Viele, G. W. (1983). Crustal Structure of Ouachita Mountains, Arkansas: A Model Based on Integration of COCORP Reflection Profiles and Regional Geophysical Data. *AAPG Bulletin*, *67*(6), 907–931. Retrieved from `http://search.datapages.com/data/doi/10.1306/03B5B6CD-16D1-11D7-8645000102C1865D` doi: 10.1306/03B5B6CD-16D1-11D7-8645000102C1865D

Liu, L., & Gao, S. S. (2018, aug). Lithospheric layering beneath the contiguous United States constrained by S-to-P receiver functions. *Earth and Planetary Science Letters*, *495*, 79–86. Retrieved from `https://doi.org/10.1016/j.epsl.2018.05.012https://linkinghub.elsevier.com/retrieve/pii/S0012821X18302838` doi: 10.1016/j.epsl.2018.05.012

Maneewongvatana, S., & Mount, D. (2002, dec). Analysis of approximate nearest neighbor searching with clustered point sets. In *Data structures, near neighbor searches, and methodology* (Vol. 59, pp. 105–123). Retrieved from `http://www.ams.org/dimacs/059` doi: 10.1090/dimacs/059/06

Mengel, K., & Kern, H. (1992, jan). Evolution of the petrological and seismic Moho-implications for the continental crust-mantle boundary. *Terra Nova*, *4*(1), 109–116. Retrieved from `http://doi.wiley.com/10.1111/j.1365-3121.1992.tb00455.x` doi: 10.1111/j.1365-3121.1992.tb00455.x

Mickus, K. L., & Keller, G. R. (1992). Lithospheric structure of the south-central United States. *Geology*, *20*(4), 335. Retrieved from `https://pubs.geoscienceworld.org/`

`geology/article/20/4/335-338/205711`   doi: 10.1130/0091-7613(1992)020⟨0335:
LSOTSC⟩2.3.CO;2

Miller, M. S., & Eaton, D. W. (2010). Formation of cratonic mantle keels by
arc accretion: Evidence from S receiver functions. *Geophysical Research Letters*. Retrieved from `http://www.mendeley.com/catalogue/formation-cratonic`
`-mantle-keels-arc-accretion-evidence-s-receiver-functions`   doi: 10.1029/
2010GL044366

Miller, M. S., & Piana Agostinetti, N. (2012, sep). Insights into the evolution of the
Italian lithospheric structure from S receiver function analysis. *Earth and Planetary
Science Letters*, *345-348*, 49–59. Retrieved from `https://linkinghub.elsevier.com/`
`retrieve/pii/S0012821X12003123`   doi: 10.1016/j.epsl.2012.06.028

Molina-Aguilera, A., de Lis Mancilla, F., Morales, J., Stich, D., Yuan, X., & Heit, B.
(2019, mar). Connection between the Jurassic oceanic lithosphere of the Gulf of Cádiz
and the Alboran slab imaged by Sp receiver functions. *Geology*, *47*(3), 227–230.
Retrieved from `https://pubs.geoscienceworld.org/gsa/geology/article/47/3/`
`227/568594/Connection-between-the-Jurassic-oceanic`   doi: 10.1130/G45654.1

O'Driscoll, L. J., & Miller, M. S. (2015, apr). Lithospheric discontinuity structure in
Alaska, thickness variations determined by Sp receiver functions. *Tectonics*, *34*(4), 694–
714. Retrieved from `http://doi.wiley.com/10.1002/2014TC003669`   doi: 10.1002/
2014TC003669

Oldenburg, D. W. (1981, may). A comprehensive solution to the linear deconvolution problem. *Geophysical Journal International*, *65*(2), 331–357. Retrieved
from `https://academic.oup.com/gji/article-lookup/doi/10.1111/j.1365-246X`
`.1981.tb02716.x`   doi: 10.1111/j.1365-246X.1981.tb02716.x

Park, J. (2000, dec). Receiver Functions from Multiple-Taper Spectral Correlation Estimates. *Bulletin of the Seismological Society of America*, *90*(6), 1507–1520. Retrieved
from `https://pubs.geoscienceworld.org/bssa/article/90/6/1507-1520/120586`
doi: 10.1785/0119990122

Pasyanos, M. E., Masters, T. G., Laske, G., & Ma, Z. (2014, mar). LITHO1.0:
An updated crust and lithospheric model of the Earth. *Journal of Geophysical
Research: Solid Earth*, *119*(3), 2153–2173. Retrieved from `http://doi.wiley.com/`
`10.1002/2013JB010626https://onlinelibrary.wiley.com/doi/abs/10.1002/`
`2013JB010626`   doi: 10.1002/2013JB010626

Pearson, D. G., & Wittig, N. (2013). *The Formation and Evolution of Cratonic Mantle Lithosphere - Evidence from Mantle Xenoliths* (2nd ed., Vol. 3). Elsevier Ltd.
Retrieved from `http://dx.doi.org/10.1016/B978-0-08-095975-7.00205-9`   doi:
10.1016/B978-0-08-095975-7.00205-9

Peterson, J. (1993). *Observations and modelling of seismic background noise. Open-File Report 93-322* (Vol. 79) (No. 2). Retrieved from `https://pubs.er .usgs.gov/publication/ofr93322{%}0Ahttp://www.mttmllr.com/ADS/DATA/ peterson{_}usgs{_}seismic{_}noise{_}ofr93-322.pdf` doi: 10.3133/ofr93322

Petrescu, L., Stuart, G., Tataru, D., & Grecu, B. (2019, jul). Crustal structure of the Carpathian Orogen in Romania from receiver functions and ambient noise tomography: how craton collision, subduction and detachment affect the crust. *Geophysical Journal International*, *218*(1), 163–178. Retrieved from `https://academic.oup.com/gji/ article/218/1/163/5382047` doi: 10.1093/gji/ggz140

Priestley, K., & McKenzie, D. (2006, apr). The thermal structure of the lithosphere from shear wave velocities. *Earth and Planetary Science Letters*, *244*(1-2), 285–301. Retrieved from `https://linkinghub.elsevier.com/retrieve/pii/ S0012821X06000331` doi: 10.1016/j.epsl.2006.01.008

Priestley, K., McKenzie, D., & Ho, T. (2018, nov). A Lithosphere–Asthenosphere Boundary—a Global Model Derived from Multimode Surface-Wave Tomography and Petrology. In *Lithospheric discontinuities* (pp. 111–123). Retrieved from `https:// onlinelibrary.wiley.com/doi/abs/10.1002/9781119249740.ch6` doi: 10.1002/ 9781119249740.ch6

Prodehl, C., Kennett, B., Artemieva, I. M., & Thybo, H. (2013). 100years of seismic research on the Moho. *Tectonophysics*, *609*, 9–44. Retrieved from `http://dx.doi.org/ 10.1016/j.tecto.2013.05.036` doi: 10.1016/j.tecto.2013.05.036

Rader, E., Emry, E., Schmerr, N., Frost, D., Cheng, C., Menard, J., . . . Geist, D. (2015, oct). Characterization and Petrological Constraints of the Midlithospheric Discontinuity. *Geochemistry, Geophysics, Geosystems*, *16*(10), 3484–3504. Retrieved from `https://onlinelibrary.wiley.com/doi/abs/10.1002/2015GC005943` doi: 10.1002/ 2015GC005943

Rondenay, S. (2009, oct). Upper Mantle Imaging with Array Recordings of Converted and Scattered Teleseismic Waves. *Surveys in Geophysics*, *30*(4-5), 377–405. Retrieved from `http://link.springer.com/10.1007/s10712-009-9071-5` doi: 10.1007/s10712-009 -9071-5

Rondenay, S., Bostock, M. G., & Fischer, K. M. (2005). Multichannel inversion of scattered teleseismic body waves: Practical considerations and applicability. In *Geophysical monograph series* (Vol. 157, pp. 187–203). Retrieved from `http://www.agu.org/ books/gm/v157/157GM12/157GM12.shtml` doi: 10.1029/157GM12

Rondenay, S., Spieker, K., Sawade, L., Halpaap, F., & Farestveit, M. (2017, jan). GLImER: A New Global Database of Teleseismic Receiver Functions for Imaging Earth Structure. *Seismological Research Letters*, *88*(1), 39–48. Retrieved from `https://pubs.geoscienceworld.org/srl/article/88/1/39-48/314321` doi: 10 .1785/0220160111

Rychert, C. A., Fischer, K. M., & Rondenay, S. (2005, jul). A sharp lithosphere–asthenosphere boundary imaged beneath eastern North America. *Nature*, *436*(7050), 542–545. Retrieved from `http://www.nature.com/articles/nature03904` doi: 10.1038/nature03904

Rychert, C. A., Rondenay, S., & Fischer, K. M. (2007, aug). P -to- S and S -to- P imaging of a sharp lithosphere-asthenosphere boundary beneath eastern North America. *Journal of Geophysical Research*, *112*(B8), B08314. Retrieved from `http://doi.wiley.com/10.1029/2006JB004619` doi: 10.1029/2006JB004619

Saha, S., Dasgupta, R., & Tsuno, K. (2018, mar). High Pressure Phase Relations of a Depleted Peridotite Fluxed by CO_2 -H_2 O-Bearing Siliceous Melts and the Origin of Mid-Lithospheric Discontinuity. *Geochemistry, Geophysics, Geosystems*, *19*(3), 595–620. Retrieved from `http://doi.wiley.com/10.1002/2017GC007233` doi: 10.1002/2017GC007233

Schaeffer, A. J., & Lebedev, S. (2014). Imaging the North American continent using waveform inversion of global and USArray data. *Earth and Planetary Science Letters*, *402*(C), 26–41. Retrieved from `http://dx.doi.org/10.1016/j.epsl.2014.05.014` doi: 10.1016/j.epsl.2014.05.014

Schimmel, M., & Paulssen, H. (1997, aug). Noise reduction and detection of weak, coherent signals through phase-weighted stacks. *Geophysical Journal International*, *130*(2), 497–505. Retrieved from `https://academic.oup.com/gji/article-lookup/doi/10.1111/j.1365-246X.1997.tb05664.x` doi: 10.1111/j.1365-246X.1997.tb05664.x

Schneider, F. M., Yuan, X., Schurr, B., Mechie, J., Sippl, C., Haberland, C., … Negmatullaev, S. (2013). Seismic imaging of subducting continental lower crust beneath the Pamir. *Earth and Planetary Science Letters*, *375*, 101–112. Retrieved from `http://dx.doi.org/10.1016/j.epsl.2013.05.015` doi: 10.1016/j.epsl.2013.05.015

Selway, K., Ford, H., & Kelemen, P. (2015). The seismic mid-lithosphere discontinuity. *Earth and Planetary Science Letters*, *414*, 45–57. Retrieved from `http://dx.doi.org/10.1016/j.epsl.2014.12.029` doi: 10.1016/j.epsl.2014.12.029

Shearer, P. M. (1993, dec). Global mapping of upper mantle reflectors from long-period SS precursors. *Geophysical Journal International*, *115*(3), 878–904. Retrieved from `https://academic.oup.com/gji/article-lookup/doi/10.1111/j.1365-246X.1993.tb01499.x` doi: 10.1111/j.1365-246X.1993.tb01499.x

Shearer, P. M. (2019). *Introduction to Seismology* (3rd ed.). Cambridge University Press. Retrieved from `https://www.cambridge.org/core/product/identifier/9781316877111/type/book` doi: 10.1017/9781316877111

Simmons, N. A., Forte, A. M., Boschi, L., & Grand, S. P. (2010, dec). GyPSuM: A joint tomographic model of mantle density and seismic wave speeds. *Journal of Geophysical Research*, *115*(B12), B12310. Retrieved from `http://doi.wiley.com/10.1029/2010JB007631` doi: 10.1029/2010JB007631

Sodoudi, F., Yuan, X., Kind, R., Lebedev, S., Adam, J. M., Kästle, E., & Tilmann, F. (2013, dec). Seismic evidence for stratification in composition and anisotropic fabric within the thick lithosphere of Kalahari Craton. *Geochemistry, Geophysics, Geosystems*, *14*(12), 5393–5412. Retrieved from `http://doi.wiley.com/10.1002/2013GC004955` doi: 10.1002/2013GC004955

Stanley, R. P. (1975). Fibonacci Lattice. *Fibonacci Quarterly*, *13*(3), 215–232.

Stein, S., & Wysession, M. (2009). *An introduction to seismology, earthquakes, and earth structure*. John Wiley & Sons.

Stuwe, K. (2007). Summary for Policymakers. In Intergovernmental Panel on Climate Change (Ed.), *Climate change 2013 - the physical science basis* (Vol. 53, pp. 1–30). Cambridge: Cambridge University Press. Retrieved from `https://www.cambridge.org/core/product/identifier/CBO9781107415324A009/type/book{_}part` doi: 10.1017/CBO9781107415324.004

Sun, W., Kennett, B., Zhao, L., & Fu, L.-Y. (2018, nov). Continental Lithospheric Layering Beneath Stable, Modified, and Destroyed Cratons from Seismic Daylight Imaging. In *Lithospheric discontinuities* (pp. 155–176). Retrieved from `https://onlinelibrary.wiley.com/doi/abs/10.1002/9781119249740.ch9` doi: 10.1002/9781119249740.ch9

Tauzin, B., Bodin, T., Debayle, E., Perrillat, J. P., & Reynard, B. (2016). Multi-mode conversion imaging of the subducted Gorda and Juan de Fuca plates below the North American continent. *Earth and Planetary Science Letters*, *440*, 135–146. Retrieved from `http://dx.doi.org/10.1016/j.epsl.2016.01.036` doi: 10.1016/j.epsl.2016.01.036

Tauzin, B., Debayle, E., & Wittlinger, G. (2010, oct). Seismic evidence for a global low-velocity layer within the Earth's upper mantle. *Nature Geoscience*, *3*(10), 718–721. Retrieved from `http://www.nature.com/articles/ngeo969` doi: 10.1038/ngeo969

Teanby, N. (2006, nov). An icosahedron-based method for even binning of globally distributed remote sensing data. *Computers & Geosciences*, *32*(9), 1442–1450. Retrieved from `https://linkinghub.elsevier.com/retrieve/pii/S0098300406000173` doi: 10.1016/j.cageo.2006.01.007

Tharimena, S., Rychert, C., & Harmon, N. (2017, aug). A unified continental thickness from seismology and diamonds suggests a melt-defined plate. *Science*, *357*(6351), 580–583. Retrieved from `https://www.sciencemag.org/lookup/doi/10.1126/science.aan0741` doi: 10.1126/science.aan0741

Thybo, H., Artemieva, I. M., & Kennett, B. (2013). Moho: 100years after Andrija Mohorovičić. *Tectonophysics*, *609*, 1–8. Retrieved from `http://dx.doi.org/10.1016/j.tecto.2013.10.004` doi: 10.1016/j.tecto.2013.10.004

Thybo, H., & Perchu, E. (1997, mar). The Seismic 8 Discontinuity and Partial Melting in Continental Mantle. *Science*, *275*(5306), 1626–1629. Retrieved from `https://www.sciencemag.org/lookup/doi/10.1126/science.275.5306.1626` doi: 10.1126/science.275.5306.1626

USGS. (1999). *Inside the Earth.* Retrieved from `https://pubs.usgs.gov/gip/dynamic/inside.html`

van Hunen, J., & Moyen, J.-F. (2012, may). Archean Subduction: Fact or Fiction? *Annual Review of Earth and Planetary Sciences*, *40*(1), 195–219. Retrieved from `http://www.annualreviews.org/doi/10.1146/annurev-earth-042711-105255` doi: 10.1146/annurev-earth-042711-105255

Wang, X., Ding, Z., & Zhu, L. (2016, aug). Lithospheric Structure of the Northeastern North China Craton Imaged by S Receiver Functions. *Pure and Applied Geophysics*, *173*(8), 2727–2736. Retrieved from `http://link.springer.com/10.1007/s00024-016-1293-0` doi: 10.1007/s00024-016-1293-0

Wang, Y., & Pavlis, G. L. (2016, feb). Generalized iterative deconvolution for receiver function estimation. *Geophysical Journal International*, *204*(2), 1086–1099. Retrieved from `https://academic.oup.com/gji/article-lookup/doi/10.1093/gji/ggv503` doi: 10.1093/gji/ggv503

Whitmeyer, S. (2007). Tectonic model for the Proterozoic growth of North America. *Geosphere*, *3*(4), 220. Retrieved from `https://pubs.geoscienceworld.org/geosphere/article/3/4/220-259/31158` doi: 10.1130/GES00055.1

Williams, H., Hoffman, P. F., Lewry, J. F., Monger, J. W., & Rivers, T. (1991). Anatomy of North America: thematic geologic portrayals of the continent. *Tectonophysics*, *187*(1-3), 117–134. Retrieved from `https://www.sciencedirect.com/science/article/pii/004019519190416P` doi: 10.1016/0040-1951(91)90416-P

Wilson, D. C., Angus, D. A., Ni, J. F., & Grand, S. P. (2006, jun). Constraints on the interpretation of S -to- P receiver functions. *Geophysical Journal International*, *165*(3), 969–980. Retrieved from `https://academic.oup.com/gji/article-lookup/doi/10.1111/j.1365-246X.2006.02981.x` doi: 10.1111/j.1365-246X.2006.02981.x

Wirth, E. A., & Long, M. D. (2014, oct). A contrast in anisotropy across mid-lithospheric discontinuities beneath the central United States—A relic of craton formation. *Geology*, *42*(10), 851–854. Retrieved from `http://pubs.geoscienceworld.org/geology/article/42/10/851/131379/A-contrast-in-anisotropy-across-midlithospheric` doi: 10.1130/G35804.1

Wittlinger, G., & Farra, V. (2007, feb). Converted waves reveal a thick and layered tectosphere beneath the Kalahari super-craton. *Earth and Planetary Science Letters*, *254*(3-4), 404–415. Retrieved from `https://linkinghub.elsevier.com/retrieve/pii/S0012821X0600865X` doi: 10.1016/j.epsl.2006.11.048

Yao, Y., & Li, A. (2016, dec). Lithospheric velocity model of Texas and implications for the Ouachita orogeny and the opening of the Gulf of Mexico. *Geophysical Research Letters*, *43*(23), 12,046–12,053. Retrieved from `http://doi.wiley.com/10.1002/2016GL071167` doi: 10.1002/2016GL071167

Yuan, H., & Romanowicz, B. (2010). Lithospheric layering in the North American craton. *Nature*, *466*(7310), 1063–1068. Retrieved from `http://dx.doi.org/10.1038/nature09332` doi: 10.1038/nature09332

Yuan, H., & Romanowicz, B. (2017, nov). *Introduction-lithospheric discontinuities* (No. 2018). Retrieved from `https://onlinelibrary.wiley.com/doi/abs/10.1002/9781119249740.ch0` doi: 10.1002/9781119249740.ch0

Yuan, H., Romanowicz, B., Fischer, K. M., & Abt, D. (2011, mar). 3-D shear wave radially and azimuthally anisotropic velocity model of the North American upper mantle. *Geophysical Journal International*, *184*(3), 1237–1260. Retrieved from `https://academic.oup.com/gji/article-lookup/doi/10.1111/j.1365-246X.2010.04901.x` doi: 10.1111/j.1365-246X.2010.04901.x

Yuan, X., Kind, R., Li, X., & Wang, R. (2006, may). The S receiver functions: synthetics and data example. *Geophysical Journal International*, *165*(2), 555–564. Retrieved from `https://academic.oup.com/gji/article-lookup/doi/10.1111/j.1365-246X.2006.02885.x` doi: 10.1111/j.1365-246X.2006.02885.x

Zhang, H., & Schmandt, B. (2019). Application of Ps Scattering Kernels to Imaging the Mantle Transition Zone with Receiver Functions. *Journal of Geophysical Research: Solid Earth*, *118*(1), 1–20. Retrieved from `https://agupubs.onlinelibrary.wiley.com/doi/abs/10.1029/2018JB016274?af=R` doi: 10.1029/2018JB016274

Zhang, R., Wu, Q., Sun, L., He, J., & Gao, Z. (2014). Crustal and lithospheric structure of Northeast China from S-wave receiver functions. *Earth and Planetary Science Letters*, *401*, 196–205. Retrieved from `http://dx.doi.org/10.1016/j.epsl.2014.06.017` doi: 10.1016/j.epsl.2014.06.017

Zheng, Z., & Romanowicz, B. (2012, dec). Do double ‘<italic>SS</italic> precursors' mean double discontinuities? *Geophysical Journal International*, *191*(3), 1361–1373. Retrieved from `https://academic.oup.com/gji/article-lookup/doi/10.1111/j.1365-246X.2012.05683.x` doi: 10.1111/j.1365-246X.2012.05683.x

Zhu, L., & Kanamori, H. (2000). Moho depth variation in southern California from teleseismic receiver functions. *Journal of Geophysical Research: Solid Earth*, *105*(B2), 2969–2980. Retrieved from `http://doi.wiley.com/10.1029/1999JB900322` doi: 10.1029/1999JB900322

Appendices

Appendix A

Additional Figures to Illustrate the Implementation

A.1   Comparisons of Velocity Models
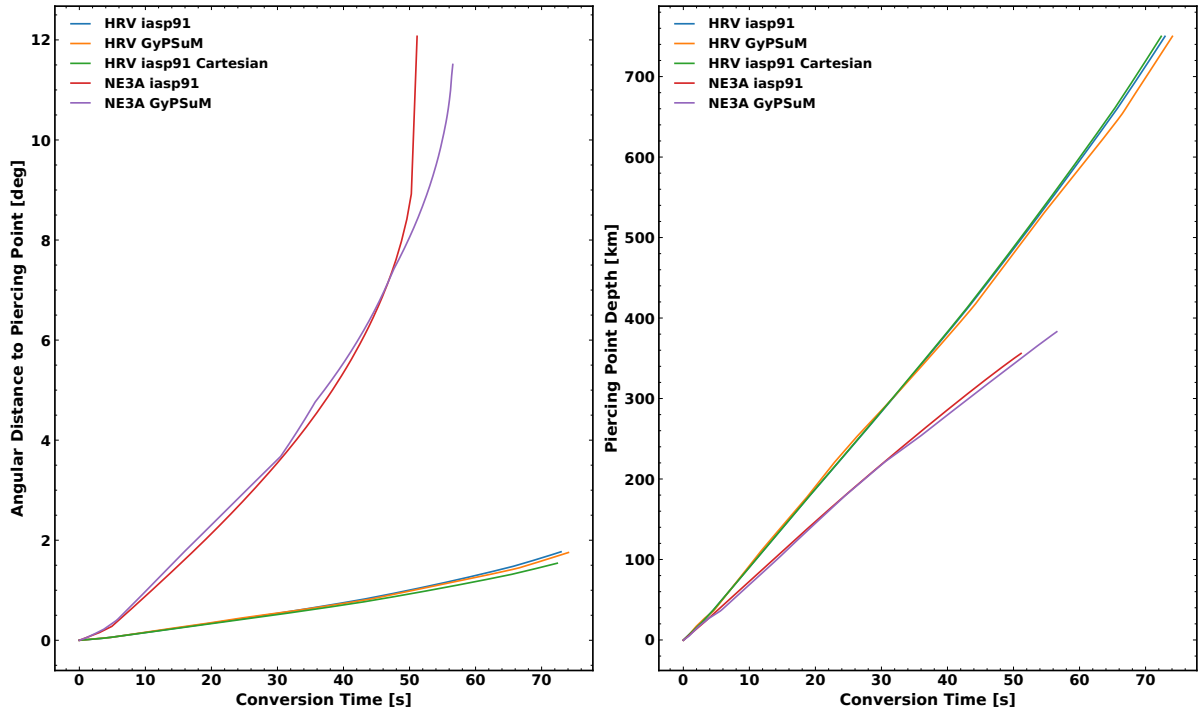
Figure A.1: **Comparisons of the different velocity models implemented in PyGLImER.** *The waveform recorded on station IU.HRV is a P-to-S waveform with a ray parameter back-azimuth $\gamma = 333°$ and a ray parameter $p = 4.98s/°$. The data for station YP.NE3A are for an S-to-P conversion with a back-azimuth $\gamma = 137°$ and a ray parameter $p = 11.91s/°$. The graph indicated as Cartesian represents computations that were done without accounting for a spherical Earth.*

A.2   Depth-Migrated Receiver Functions Created with Spectral Division
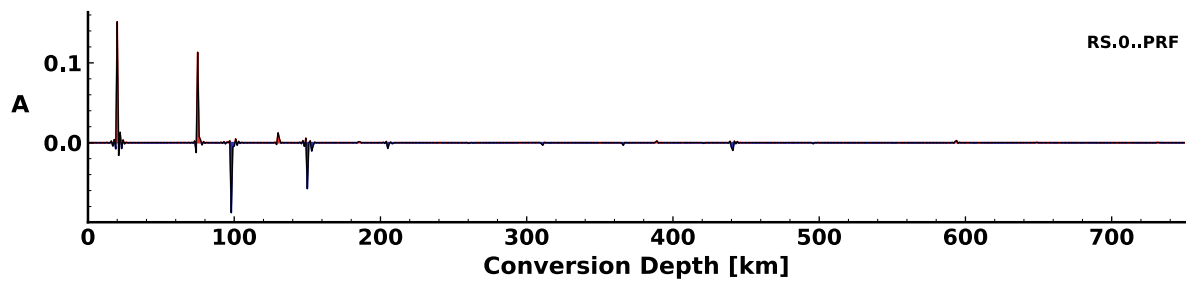
(a)
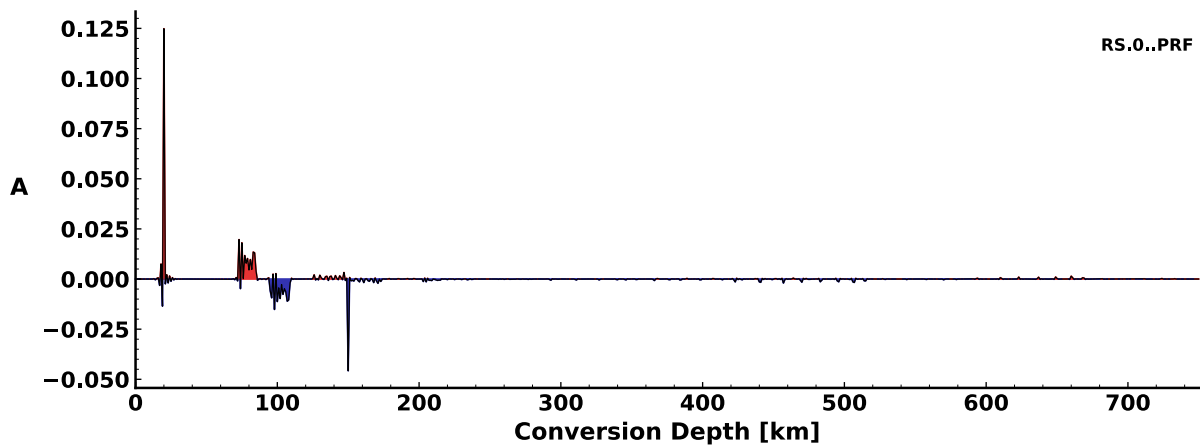
(b)

Figure A.2: **The synthetic P-receiver functions resulting from deconvolving the P from the SV component migrated to depth (a) and stacked (b).** *The RF was produces using waterlevel spectral division.*

A.3   CCP Stacks from Synthetic Data
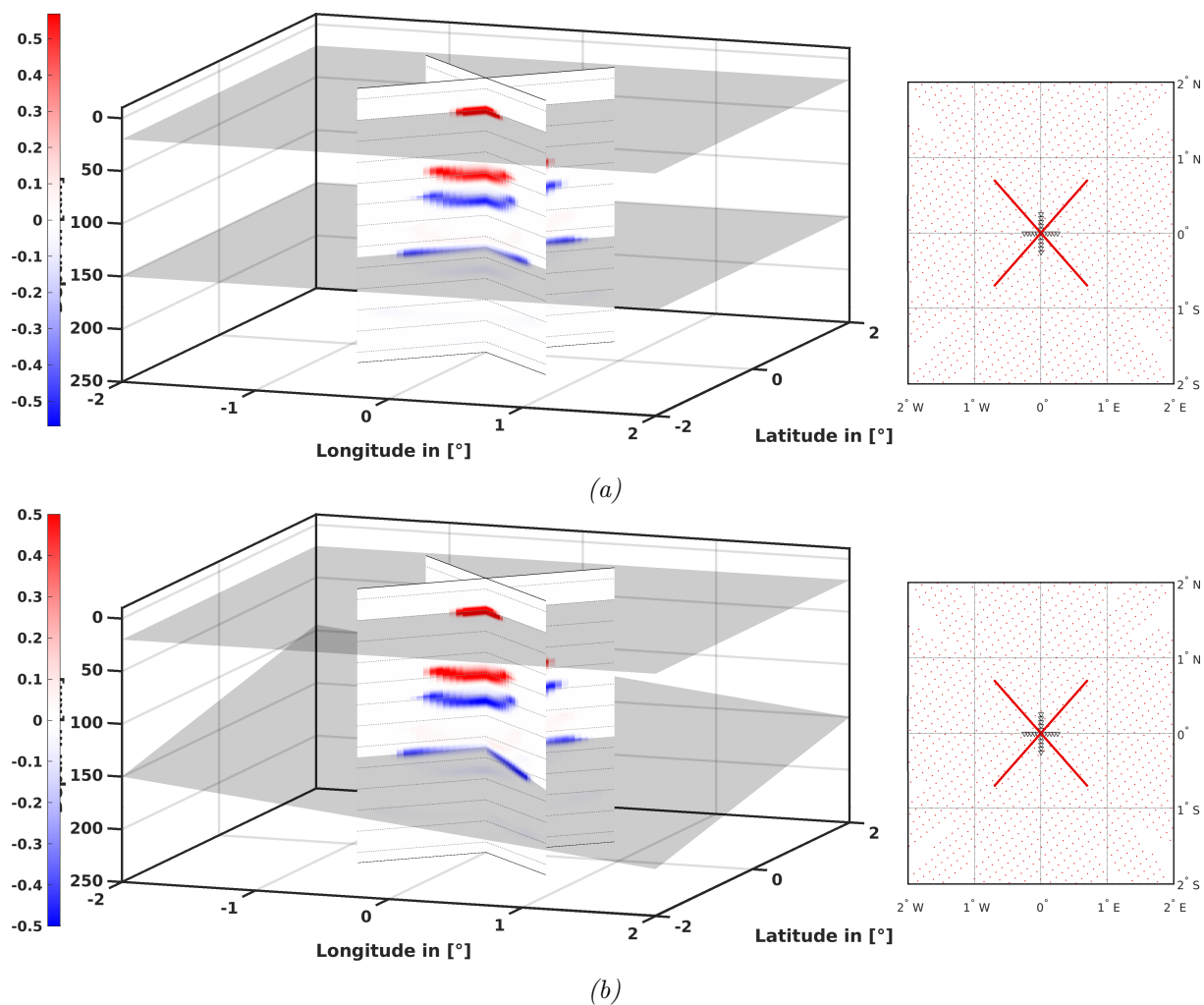
Figure A.3: **Slices through a CCP volume created using PRFs.** *The dip of boundary d2 increases with every panel from 0° to 30 °. The traces of the velocity discontinuities d1 and d2 are indicated. d2 is horizontal in (a) and has a dip of 10° in (b).*

(a)

(b)
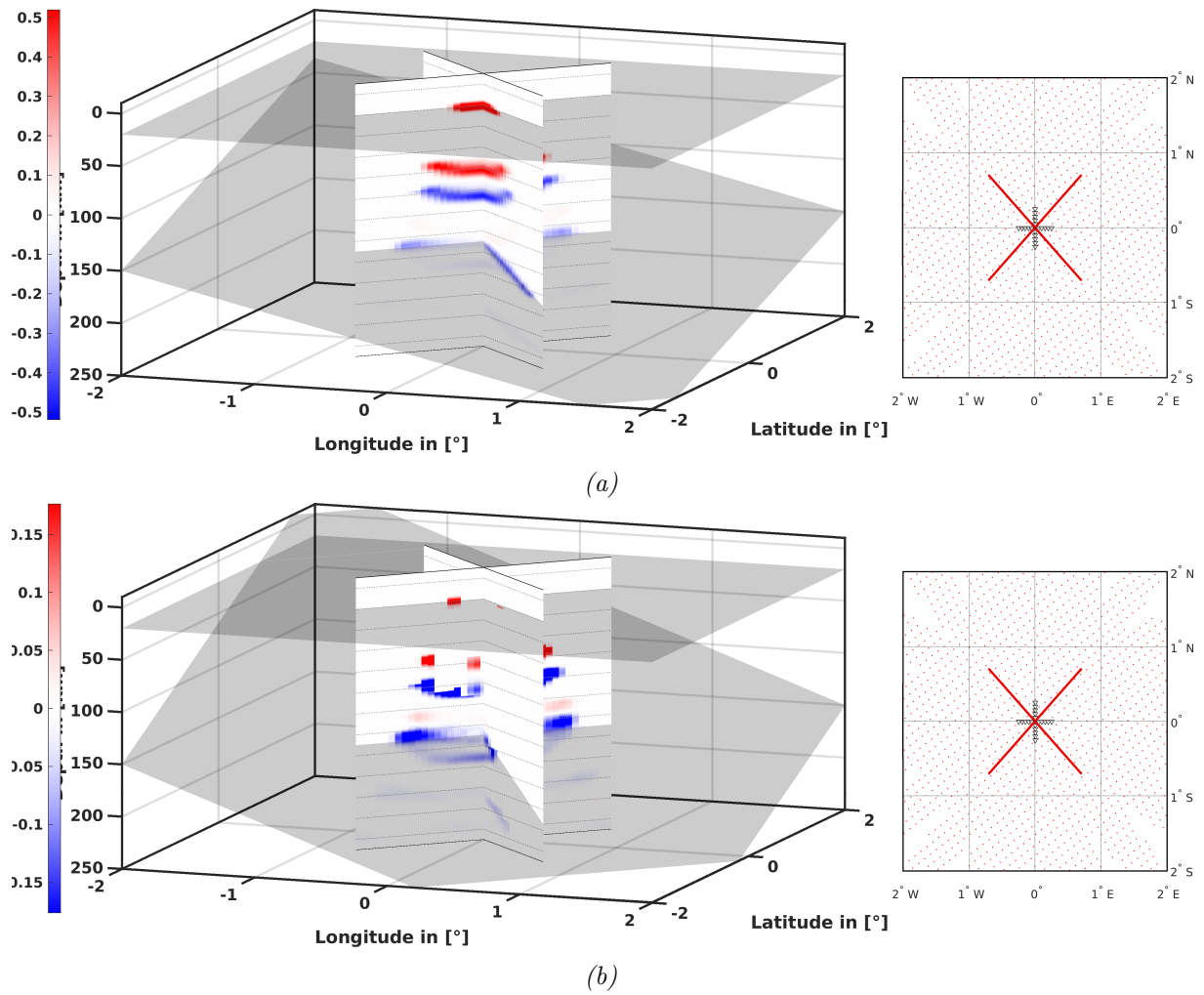
Figure A.4: **Continuation of Figure A.3.** *d2 dips by 20° in (a) and 30° in (b).*
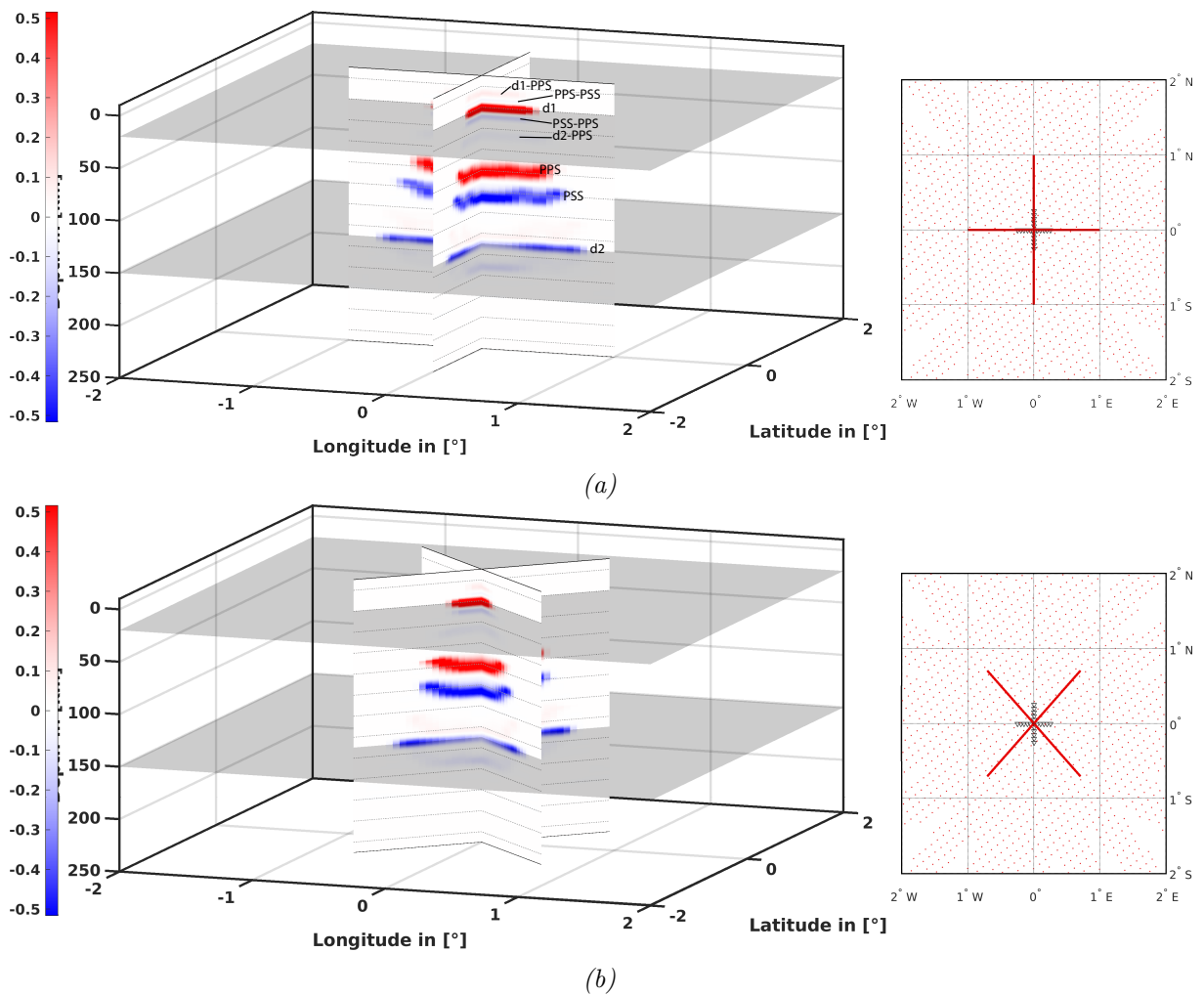
Figure A.5: **Slices through a CCP volume created using PRFs and taking multiples into account with constant weights (see equation 4.5).** *The dip of boundary d2 increases with every panel from 0° to 30° by 10°. The traces of the velocity discontinuities d1 and d2 are indicated.*

(a)

(b)
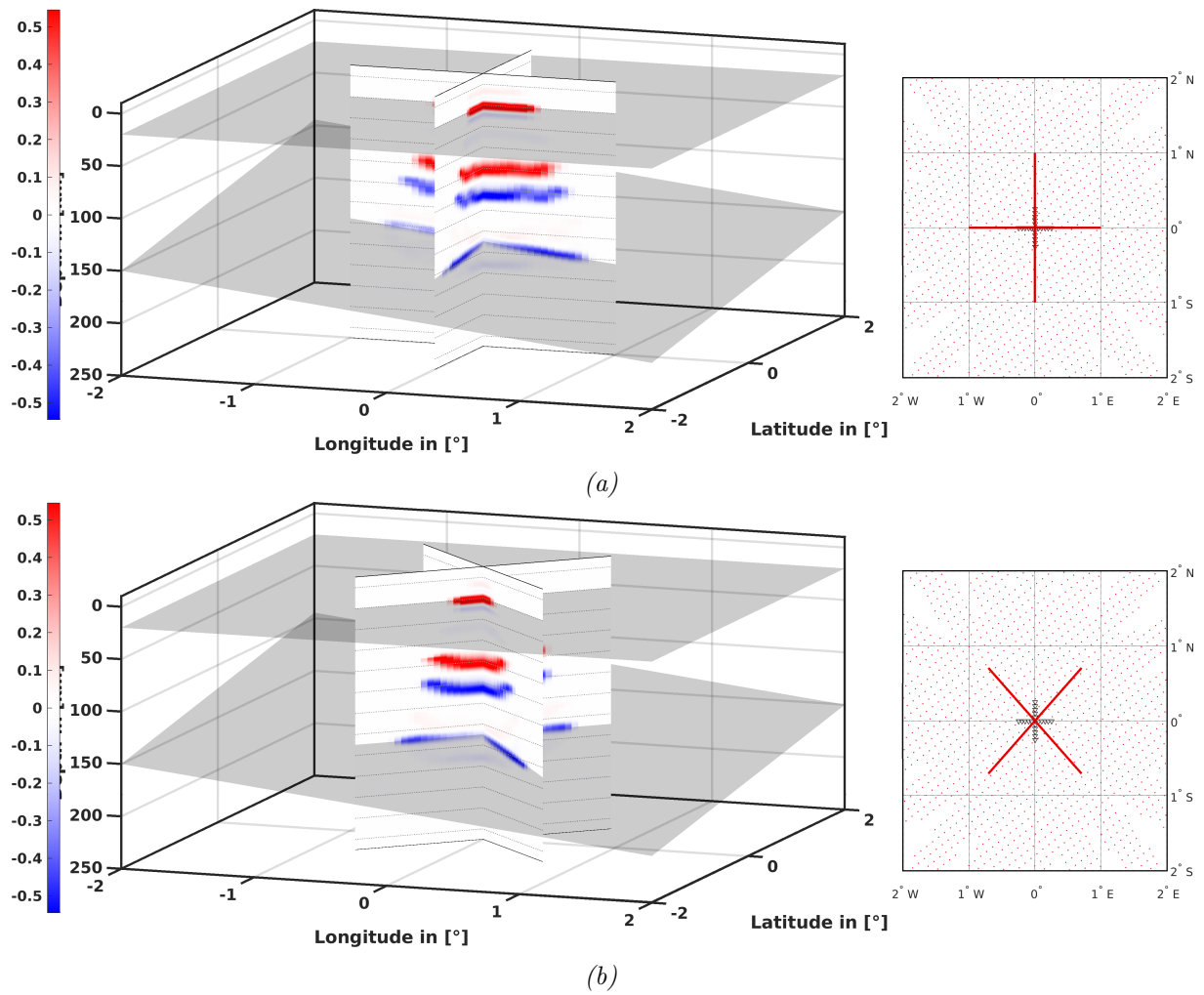
Figure A.6: ***Continuation of Figure A.5.*** *d2 has a dip of 10° in both panels.*

(a)

(b)
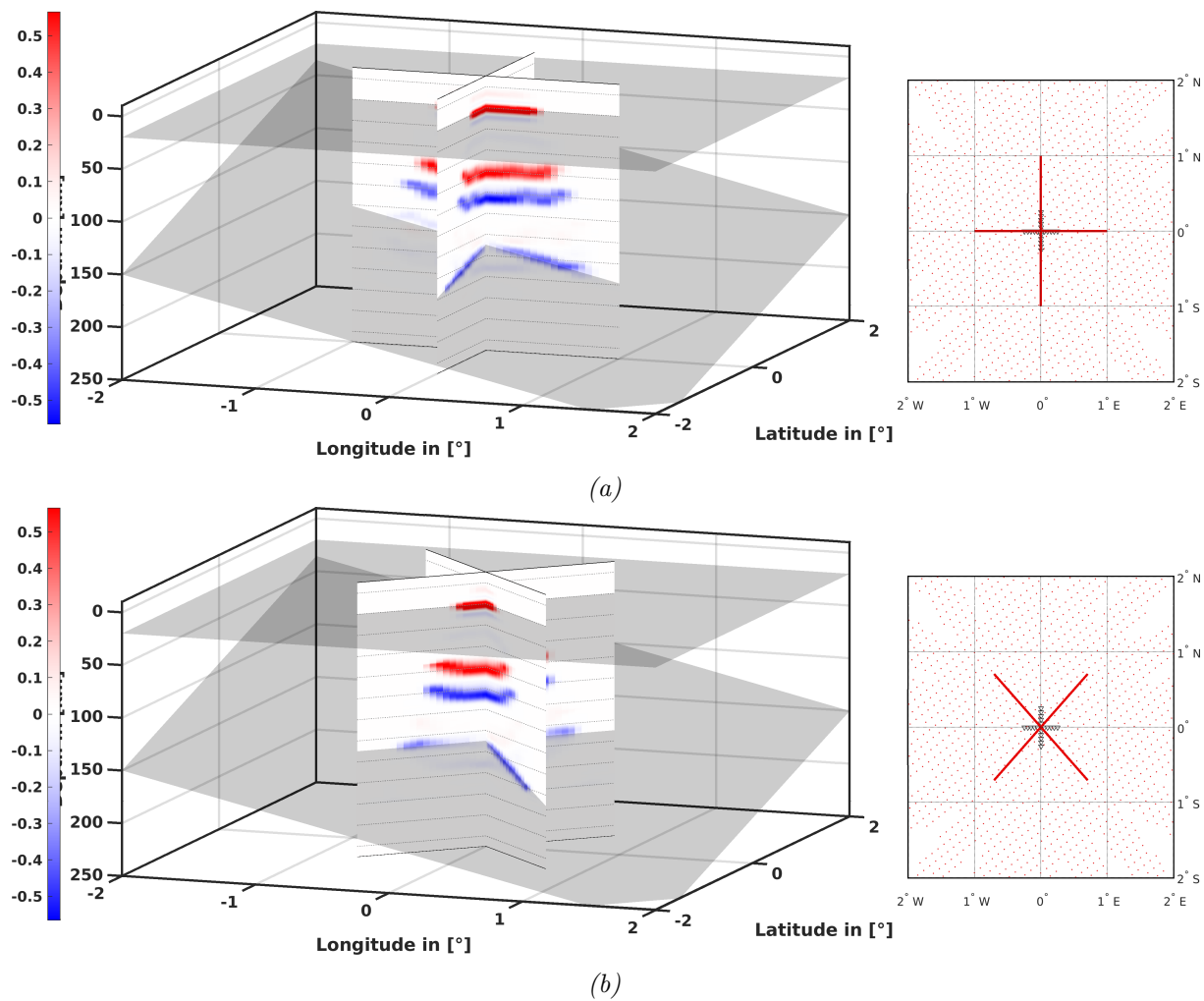
Figure A.7: **Continuation of Figure A.5.** *d2 dips by 20° in both panels.*
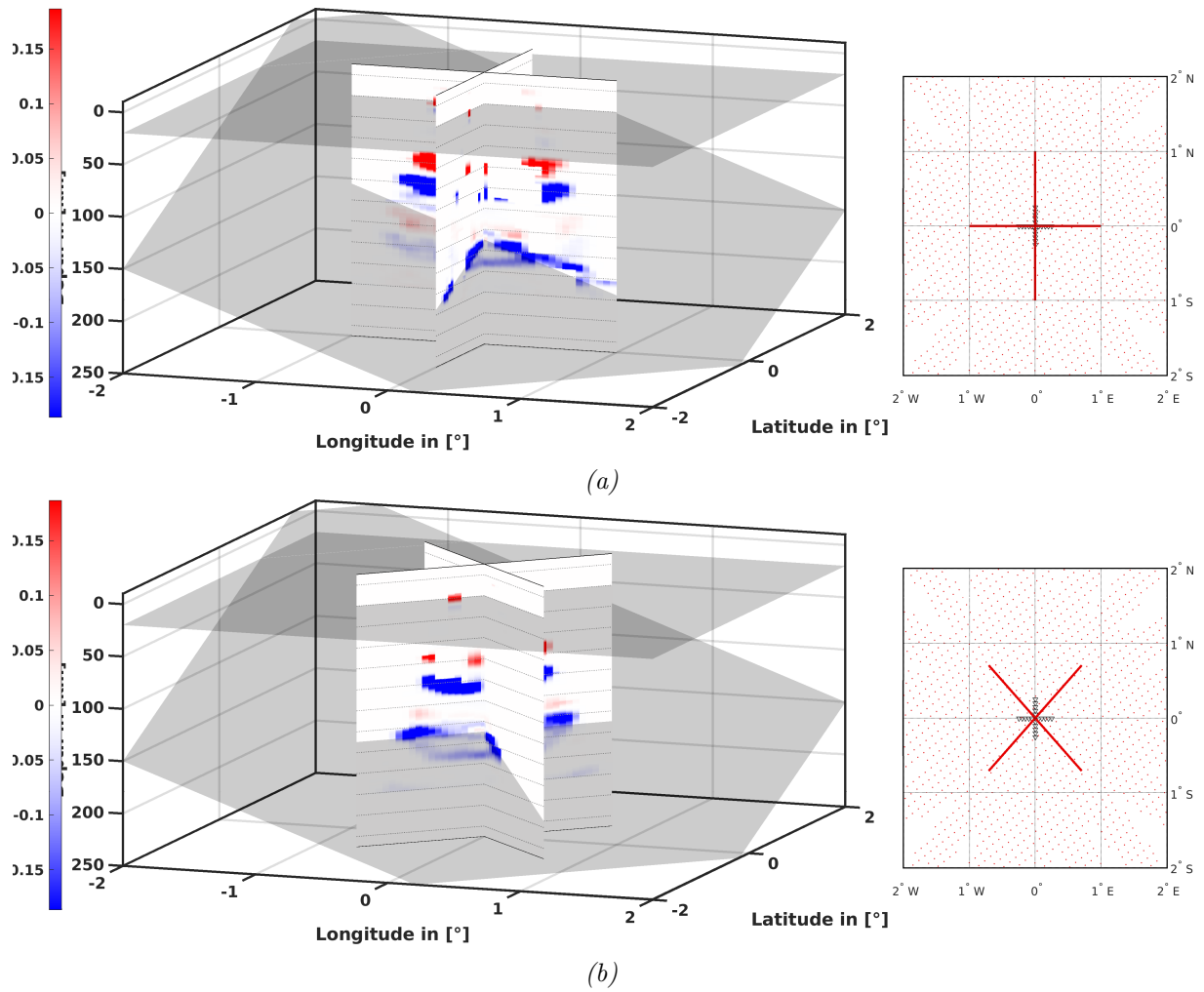
Figure A.8: **Continuation of Figure A.5.** *d2 dips by 30° in both panels.*
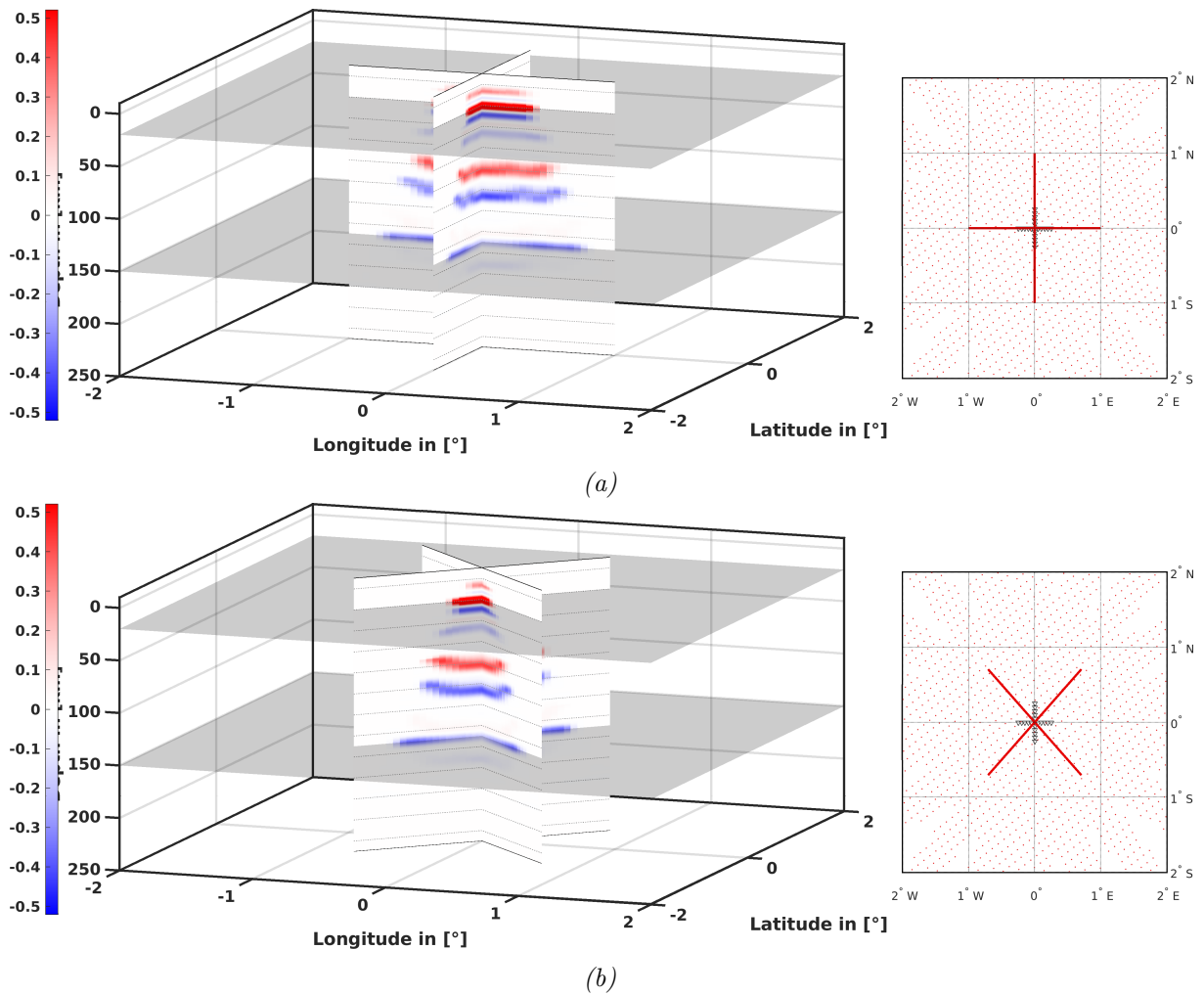
Figure A.9: **Slices through a CCP volume created using PRFs and taking multiples into account with linear weights.** *The dip of boundary d2 increases with every panel from 0° to 30°. The traces of the velocity discontinuities d1 and d2 are indicated. d2 dips by 0° in both panels.*

(a)

(b)
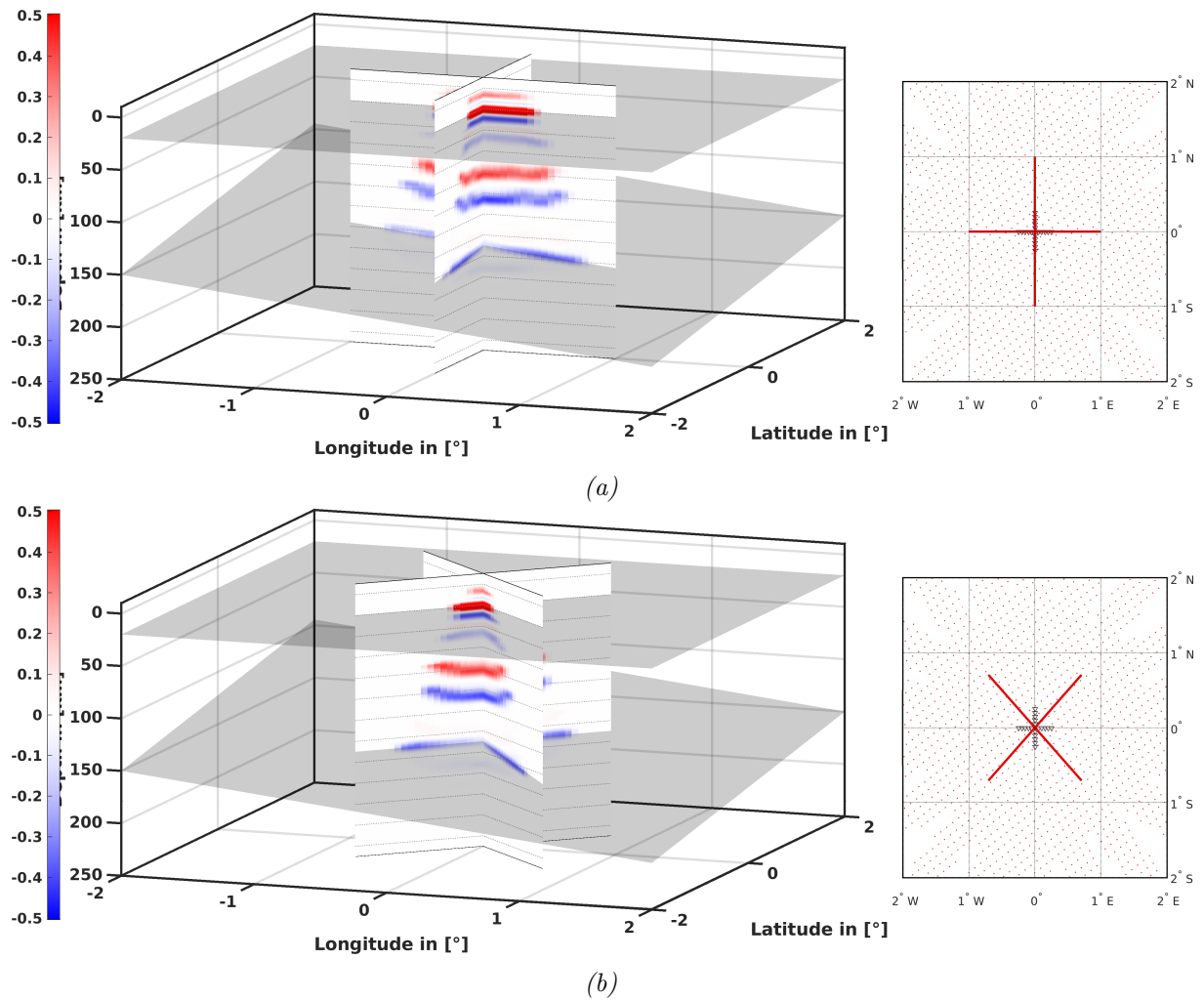
Figure A.10: **Continuation of Figure A.9.** *d2 dips by 10° in both panels.*

(a)

(b)
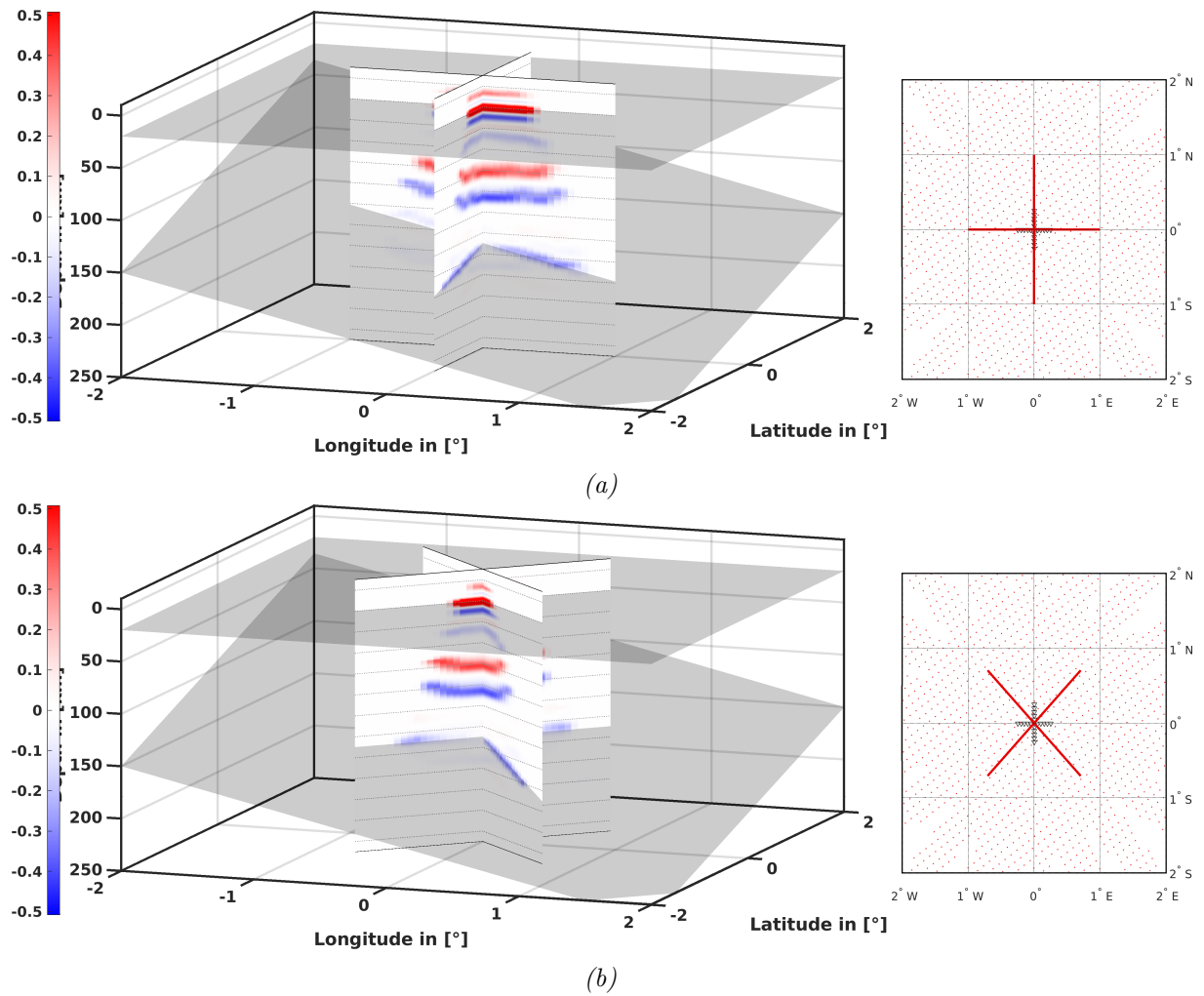
Figure A.11: **Continuation of Figure A.9.** *d2 dips by 20° in both panels.*

(a)

(b)
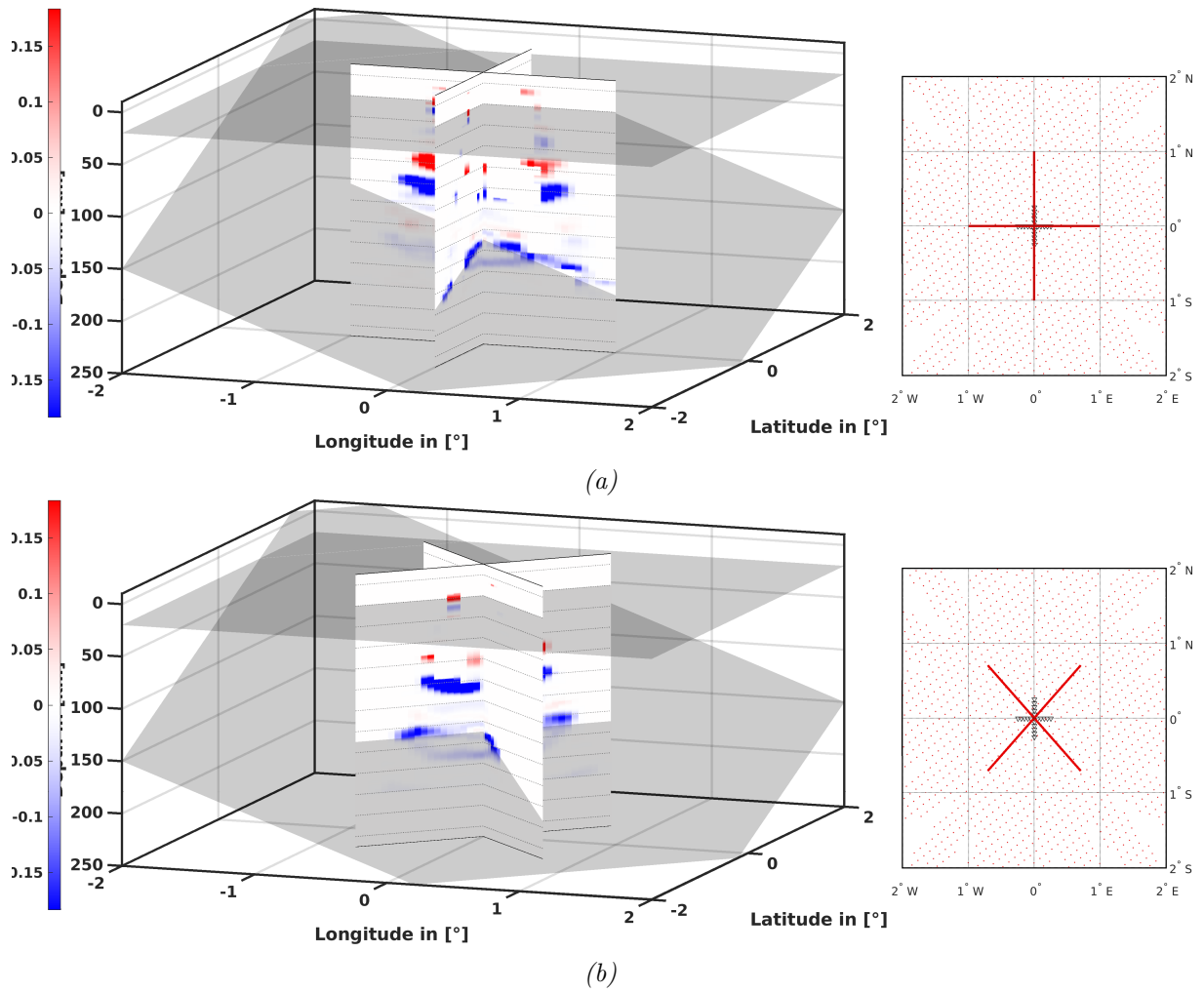
Figure A.12: **Continuation of Figure A.9.** *d2 dips by 30° in both panels.*

(a)

(b)

(c)
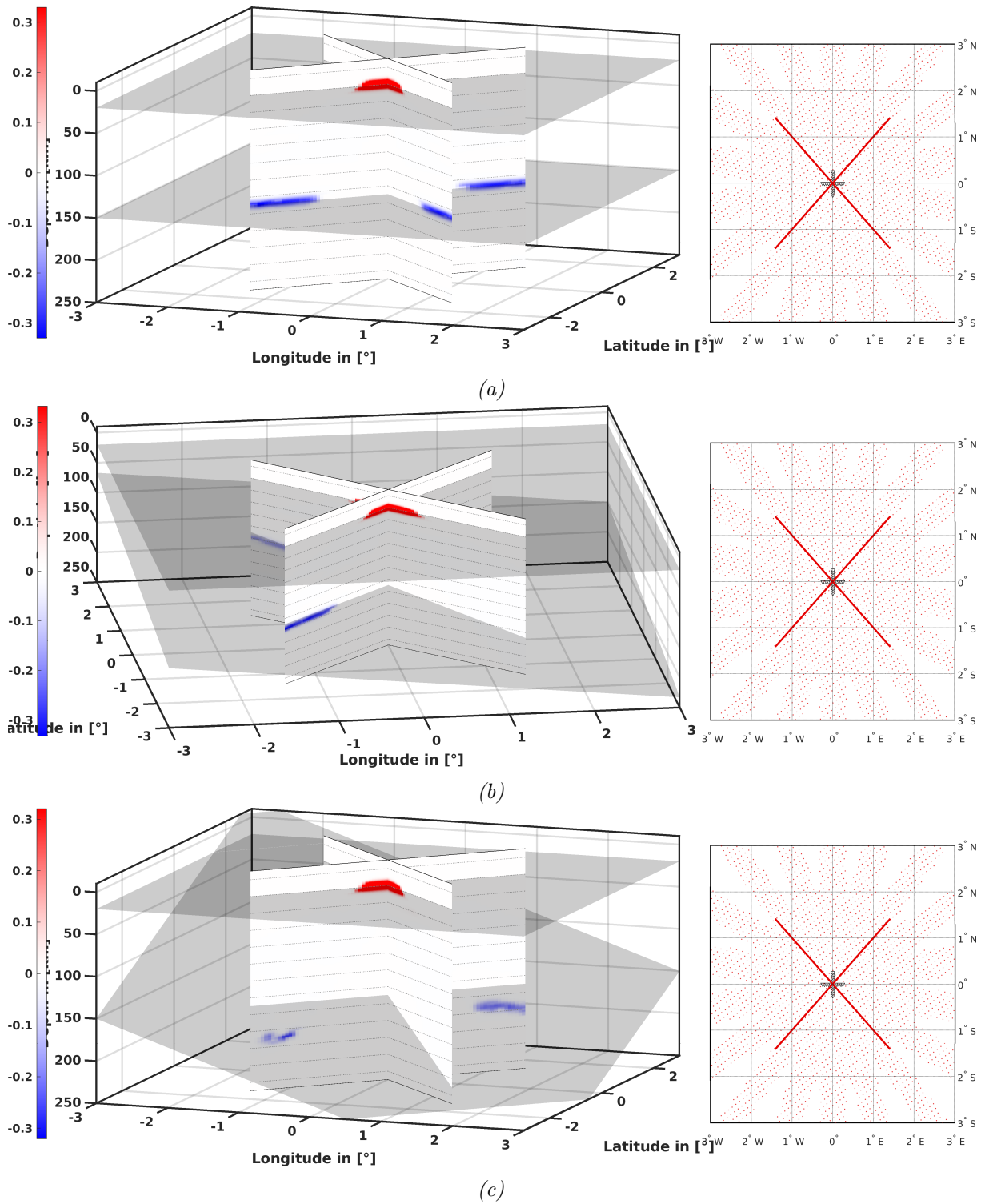
Figure A.13: **Slices through a CCP volume created using SRFs.** *The dip of boundary d2 increases with every panel from 0° to 20° by 10°. The traces of the velocity discontinuities d1 and d2 are indicated.*

Appendix B

Additional Results from the Continental US

B.1 Additional Cross-Sections
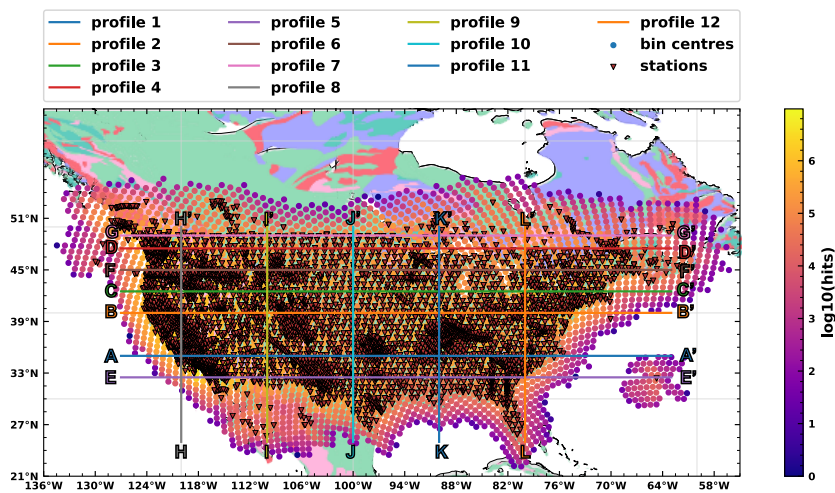
Figure B.1: **Map view of the cross-sections through North America provided in the appendix.** *The figure shows the locations of the stations, for which RF data has been used, the bin locations, illumination per bin, and the exact location of the cross-section. The illumination is given as depth-cumulative illumination per bin for PRF-data*
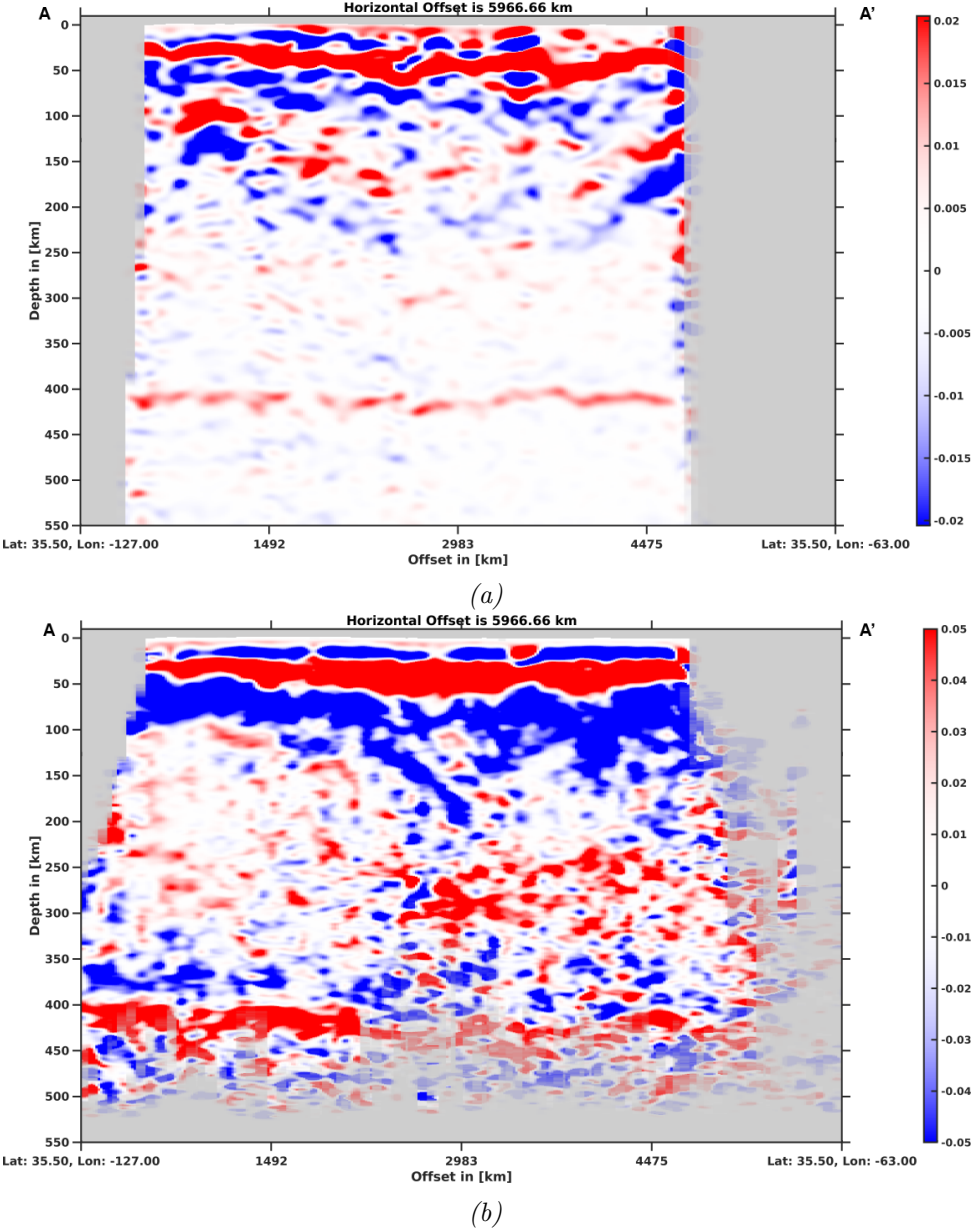
Figure B.2: **Slices through the CCP objects for P-to-S (a) and S-to-P data at 35.5° north (corresponds to profile 1 in Figure B.1).** *The data start greying out for less than 50 and 25 hits per grid point for (a) and (b), respectively.*
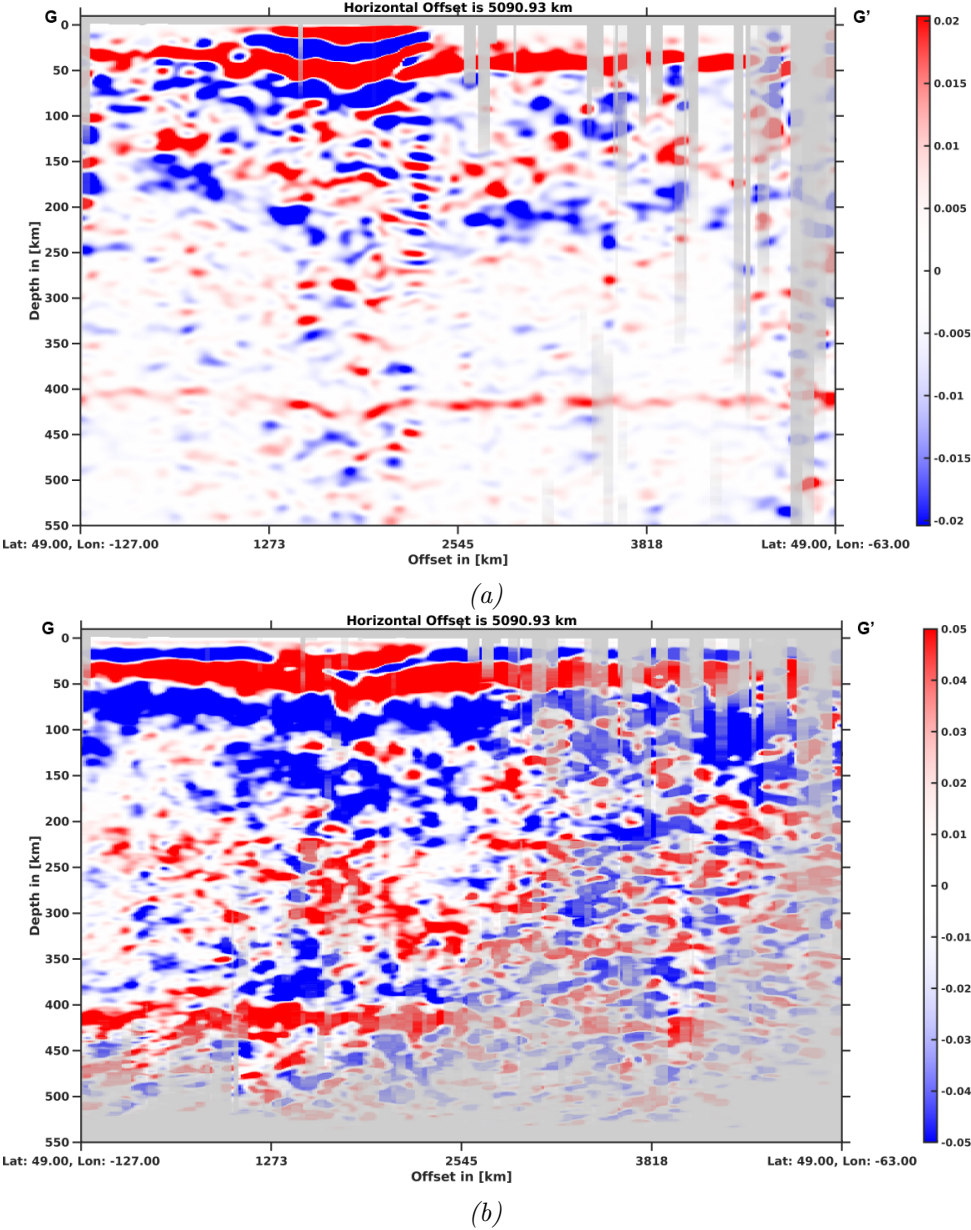
(a)

(b)
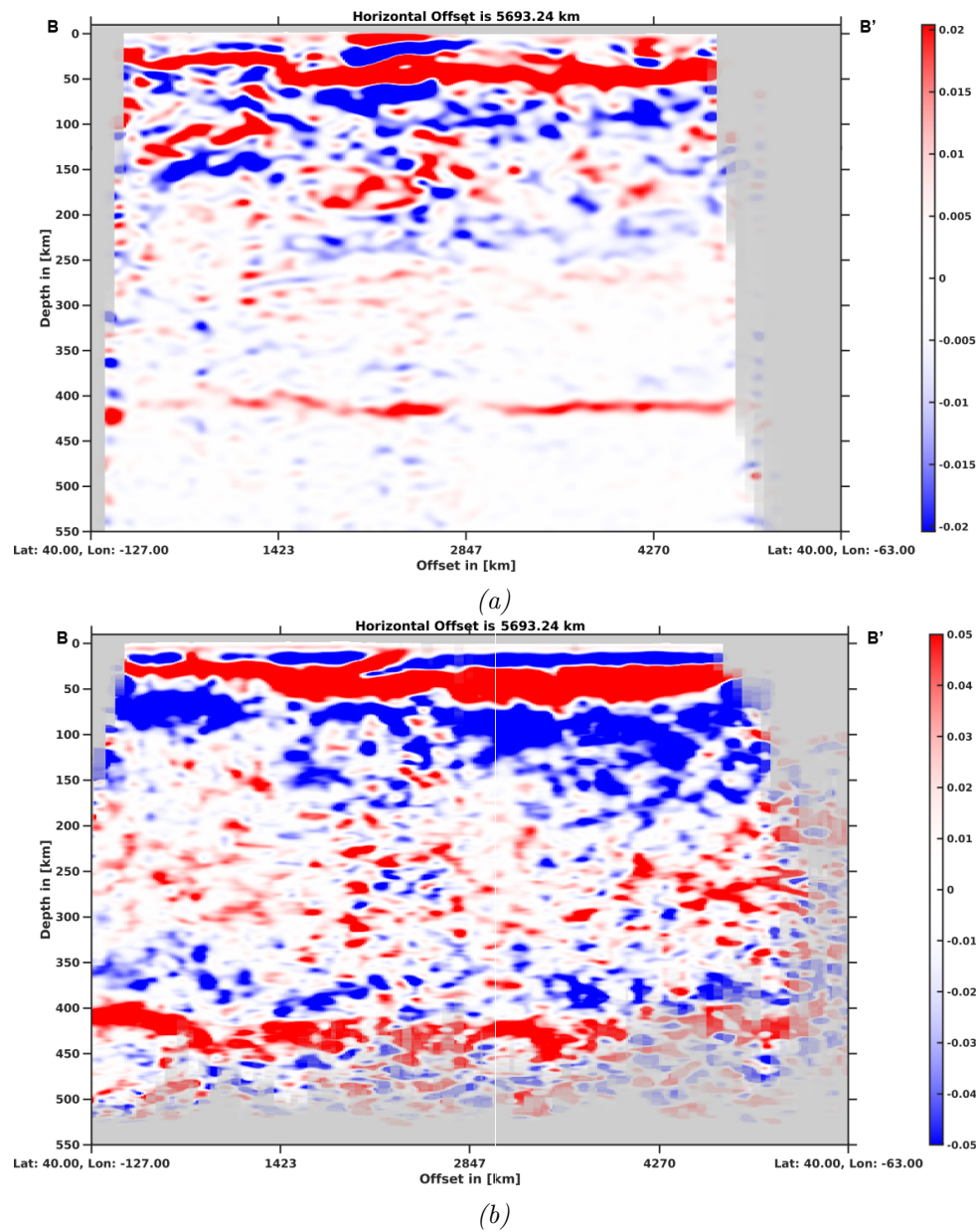
Figure B.3: **Slices through the CCP objects for P-to-S (a) and S-to-P data at 40° north (corresponds to profile 2 in Figure B.1).** *The data start greying out for less than 50 and 25 hits per grid point for (a) and (b), respectively.*
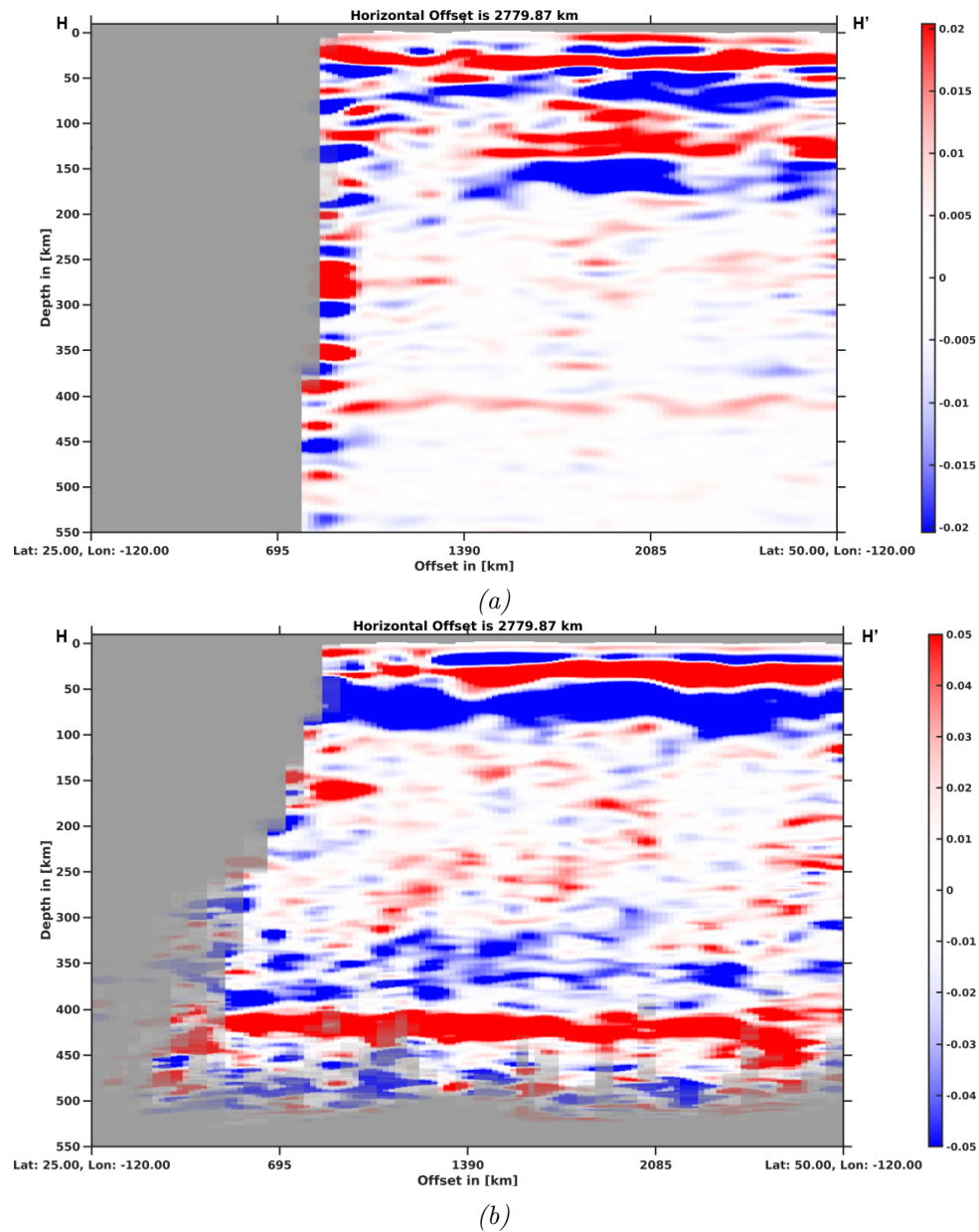
(a)

(b)
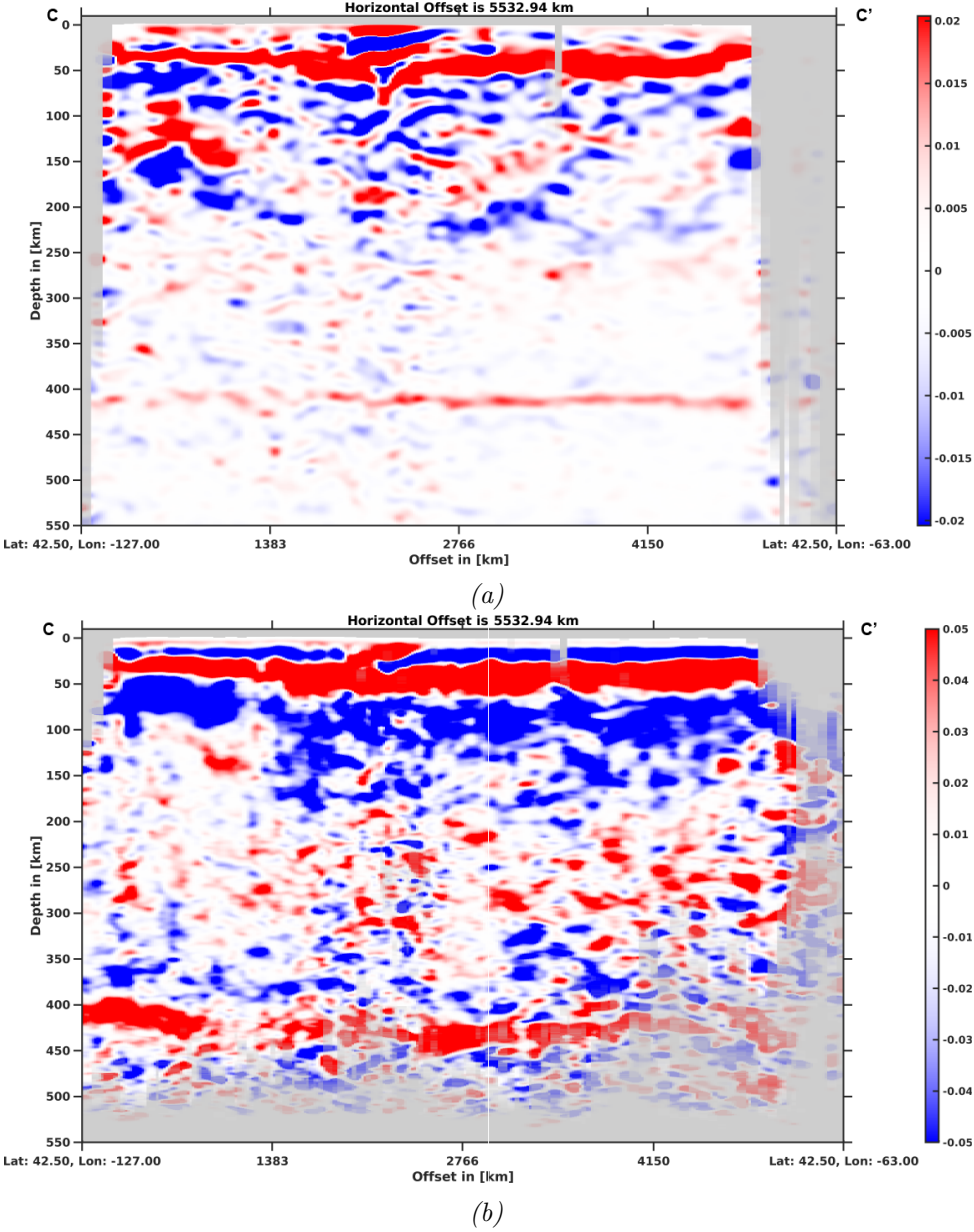
Figure B.4: **Slices through the CCP objects for P-to-S (a) and S-to-P data at 42.5° north (corresponds to profile 3 in Figure B.1).** *The data start greying out for less than 50 and 25 hits per grid point for (a) and (b), respectively.*
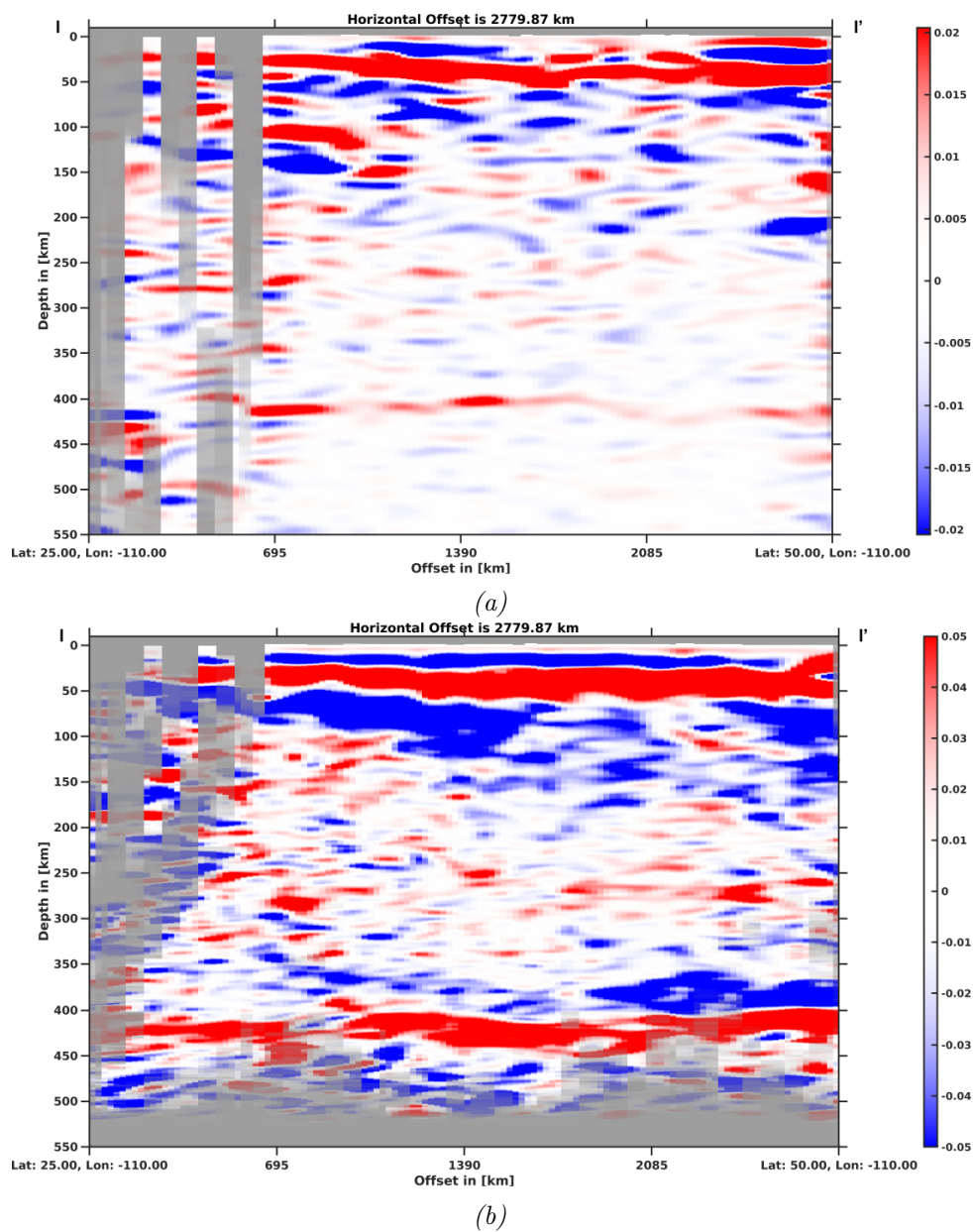
(a)

(b)
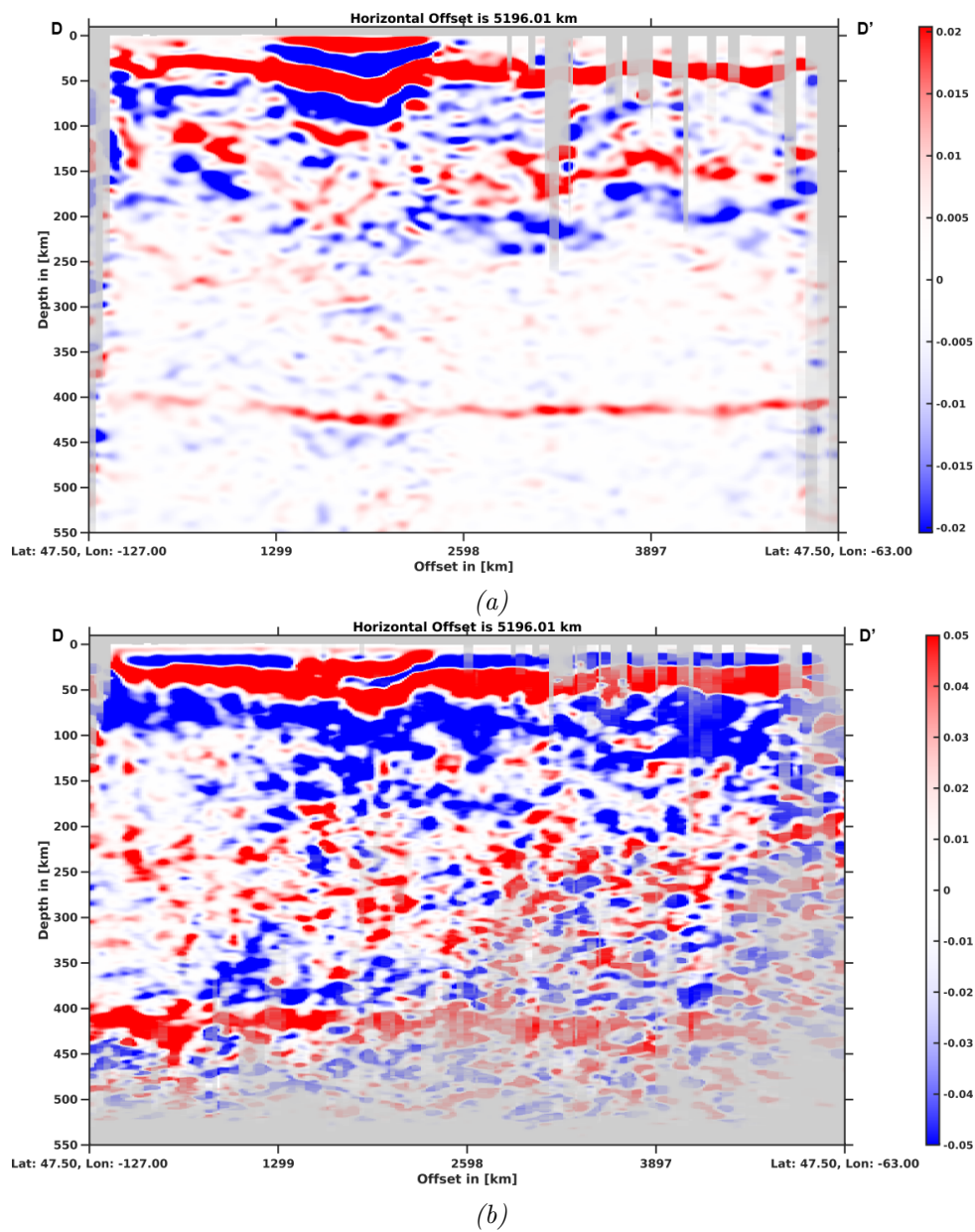
Figure B.5: **Slices through the CCP objects for P-to-S (a) and S-to-P data at 47.5° north (corresponds to profile 4 in Figure B.1).** *The data start greying out for less than 50 and 25 hits per grid point for (a) and (b), respectively.*

(a)

(b)
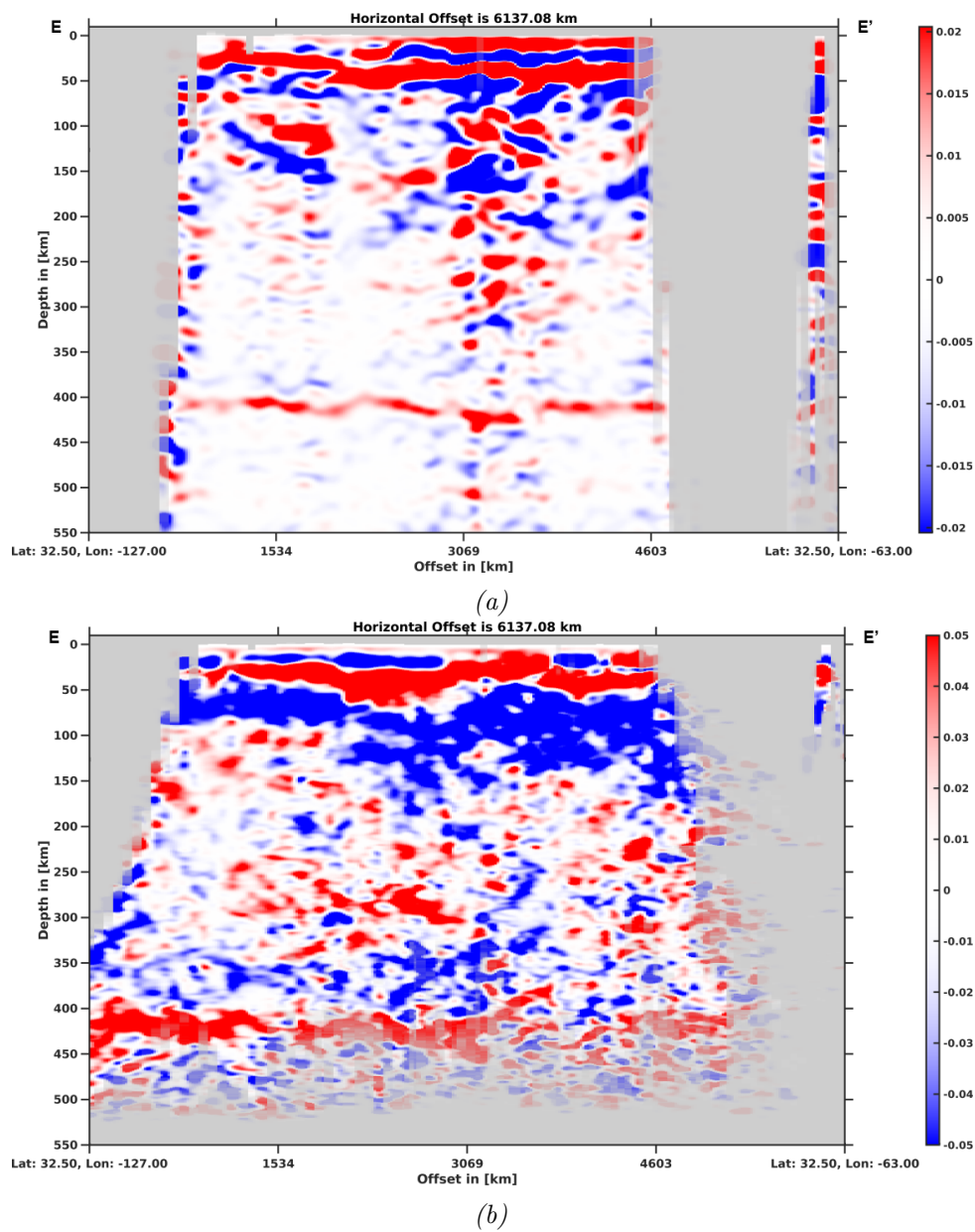
Figure B.6: **Slices through the CCP objects for P-to-S (a) and S-to-P data at 32.5° north (corresponds to profile 5 in Figure B.1).** *The data start greying out for less than 50 and 25 hits per grid point for (a) and (b), respectively.*
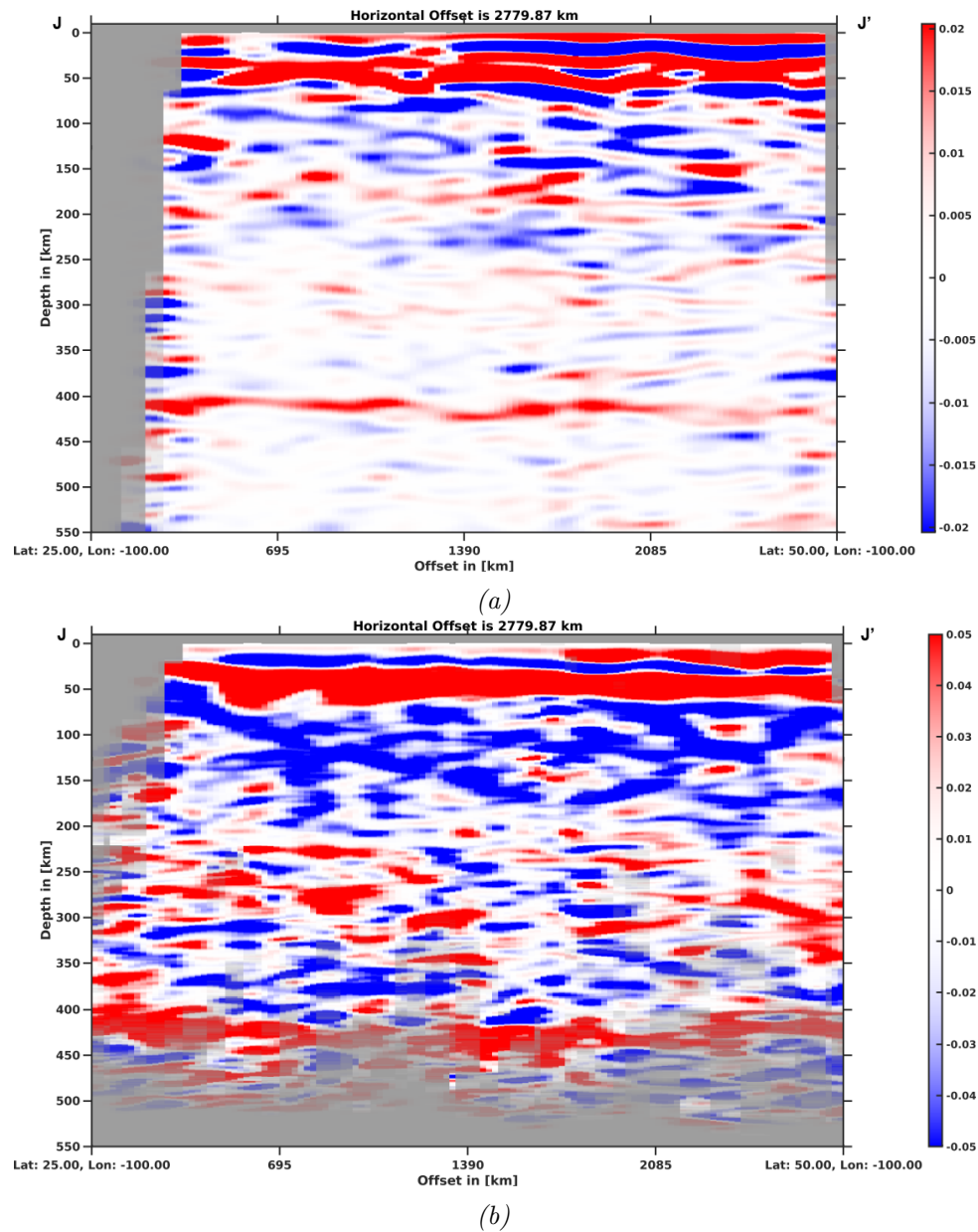
(a)

(b)
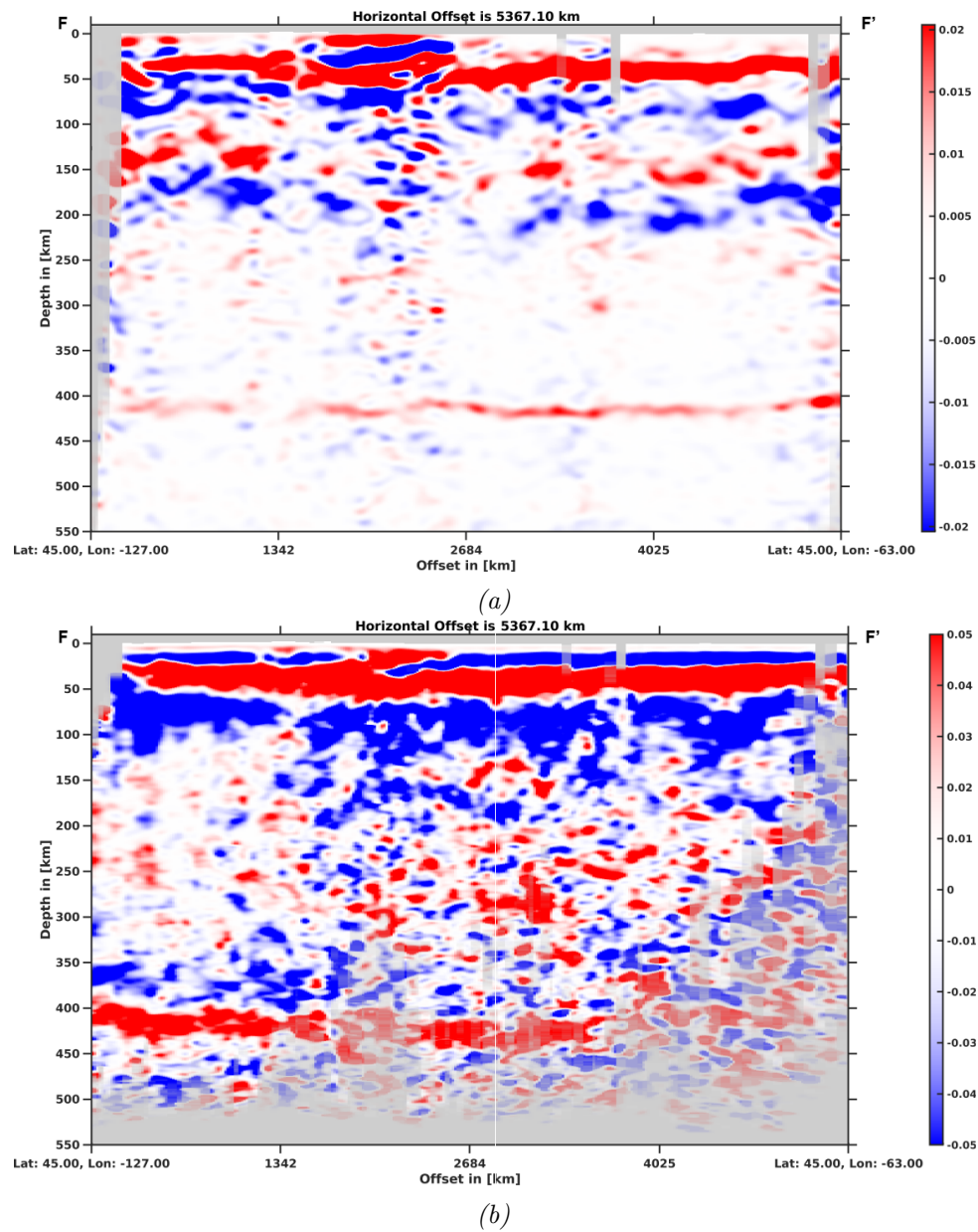
Figure B.7: **Slices through the CCP objects for P-to-S (a) and S-to-P data at 45.0° north (corresponds to profile 6 in Figure B.1).** *The data start greying out for less than 50 and 25 hits per grid point for (a) and (b), respectively.*
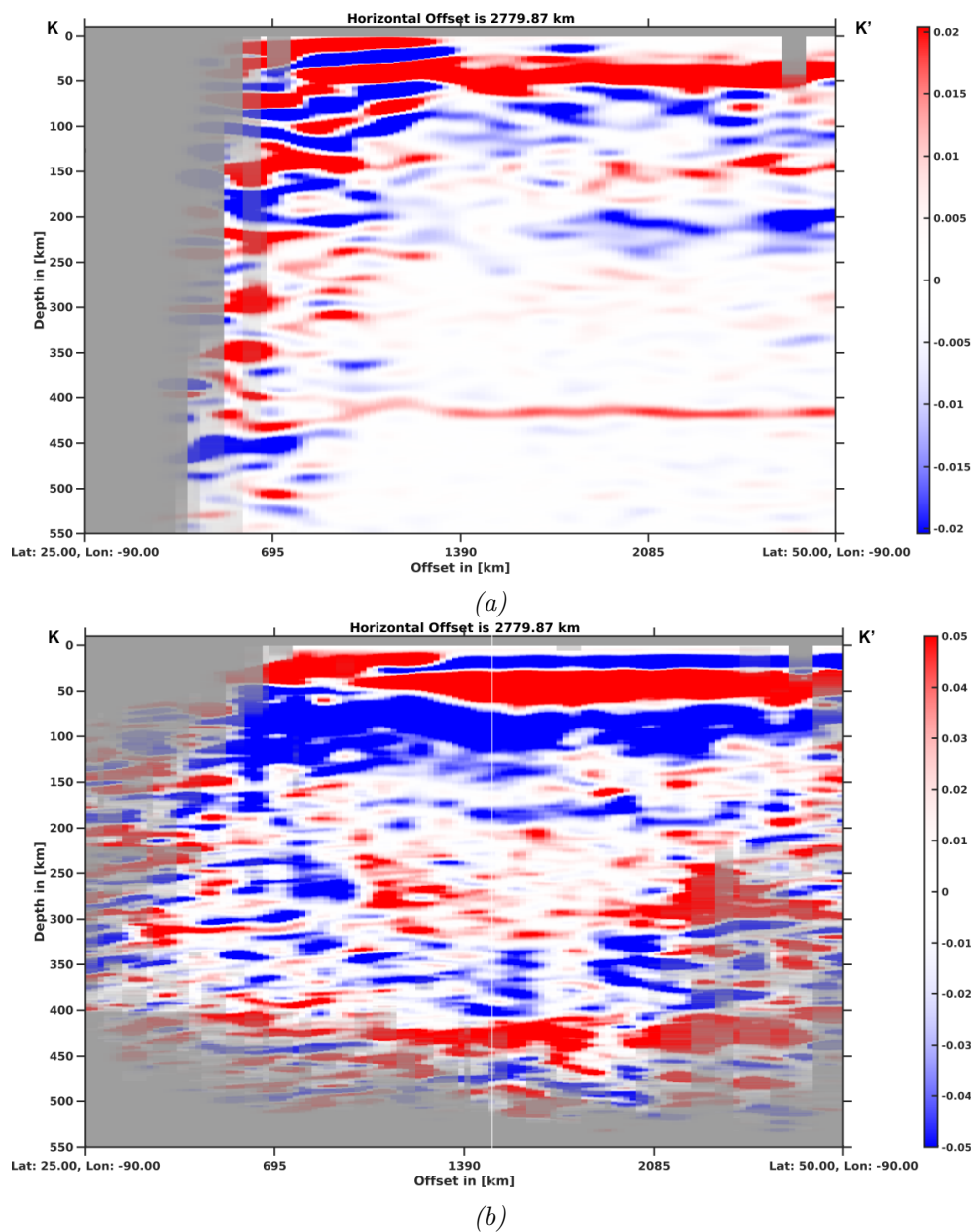
(a)

(b)

Figure B.8: **Slices through the CCP objects for P-to-S (a) and S-to-P data at 49.0° north (corresponds to profile 7 in Figure B.1).** *The data start greying out for less than 50 and 25 hits per grid point for (a) and (b), respectively.*

Figure B.9: **Slices through the CCP objects for P-to-S (a) and S-to-P data at 120° west (corresponds to profile 8 in Figure B.1).** *The data start greying out for less than 50 and 25 hits per grid point for (a) and (b), respectively.*
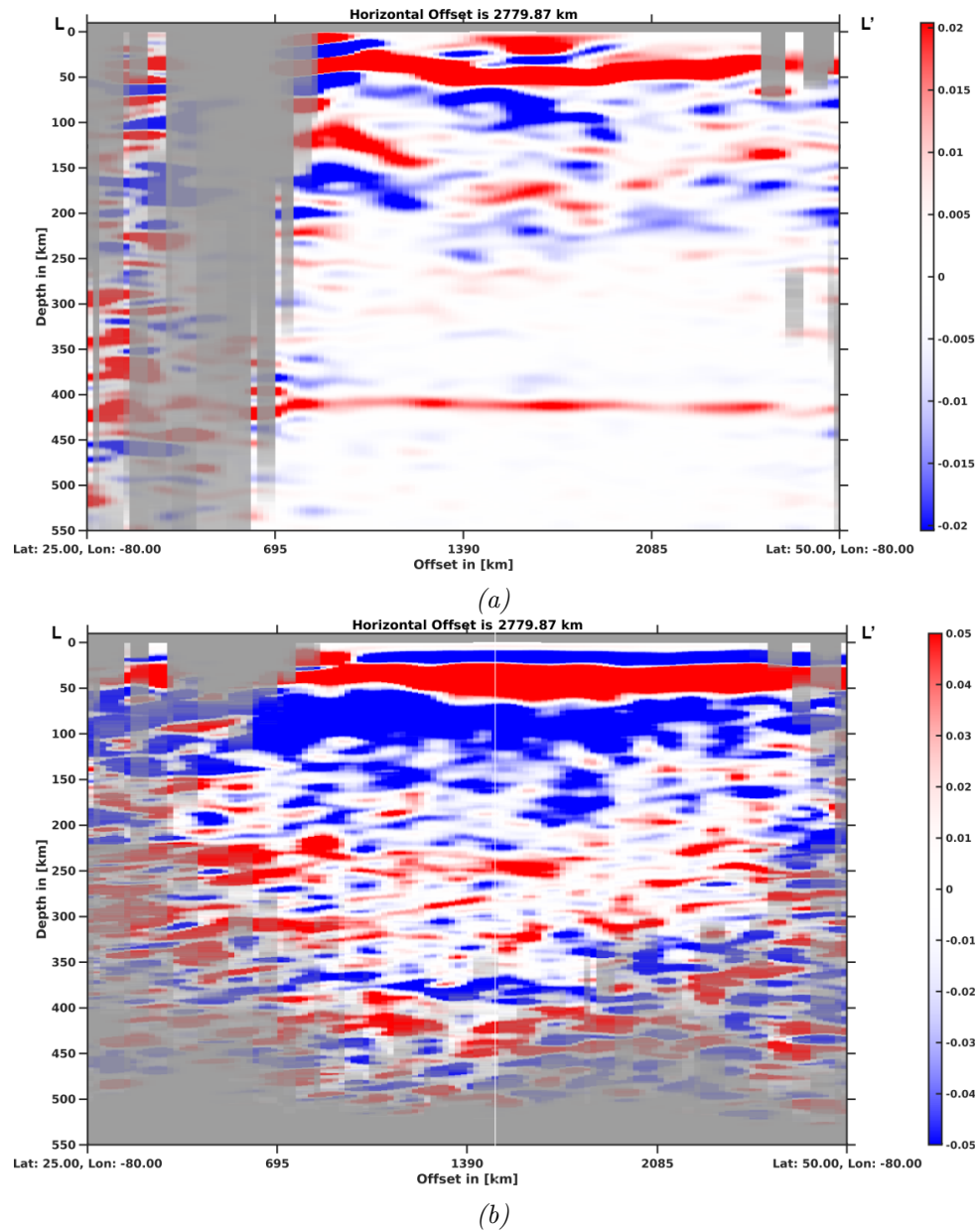
(a)

(b)

Figure B.10: **Slices through the CCP objects for P-to-S (a) and S-to-P data at 110° west (corresponds to profile 9 in Figure B.1).** *The data start greying out for less than 50 and 25 hits per grid point for (a) and (b), respectively.*

(a)

(b)

Figure B.11: **Slices through the CCP objects for P-to-S (a) and S-to-P data at 100° west (corresponds to profile 10 in Figure B.1).** *The data start greying out for less than 50 and 25 hits per grid point for (a) and (b), respectively.*

(a)

(b)

Figure B.12: **Slices through the CCP objects for P-to-S (a) and S-to-P data at 90° west (corresponds to profile 11 in Figure B.1).** *The data start greying out for less than 50 and 25 hits per grid point for (a) and (b), respectively*

(a)

(b)

Figure B.13: **Slices through the CCP objects for P-to-S (a) and S-to-P data at 80° west (corresponds to profile 12 in Figure B.1).** *The data start greying out for less than 50 and 25 hits per grid point for (a) and (b), respectively*

B.2   Negative Velocity Gradient in the Lower Lithosphere
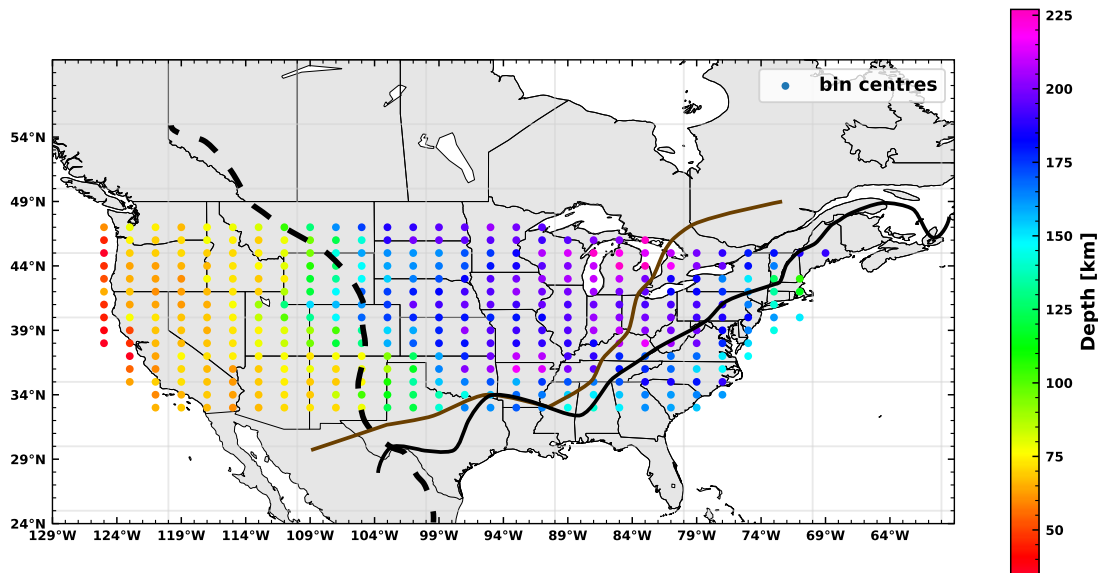
Figure B.14: **Alternative depth pick for the negative velocity gradient in the deep cratonic lithosphere discussed in section 5.2.3.4.** *The picks are indicated as a black, dashed line in the following figures.*
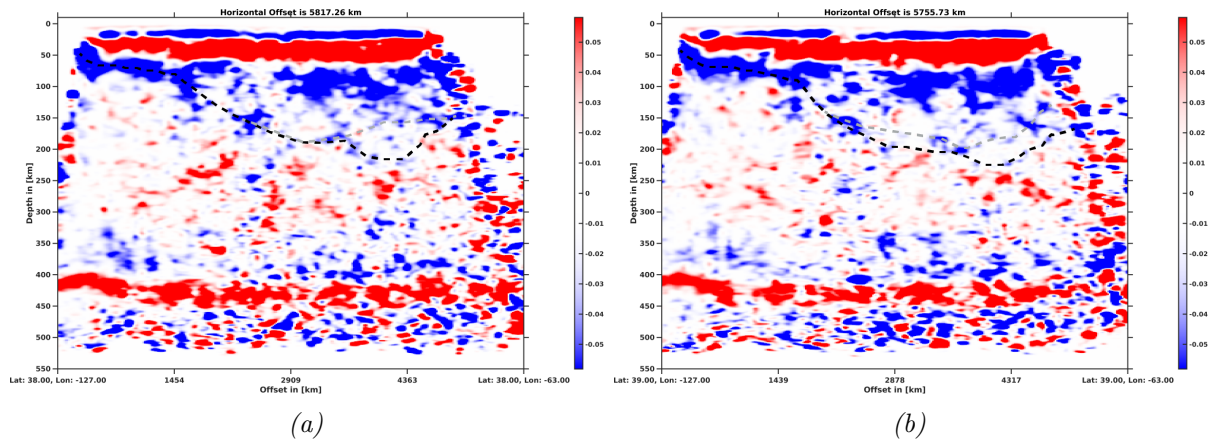

(a)   *(b)*
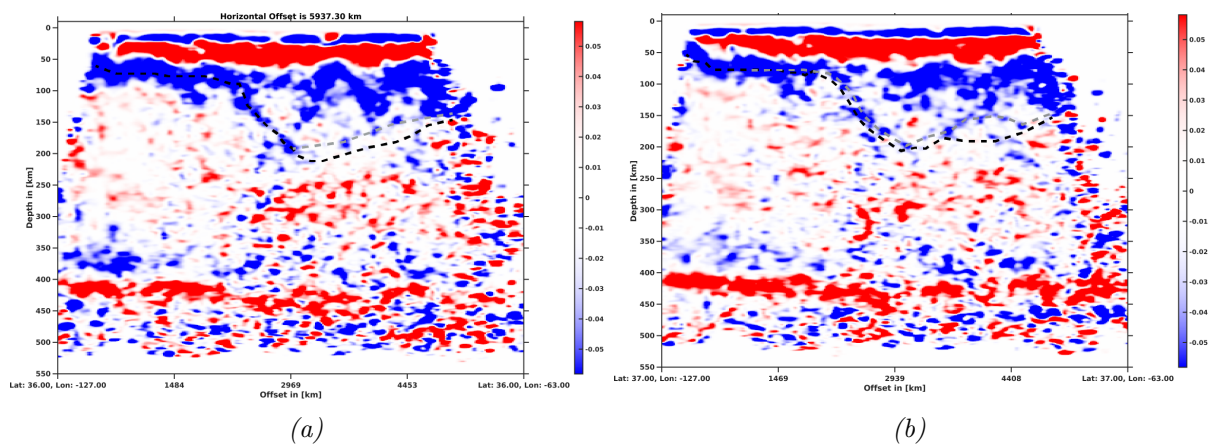
Figure B.15: **The two discussed picks for the deep NVG at 36° north (a) and 37° (b) north.** *The black, dashed line corresponds to the picks for Figure B.14, while the grey, dashed line demarks the picks for Figure 5.24. The sections are slices through S-to-P CCP stacks.*
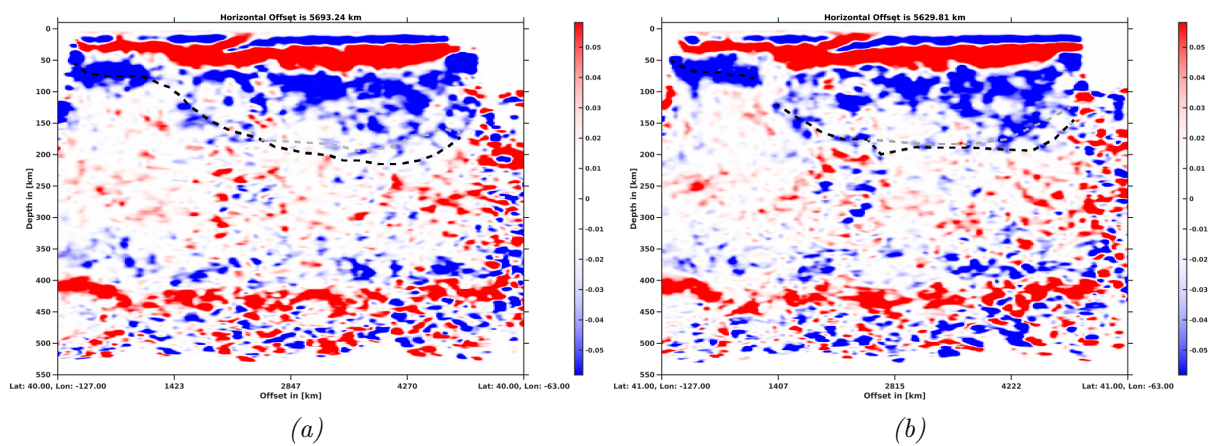
Figure B.16: **The two discussed picks for the deep NVG at 38° north (a) and 39° (b) north.** The black, dashed line corresponds to the picks for Figure B.14, while the grey, dashed line demarks the picks for Figure 5.24. The sections are slices through S-to-P CCP stacks.
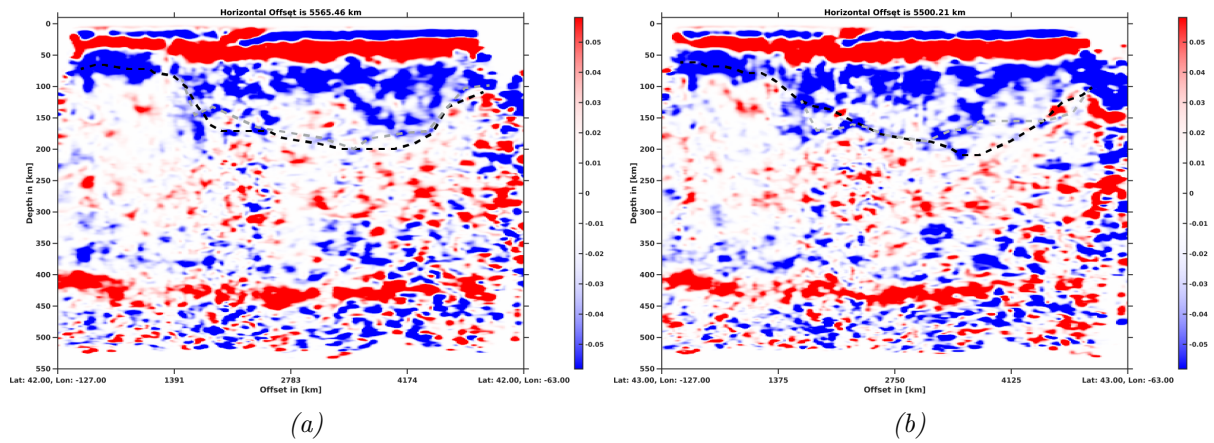

Figure B.17: **The two discussed picks for the deep NVG at 40° north (a) and 41° (b) north.** The black, dashed line corresponds to the picks for Figure B.14, while the grey, dashed line demarks the picks for Figure 5.24. The sections are slices through S-to-P CCP stacks.

Figure B.18: **The two discussed picks for the deep NVG at 42° north (a) and 43° (b) north.** *The black, dashed line corresponds to the picks for Figure B.14, while the grey, dashed line demarks the picks for Figure 5.24. The sections are slices through S-to-P CCP stacks.*
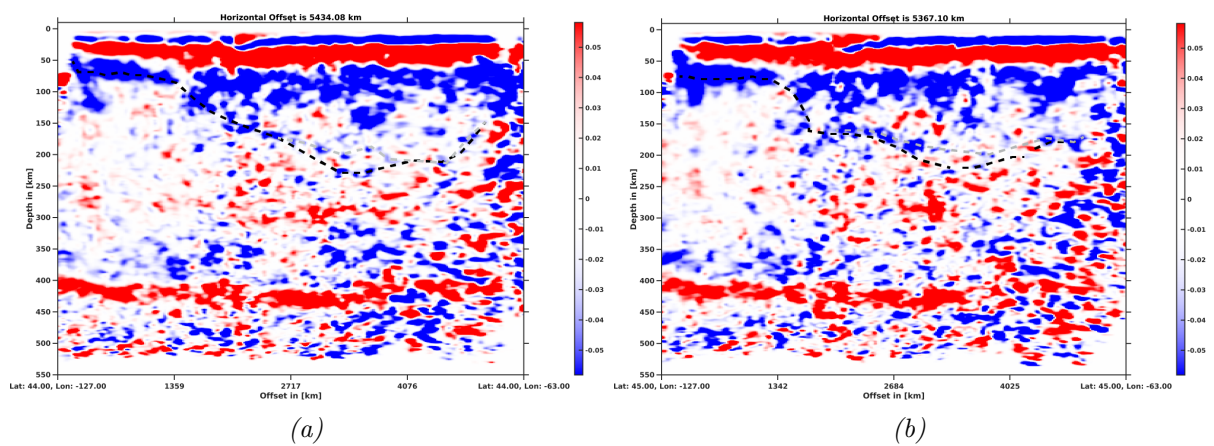

Figure B.19: **The two discussed picks for the deep NVG at 44° north (a) and 45° (b) north.** *The black, dashed line corresponds to the picks for Figure B.14, while the grey, dashed line demarks the picks for Figure 5.24. The sections are slices through S-to-P CCP stacks.*
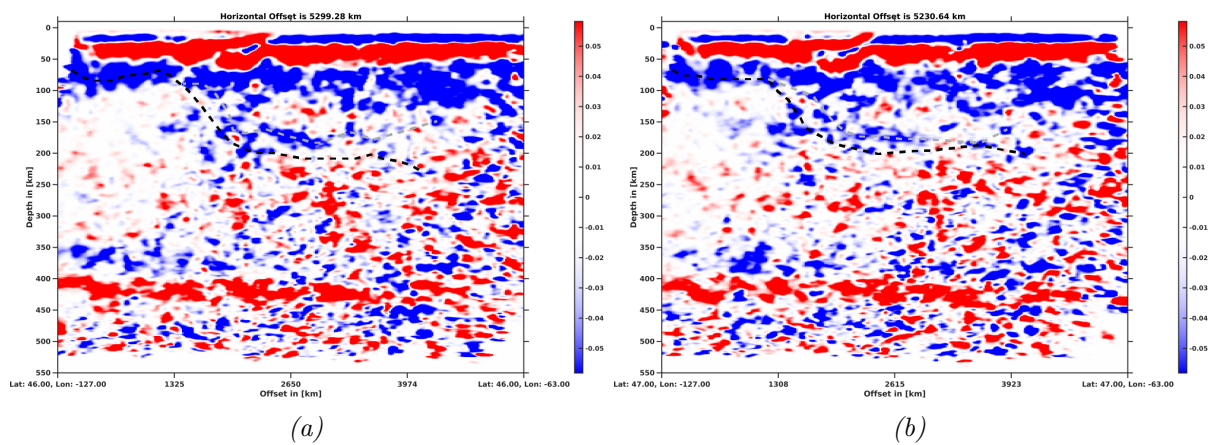
Figure B.20: **The two discussed picks for the deep NVG at 46° north (a) and 47° (b) north.** *The black, dashed line corresponds to the picks for Figure B.14, while the grey, dashed line demarks the picks for Figure 5.24. The sections are slices through S-to-P CCP stacks.*

Appendix C

PyGLImER Source Code (digital)

Due to its length (about 250 pages), the PyGLImER source code is provided in form of a digital appendix containing:

- The PyGLImER source code
- A *Jupyter* notebook to get started with PyGLImER in *./examples* (by Lucas Sawade)
- A *Sphynx* documentation in *./docs/_build/html*

Those contents can be downloaded by following the link below and, subsequently, entering the provided password. The link will expire on 15.12.2020 at 12pm (noon) and should not be distributed to third parties.

`http://u.pc.cd/KQectalK`

Password: **PyhonI5Fun!**

To install PyGLImER follow the instructions below (Those steps require anaconda to be installed and the commands have to be executed in the directory containing *setup.py*):

```
# Create the conda environment and install dependencies
conda env create -f environment.yml


# Activate the conda environment
conda activate PyGLImER


# Install your package
pip install  $InstallationDirectory$
```